A Performance and Model Complexity Study of a Phase Change Material Thermal Energy Storage Heat Exchanger

by

Payton Bartow

A dissertation submitted in partial fulfillment of
the requirements for the degree of

Master of Science

(Mechanical Engineering)

at the

UNIVERSITY OF WISCONSIN-MADISON

2025

Date of final oral examination: December 1, 2025

The dissertation is approved by the following members of the Defense Committee:
Allison Mahvi, Assistant Professor, Mechanical Engineering
Michael Wagner, Assistant Professor, Mechanical Engineering
Douglas Reindl, Professor, Mechanical Engineering

Dedicated to my wife, Ally

Acknowledgments

This work was made possible by many individuals and was part of a larger collaborative effort between several institutions. The institutions and companies on the larger project were UW-Madison, Texas A&M, Purdue, NREL, NETenergy, and Daikin. The work was completed as part of a Department of Energy BENEFIT grant (DE-EE0010905). The opinions expressed in this thesis are the authors and do not reflect those of the US government.

First I'd like to thank the folks at my own institution for their help on this work – my advisors Professor Mahvi and Professor Wagner, and my fellow EOSL and SEL student Ty. Allison, thank you for taking the time to review my work, answer my questions, and fill in gaps where needed. Your patience and generosity has been invaluable throughout this work. My work is a product of your mentorship – thank you for investing in me. Mike, thank you for the advice throughout the project, I don't think my work would be nearly as good without your critiques at our weekly meetings. Thank you both for the time and effort you put into mentoring me, I look forward to continuing to work with you in my PhD. Ty, thanks for building the finite difference model used in this work, answering my questions on it, and giving feedback on my work. I appreciate you and have enjoyed working with you on this project and studying for qualifying exams with you.

A few other people at UW-Madison outside of the DOE project impacted this work as well. Prof. Reindl, thank you for giving me advice on handling refrigerants and for serving on my committee, your feedback was very helpful. I'd also like to thank the undergraduates I had the pleasure of mentoring. Jaclyn, Olivia, and Amelia thanks for helping me with my research and giving me the opportunity to teach y'all about engineering. Each of you made significant contributions to this work - building the experimental facility and prototype, and taking data, and

documenting loop operations. Additionally, the advice and questions from my fellow LET+S, ESOL, and SEL graduate students at weekly meetings or through random conversations also made a big impact on the quality of this thesis, and perhaps my sanity.

Second, thank you to the folks at other institutions. Texas A&M provided the differential scanning calorimetry data used, and some of the corresponding graphics for material property calculations. NETenergy also provided material properties and supplied the parts for the prototype, and support during manufacturing. I learned a lot by visiting y'all in Chicago. Purdue, NREL, and Daikin all provided feedback on the work as well, which improved the quality of this thesis. A list of the folks who helped out at each organization is included below:

- Texas A&M: Dr. Patrick Shamberger and Denali Ibbotson
- Purdue University: Dr. Neera Jain and Joe Broniszewski
- NREL: Dr. Jason Woods and Dr. Ransisi Huang
- NETenergy: Dr. Said Al-Hallaj, Dr. Monica Cook, and Dr. Yana Galazutdinova
- Daikin: Dr. Khaled Saleh and Dr. Keitarou Hoshika

Finally, I'd like to thank my family, friends and prior mentors for giving me the foundation to get here. A large thank you go's to my wife Ally, without your support this wouldn't be possible. A big thank you also goes out to my parents for supporting me and taking interest in my work. Furthermore, I would like to acknowledge my brother Reilly, step family, and in laws – y'all make life worthwhile and were very supportive during this work. To my close friends throughout the past few years – Ethan, Jane, and Jeremy – thanks for the fun distractions skiing, running, and climbing. I couldn't possibly mention everyone, but no one will probably ever read this anyway.

Abstract

Phase change material (PCM) thermal energy storage (TES) heat exchangers (HXs) have the potential to shave and shift loads behind the meter if integrated into heat pumps as a substitute for the outdoor coil during discharge. Traditional design methods for PCM TES HX's in this application require complex and computationally expensive models. This thesis compares a simple analytical model and a detailed finite difference model to determine if the analytical model can accurately capture the physics of these devices and be used for design. The analytical model predicts the time of full discharge given a phase change composite thickness for simulation problems. For design problems the model predicts the thickness of a phase change composite slab given a target discharge time. Therefore, the comparison is conducted by evaluating each model's discharge time against experimental results of the PCM TES HX prototype. Good agreement would indicate an accurate thickness prediction by the analytical model.

Experiments were run to capture on-design and off-design conditions for constant pressure inlet conditions. Off-design conditions include tests that simulate a requirement for greater load or less compressor power in a heat pump. However, the results are not directly extendable to constant power testing, which is what would typically occur in the field in a heat pump. The finite difference model can extend to constant power tests if properly validated, and the analytical model could be upgraded. The experimental results reveal that the analytical model predicts full discharge time for on-design cases with satisfactory accuracy (13.1%) for constant inlet conditions. However large errors in predicted heat transfer rate (148.66 W compared to a maximum heat transfer rate of 500 W) show the analytical model does not work well for simulation problems. In simulation problems instantaneous heat transfer rate is important because it reflects the models ability to predict the load the heat exchanger can handle. The finite difference model suffers from similar error but is able to predict temperature distribution, which could be helpful for device design. Therefore, the

finite difference model will still be an important part of product development. Additionally, the analytical model assumes the phase front moves vertically and does not include sensible heat transfer, which leads to errors in predictions in certain cases.

This work recommends the following work flow for product development: **Use the analytical model to select a prototype thickness, then build and simulate the model with a more complex continuum approach.** Testing and simulating with a finite difference model will help solve problems in design commonly observed like PCM supercooling and hysteresis. Hysteresis was observed in the experimental results for this work. The capacity for melting tests was near the theoretical target, 0.846 kW-hr, but the capacity for evaporator tests varied from 0.77 kW-hr to 0.614 kWhr for final temperatures of 15.1°C and 18.97°C respectively. The results indicate higher discharged energy at lower temperatures, which shows that energy is still stored in the chemical bonds of the PCM and that differences in nucleation of crystals is leading to different behavior in freezing than melting (hysteresis). The temperature distribution prediction in the finite difference model were helpful for diagnosing this issue.

Table of Contents

List of Tables

List of Figures

List of Symbols and Abbreviations

A	area [m^2]
C_p	specific heat [J kg^{-1} K^{-1}]
V	Volume [m^3]
D	diameter [mm]
q	Heat transfer rate or discharge rate [W]
E	Discharged Energy [kW-hr]
k	Conductivity [W/m-K]
L	Latent heat [J/kg]
h	Enthalpy [J/kg]
R	Thermal Resistance [W/K]
T	Temperature [°C] or [K]
ΔT	Temperature difference [°C] or [K]
P	Pressure [pa] or [kPa]
htc	Heat transfer coefficient [W/m^2-K]
th	Thickness [m]
s	Entropy [J/kg-K]
w	Mass fraction [-]
W	Work [W]
t	Time [s]
$\dot{m}$	Mass flow rate [g/s]
C_v	Flow Coefficient [Gal/min] of water at standard conditions

$\dot{V}$	Volumetric Flow Rate [m^3/s]
N_1	Unit Constant for Flow Coefficient
SG	Specific Gravity [-]
ΔP	Pressure Drop [kPa]
%PO	Percentage open [%]
u	Uncertainty (units vary)
r^2	Coefficient of determination [-]

Greek Symbols

ρ	Density [kg/m^3]
Φ	Volume fraction [-]
κ	Integration Constant [J] or [kW-hr]

Subscripts, Superscripts, and Abbreviations

in	inlet
out	outlet
hx	heat exchanger
pcc	Phase change composite
s	Solid
l	liquid
t	Phase change material transition temperature
melt	Melt temperature

$\dot{q} - const$	When the constant power region ends
Final	When the phase front reaches the thickness of the HX prototype
HTF	Heat transfer fluid
TES	Thermal Energy Storage
Sat	Saturated
Amb	Ambient
“	Per unit area
Conv	convection
Cond	condenser
Evap.	Evaporator
Exp	Experiment
Unc	Uncertainty
RMSE	Root Mean Square Error
Sub	Subcooling (relative to PCM or refrigerant)
Sup	Superheat (relative to PCM or refrigerant)
Gr	graphite
Tot	total
VC-Orig.	Original Vapor Compression Cycle
VC-TES	Vapor Compression Cycle with TES
∥	Parallel (axial – x)
⊥	Vertical (height – y)
Heat-element	Heating element in post heater or preheater

Post	Postheater
Reg	regression
DSC	Differential Scanning Calorimetry

Chapter 1: Introduction

Energy storage has the potential to reduce electricity costs for consumers and suppliers of the current grid. The current electrical grid needs energy storage to reduce suboptimal economic effects from variation in electricity demand and production, including the mismatch between the time generation of electricity (supply) occurs and demand. Figure 1.1 illustrates the variation of electricity use over a 24-hour period with and without energy storage.

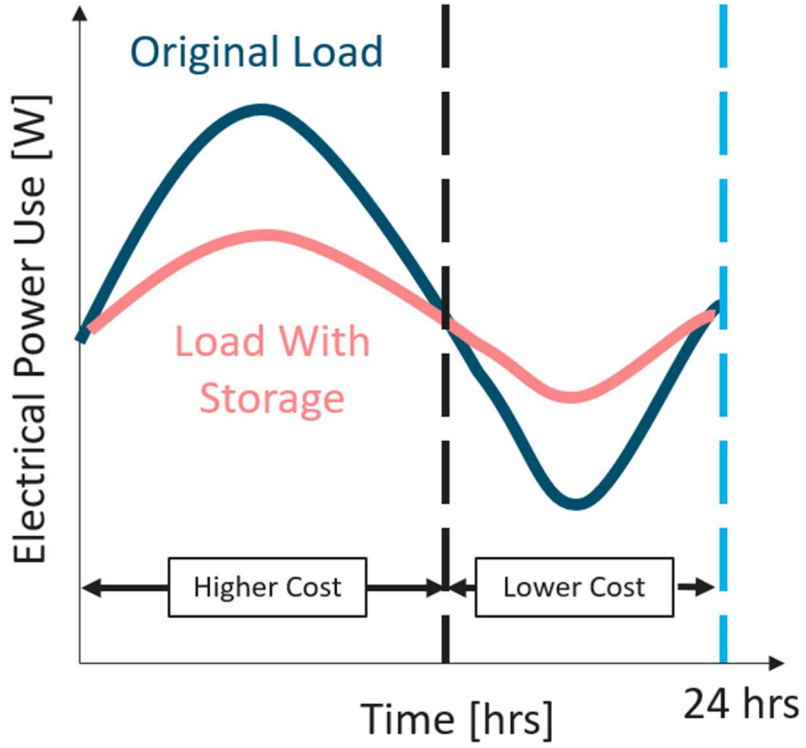

Figure 1.1: A generalized electrical power use profile for a day in the United States current grid. This plot was drawn by hand and is not actual data.

The original electricity use profile has peaks during the day and valleys at night. Users can discharge storage at peak times and reduce peak load, which is often called *peak shaving* in literature. These peak loads are shifted to the times when the electricity use is low by charging the storage, which is called *load shifting*. If discharge occurs at times when electricity cost is high and charging occurs when electricity cost is low, energy storage can save consumers money.

Furthermore, during peak hours utilities need to have infrastructure (power plants, transmission, and distribution) available to meet demand. Storage can shave the peak demand and reduce the scale of infrastructure needed, lowering capital costs for utilities and possibly increasing profit. Therefore, there are potential economic incentives for consumers and utilities to implement energy storage. The interaction of these parties is complicated though and has socioeconomic and policy dimensions, which are further complicated by penetration of renewable energy into the grid.

The future grid will have greater electricity variation, which will increase the need for energy storage. As the cost of solar and wind continues to decrease [1] and decarbonization initiatives continue globally their integration into the grid will increase. In some regions of the United States renewables already make up a significant portion of the electricity mix, and nationally make up 21.4% of electricity generation [2]. Solar and wind have a great degree of variability. Sunshine, and therefore solar, is abundant during the waking hours and absent at night. Wind also varies daily but has a more consistent load generation profile (depending on location). Different regions will likely have different mixes of renewable electricity generation methods. To deal with the variation in generation intrinsic to renewables, suppliers and consumers will need to implement short duration and long duration storage – short duration storage is the subject of this thesis.

To align energy storage incentives for consumers and distributors in a high variability grid careful policy design is needed. In a high variability grid, a storage distributor (power plant) or user (consumer) would charge energy storage when production is abundant and discharge when energy flows are scarce. In this scenario, the cost of electricity may be low when energy is abundant and high when it is not. However, consumers could use behind the meter storage and on-site renewables, becoming prosumers (selling net electricity back to the grid), and complicating

interaction with power markets. Although, not all utilities allow prosumer interaction with the grid. The energy storage developed in this work could be implemented behind the meter. Forrester et al. discuss the implementation of behind the meter storage with residential solar and its interaction with electricity markets. They suggest incentives for behind the storage meter users to interact with the market when storage is idle [3]. The research summarized in this thesis does not address this topic. However, this discussion highlights the complexity of the economics and policy of integrating storage into the grid on the consumer side, and that more work is needed to develop policies that ensure the technology works for all parties involved.

Buildings are a target area for energy storage, and thermal energy storage (TES) integrated into space heating and cooling systems could fill some of the demand. Buildings account for 40% of energy use and 75% of electricity use in the United States [4], [5]. Additionally, in the United states buildings account for 31.1% of CO_2 emissions (17.7% indirectly through electricity use and 13.5% from on-site emissions) [6]. Therefore, decarbonizing buildings is essential to a low carbon economy. Heating and cooling specifically accounts for 37% of electricity use in the United States [4], [5]. Thus, building space heating and cooling is key area for energy storage implementation. Odukomaiya et al. compared the levelized cost of storage of lithium ion batteries and thermal batteries (thermal energy storage) in buildings and showed that thermal battery cost was less for many levels of technology maturity and climates [7]. Thus, integrating thermal energy storage (TES) directly into electrically driven space heating and cooling can decrease costs for current grid users and suppliers, and enable increased low carbon generation.

1.1 Thermal Energy Storage Review

Thermal energy can be stored in sensible, latent, and thermochemical materials, and each of these categories has different energy density, technology maturity, and cost. Different physical

phenomena describe each form of TES. Sensible materials store energy via an increase in temperature proportional to specific heat, while latent thermal energy storage utilizes phase change (usually liquid to solid or vice versa), and thermochemical TES uses a reversible chemical reaction. Figure 1.2 shows a qualitative sketch of the behavior of each of TES in a heat exchanger (HX) and their qualitative energy storage vs. temperature curve.

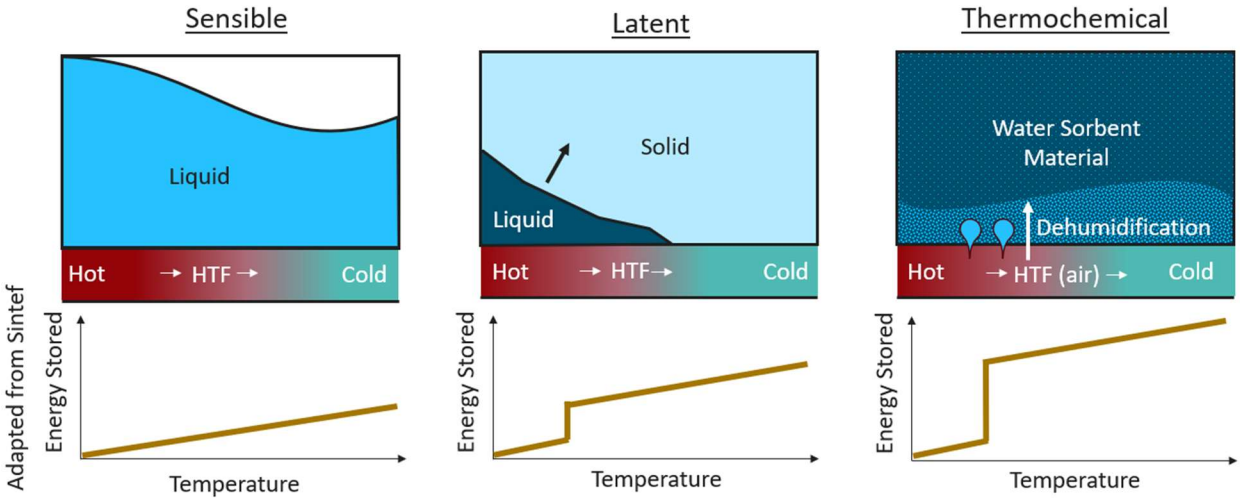

Figure 1.2: The physical behavior of different types of TES illustrated using a heat exchanger. The energy stored vs. temperature defines the physical behavior as well and gives the reader an idea of energy density. These plots were inspired by an article put together by European R&D firm, Sintef [8]. The heat transfer fluid always transfers heat to the TES medium. So if the TES typically functions as a heat sink it's discharging mode, and if it's typically a heat source it's charging.

In the heat exchanger the fluid comes in hot and leaves cold transferring its heat to the energy storage medium. This heat transfer discharges or charges the storage depending on the desired operation, which depends on the system it's implemented in. For the sake of this discussion the heat transfer is charging the energy storage medium. The energy vs. storage curves show the relative energy density of each type of PCM, indicated by the energy stored at the end of charging (hotter temperatures). Sensible has the lowest energy stored, while latent is somewhere in the middle, and thermochemical has the highest storage capacity. Table 1.1 quantifies the energy density differences as well as the technology maturity and cost.

Table 1.1: The energy density, maturity, and cost of each type of TES are compared to show the benefits and drawback of each form of TES. The sources for information are cited. No source could be found on a real-world implementation of thermochemical TES. Additionally, the latent energy density finds the lower bound in [9] and the upper bound in [10] .

	Sensible	**Latent**	**Thermochemical**
Energy Density	39.3-74.7 kWh/m^3 [10]	41.7-130 kWh/m^3 [9], [10]	100-800 kWh/m^3 [9]
Maturity	High	Low-Medium	Low
Cost	Low [10]	Medium [9]	Medium-High [9]

The DOE and Sandia both state that latent and thermochemical have lower technology maturity [5], [11] than sensible TES. To that point, sensible TES for high temperatures has been implemented in concentrated solar power plants using molten salts, common household water heaters, and many other areas. Latent TES's maturity is listed as low-medium because it has been implemented in some applications [12]. Thermochemical TES is the youngest technology as a brief literature search yielded no evidence of its implementation. The cost of the sensible TES in building applications is less than latent and thermochemical according to James et al. [10], although this is not true at small scale. A recent paper by Zhang et al. comparing latent and thermochemical TES in the United Kingdom states that domestic capital costs for each category are 9-46 and 9-91 £/kWh respectively [9]. Hence, the reason why latent is listed as having a medium cost and thermochemical is listed as having a medium-high cost.

Currently, all types of TES have active research and development, because one type is likely not a one size fits all solution for electricity grids around the globe. Climate, policies, and social factors also determine whether these types of TES suit a particular region and application.

Research and development focuses on a variety of areas from control schemes that take into account weather and electricity prices [13] to storage material design [14]. All types of TES have had research conducted on applying devices (heat exchangers) to buildings. For example, much of the information on sensible TES in Table 1.1 came from a paper by James et al. on the design of a high energy density low cost sensible TES devices [10]. Furthermore, Woods et al's paper on Ragone plots for latent TES provides a good discussion of latent TES device design [15]. Lastly, there are a variety of groups developing thermochemical TES: Zaleski et al. [16] and Zeng et al. [17] discuss system design, while Galazudinaova et al. focus on device design [18].

This project uses latent TES because it stores and releases heat at constant temperature and because it has some advantages over other TES types, although there are disadvantages as well. James et al. showed that sensible TES could be competitive with some latent TES materials or phase change materials at a 21.2 kW-hr scale between temperatures of 20 and 80 °C (PCMs – in literature latent TES is often referred to as PCM TES, and this work will use these terms interchangeably). Sensible TES was more competitive than paraffin wax PCM TES, but less competitive than salt hydrates [10]. Salt hydrates are not a panacea though. An additional factor not recorded in Table 1.1 is degradation of storage mediums. Latent and thermochemical TES both experience significant degradation. Latent TES experiences degradation when salt hydrates are used, which is not ideal because salt hydrates set the upper limit on energy density in Table 1.1 [10], [19]. On the other hand, thermochemical TES is generally known to experience degradation (and often also uses hygroscopic salt hydrates), which is a key focus of its research and development [5], [20]. Less energy dense PCM's, like paraffin wax don't suffer from as great of chemical degradation [19]. In summary, latent TES is competitive with sensible TES's energy density, but low cost, high density salt hydrates need work.

1.2 Project Background

The history of latent TES frames the need for innovation. Latent TES has been in use for at least two centuries, if not longer. The ice box was first documented in 1802 by Thomas Moore, which was an early form of latent TES for food storage [5]. The timeline in Figure 1.3 shows a picture of a 1920's ice box and a timeline of development events that followed.

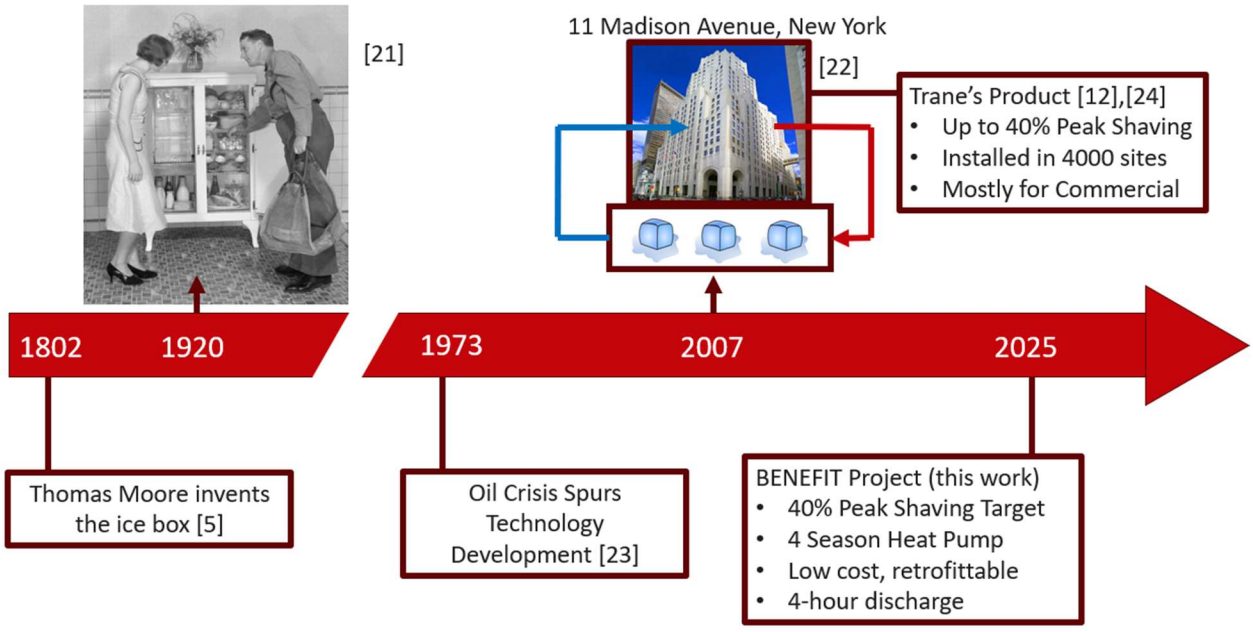

Figure 1.3: A timeline of latent (PCM) TES development that puts the project into context at a high level. Images for the icebox come from [21]. Images for the 11 Madison, Avenue building come from [22].

The timeline shifts during the oil crisis in 1973 because President Richard Nixon's project independence motivates energy technology development in the US. This eventually leads to implementation in buildings [23]. For example, latent TES is currently being used for up to 40% peak demand reduction (peak shaving) at the 11 Madison Avenue building in New York. The "ice battery" system at 11 Madison Avenue has been installed since at least 2007 [24], and similar thermal batteries are installed in 4000 other commercial buildings. However, there are 6 million commercial buildings globally so the penetration of the technology is not very high thus far [12]. Ice's energy density is 84.96 kWh/m^3, so recent efforts have focused on increasing volumetric

energy density using salt hydrates as already discussed. However, innovation is required beyond the material level to increase technology readiness. Therefore, this project focuses on developing a TES HX that can be integrated into existing HVAC systems and meet a minimum of 40% peak shaving in heating and cooling seasons over a four-hour discharge cycle.

The broader project focuses on the development of an HVAC TES heat pump system, and this thesis focuses on the TES HX. The system is shown in Figure 1.4.

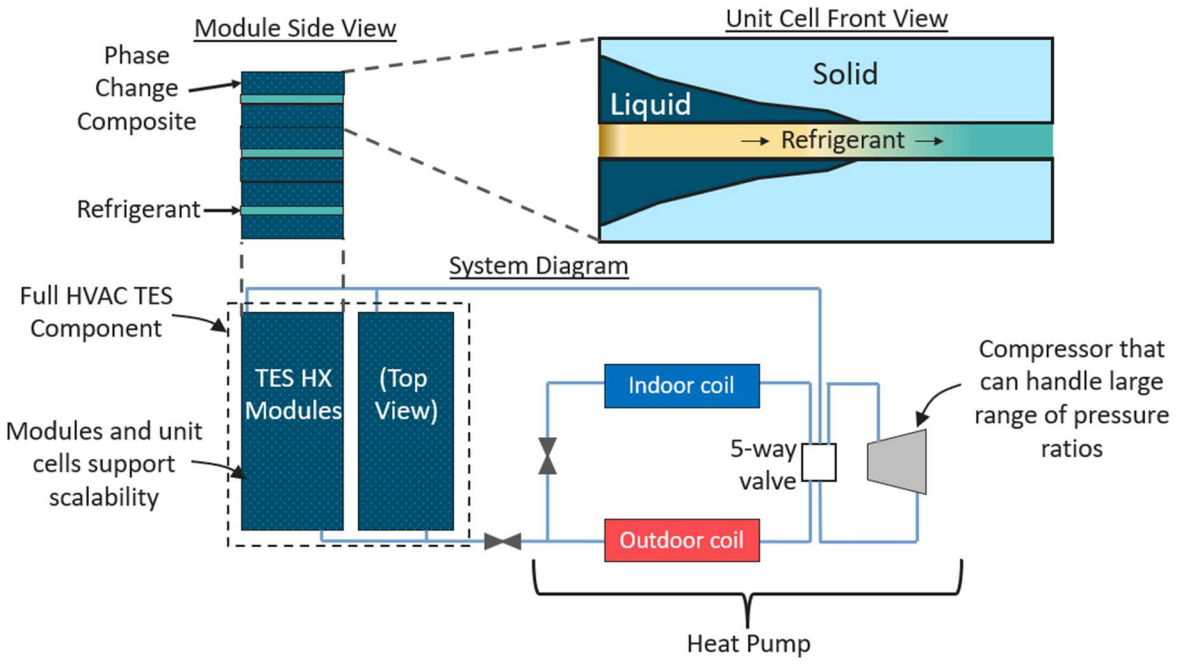

Figure 1.4: The heat pump-TES system with different scales of the TES unit indicated ranging from unit cell to full scale.

The system is a variable refrigerant flow style vapor compression system with a PCM TES HX in place of one of the indoor heads. The TES component has several HX modules plumbed in parallel. Each module is made up of ~2 kWh unit cells stacked on top of each other, which are also plumbed in parallel. This makes the system extremely scalable so it can be used in a variety of building sizes and types (commercial vs. residential). Finally, the PCM is combined with high thermal

conductivity porous graphite to improve the charge and discharge performance. The combined material is called phase change composite (PCC).

1.3 System and TES HX Operation

The system operates in three distinct modes, standard heat pump mode, discharge mode, and charge mode. Heat pump mode is presented in Figure 1.5.

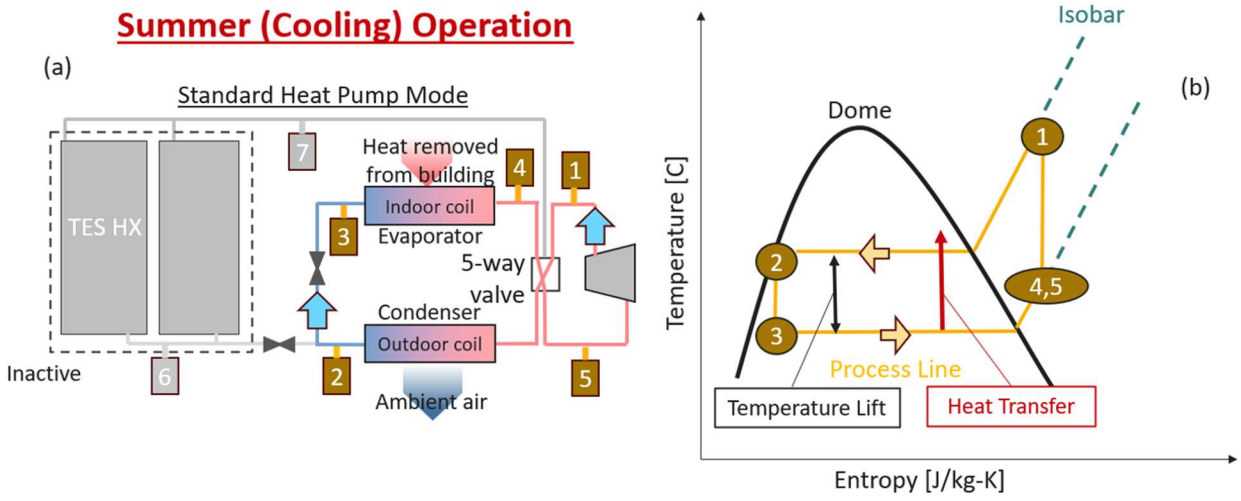

Figure 1.5: (a) The system in standard heat pump mode and cooling operation (b) the idealized T-s diagram for the vapor compression cycle.

The heat pump illustrated in Figure 1.5a is a standard vapor compression cycle operating in cooling mode. The idealized (isentropic) vapor compression cycle is illustrated in Figure 1.5b on a T-s (temperature-entropy) diagram. The work added by the compressor moves heat across an adverse temperature gradient, which is often called the temperature lift. The key to achieving peak shaving in this system is lowering the temperature lift during discharge. This is done by selecting a PCM transition temperature that is lower than the ambient temperature. System operation during discharge mode illustrates this well, as seen in Figure 1.6.

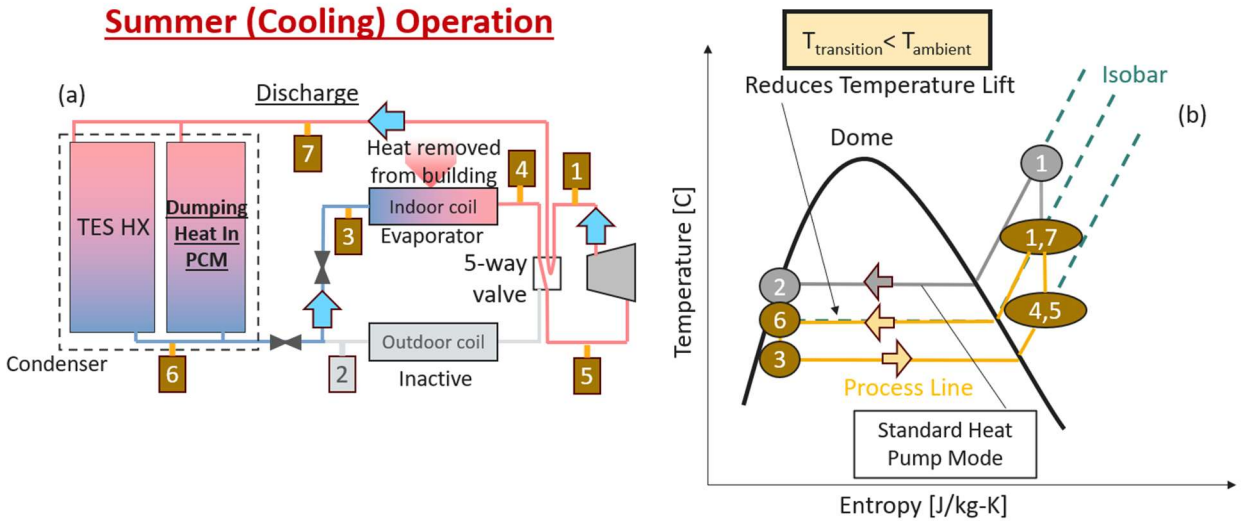

Figure 1.6: (a)The system in discharge mode during cooling operation (b) the idealized T-s diagram for discharge of the system

In discharge mode the TES HX replaces the outdoor coil (condenser in cooling mode), as seen in Figure 1.6a. The refrigerant saturation temperature inside the condenser is then fixed relative to the PCM transition temperature instead of the outdoor temperature. The difference in condenser operating temperature is illustrated in Figure 1.6b. The lower temperature lift reduces the pressure ratio across the compressor, ultimately reducing power consumption and therefore achieving peak shaving. Throughout discharge operation the condenser pressure will rise to accommodate constant pressure discharge.

After the TES has been discharged, it must be charged so it is ready for the next peak period. Charging mode as illustrated in Figure 1.7, where refrigerant is split between TES and the indoor coil that provides cooling to the building.

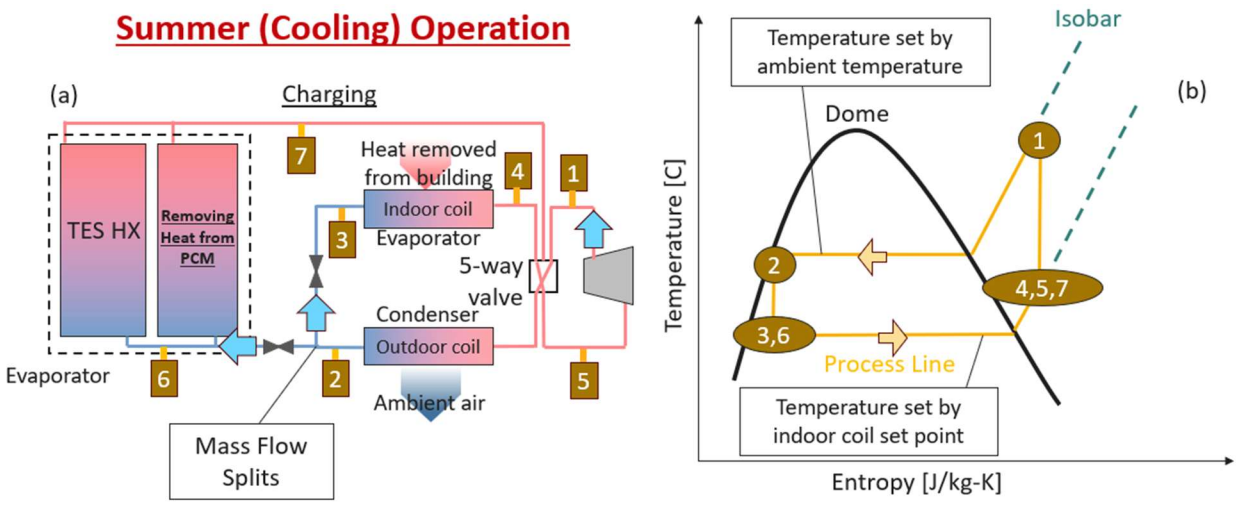

Figure 1.7: (a) The system charging the TES during summer operation.(b) the idealized vapor compression cycle for charging.

To operate the system in charging mode in the summer, the TES HX and indoor coil both act as evaporators. Therefore, the system must operate at a higher mass flow rate because mass flow rate splits as seen in Figure 1.7a. The operating temperatures of the system are still the same as in standard heat pump mode because the temperature lift is set by the ambient temperature and room set point, as illustrated in Figure 1.7b. Ultimately, the compressor operates at higher rotational frequency (rpm) to achieve a higher mass flow rate and the same pressure ratio as in standard heat pump mode.

The system is designed for operation during cooling and heating seasons, which informs PCM selection. To operate the system during heating season the cycle is the same except the location of evaporation and condensation switch in each mode. In standard heat pump mode the indoor coil becomes a condenser and the outdoor coil becomes an evaporator. Heating season discharge mode is illustrated in Figure 1.8.

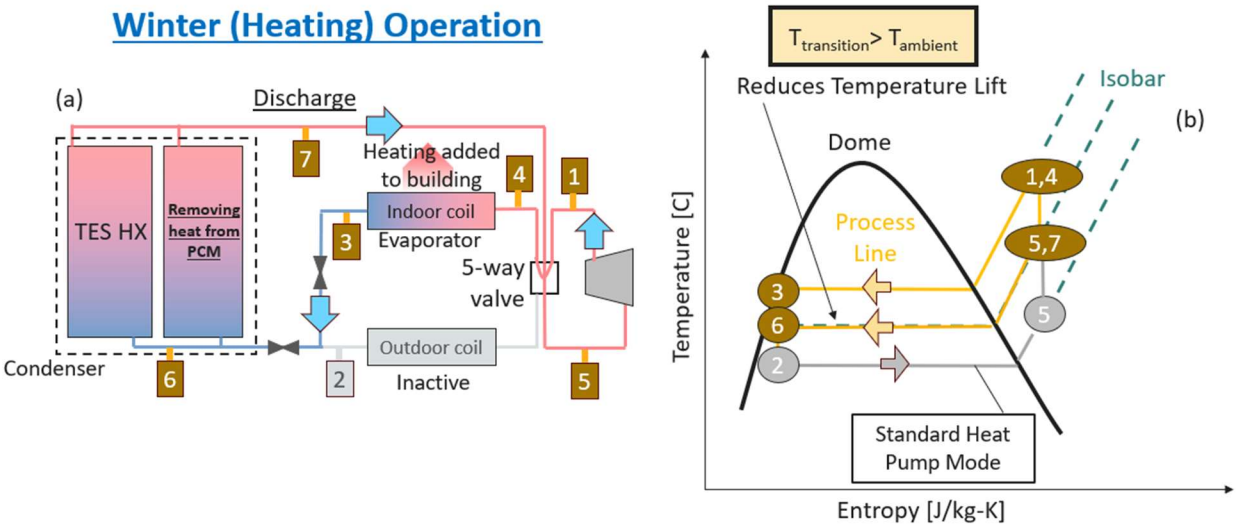

Figure 1.8: (a) Discharge mode during winter operation.(b) the vapor compression cycle during heating discharge.

In heating discharge the TES HX becomes an evaporator (adding heat to refrigerant) as seen in Figure 1.8a, and in charging it's a condenser (heating PCM back up). For peak shaving to occur during heating discharge the PCM transition temperature must be greater than the ambient temperature as illustrated in Figure 1.8b. Furthermore, the compressor operates over a smaller pressure ratio than in standard heat pump, heating mode, requiring less work. Therefore, to design a system that can operate in heating and cooling without changing the PCM transition temperature must be selected based on the ambient temperature during heating and cooling season. During cooling season the PCM transition temperature must be lower than the ambient temperature and during heating season the PCM transition temperature must be higher. Therefore, a PCM temperature near a comfortable room temperature (~20 °C) was selected for this work to ensure this requirement was met.

To implement the thermal energy storage system innovation needs to occur at the TES HX level first. The design and performance of the TES HX is the main subject of this thesis. The unit cell scale TES HX demonstrates the basic operation of the device and is the main focus of this

work. The TES HX consists of a fluid domain and a PCM domain, which both undergo phase change. A simplified illustration of a unit cell at two different times during a constant inlet test are shown in Figure 1.9.

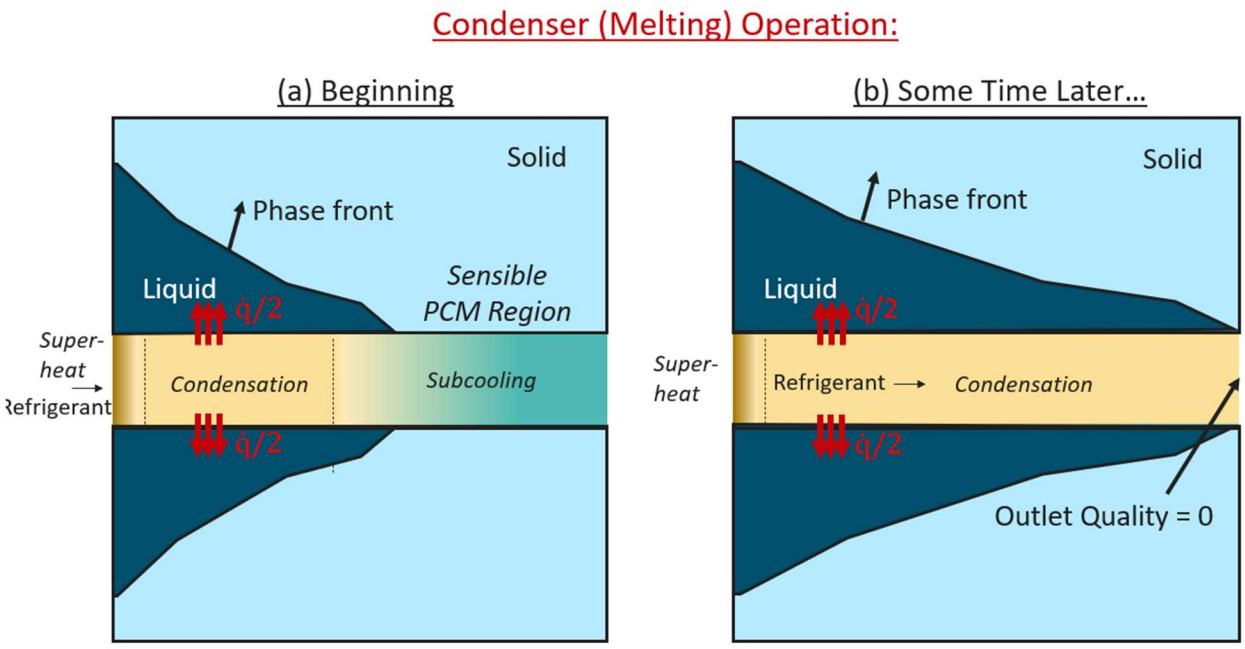

Figure 1.9: The evolution of the PCM TES HX throughout testing. The gradient in the refrigerant domain is used to indicate temperature. (a) represents the beginning of the test and (b) represents some time midway through the test when the outlet becomes a saturated liquid.

Figure 1.9a shows the beginning of the test. The refrigerant enters superheated and then after a short length of travel begins to condense, heating up the initially solid PCM and ultimately melting it. Most of the heat transfer occurs during condensation as the latent heat of phase change of the refrigerant defines the majority of the possible heat transfer available. Initially, the outlet of the TES HX will be subcooled and a small sensible PCM heat transfer region will exist downstream in the HX. As time progresses the magnitude of outlet subcooling will decrease until the outlet becomes a saturated liquid as seen in Figure 1.9b. Simultaneously the phase front will develop and reach the outlet of the heat exchanger. After the time illustrated in Figure 1.9b the phase front will move vertically until no solid PCM is left. The progression of the melt front (phase front) defines

the performance of the HX. Demonstrating and modeling the performance of the heat exchanger is the main subject of this thesis.

1.4 Research Questions & Thesis Organization

The goal of this thesis is to address gaps in literature in device design, demonstration, and modeling. PCM TES HX's are abundant in literature – prior efforts have focused on a variety of systems, and modeling efforts cover the entire range of computational complexity. The goal of this work was to address two research questions:

1. *How is this PCM TES HX original, and how does it perform?*
2. *What computational complexity is needed to characterize PCM TES HX devices with evaporating or condensing heat transfer fluids?*

The first question focuses on defining the originality of the device in the context of literature and demonstrating its performance. The second question focuses on comparing high fidelity and low fidelity modeling methods to create modeling tools whose target audience could be HVAC designers rather than researchers.

Each chapter will help address both research questions. The chapters that make up this thesis are listed below:

- **Chapter 1: Introduction** – Specifies the scope of the work conducted
- **Chapter 2: Literature Review** – Contextualizes each research question relative to field
- **Chapter 3: Design & Modeling** – Defines geometry, material, and models
- **Chapter 4: Experimental Set Up** – Explains experimental facility and prototype
- **Chapter 5: Experimental Results** – Illustrates findings from experiments
- **Chapter 6**: **Model Complexity Study** – Validates and compares models for design
- **Chapter 7: Conclusion** – Summarizes findings and future directions

To address the first question a literature review defines the originality, while modeling and experiments demonstrate the performance of the HX. A literature review of PCM TES HX's in the domestic, food refrigeration industry and building industry was conducted to contextualize the HX developed in this work relative to vapor compression cycles. Furthermore, experimental observations demonstrate the performance of the device, and analytical modeling illustrates the parameters which drive the behavior observed in the HX.

The second research question was addressed by constructing an analytical model and validating its performance against the finite difference model and experiments. The analytical model reduces the computational effort needed to design PCM TES HX's for similar systems, which could have a big impact on technology adoption by providing a simple tool for designers to use. A literature review defines the modeling field and the analytical models that have been developed in the past. Moreover, the design and modeling section defines the mathematics of each approach used in this work and ultimately the geometry chosen for experimental validation. The experimental set up section describes the experiments run to validate the models and the complexity study illustrates the findings.

Chapter 2: Literature Review

The literature review contextualizes both research questions relative to work previously conducted on PCM TES HX's. The first section reviews PCM TES HX's in the HVAC&R field to demonstrate the originality of the system this HX is designed for. Furthermore, the second section describes modeling efforts previously conducted.

2.1 Literature Review of PCM TES HX's in Vapor Compression Cycles

Literature on TES PCM HX's is broad and covers many fields. Some researchers have integrated PCM TES HX directly into vapor compression cycles, while others have added them to secondary fluid loops. Direct integration into vapor compression cycles implies that refrigerant flow directly through the PCM TES HX to transfer heat to the PCM. Domestic food refrigeration provides a litany of examples directly integrated into vapor compression cycles, while the building technology field only has a few examples. This section will cover work in both industries to contextualize the PCM TES HX studied in this thesis.

2.1.1 Literature on PCM TES HX's in Domestic Refrigerators

Although this work is not focused on domestic refrigeration, past work in the field is still pertinent because it gives insight into PCM TES HX's that use two phase fluids. In addition to summarizing the prior work, this section will describe how these PCM TES HX's in the domestic refrigerators could be implemented in buildings. A review paper on the use of PCM in refrigeration, by Bista et al., describes coupling PCM to the evaporator and condenser in vapor compression cycles. This subsection summarizes their review and incorporates some additional sources [25]. Figure 2.1 illustrates the modifications made to the evaporator and condenser by comparing to a typical refrigerator vapor compression cycle.

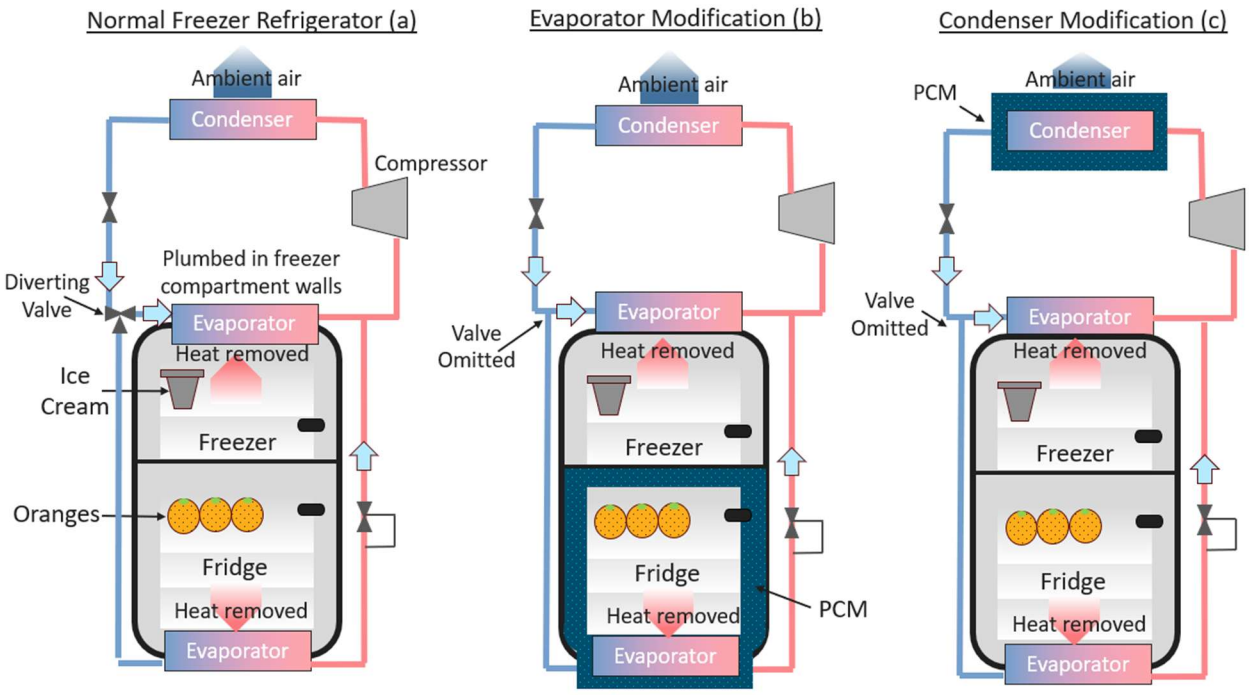

Figure 2.1: Some relevant modifications to vapor compression cycles within domestic refrigeration. The fridge has a transparent door. (a) is a normal refrigerator (b) is a PCM added to the evaporator and the food compartment (c) is the PCM added to the condenser.

A refrigerator freezer can have a single or dual evaporator for freezer and fridge compartments. Figure 2.1a illustrates a dual evaporator system without modification. One evaporator modification reviewed uses a dual evaporator set up [26], while the other uses a single evaporator set up (although this is not clear from their paper, and an inference by the author of this thesis) [27]. The dual evaporator only sends mass to one evaporator at a time using a diverter valve. Modifications have also been made to the condenser as illustrated in Figure 2.1c. The condenser is typically placed on the back of the refrigerator, which is not illustrated in Figure 2.1.

Evaporator enhancements are well studied in literature but are often designed as semi-active devices. Active devices consume electricity to move heat into PCM, while passive (inactive) devices do not use electricity. The evaporator enhancements place PCM slabs on one side of static freezer evaporator, which is located in refrigeration compartments and convection to the air is driven by natural convection [26], [27]. For these configurations, the refrigerant can remove heat

from both the refrigeration compartment and the PCM. Then, when the evaporator has no refrigerant flow, the PCM will melt and continue to cool the compartment. Both efforts included experiments, while Elarem et al. conducted modeling as well.

The transition temperature of the PCM governs the behavior of the system, and was 0 °C in Visek et al.'s study and 4 °C in Elarem et al.'s study, which was higher than the operating temperature of the evaporator and lower than the set point of the refrigerator. When the compressor is on, the PCM is recharged (frozen) along with the rest of the compartment, and when the compressor is off the PCM discharges by absorbing heat from the food compartments (melting). Although the PCM is storing energy while melting, this mode is thought of as discharging because the PCM TES HX primary function is to absorb heat from the food. This concept is a semi-active device because its charged by a compressor, but discharged was not directly controlled – heat was absorbed via natural convection when the compartment temperature increased above the PCM transition temperature. This set up reduces the overall compressor on time and saves energy. Elarem et al. state their design lead to a 12% energy savings and an 8% increase in COP [27]. Neither researcher discuss heat transfer characteristics of the PCM TES HX they tested. They both focus on system design and Elarem et al. conducts modeling of natural convection in the refrigerator.

Other researchers have focused on the heat transfer characteristics of the evaporating PCM TES HX. Rahimi et al. added fins to a PCM HX placed of an evaporator and studied the use of different configurations and fin materials. They found that higher conductivity materials and a larger number of fins lead to lower consumption, as much as 13.7%. They also evaluated the temperature distribution on the PCM side of the HX, which has not been done in many two phase

fluid PCM TES HX [28]. However, their main focus was system testing, and they did not discuss the thermal resistances within the heat exchanger in great detail.

Analogies to the building industry frames the applicability of domestic refrigerator evaporator modifications. Implementing this HX concept in the HVAC industry would require designing a hydronic cooling system (heat transfer fluid pipes in floors and ceilings) that couples with PCM insulation to make a rechargeable insulation with a TES HX. This idea is illustrated in Figure 2.2.

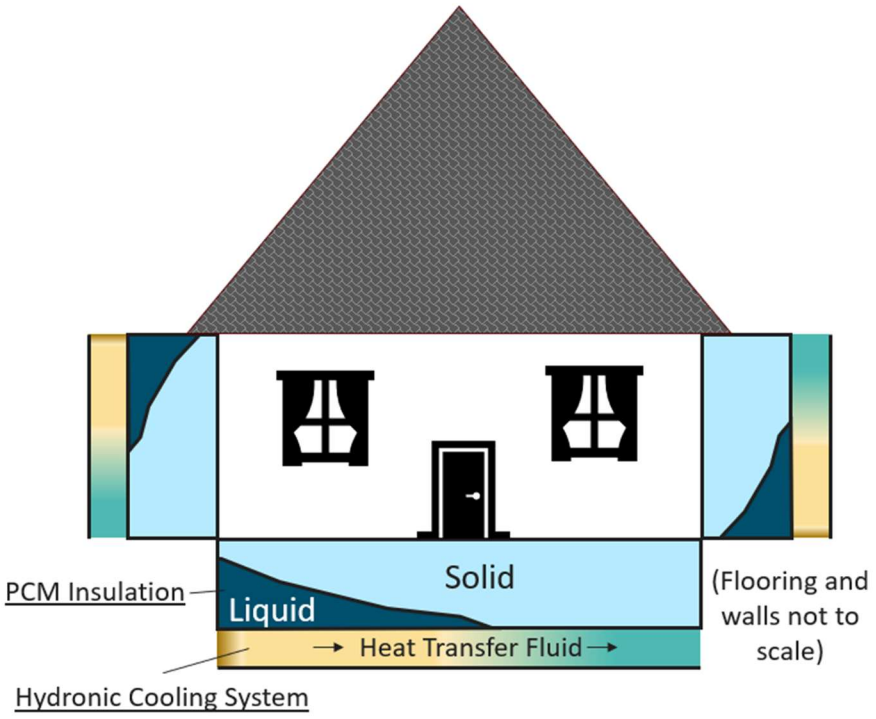

Figure 2.2: A building with rechargeable PCM insulation. Insulation is not added to the ceiling, but could be in an actual home.

Home hydronic systems typically use water as the heat transfer fluid and wouldn't couple directly to the evaporator of a vapor compression cycle. The system could also remove the heat transfer fluid, and melt and freeze the insulation via natural convection from space cooling and heating of central air and radiation from the sun. More information is included in a review paper by Arumugam et al. [29]. However, this would make this a passive system and not a direct

modification to the vapor compression cycle. Active and passive PCM TES insulation could enable energy savings over the entire day, which would be positive for consumers and decarbonization. However, implementing this set up in existing HVAC building systems would require home renovations to add the insulation and potentially the hydronic system. This would increase consumer costs and potentially decrease adoption.

Modifying the condenser in domestic refrigeration was far less common and also semiactive. Cheng et al. [30] and Sonnenrein et al. [31] conducted experiments on a household refrigerator that had a condenser with PCM surrounding its plumbing. This is illustrated in Figure 2.1c, and is analogous to placing PCM around the outdoor coil of a building air conditioning unit. In each study the PCM transition temperature was selected so that it was lower than the compressor operation temperature, but hotter than the ambient temperature. So, when the compressor was on the PCM absorbed heat from the condenser. Then, when the compressor was off the PCM rejected heat to the ambient environment via natural convection. With this set up Cheng et al. observed energy consumption reductions of 12% and Sonnenrein et al. observed reductions of 10%. The reduction in energy caused by adding PCM with a transition temperature higher than ambient to a condenser is counterintuitive because it should increase the temperature lift required by the cycle. However, condenser temperature results reported by both groups illustrate that the condenser temperature is reduced during compressor on time relative to refrigerators without PCM. The researchers state the reasoning behind this is that the PCM can discharge heat to the ambient during compressor off time, which is not a satisfactory explanation of the actual mechanism.

Sonnrein et al. researched multiple PCM's, which gives greater insight into the heat transfer that happens as a result of condenser enhancement [31]. They don't discuss the difference in heat transfer characteristics, but some analysis reveals why the PCM lowers energy consumption

despite increasing temperature lift in theory (but not in practice, as seen in their observations). They observed the highest energy reduction for the PCM with the highest thermal conductivity (10%). This PCM also had lower latent heat. Therefore, their work suggests that a phase change material is a more effective heat sink than the ambient environment because conductivity is the dominant factor behind lowering energy consumption. The heat transfer to the heat sink is governed by Equation (1).

$$q^{"} = \frac{\Delta T}{R^{"}} = \frac{T_{sat} - T_t}{R^{"}} \; or \; \frac{T_{sat} - T_{amb}}{R^{"}} \tag{1}$$

In Equation (1) $R^{"}$ is the thermal resistance and $q^{"}$ is the heat flux, and T_t is the transition temperature. Equation (1) illustrates that if the ambient temperature rises the saturation temperature in the compressor increases requiring additional compressor work. However, if the thermal resistance decreases then the driving temperature difference does as well assuming the heat flux is constant, which lowers the saturation temperature required in the condenser and the temperature lift. So, using a PCM with a transition temperature higher than the ambient increases the required temperature lift, but decreases the thermal resistance which lowers the saturation temperature required in the condenser. Balancing these competing effects can lower the high side pressure and reduce power consumption.

The PCM absorbs heat via conduction, while the environment absorbs heat via natural convection in condenser modifications, which explains why the PCM is a more effective heat sink. Analysis of the resistance to heat transfer via conduction through the PCM and natural convection without the PCM quantitatively proves the PCM is a more effective heat sink than natural convection to the ambient. Comparing area specific conduction resistances for Sonnemrein et al.'s work (conductivity of 0.67 $W/m-K$ and thickness of 4 mm) and convection resistances with

average natural convection coefficients (4.5 $W/m^2 - K$) for heated vertical plates [32] is done using Equation (2) and the convection resistance is calculated using Equation (3).

$$R^{"}_{conduction} = \frac{th}{k} \tag{2}$$

$$R^{"}_{conv} = \frac{1}{htc} \tag{3}$$

The calculation results in a conduction resistance of 0.00625 $K - m^2/W$, while natural convection gives 0.22 $K - m^2/W$, so the resistance due to natural convection is much higher. This analysis takes the liberty of using data outside of the experiment for the natural convection heat transfer coefficient, and assumes the area for convection and conduction would be the same. Both assumptions are limited by data available in Sonnenrein et al..

Placing PCM around the condenser coils of an existing building HVAC unit may actually increase energy consumption if done in the same manner as in domestic refrigerators. Cheng et al. and Sonnreinen et al. both added PCM on top of a condenser coil in a premade vapor compression cycle for refrigeration without any other modifications. The type of convection in the condenser in buildings is different than in household refrigerators. Buildings utilize forced convection to reject heat, which has higher heat transfer coefficients and lower thermal resistance than natural convection. The same back of the envelope calculation done to compare resistances in Sonnenrein's experiment can be used to find the convection coefficient required for the heat sink to become competitive. Finding the heat transfer coefficient needed to equal the conduction resistance in Sonnenrein et al.'s work yields a ball park requirement of 160 W/m^2K, which seems reasonable for forced convection coefficients measured for similar heat exchanger geometries based on Gönül et al.'s work [33]. Therefore, adding a PCM that has a higher transition temperature than the ambient temperature to a building condenser could actually increase energy

consumption because it may increase thermal resistance. Adding a PCM with a lower transition temperature than ambient could reduce temperature lift and reduce energy consumption during compressor on time. However, if the transition temperature is lower than the ambient temperature the TES will not passively discharge to ambient when the compressor is off because the ambient natural convection will continue to melt the PCM. So, the set up researched in domestic refrigerators has limited applicability to buildings.

Additional vapor compression cycle modifications have been made. One researcher studied adding each modification shown in Figure 2.1b and c to one refrigerator. In 2024 Harun-Or-Rashid et al. observed a 12.7% COP increase and a 25.1% reduction in power consumption in an experiment [34]. Cheng et al. modeled a similar system [35]. Bista et al. also included modifications that added PCM TES in line with traditional evaporator condenser heat exchanger in their review [25]. However, this research was conducted with HVAC in mind as the application. Therefore, this modification is addressed in the next subsection. Research on domestic refrigerators has likely occurred on in line modifications, before, but since there is a representative example in the HVAC Industry a search for a source on this information in the domestic refrigeration field was not conducted.

Adding an additional heat exchanger to the system in place of the outdoor coil could enable load shifting or load shaving. Dandotiya and Banker [36] developed a system that operates the same way as the system discussed in the introduction, but uses natural convection during the night to charge the PCM leading to load shaving rather than load shifting. This requires selection of a PCM with a transition temperature below ambient during the day and above ambient at night. The PCM TES HX in Figure 2.1b is used during the day when the temperature is hot. They run through the air cooled condenser in Figure 2.1a when the PCM TES HX is fully discharged. They tested

multiple PCM's, and used copper fins to enhance conductivity. They didn't discuss their PCM TES HX design in detail, but their prior publications may. They experimentally validated a finite volume model of their PCM TES HX, and their experiments showed a 30.8% increase in transient COP with the PCM TES HX. The main drawback of their design is that it relies on natural convection to charge the PCM, which doesn't use power but for larger TES may not be an effective way to charge the PCM due to high thermal resistance.

Extensive research has been carried out on adding PCM TES HX's to domestic refrigerators for load shifting. Rodrigues et al. provide an extensive review on this topic [37]. Several researchers have tested using refrigerators to shift loads. Brazin et al. [38] tested a device similar to the evaporator modification illustrated in Figure 2.1b. They also tested a room with PCM insulation created by Dupont. The benefits and drawbacks of this approach were previously discussed for refrigerators. Ultimately this design would not be very useful for buildings because the heat transfer would occur via natural convection (the mode in Brazin et al.) or a renovation of a buildings HVAC system would be required to implement a hydronic system. Another study by Taneja et al. implemented load shifting in a refrigerator by placing PCM in the freezer compartment and coupling it to a third fluid loop for charging in an experiment [39]. The benefits and drawbacks of a third fluid loop will be discussed in greater detail in the HVAC industry subsection because these heat exchangers have been researched in great detail in that field, and are more applicable to this thesis.

In summary, the findings from modifications to vapor compression cycles in the domestic refrigeration can inform decisions made to modify vapor compression cycles in buildings. There are energy savings benefits for all studies discussed, but these savings may not translate to buildings. The evaporator modification in Figure 2.1b would require costly remodeling of HVAC

systems in buildings, and does not enable load shifting. Furthermore, the benefit of condenser modifications for domestic refrigerators is governed by the differences between natural convection to an ambient heat sink and conduction to a PCM heat sink. Ultimately, this approach isn't analogous to building condensers because they work via forced convection. Several papers discussed PCM TES HX, but there is additional room for investigation. The thermal resistances and transient behavior of the TES HX's was not investigated in great detail. Although, many researchers reported increasing conductivity of the PCM TES HX lead to better performance, which is consistent with a variety of literature in other applications.

2.1.2 Literature on PCM TES HX's in the Building Industry

The building space conditioning field (HVAC) has done extensive work on PCM's since the first oil crisis in 1973 [23], and there are a huge variety of systems in literature. Figure 2.3 shows examples of a few categories of implementations.

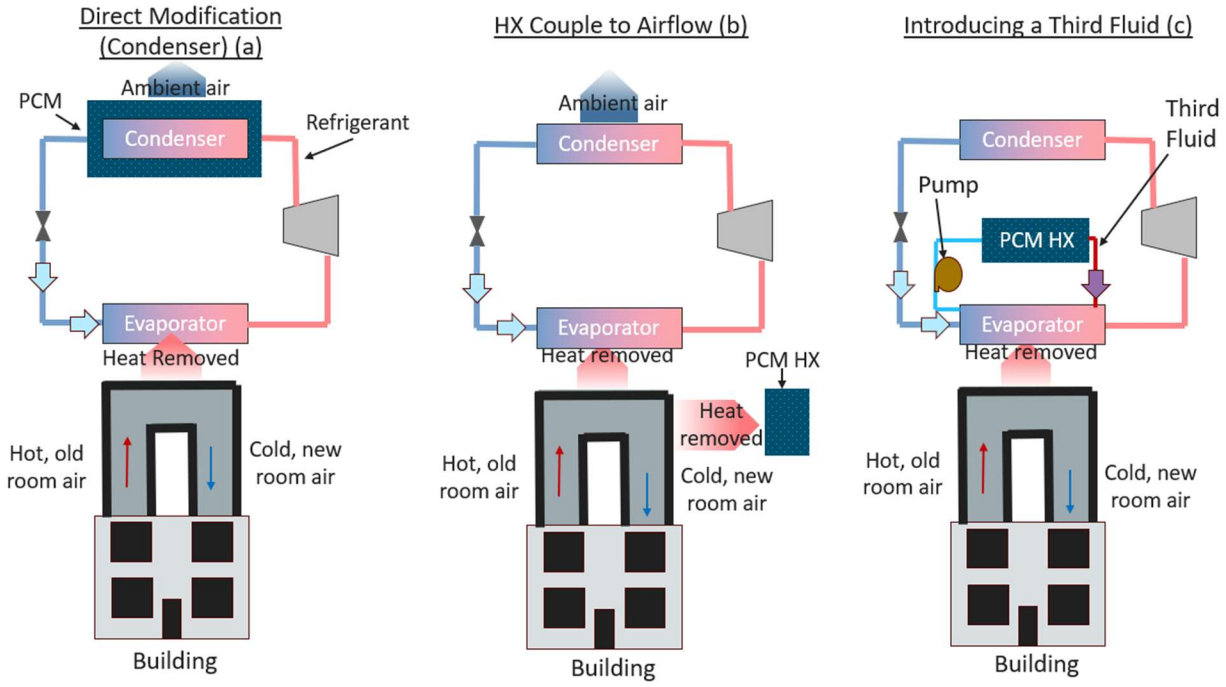

Figure 2.3: Different Integrations of PCM TES HX's in the HVAC field. (a) represents a direct modification (b) illustrates an air side modification, and (c) introduces a third fluid to the system.

A few implementations are directly integrated into vapor compression cycles (Figure 2.3a), while many other's use secondary fluid loops (Figure 2.3b and c). Secondary fluid loops could utilize building air intake and exhaust or introduce a third fluid. Each configuration has various advantages and disadvantages that will be discussed in the rest of this subsection.

Several researchers have looked into coupling PCM TES heat exchangers to air streams, their general design is relevant to the discussion because it highlights benefits and drawbacks. See Figure 2.3b for an illustration of how this can be accomplished. The work conducted on this in HVAC field is broad and a few examples are given as references, and not discussed in detail because this configuration is not the focus of this thesis. The literature has included detailed discussion of how design features affect heat transfer perfromance. For example, Promoppatum et al. studied a cross flow heat exchanger where air flow was driven across tubes of PCM to charge and discharge the TES [40]. Furthermore, Hu et. al. stacked plates of PCM encapsulated in plastic in an insulated box that had plumbing for air flow between the plates [41]. Lastly, Sadari et al. designed PCM composites in direct thermal contact with airflow via a rectangular channel [42].

Other researchers have investigated coupling PCM TES to HVAC systems using a third fluid loop such as a water Ethylene Glycol mixture. This is illustrated in Figure 2.3. Maccarani et al. charged PCM using a water loop and discharged using an airstream [43]. Moreover, Aljehani et al. and Goyal et al. designed an HVAC system that was coupled to a refrigeration cycle using an ethylene glycol loops [44], [45]. Adding a third fluid loop simplifies the design of heat exchangers for the TES HX because distribution of two phase fluids does not need consideration. Designing a TES HX to act as an evaporator requires proper mass distribution amongst parallel channels in the heat exchanger and was a challenge encountered in this thesis that will be discussed in the results section. More information on maldistribution can be found in a review paper by

Xiong et al. [46]. Secondary fluid loops have draw backs relative to the research conducted in this thesis though. Secondary fluid loops provide an additional the opportunity for losses and increase capitol costs.

There are several configurations of PCM TES HX that have been integrated directly into vapor compression cycles. Figure 2.4 shows an illustration of the prior work done in the area.

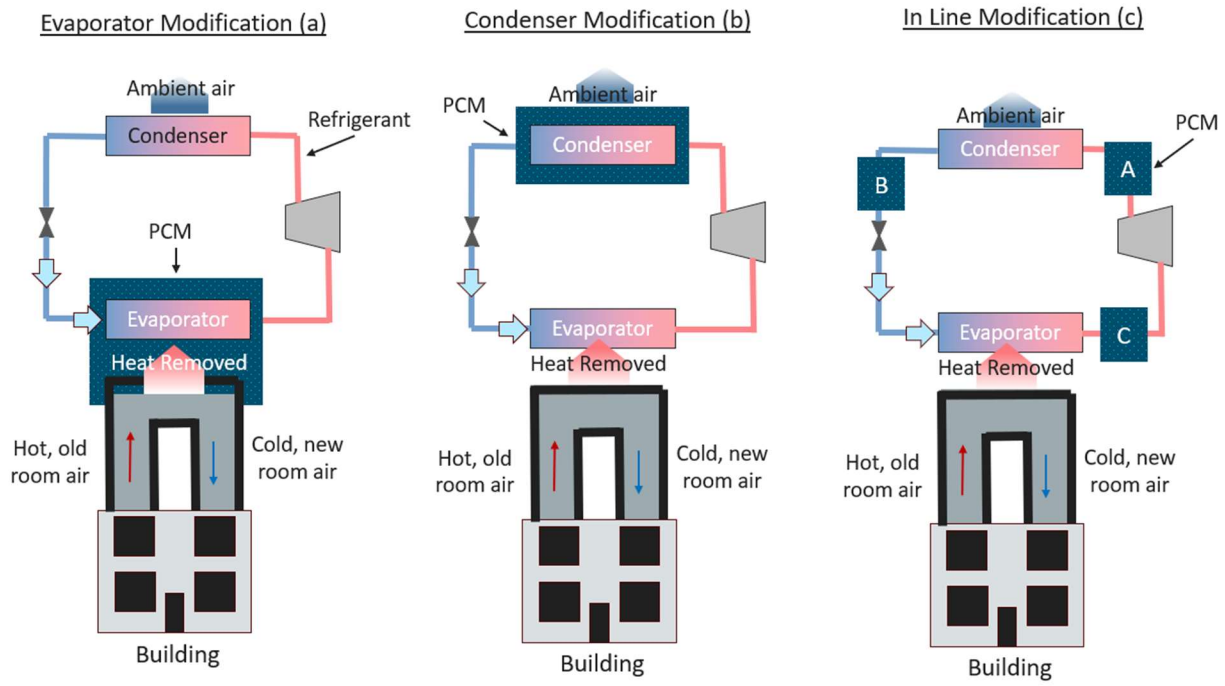

Figure 2.4: The different direct integrations of PCM TES HX's into vapor compression cycles in the HVAC field. (a) illustrates an evaporator modification that also integrates into airflow. (b) illustrates a condenser modification, and (c) illustrates inline modifications.

Researchers in HVAC space have done similar work to those in domestic refrigeration by adding PCM's to the evaporator or condenser. Researchers in the HVAC space have also looked into implementing TES HX's with in line in a vapor compression cycle as illustrated in Figure 2.4c.

A brief search on integration of PCM's into the evaporator of PCM HX's yielded one recent study by Kedzierski and Lin [47] that sought to integrate directly, but had issues with supercooling via design and experiments. Kedzierski and Lin designed a PCM HX with the PCM and refrigerant in direct physical contact. Direct physical contact means that the refrigerant was directly injected

into the PCM, melting regions as it flows through it. The refrigerant used was R134a, but the target refrigerant for the application is R410a. They conducted modeling of their overall system, which charged by a vapor compression cycle and discharged within the air handling unit [48], which is illustrated in Figure 2.4a. The phase change material used was glycerin, which was chosen because its immiscible with the refrigerant. Large supercooling (48.7°C) prevented the study from yielding valuable information because the PCM did not change phase in the experiment. The device tested was scaled for residential HVAC, and had an approximate capacity of 7 kWh. Kedzierski and Lin did provide information on their PCM TES HX design though. They used PTFE rings to support the pathways engineered in the PCM, but only filled one third of the height of the heat exchanger. Their designs major drawback is that it will likely have excessive pressure drop and could have issues maintaining its shape. So while the physical contact between the two heat transfer mediums removes thermal resistances (an advantage)- it also could lead to drawbacks that make this heat exchanger fail. Their work mostly focused on documenting their struggles with building the device and did not include discussion of charging the storage media. Other literature on TES PCM HX's directly integrated into evaporator's for buildings does not exist to the author of this thesis' knowledge.

Direct integration of PCM's into condensers has been done in personal cooling applications that run the cycle in reverse with a thermosiphon to recharge the device as an evaporator. This modification is illustrated in Figure 2.4b. At the University of Maryland work on the Roving Comforter (a personal comfort device) was documented in Qiao et al. [49], Dhumane et al. [50], and Ling et. al. [51]. Qiao et al. gives details on experimental set up, which is of particular relevance to this work because it provides heat exchanger device comparison. Dhumane et al. documents their numerical modeling efforts, which will be summarized in the modeling section of

this thesis. Ling et. al. studies the effectiveness of the device through occupant comfort and will not be covered because it doesn't focus on heat exchanger design. Qiao et al. investigated the effect of different thermal conductivity enhancements on the PCM HX performance, finding graphite to have the best performance – 49% greater COP than their control test.

Qiao et al.'s HX design is a semi-active device that uses a vapor compression cycle to charge the TES and a thermosiphon to discharge the TES. The thermosiphon works by using density difference in liquid and gaseous refrigerant (natural convection) to drive flow, which is ultimately passive. So this device is a semi-active device as it's charging is not active. The personal cooling concept allows one to cool themselves locally (for example, at their desk), rather than through central air (what is required for an entire room or building). Thus, removing load from central air units and decreasing electricity costs by requiring space cooling only for a localized area. During discharge the PCM stores the heat rejected from the space. During charging the system must move to another location to remove heat from the PCM. Otherwise, the system will just dump heat into the room at a different time, defeating it's purpose. The final device, described in Ling et al. had a capacity around 1.2 kW-hr [51]. Qiao et al. was one of the few papers that discussed design and testing of the heat exchanger in detail. They documented temperatures at different locations, discharge rate (heat flow), and thermal resistances, making their work the most complete reviewed on PCM TES HX coupled to two phase fluids thus far.

In line systems have been studied in literature as well and can increase COP. Wang et al. published two papers on this, the first was on an experimental effort [52] and the second was on modeling [53]. His work is illustrated in Figure 2.4. Their experimental work is of particular interest because it validates the model, and the modeling was done at the system level, which is not the focus of this work. The COP was found to increase 6% for configuration A, 8% for

configuration B, and not increase at all for C relative to the system without a TES HX. The TES HX in configuration A and B increased the capacity of the condenser leading to the performance benefits, while the TES HX in configuration C had negligible impact because it increased pressure drop, which caused the compressor to work harder. The pressure drop likely increased in B and C as well, but was not as large because of the flow regime of the fluid. In A the fluid will condense, in B the fluid will subcool, and in C the fluid will superheat. The superheated fluid will move at a faster velocity and have a higher pressure drop. This system increases performance, but ultimately does not accomplish load shifting.

Raifi et al. [54] used an in line system to accomplish load shifting by using configuration A to discharge and configuration B to charger a PCM TES HX. They reported up to 69% peak shaving. Their investigation was conducted via modeling. They modeled an annular PCM TES HX using resistance based methods in EES, and applied the effectiveness NTU method. They assume that the refrigerant won't condense in configuration A, which is inaccurate based on observations in Wang et al. The major advantage of in line systems for peak shaving is that they reduce the required condenser heat rejection. Decreasing the required heat transfer in the condenser decreases the needed driving temperature difference to cool the load at the condenser. Thus, lowering the condenser pressure and energy consumption. The major drawback of these systems is that the condenser pressure is still set by the ambient environment, so there is a limit on how low the condenser temperature can get and still transfer heat via natural convection.

2.1.3 Summary

There is a gap in research in the design and evaluation of PCM TES HX's coupled directly to two phase refrigerants, and that are actively charged and discharged. The domestic refrigeration field has covered devices that act as an evaporator and condenser in detail, but their devices are

much smaller in scale and are semiactive because they discharge during compressor off time through natural convection. Additionally, a few researchers in domestic refrigeration focus on PCM TES HX design find increasing conductivity reduces energy consumption, but they don't discuss the heat transfer in the PCM TES HX in detail. This review concludes the mechanism is likely that the PCM is a more effective heat sink than natural convection. The HVAC industry has also investigated coupling PCM's to evaporators and condensers. Evaporators have been researched, but with little success, and condensers have been studied in small scale personal cooling devices, which are also semi-active because they discharge using a thermosiphon. So, limited research has been conducted on devices that actively charge and discharge to the author's best knowledge.

This thesis will demonstrate the performance of a TES HX device that can actively melt and freeze the PCM. The main contribution of this work relative to PCM TES HX vapor compression cycle integration is not novelty, but rather an addition to the literature on PCM TES HX heat exchangers that incorporate two phase fluids. The study documents the performance of a HX that can easily integrate into vapor compression cycles and is simple to model and build, which could prove advantageous for future researchers' work.

2.2 Literature Review of Modeling of PCM TES HX's

PCM TES HX modeling literature varies in computational fidelity. This review will narrow in scope from a general overview of modeling techniques to low fidelity methods, and finally analytical modeling. The review focuses on continuum scale modeling of devices (HXs) and does not cover atomistic, mesoscale, or system modeling.

2.2.1 Overview of continuum scale modeling

HX modeling is often categorized by design problems and simulation problems. Design problems seek to size a heat exchanger given some performance requirements, while simulation problems determine the performance of a design. This review focuses on modeling schemes for design problems, but includes simulation problems where relevant to the discussion. Studies often focus on simulation problems to validate modeling schemes. Researchers can use simulation problem frameworks for multiple designs to represent the design space without going through optimization routines.

Design problems for PCM TES HX's differ from classical heat exchangers because the HX includes an energy storage medium and a heat source or sink (a single phase or two-phase fluid), rather than two fluids. The design of TES heat exchangers has often focused on balancing thermal storage capacity and the ability to efficiently pass heat in and out of the device. PCMs usually have poor thermal conductivity, so most TES heat exchanger designs either increase the effective conductivity with metal or graphite additives [55], or significantly increase the heat transfer area between the fluid and the PCM, as done in Calmac tanks [56]. Calmac tanks have been implemented in many commercial sites, including the 11 Madison Avenue building in New York, and have been studied experimentally in the past [57]. In both cases, the high conductivity materials or excess tubing takes possible storage volume away from the PCM and typically do not possess any storage capacity themselves. Adding additional tubing could increase capital cost due to additional labor and materials.

Prior studies on adding metal fins as a conductivity enhancement material are ubiquitous in literature. Researchers have looked at regular geometries (rectangles), and exotic topology optimized solutions. Regular fin geometry optimization focuses on fin length, frequency (pitch) [58], and angle to optimize natural convection [59], storage capacity, and conductivity

simultaneously. Regularly shaped fins are common in literature due to their low manufacturing cost and ease of installation [55]. Topology optimized fins can optimize storage volume and effective PCM conductivity (the conductivity the PCM and fin collectively) [60]. However, topology optimized solutions require metal additive manufacturing, which is expensive to do in large quantities. Adding PCM TES HX's to the existing building stock will require numerous HX's making cost an important design consideration.

Metal foams enhance conductivity uniformly and have high porosity, which optimizes conductivity and storage capacity. One advantage of metal foams over regular fins is that foams can enhance conductivity uniformly. Metal foams do have one notable drawback relative to fins, they surpress natural convection. However, lack of natural convection simplifies modeling. Many researchers have studied metal foam PCM composites in the past, and their work has focused on evaluating different materials and foam configurations. Qiao et al. looked at different metal foam types in an experimental and computational effort [49], Ferrera and Madani studied composites with different pore densities [61], and others have focused on model validation for applications [42], [45]. Design problems can also be very simple. For example, one could focus on the thickness of the phase change composite or the area with an objective function that maximizes peak shaving or minimizes capital expenses.

The usefulness of PCM TES HX model formulations for design depends on the geometry and model audience. Many researchers have used finite element and finite volume models in their research in the past [42], [61], [62], [63]. These modeling methods are good for capturing intricate 2D and 3D heat transfer of complex geometry. However, expertise is likely a barrier for building designers adopting these modeling techniques. Running optimization schemes for thickness of a PCM slab would require use of generative meshing techniques, and statistical models. Building

designers could learn these skills, but doing so would require taking significant time away from their main job function – sizing heating and cooling systems for buildings.

Typical desktop computers are not capable of solving highly resolved 2D and 3D multiphysics simulations in a timely manner even if packaged and compiled for designers to use as a calculator. Sadari et al. stated their finite element simulation took hours-days to run [42]. Solve times depend on the computer, but regardless hours-days of computation time for a building design firm would likely decrease the likelihood of using finite element and finite volume schemes. For PCM TES HX adoption to occur in the HVAC&R industry design engineers need quick user friendly computational methods to size HX's. However, these models still need to capture enough physics to give realistic estimates. Therefore, this thesis focuses on low fidelity modeling techniques to bridge the gap between researchers and designers.

The modeling techniques considered low fidelity in this thesis vary from simplified finite difference, finite volume, and finite element models to analytical solutions of differential equations. The range of complexity is illustrated in Figure 2.5.

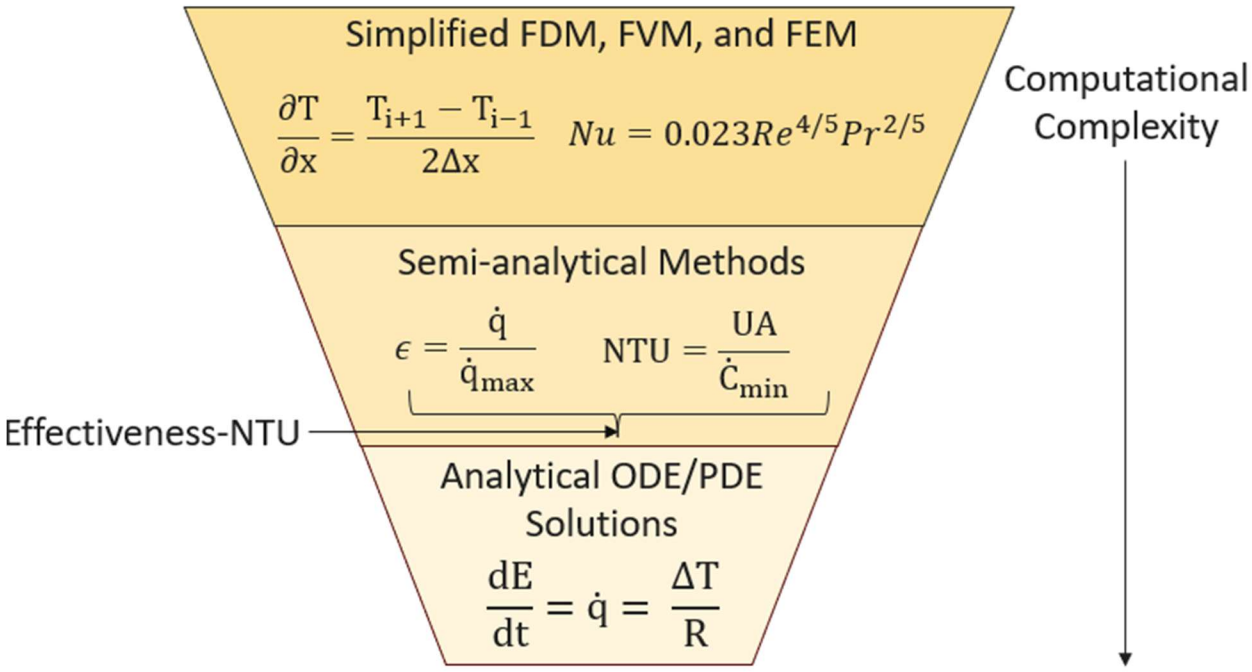

Figure 2.5: The range of low fidelity modeling methods considered in this review and their computational complexity. Refer to the nomenclature section for a definition of different variables.

Simplified finite difference, finite volume, and finite element models are the highest level of computational complexity needed for design if the geometry is simple. This thesis used a finite difference model in the design phase because of prior success with this modeling technique [15]. The next step down in fidelity is semi-analytical solutions. These solutions are numerical solutions to simple formulations of PDE's and ODE's. Lastly, analytical ODE and PDE solutions that are easily extendable and require little computational capabilities are included in the complexity category. These methods present the simplest methods for designing and simulating heat exchangers.

2.2.2 Simplified Finite Difference, Finite Volume, and Finite Element Methods

Many researchers have used simplified finite difference, finite volume, and finite element models to design PCM TES HX's and have had great success; however, these techniques still require research expertise. Goyal et al. created a finite volume model using thermal resistances to

simplify the computation in a 2D domain [45]. Similarly, Woods et al. created a finite difference model using resistances for different geometry and their model was modified as part of this work [15]. Lastly, Messenger et al. solved a simple 1D finite element model using the enthalpy method [64]. All studies were for a single phase heat transfer fluid. Each of these methods requires knowledge of PCM TES HX design, PCM material properties, and numerical methods. Additionally, the solution scheme developed in the resistance based finite volume and finite difference methods is specific to the geometry analyzed and not generalizable. Although, the general idea can be applied to a variety of geometries.

Research has been done on low fidelity 2-D finite volume methods to simulate a TES HX coupled to a two-phase fluid, which showed reasonable results but still has drawbacks for designers. Qiao et al. modeled the roving comfort heat exchanger originally using Modelica [50], but moved to a finite volume approach later on. Their finite volume approach used the enthalpy method and predicted experimental performance within 7% of their results [65]. Although their approach was accurate, a 2D finite volume technique still does not satisfy the simplicity needed for HVAC designers for modeling TES HX with two phase fluids.

Statistical models derived from finite difference, finite volume, and finite element techniques lie next in the computational complexity ladder and are included in this subsection. Some researchers have looked into creating statistical models that represent the physics of the simulation problem. To train these models a large number of simulations are run and then used to train models that represent the design space (machine learning included). Huang et al. validated this approach for system level simulation [66]. These statistical models can also be used for design optimization of parameters like PCM thickness.

2.2.3 Semi-analytical Schemes

The second category of low fidelity computational schemes in this review are semi-analytical schemes, which include solutions to ODE/PDE's that require numerical techniques to solve. The literature on these techniques is exhaustive because some PCM TES HX geometries and materials cannot be easily modeled without computers. Some of the categories not covered include inverse Laplace transforms, asymptotic analysis, perturbation methods, and conductance focused design methods [67], [68], [69], [70]. Laplace transforms, asymptotic analysis, and perturbation methods are not covered because they may require tuning solvers for different geometries and materials. Additionally, using them requires a high degree of mathematical knowledge, and building designers practically do not need that degree of education. Conductance methods are not covered because effectiveness-NTU methods will be covered in great detail, which are very similar. None of the methods reviewed covered PCM TES HX that used two phase fluids to the authors' knowledge.

Many of these techniques require discretization in time and space to solve. These regions have differing material properties because they're different states of matter. One example is the effectiveness NTU method. The effectiveness NTU method is a standard method used to characterize fluid-fluid indirect heat exchangers, which is a packaged form of an analytical solution to differential equations that define each fluid domain. The method becomes much more complicated when applying it to PCM TES HX's though because the underlying steady state assumptions used for fluid-fluid HX fail. As the phase front progresses sensible and latent PCM regions develop requiring discretization of the heat exchanger in time and length [66], [71], [72], [73]. Adding a two-phase fluid would complicate this more because sensible and latent regions would likely exist on the fluid side of the heat exchanger.

Beyne et al. applied the effectiveness NTU model to a PCM TES HX with a single phase fluid in manner that could be useful for HVAC designers in the future. They discretized their domain in time and space to capture different heat transfer regimes defined by different phases of the PCM as previously discussed. Furthermore, their approach is generalizable to other PCM TES HX because their solution technique is not specific to material properties, and generalizations could be made for more complex geometries [71], [72]. This solution scheme requires detailed knowledge of PCM TES HX and therefore would be difficult for designers to implement, and use to develop intuition about PCM TES HX design. However, designers could likely use this approach in a packaged form to solve design problems. Packaging the solution would require creating a piece of code that required a building designer to input material information, building loads, and location weather to a user interface to get a design (in the case of this thesis, a PCM thickness).

2.2.4 Analytical Solutions

The original analytical solution for solid-liquid phase change was developed from 1889-1891 by Josef Stefan, and still provides simple elegant solutions to PCM TES HX problems today. Stefan was a Slovenian born professor of physics at the University of Vienna. He solved many problems in heat transfer. His work on solid liquid phase change began by solving boundary value problems for a semi-infinite 1D PCM with a constant temperature boundary condition at one surface, which is commonly referred to as the 1D semi-infinite Stefan problem [74].

Today solutions to Stefan problem have been used by multiple researchers. Messenger et al. compared Stefan problem solutions to their 1D enthalpy method finite element solution, and found good agreement [64]. Furthermore, Tamraparni et al. develop solutions similar to the Stefan solution, although form of the solution doesn't match that used in Messenger et al. and is for

constant heat flux. Tamraparni et al. also see good agreement, however, their study does little to consider the effect of the heat transfer fluid, and instead focuses on PCM material properties. Ultimately, they consider a the heat transfer fluid in an analysis that is developed form a literature review, which has limited applicability and scope [75]. Neither work considers experimental validation of a PCM TES HX with a two-phase fluid.

Current analytical approaches model the temperature distribution of PCM TES HX in different heat transfer regimes using methods similar to the Stefan problem, with some modifications to create 2D solutions. Bechiri and Mansouri created a 2D solution for a PCM TES HX with a single-phase flow, but their work required numerical iteration, which complicated the scheme [76]. Ding et al. developed a similar scheme that could be solved explicitly. They created a piecewise solution to represent sensible and latent heat transfer regimes. Their work is quite detailed and is validated against other approaches in literature [77]. The main drawback of their work is the mathematical complexity. However, an HVAC design engineer could easily plug in values to their solution to solve a design problem because it has a closed form solution.

2.2.5 Summary

This thesis seeks to build on the literature on PCM TES HX's by using simple resistance based solutions to the governing differential equations to come up an intuitive and low complexity approach for HVAC designers. The finite difference and low fidelity/semi-analytical computational solutions would be difficult for building design engineers to use. Their use is best for researchers and product designers who need to model detailed non-ideal behaviors and complex geometries in detail. However, analytical models cannot replace detailed modeling entirely. Instead, this review suggests using each model in the appropriate setting. Building designers could use analytical models to size PCM TES HX for real world buildings, while researchers and product

development engineers could use them for sanity checking higher fidelity simulations. Therefore, this work seeks to bridge the gap between researchers and building designers by developing analytical solutions in conjunction with high fidelity finite difference solutions. The analytical solution could be used to design the thickness of a PCM TES HX, while the finite difference solution may be more useful for more complex design problems or simulation problems.

In addition to bridging a gap between academia and building designers, this thesis fills a gap in literature by developing a piecewise analytical solution for a TES HX with a two-phase heat transfer fluid and validating it against an experiment and numerical model. The analytical model itself is not novel as the 1D Stefan problem can be easily applied to a condensing or evaporating heat transfer fluid in a PCM HX, because the heat transfer fluid has a constant temperature. However, this review did not find any comparisons of analytical solutions to PCM TES HX with condensing and evaporating HX to experimental measurements. So, the validation effort adds to the literature to the best of the author's knowledge.

Chapter 3: Design & Modeling

Chapter 3 covers the device modeling validated in this work. High and low fidelity models were developed for device design. The high fidelity model is a finite difference model developed by Ty Glisczinski [78]. The model has not been documented yet in literature so I'm summarizing it in this work. The design of the device was done by Ty and Dr. Allison Mahvi, and is also documented because it hasn't been published [78], [79]. The author of this thesis did not contribute to developing the model or the design of the TES HX tested in this work. NETenergy and Texas A&M also aided in the design by providing information about PCM material properties. The low fidelity analytical model was developed as part of this thesis.

3.1 Finite Difference Modeling

The TES heat exchanger model is based on the numerical model first presented in 'Rate capability and Ragone plots for phase change thermal energy storage' [15] but with some key modifications. These modifications were made to capture changes to the coupling fluid (evaporating/condensing refrigerant instead of a single-phase fluid) and decrease the computational time. The updates to the model are discussed in this section.

3.1.1 Modeling Approach

The model was built with several assumptions. A few basic assumptions that come from the use a of a conductivity foam are listed below:

- Natural convection can be neglected because the graphite foam used to enhance thermal conductivity suppresses natural convection, based on prior work [15]
- Effective properties can accurately represent the composite (PCM + graphite) properties

Furthermore, the model assumes the PCM HX can be accurately modeled symmetrically as illustrated in Figure 3.1.

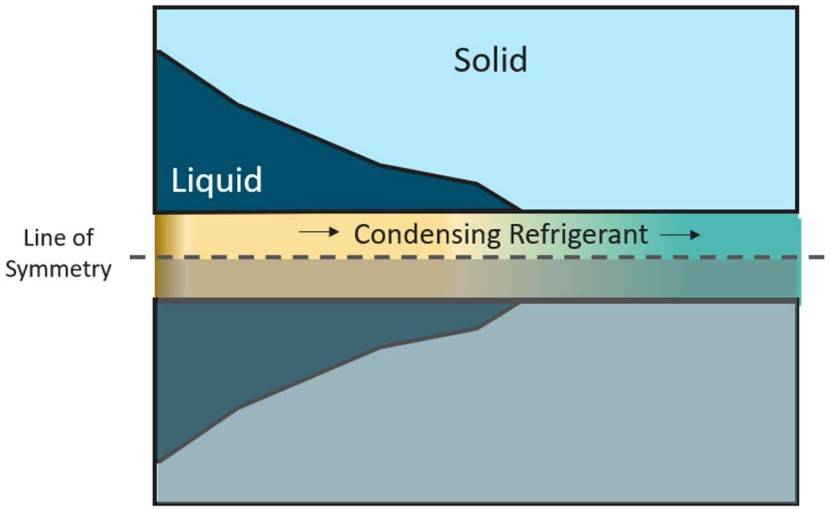

Figure 3.1: The PCC symmetry boundary condition is indicated on the unit cell.

This leads to an adiabatic boundary condition at the line of symmetry. This assumption will be verified in Chapter 5.

The full scale PCM TES HX component will use insulation to limit losses when not in use. The insulation is modeled using adiabatic boundary conditions at the sides of the PCC slab as illustrated in Figure 3.2.

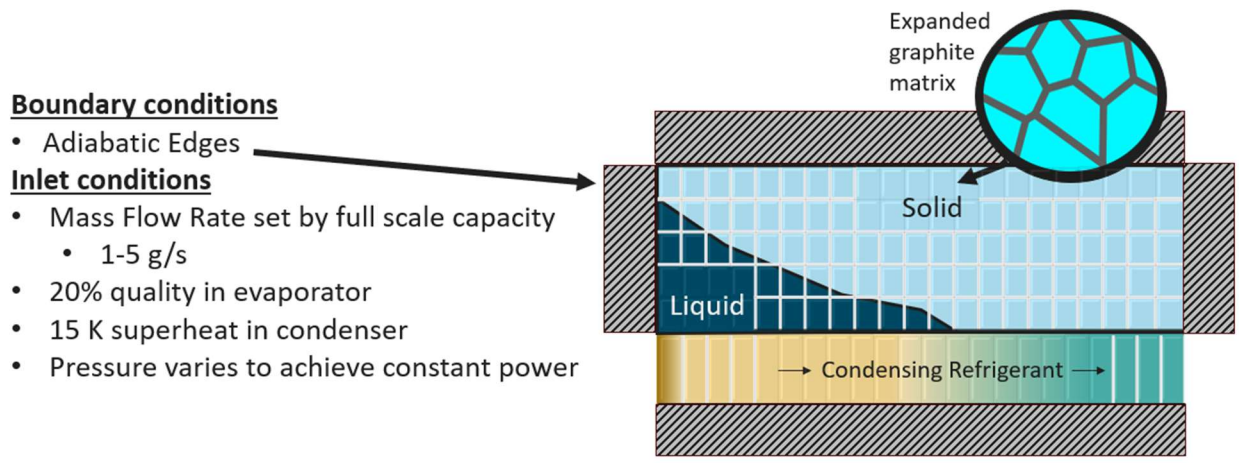

Figure 3.2: The boundary conditions, and initial conditions are illustrated. Adiabatic boundary conditions are used at all edges.

Figure 3.2 also indicates the inlet conditions used for the design phase. The inlet conditions were set by average vapor compression cycle inlet conditions for evaporators and condensers.

The initial model tracked the state of the PCC through enthalpy. The model developed in this work tracks the state through evaluating the change in temperature of the PCC using an energy balance as seen in Equation (4).

$$C_{i,j}\frac{dT_{i,j}}{dt} = \frac{k_{\perp dx}}{dy}\left(T_{i-1,j} + T_{i+1,j} - 2T_{i,j}\right) + \frac{k_{\parallel dy}}{dx}\left(T_{i,j-1} + T_{i,j+1} - 2T_{i,j}\right) \quad (4)$$

In Equation (4) T is the temperature, C is the thermal mass, $k_{\perp dx}$ is the vertical conductivity, and $k_{\parallel dy}$ is the axial conductivity. The thermal mass represented by C is sometimes called the capacitance and is the product of the mass and specific heat of the PCC. Determining the state of the PCM on a temperature basis allows implicit numerical methods to be used when stepping forward in time. This is discussed in more detail in the next subsection.

Another update to the prior model is the working fluid. The thermodynamic properties of the fluid are based on the refrigerant R410a rather than a 10% mixture of propylene glycol and water. Furthermore, the TES heat exchanger is expected to act as both a condenser or evaporator,

hence the fluid is modeled as two-phase. This requires the state of the refrigerant to be determined on an enthalpy basis using an energy balance as seen in Equation (5).

$$\dot{m}\left(h_{f,i} - h_{f,i+1}\right) = 2\dot{q}_i \tag{5}$$

In Equation (5) $\dot{q}_i$ is the heat transfer between the fluid and PCM at node i. The model assumes that the fluid is in steady state with the PCM at all times. This assumption was made because the thermal mass of the refrigerant is far less than the PCM, meaning that the refrigerant responds quickly to changes in the system.

3.1.2 Implicit vs. Explicit

To track the state of the PCM forward in time an explicit or implicit numerical approach can be used. When the energy balance shown in Equation (4) is written on an enthalpy basis, as seen in Equation (6), an explicit method (Euler), Equation (7), must be used to step forward in time.

$$\frac{dh_{i,j}}{dt} = \frac{k_{\perp d}}{dy}\left(T_{i-1,j} + T_{i+1,j} - 2T_{i,j}\right) + \frac{k_{\parallel dy}}{dx}\left(T_{i,j-1} + T_{i,j+1} - 2T_{i,j}\right) \tag{6}$$

$$h_{i,j}^{t+1} = h_{i,j}^{t} + \frac{dh_{i,j}^{t}}{dt}dt \tag{7}$$

The initial model, developed by Woods et al. used this method. This approach requires a sufficiently small timestep to maintain stability. A small timestep requires more computations to be performed; increasing computation time. In this model, we are not concerned about changes that happen on the sub-second time scale, therefore the stability criterion of the Euler approach severely limits the speed of the simulation.

To improve the computation time needed to simulate the discharge/charge process an implicit method may be used to increase the time step. The implicit method used here is Crank-Nicholson and is presented in Equation (8).

$$T_{i,j}^{t+1} = T_{i,j}^{t} + \frac{1}{2}\left(\frac{dT_{i,j}^{t}}{dt} + \frac{dT_{i,j}^{t+1}}{dt}\right)dt \tag{8}$$

The computational expense of solving Equation (8) is greater than that needed to solve Equation (7). However, implicit methods experience a higher order of stability, allowing for a larger timestep. The larger timestep reduces the number of computations, overcoming the increase in computational expense and reducing the total simulation time relative to the explicit scheme.

Running the explicit and implicit schemes shows evidence of the decrease in computational time created by moving to a larger timestep. Figure 3.3 shows the root mean square error and run time ratio between the explicit and implicit schemes.

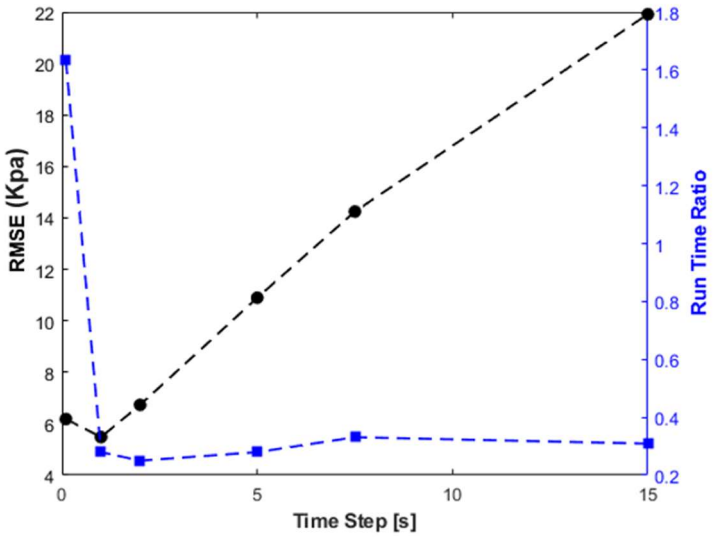

Figure 3.3: Root Mean Squared Error between explicit and implicit schemes (left axis) and ratio of implicit scheme run time to explicit run time (right axis) against the time step used for the implicit scheme.

The total runtime for the explicit scheme on a standard windows PC is 34 seconds per hour of simulation time. The explicit scheme is performed a single time using a time step of 0.1 seconds. The implicit scheme is performed multiple times, increasing the time step for each simulation. The root mean square error is based on the refrigerant pressure predicted by each numerical scheme at 30 second intervals over a discharge process. It can be observed that using an implicit scheme with an increased timestep relative to the explicit scheme can produce results in close to half the time without incurring excessive error.

3.2 PCM TES heat exchanger design:

The PCM TES HX design was completed using the finite difference model, and its key components are a graphite phase change composite slab and microchannels. The selection of the PCM transition temperature is described in the introduction and won't be covered in detail in this thesis. The major design constraints for the PCM TES HX design were:

- Peak shaving >40% for 4 hours on summer and winter day
- Fits on a standard pallet (1.2 m x 1 m)
- Can be carried by 2 people (<200 lbs)
- Microchannels stay in one horizontal plane (prevent stresses on channels during cycling)
- Reasonable pressure drop (<10 kPa)

These design constraints were selected to increase the likelihood of adoption by the HVAC industry. Therefore, the size and weight of the heat exchanger is limited to a size that would be reasonable for an HVAC technician to install. The final design selected was originally 1 m by 0.5 m, however, time constraints changed the design to 1 m by 0.25 m because the original HX could not be fabricated to meet project deadlines. The initial design was conducted for the 1 m by 0.5 m

area and translated to the 1 m by 0.25 m heat exchanger. This section recounts the design of the 1 m by 0.5 m device.

3.2.1 PCC Slab Design

The PCC slab was a composite of an organic paraffin-based PCM, PT23, and expanded graphite. The graphite enhanced the conductivity of the PCM. To create the composite a graphite slab is created with a certain void fraction as illustrated in Figure 3.4.

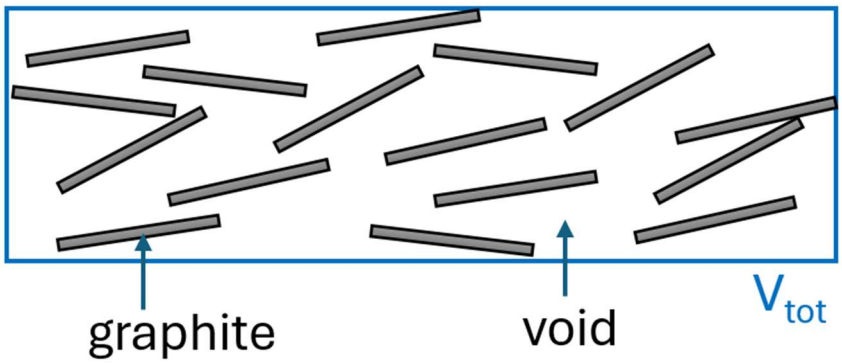

Figure 3.4: The graphite foam composite without any PCM. This figure was adapted from private communication with Patrick Shamberger [80].

The graphite and void volumes have a volume fraction that is relevant for computing effective properties. The volume fraction of the graphite is defined in Equation (9), and the volume fraction of the void is defined in Equation (10).

$$\phi_{gr} = \frac{V_{gr}}{V_{tot}} \tag{9}$$

$$\phi_{void} = 1 - \phi_{gr} \tag{10}$$

In equation (9) and (10) V is the volume, and ϕ is the volume fraction. The methodology for the material property calculations was developed with the help of Texas A&M [80] and NETenergy [81].

To create the storage medium the graphite slab is filled with PCM. The graphite can either be fully filled or partially filled as illustrated in Figure 3.5.

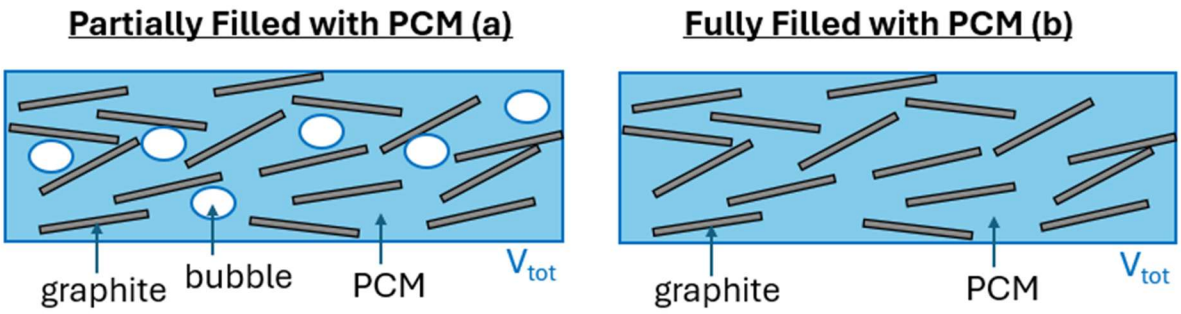

Figure 3.5: (a) A partially filled PCM composite and (b) a fully filled PCM composite. This figure was adapted from private communication with Patrick Shamberger [80].

The PCM is held in the graphite by capillary forces, but will leak out if it doesn't have enough space to expand into when transitioning from solid to liquid, causing capacity fade over time. So optimizing the fill fraction to reduce PCM leakage and maximize the energy storage is a key design consideration.

The computation of the PCM volume fraction for partially filled and fully filled slabs differ. Finding the volume fraction of the fully filled PCM is easy because the volume fraction of PCM is equal to the void volume fraction. However, finding the volume fraction of the PCM in the partially filled case is more complicated, and is given by Equation (11).

$$\phi_{PCM} = \left(\rho_{PCC} - \rho_{gr}\phi_{gr}\right)/\rho_{PCM} \tag{11}$$

In Equation (11) ρ_{PCC} is the density of the partially filled slab, which can be calculated from Equation (12) if one assumes the bubble's mass is negligible.

$$\rho_{PCC} = \rho_{gr}\phi_{gr} + \rho_{PCM}\phi_{PCM} \tag{12}$$

The properties of the composite slab were measured at NET Energy and calculated with the help of colleagues at Texas A&M University. The latent heat of PCM was calculated using Equation (13).

$$L_{PCC} = \frac{m_{PCM}}{m_{tot}} L_{PCM} = \frac{\rho_{PCM}\phi_{PCM}}{\rho_{gr}\phi_{gr} + \rho_{PCM}\phi_{PCM}} L_{PCM} \tag{13}$$

In Equation (13) L is the latent heat of fusion of the material. The composite latent heat and density were initially used to find the capacity of the system. Equation (14) was used to calculate the theoretical capacity of the TES heat exchanger.

$$C_{th} = \rho_{PCC} V_{tot} \left(c_{p,s} \Delta T_{sub} + \mathrm{L_{PCC}} + c_{p,l} \Delta T_{super} \right) \tag{14}$$

where $c_{p,s}$ and $c_{p,l}$ are the specific heat of the PCM composite in the solid and liquid phase, respectively, and ΔT_{sub} and ΔT_{super} are the sensible solid and liquid regions considered in the total capacity. In this work, the solid and liquid sensible band is set to ±5 °C, so the target operational temperatures vary between 18 and 28 °C.

Comparing the idealized enthalpy vs. temperature curve and the curve generated directly from DSC highlights failure of the idealization of the curve. The comparison is presented in Figure 3.6 for a PCM volume fraction of 44.7%.

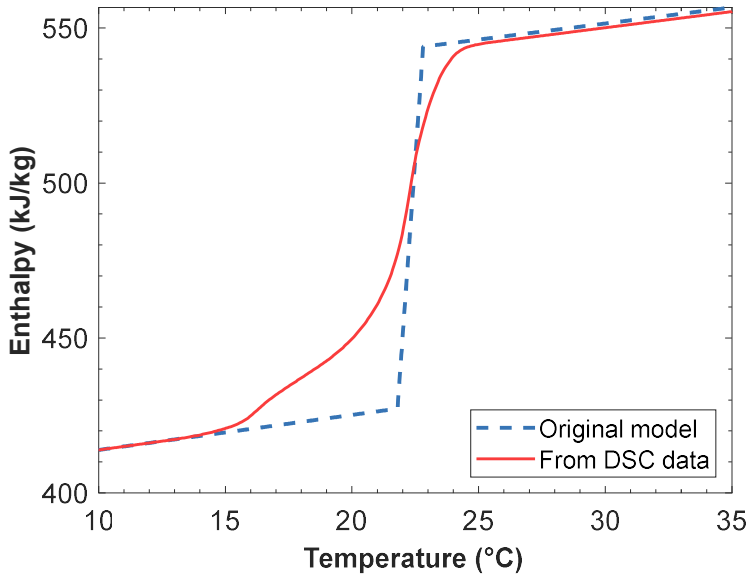

Figure 3.6: The idealized and DSC generated enthalpy vs. temperature curves.

It's easy to see the non-ideal phase change behavior between 15 and 23 C. The PCM begins to change phase at 15 °C, far before the desired transition temperature. The idealized curve was used in the design phase, and the DSC generated curve was used for model validation. The decision to

switch will be discussed in greater detail in Chapter 5. In addition, the generation of the enthalpy vs. temperature curve from DSC data is not trivial and is discussed in Appendix A.

Several volume fractions of PCM were simulated in the finite difference model to determine the optimal fill fraction for the design. The parameters simulated are included in Table 3.1, and were originally calculated by NETenergy.

Table 3.1: Key properties of compressed expanded graphite options that can be manufactured by NETenergy.

PCC*	$K_{\parallel}$ $(\mathrm{W} \cdot m^{-1} K^{-1})$	$K_{\perp}$ $(\mathrm{W} \cdot m^{-1} K^{-1})$	Mass Fraction (−)	Vol. Fraction (−)
A	8	4	0.9	0.797
B	16	5	0.8	0.729
C	24	6	0.7	0.695

The conductivity in Table 3.1 was approximated based on prior measurements of similar expanded graphite. Varying volume fraction has benefits and drawbacks. Low volume fraction improves cyclability and thermal conductivity. While high volume fraction increases storage capacity.

The volume fraction's in Table 3.1 were run through the finite difference model, and each porosity was evaluated by it's peak shaving (Energy shaving). The peak shaving was computed by coupling the finite difference model to a system model of a vapor compression cycle. The system model found the amount of work needed to meet the room load requirements for the original vapor compression cycle, and the vapor compression cycle with the TES acting as the outdoor coil to calculate the peak shaving, which is done with Equation (15).

$$\%\ Peak\ Shaving = \frac{W_{VC-T}}{W_{VC-original}} * 100 \tag{15}$$

In Equation (15), W is the energy required to run the compressor during peak operation. The system model used to calculate the % Peak Shaving is outside of the scope of this work.

Over a four-hour period peak shaving varies, so the minimum peak shaving was used to compare the PCC slabs, as seen in Figure 3.7.

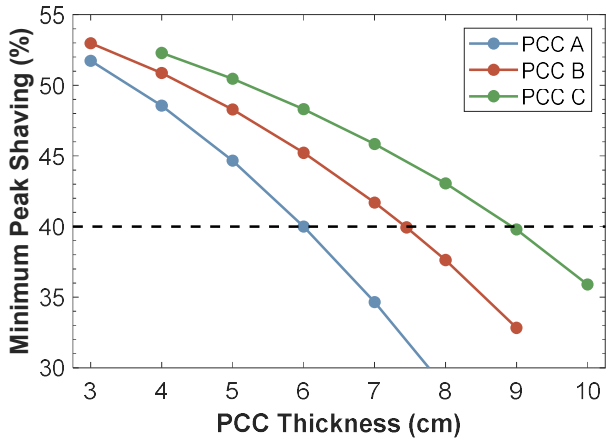

Figure 3.7: Minimum peak shaving as a function of PCC thickness for the three different graphite options shown in Table 9.

The higher composite conductivity of option C allows for thicker PCC slabs, but results in a lower energy density of each slab. As a result, the total number of unit cells in the system does not change significantly between fill fractions. So the fill fraction was selected based on the optimal fill for preventing PCM leakage, which was 44.7% by volume.

The final fill fraction was calculated from graphite properties, and lead to the calculation of slab material properties. The density and estimated porosity of the compressed expanded graphite was 280 kg/m^3 and 87.6%, respectively. Using the measured phase change composite density, Equation (11) was used to calculate the PCM volume fraction. Air filled the remaining volume (42.9%). The effective properties were calculated using DSC data of the pure PCM measured at Texas A&M and are included in. Table 3.2.

Table 3.2:The pure PCM and PCC properties

	PCM	**PCC**
Transition temperature	22.3°C	22.3°C
Average density	869 kg/m^3	650 kg/m^3
Latent heat	201 J/g	114 J/g
Specific heat	Liquid: 1.99 J/g·K Solid: 1.84 J/g·K	Liquid: 1.13 J/g·K Solid: 1.04 J/g·K
Thermal conductivity	Solid: = 0.15 W/m·K Liquid = 0.25 W/m·K	$k_\perp$ = 9 W/m·K* $k_\parallel$ = 20 W/m·K

*Note: The graphite had a thermal conductivity of 9 W/m·K perpendicular to the compression direction before soaking, but modeling efforts show that this is likely an overestimate of the composite conductivity due to delamination. See chapter 5.

The specific heat was calculated using effective medium theory. The average thermal conductivity of PureTemp 23 alone is 0.2 W/m-K. This low conductivity would prevent effective heat transfer into the storage material, substantially lowering its useable capacity within the system. The interconnected compressed expanded graphite was expected to boost the effective thermal conductivity to 9 W/m-K perpendicular to the refrigerant channels ($k_\perp$) and 20 W/m-K in the axial direction ($k_\parallel$). However, initial finite difference model validation efforts showed the conductivity perpendicular to the compression direction dropped from 9 to 4 W/m-K. This is discussed in more detail in the experimental set up and results chapter of this thesis.

The main factor driving device performance is the PCC thickness between adjacent microchannels because the PCC represents the dominant thermal resistance in the device. An example of the impact on peak shaving is shown in Figure 3.8.

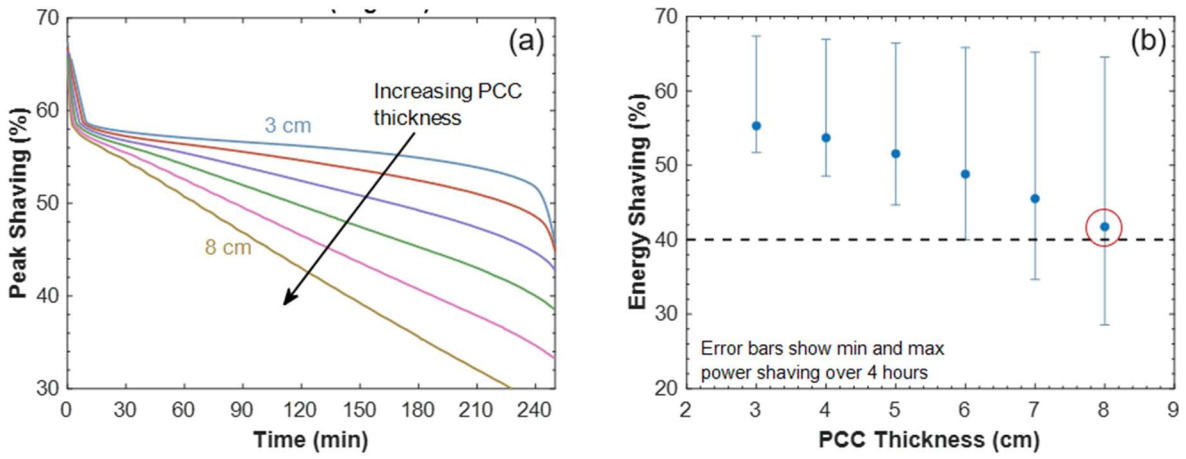

Figure 3.8: (a) Electrical peak shaving and (b) total energy shaving for different TES component designs.

In Figure 3.8a the thicker the PCC slabs, the faster the drop in peak electrical power shaving throughout the discharge process. Although all designs start with a peak shaving around 60%, the 8 cm slabs can only provide shaving above 40% for about 2 hours whereas the 3 cm slab can easily provide peak shaving above 50% for the entire discharge period. The slab thickness comes with tradeoffs though. Although the thinner slabs offer better peak shaving performance, they also require more microchannel arrays, increasing the cost of the device. Figure 3.8b shows the total energy shaving throughout the discharge period. In this figure, the error bars show the minimum and maximum power shaving for each design. We selected the largest PCC thickness that resulted in peak shaving above 40% for the 4-hour discharge process to reduce cost. This criterion could be modified in the future for optimal cost.

3.2.2 Microchannel Design

Next, the microchannel was selected for the design. 22 different microchannel geometries were evaluated based on a list from NETenergy's supplier. The best performing options are shown in Figure 3.9, along with the baseline microchannel previously in the model.

Channel	Width (mm)	Height (mm)	# Voids $(-)$	D_h (mm)
Baseline	25.4	1.3	26	0.70
1	12	1.0	12	0.61
2	14	1.2	4	1.28
3	26	1.4	6	1.60
4	42	1.65	10	1.65
5	48	1.65	10	1.70

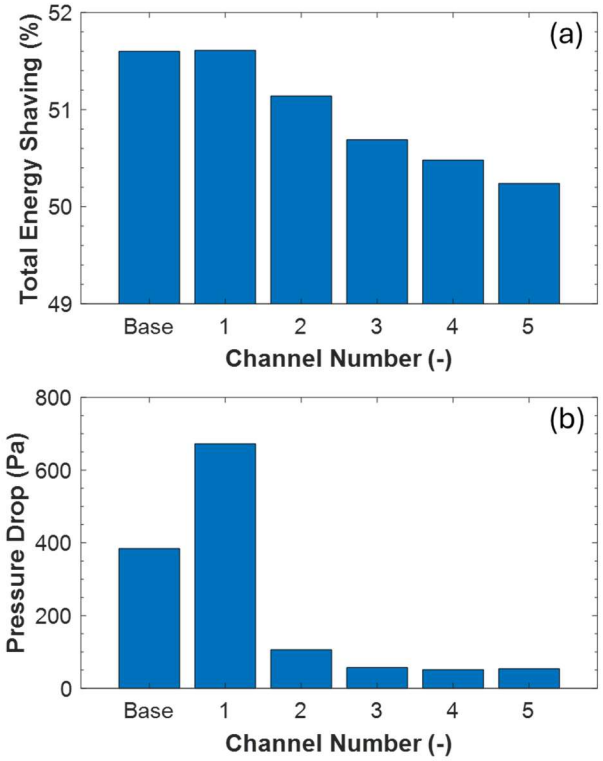

Figure 3.9: Impact of different microchannel geometries (table) on the (a) total energy shaving and (b) pressure drop in the TES device.

The microchannels had a much lower impact on the energy shaving than PCC thickness, as shown in Figure 3.9a. All options shown are within 1.5% of the baseline. The microchannel geometry does have a significant impact on the pressure drop, however. Microchannels 2 – 5 have a pressure drop much lower than desired, raising concerns over flow maldistribution. As a result, channel 1 was selected for the prototype, prior to the change in heat exchanger design due to the deadline. Channel 1 was selected since the pressure drop is well below the limit and it also has energy shaving performance equivalent to the baseline option.

Finally, with the PCC and microchannel designs, a footprint and pass configuration were selected for the device. Prior to the shift in design due to deadlines a footprint of 1 m x 0.5 m was selected to satisfy the pallet constraint and limit the manifold length based on prior experience of the group. The results for fill ratio and thickness all assume that the refrigerant flows through the

heat exchanger in a single pass. Multi pass configurations were also evaluated. Multiple passes have the advantage of potentially better refrigerant distribution but will increase the pressure drop. The pressure drop of different flow configurations is shown in Figure 3.10.

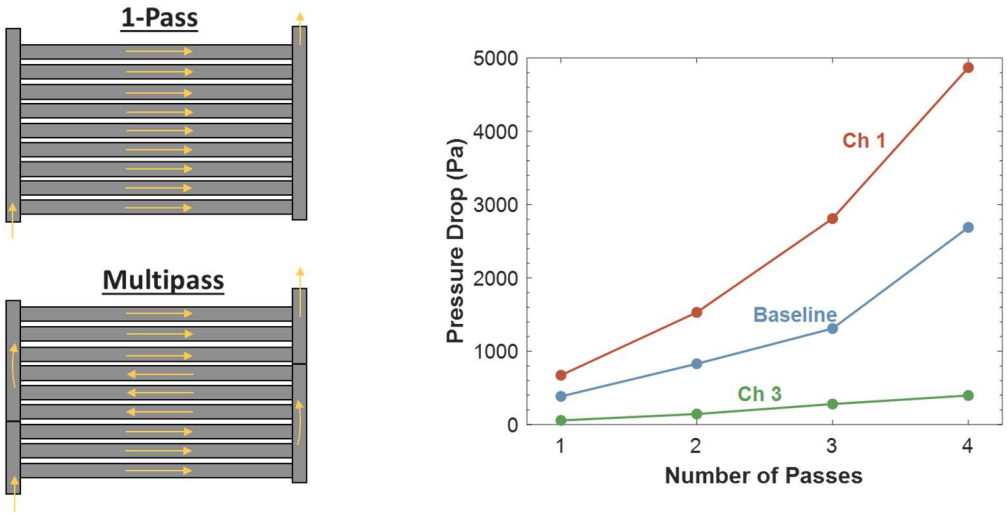

Figure 3.10: Pressure drop for different refrigerant flow configurations in the TES heat exchanger.

Based on these results, a 3-pass design was selected because it balances the risks of maldistribution with increases in pressure drop.

Ultimately, the design selected was not the one tested due to time constraints. NETenergy had a 1 m by 0.25 m single pass microchannel available for testing, which was the microchannel design used. This microchannel is pictured in Figure 3.11.

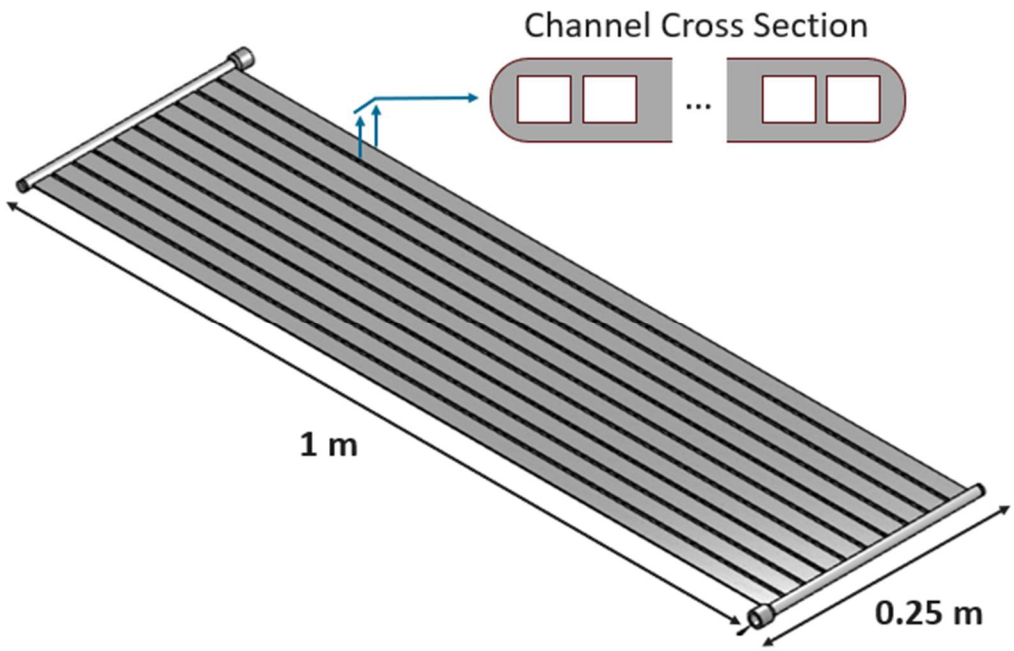

Figure 3.11: A CAD drawing of the microchannel heat exchanger and a section view of one of the channels.

The heat exchanger contains 10 Aluminum multi-port extruded tubes that are connected in parallel by inlet and outlet manifolds designed to distribute the refrigerant into each flow path. Each multi-port extruded tube is 1 meter long and has 40 rectangular subchannels within it, as shown in the Figure 3.11 cross section. Each subchannels had a hydraulic diameter of 0.3344 mm. When received the heat exchanger was actually 0.972 m by 0.27 m.

3.3 Analytical Model

The analytical model was developed with knowledge of the experimental results. This section will discuss the qualitive behavior of the heat exchanger. However a detailed discussion of the experimental observations is included in Chapter 5. Additionally, the assumptions and derivation of the model are also included. The rest of this section is the derivation of the solution.

3.3.1 Modeling Approach

The PCM TES HX behavior can be described in two regions. There is a constant power region and a varying power region as illustrated in Figure 3.12. The constant power region is a region of constant thermal energy transfer and should not be confused with electrical power.

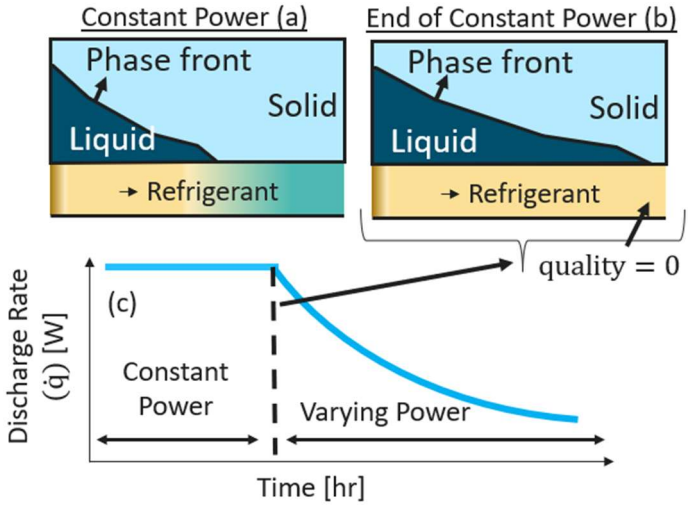

Figure 3.12: (a) The PCM TES HX during constant power discharge. (b) The PCM TES HX at the end of constant power discharge. (c) The Discharge rate as a function of time for a constant inlet test.

Half of the heat exchanger is used to illustrate the phase front of the PCM TES HX in Figure 3.12a and b. Initially as the constant power region begins the phase front moves axially along the heat exchanger from Figure 3.12a to b. In Figure 3.12b the phase front reaches the full length of the heat exchanger. At this time the outlet is a saturated liquid. Because the latent heat of vaporization (or condensation) has more energy content than the sensible heat transfer regime of the fluid the power discharged to the PCM begins to vary in time as seen in Figure 3.12c. Each of these regions was modeled separately to create a piecewise solution that can predict the PCM TES HX discharge time given a PCC thickness, heat exchanger area, and material properties. Furthermore, to solve the model as a design problem a discharge time is taken as input and a PCC thickness is calculated.

The modeling approach uses a single conduction resistance to capture the physics of the PCM and an energy balance to capture the physics of the refrigerant. Conduction through the PCC

governs the heat transfer performance as discussed in section 3.2. The conduction resistance model is illustrated in Figure 3.13.

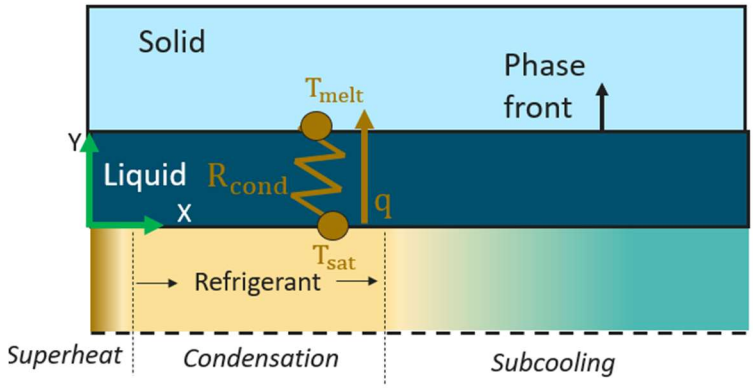

Figure 3.13: The conduction resistance model illustrated for a vertically moving phase front.

The conduction resistance model in Figure 3.13 is also presented in Equation (16)

$$\dot{q} = \frac{2\Delta T}{R_{cond}} = \frac{2(T_{sat} - T_t)}{\frac{th_{pcc}}{k_{PCC}A_{HX}}} \tag{16}$$

In Equation (16) T_t is the transition temperature of the PCM which is the melt temperature in Figure 3.13. In addition, k_{PCC} is the conductivity of the PCC slab, and A_{HX} is the surface area of the top of the heat exchanger. The contact resistance and convection resistance are neglected. The contact resistance is neglected to simplify the model, and the convection resistance will be low because the fluid is in the two-phase regime, which has a high heat transfer coefficient. The resistance equation has a factor of 2 included because there are two slabs so there are effectively two conduction resistances in parallel. Lastly, to reduce the model to one dimension the conduction is only modeled in the vertical direction.

3.3.2 Model Derivation

The model derivation begins by defining the required solution. Equation (17) presents the desired form of the solution.

$$E(t) = \begin{cases} 0 \le t \le t_{\dot{q}-con} & E = \int \dot{q}(t)dt \\ t_{\dot{q}-const} \le t \le t_{final} & E = \int \dot{q}(t)dt \end{cases} \quad (17)$$

In Equation (17) t is the time, $t_{\dot{q}-const}$ is the time when the constant power region ends (Figure xa), and t_{final} is the time when PCC slab has fully changed t_{final}. Additionally, E is the energy discharged by the PCC slab and $\dot{q}$ is the heat transfer rate into between the refrigerant and PCM. To derive the model the resistance equation's are solved for the discharged energy in the constant power and varying power regions. The definition for discharged energy in one dimension is given by Equation (18).

$$E(t) = 2\left(\rho_{pcc} A_{HX} th_{\mathrm{PCC}} L_{PCC}\right) \quad (18)$$

Equation (17) and (18) govern the behavior of the heat exchanger.

The constant power region is pretty simple to model. The maximum heat transfer rate of the heat exchanger is given by Equation (19).

$$\dot{q}_{max} = \dot{m}\left(h_{in} - h_{T=T_t}\right) \quad (19)$$

In Equation (19) h is the enthalpy. Equation (19) is derived considering an energy balance on the refrigerant channel. The properties in the PCC slab are assumed to be constant through the conduction thickness. During the constant power region the refrigerant will enter superheated and fully condense to a subcooled fluid. Therefore, the heat transfer rate in this region approaches the maximum possible heat transfer rate (Equation (19)). Thus, deriving the solution to the discharged energy in the constant power region is simple. The integration is carried out in Equation (20).

$$E(t) = \int_0^t \dot{q}_{max}\, dt = \dot{q}_{max} t \quad (20)$$

The solution in Equation (20) is valid from 0 to $t_{\dot{q}-co}$.

The definition for discharged energy and Equation (16) can be used to find the time when the constant power region ends ($t_{\dot{q}-const}$). First, rearranging Equation (16) leads to a solution for the thickness when the constant power region ends ($th_{\dot{q}-const}$) in Equation (21).

$$th_{\dot{q}-co} = \frac{2k_{pcc}A_{HX}\Delta T}{\dot{q}_{max}} \tag{21}$$

Equation (21) defines the thickness when the constant power regions because it captures the resistance at the time illustrated in Figure 3.12b. Prior to Figure 3.12b the area of the phase front does not cover the full heat exchanger as illustrated in Figure 3.12a. The model assumes prior to this time that the area for phase change is A_{HX}, to ensure the model remains 1D. The thickness at times less than $t_{\dot{q}-const}$ is smaller than $th_{\dot{q}-co}$, and grows linearly as shown in Equation (20). Setting the discharged energy in Equation (18) and (20) equal leads to Equation (22).

$$t_{\dot{q}-co} = \frac{4k_{pcc}A_{HX}^2\Delta T\rho_{pcc}L_{PCC}}{\dot{q}_{max}^2} \tag{22}$$

Equation (22) completes and bounds the constant power region solution.

The varying power region isn't as easy to derive, but ultimately is the Stefan solution [74]. The derivation begins by redefining the discharge rate as the derivative of the discharged energy with respect to time, as seen in Equation (23).

$$\dot{q} = \frac{dE}{dt} \tag{23}$$

Now the discharged energy can be solved for in Equation (23) using separation of variables. However, several substitutions need to be made before solving. First, the resistance, Equation (16) is substituted in, which gives Equation (24).

$$\dot{q} = \frac{dE}{dt} = \frac{2\Delta T}{\frac{th_{PCC}}{k_{pcc}A_{HX}}} \tag{24}$$

Then to get Equation (24) in terms of only time, discharged energy, and constant values the definition of discharged energy, Equation (18), is rearranged and substituted for the thickness The substitution leads to Equation (25).

$$\frac{dE}{dt} = \frac{4\left(\Delta T A_{HX}^2 k_{pcc} L_{PCC} \rho_{pcc}\right)}{E} \tag{25}$$

Separating variables and solving leads to Equation (26).

$$E = \sqrt{2\left(4\left(\Delta T \rho_{pcc} A_{HX}^2 L_{eff} k_{pcc}\right)t + \kappa\right)} \tag{26}$$

In Equation (26) κ is an integration constant, which is given by the energy discharged when time equals $t_{\dot{q}-const}$. The constant is given in Equation (27).

$$\kappa = \frac{E_{\dot{q}-const}^2}{2} - 4\left(\Delta T \rho_{pcc} A_{HX}^2 L_{PCC} k_{pcc}\right) t_{\dot{q}-const} \tag{27}$$

This is the solution to the differential equation.

Finally to bound the varying discharge solution the time when the PCC slabs have fully discharged can be solved by equating Equation (18) and (26), which leads to Equation (28).

$$t_{final} = \frac{(2\rho_{pcc}A_{HX}th_{pcc-total}L_{PCC})^2 - \kappa}{4\Delta T\rho_{pcc}A_{HX}^2 L_{eff}k_{pcc}} \tag{28}$$

Between $t_{\dot{q}-con}$ and t_{final} the phase front progresses vertically until the full latent capacity is gone. This happens when the thickness is equal to $th_{pcc-total}$, the full thickness of the PCC slab. Equation (28) can be easily rearranged to solve for the to PCC thickness.

The full piecewise solution is given in Equation (29).

$$E(t) = \begin{cases} 0 \le t \le t_{\dot{q}-co} & E = \dot{q}_{max}t \\ t_{\dot{q}-c} \le t \le t_{final} & E = \sqrt{2\left(4\left(\Delta T\rho_{pcc}A_{HX}^2 L_{PCC}k_{pcc}\right)t + \kappa\right)} \\ & \text{where: } \kappa = \frac{E_{\dot{q}-const}^2}{2} - 4\rho_{pcc}A_{HX}^2 k_{pcc}L_{PCC}t_{\dot{q}-cons} \end{cases} \tag{29}$$

The time $t_{\dot{q}-const}$ is given by Equation (22) and the time t_{final} is given by Equation (28). The solution is validated in Chapter 5 as a simulation problem. This thesis does not discuss the use of the solution as a design problem, which is future work.

Chapter 4: Experimental Set Up

This chapter describes the design, build and validation of the experimental facility, the build of the PCM TES HX, and calculations used to characterize the TES heat exchanger. The experimental facility was constructed specifically for this work, and is one of the major accomplishments of this thesis.

4.1 Experimental Facility Design

The experimental facility shown in Figure 4.1 was constructed to circulate a refrigerant (R410a) through a unit cell TES heat exchanger described in Chapter 1 and 3.

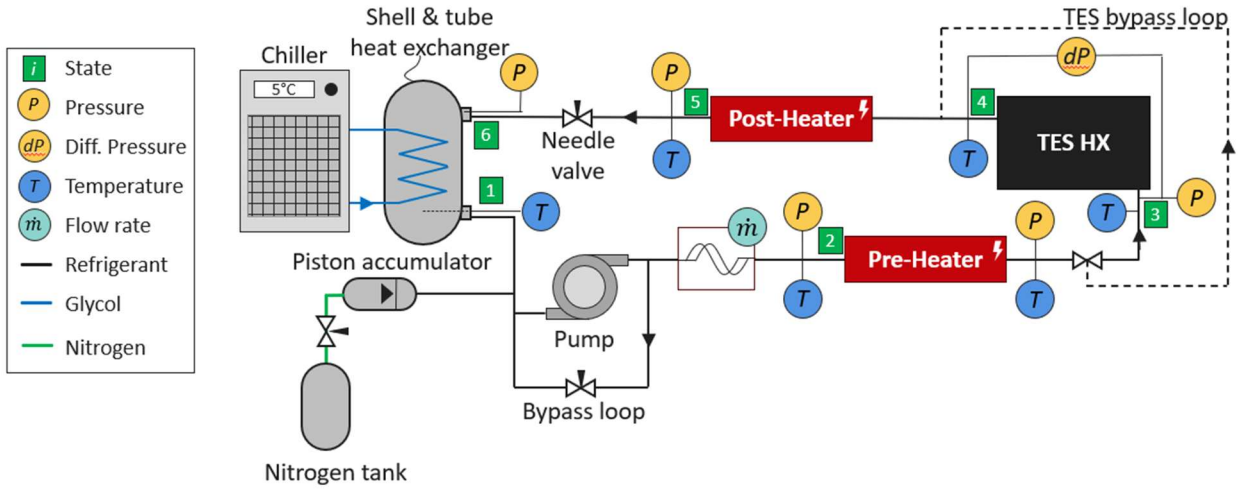

Figure 4.1: A schematic of the experimental facility described in this work.

The facility was designed to supply refrigerant at a user-specified flow rate and thermodynamic state (pressure and enthalpy) to the inlet of the TES heat exchanger (state 3). The facility can support a wide range of conditions that the unit cell could experience in a multi-split vapor compression system during charge and discharge. Finally, the facility was designed to measure the outlet state regardless of the refrigerant phase leaving the TES component, allowing measurement of key quantities like the heat removal rate (discharge rate) and discharged energy.

4.1.1 Facility Operation Requirements

The facility was designed to supply refrigerant to the TES heat exchanger in a way that mimics what the unit cell should see during discharge on a hot summer and cold winter day. The inlet flow conditions for these two "design days" are shown in Table 4.1.

Table 4.1: The inlet conditions specified for the TES HX experimental facility

	Summer (condenser)	**Winter (evaporator)**
Pressure	1600 – 1800 kPa	1700 – 1450 kPa
Enthalpy	15°C superheat	0.2 quality
Flow rate	3 g/s	3 g/s
Discharge time	4 hours	4 hours

The initial PCM transition temperature used to design the facility was 25 °C, however a transition temperature of 22.3 °C was used in testing as discussed in Chapter 3. The PCM transition temperature is relevant because it changes the pressures chosen for operation. The pressure and enthalpy were informed by system modeling conducted at NREL that captures how the PCM TES HX component works with vapor compression cycle equipment [82]. Additionally, a flow rate of 3 g/s was chosen for facility design based on target PCM TES HX capacity, target discharge time, and desired outlet state. The desired outlet state for the condenser was 2 °C subcooled, while the target for the evaporator was a saturated vapor. The outlet targets were also informed by NREL's system modeling.

The pressure is set by the driving temperature difference needed to efficiently transfer heat to and from the PCM at the constant power discharge rate demanded by the room load. Equation (30) presents the driving temperature difference.

$$Driving\ \Delta T = |T_t - T_{sat}| \tag{30}$$

The inlet pressure sets the saturation temperature, T_{sat}, and the PCM chosen sets the transition temperature, T_t. The TES HX will operate at constant power when integrated into the vapor compression cycle. The TES HX operates at constant power to meet a constant room load, which requires the inlet pressure (and therefore driving temperature difference) to vary in time as thermal resistances build up in the PCM TES HX.

The variation in pressure for condenser and evaporator discharge at a constant flow rate in a vapor compression cycle is shown in Figure 4.2.

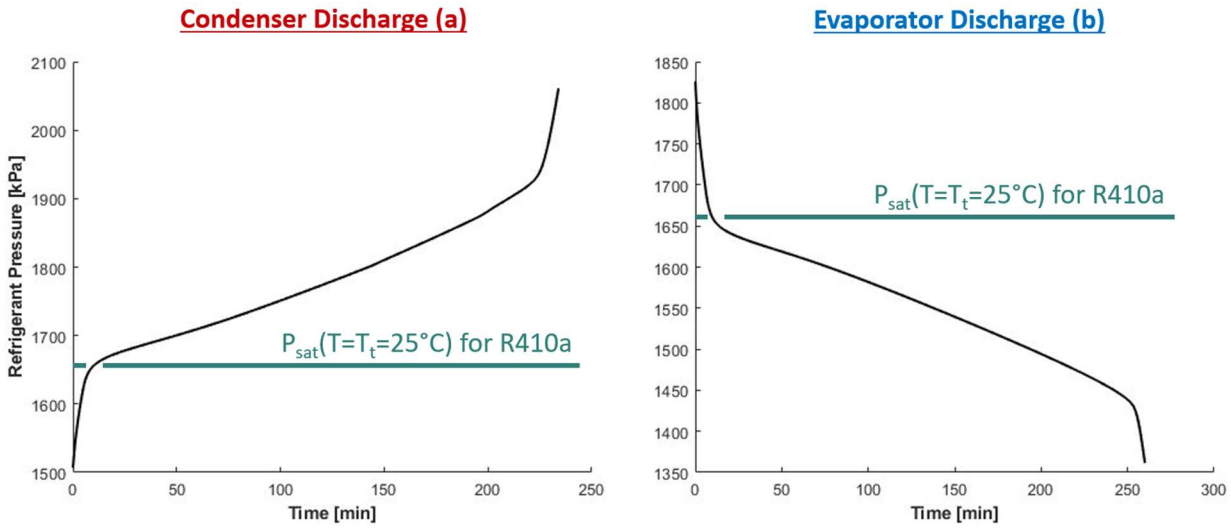

Figure 4.2: The refrigerant pressure for condenser and evaporator discharge for a module with a PCM transition temperature of 25 °C.

In the beginning, the pressure changes rapidly to increase the driving temperature difference to overcome surface resistances (contact, microchannel conduction, and heat transfer fluid convection). Then as the test progresses the conduction resistance through the PCC increases and the driving temperature difference needed to maintain constant power does as well, so the pressure increases. In this regime the resistance increases at a relatively constant rate because phase change is the dominant resistance. Finally, at the end of the test phase change ceases and sensible heating

of the PCM occurs requiring a rapid increase in driving temperature difference to maintain constant power discharge.

A walk through the operation of the facility in its condenser mode illustrates how each component helps achieve the TES HX inlet state required and maintain operation of the facility. Figure 4.3 shows each state of condenser operation on a temperature-enthalpy (T-h) diagram at 1800 kPa.

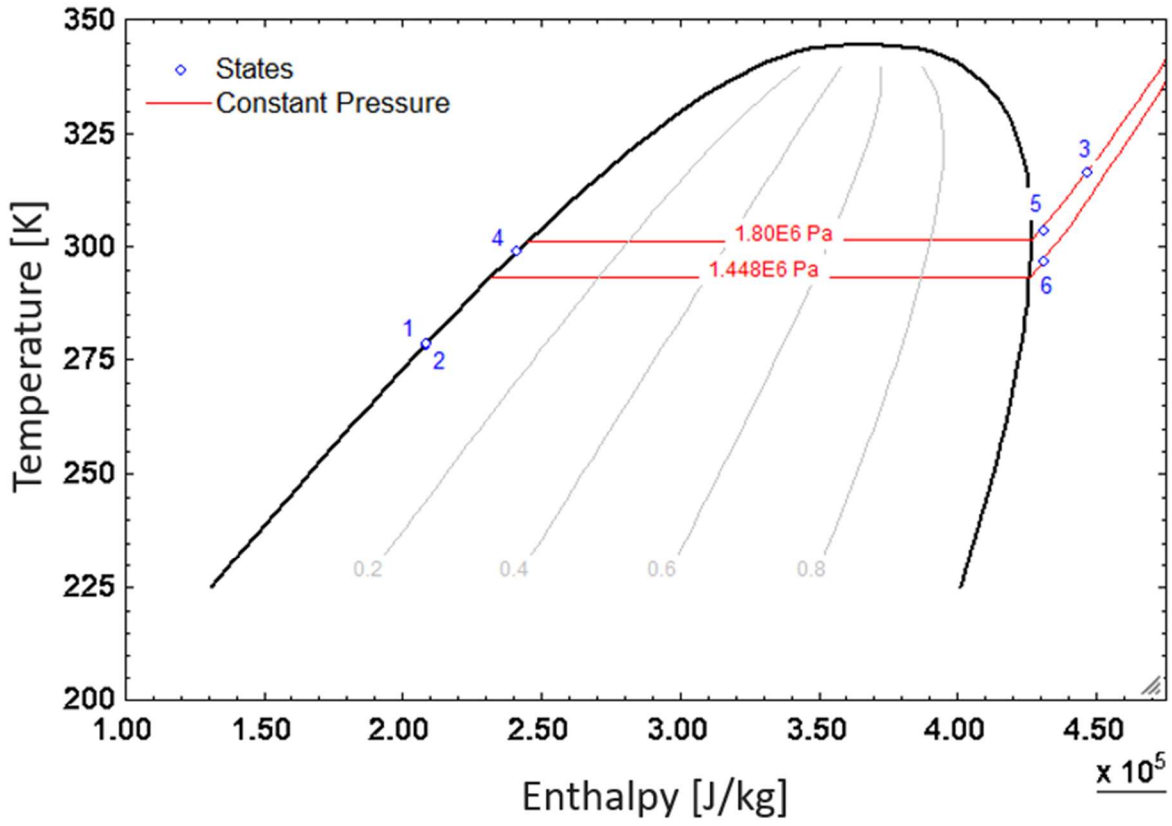

Figure 4.3: A T-h diagram of R410a during operation of the condenser mode at maximum pressure.

At state 1, the pump requires a 1°C subcooled liquid to operate properly. Next, at state 2 the pump drives flow, increasing the refrigerant pressure. Following the pump the refrigerant passes through the pre-heater, heating to a 15°C superheated state. Following the pre-heater the refrigerant loses heat to the PCM within the TES HX and condenses. The fluid ideally condenses to 2°C subcooled

state, but if the TES HX doesn't function as designed, or a constant pressure test is run, refrigerant will exit the TES HX as a saturated mixture (two-phase). The enthalpy of a two-phase fluid cannot be measured with pressure and temperature, so an energy balance needs to be done instead. The fluid is heated as it passes through the postheater, and enough heat is added (through Joule heating) to reach a 3°C superheated state, which is measurable using temperature and pressure. In the worst-case scenario, the post heat heater must add enough heat to the refrigerant to fully evaporate and superheat it (from a quality of 0 to a 3°C superheated state). To provide some extra capacity the post heater was required to heat a fluid from a 2°C subcooled state to a 3°C superheated state. The needle valve sits just upstream of the post heater and throttles the pressure down to control the flow rate and pressure of the system. Finally, the shell and tube heat exchanger takes on the refrigerant's heat and brings the fluid back to a 1°C subcooled state at state 1. If the fluid in the pump is not liquid, the pump may not function properly. Two phase conditions at the inlet of the pump could cause cavitation, and superheated conditions could lead to dry running the pump and blowing a fuse.

The main difference in facility operation in condenser and evaporator mode is the operation of the heaters. The preheater sets a 15 K superheated state in condenser mode, but for evaporator mode it sets a 20% quality inlet state. Therefore, less preheater power is needed because the preheater doesn't need to move the refrigerants state all the way across the vapor dome. Additionally, the outlet will already be a superheated vapor in the evaporator case so very little power is needed from the post heater to achieve a 3°C superheated state.

The thermodynamic states in Figure 4.3 are constrained by a combination of the facility operation requirements and the components selected. The thermodynamic constraints for each state are shown in Table 4.2.

Table 4.2: The thermodynamic state constraints of the facility.

State	Thermodynamic Constraints	
1	$P_1 = P_6 - \Delta P_{SH}$ & $\Delta P_{SH} \approx 1$ psi 1°C subcooled	
2	Pump efficiency (Assumed 90%) $P_2 = P_3 + \Delta P_{PeH}$ & $\Delta P_{PeH} \approx 1$ psi	
3	Condenser 1600 – 1800 kPa 15°C superheat	Evaporator 1700 – 1450 kPa 0.2 quality
4	$P_4 = P_3 - \Delta P_{TES}$ & $\Delta P_{TES} \approx 10$ kPa Condenser 2°C Subcooled	Evaporator x=1
5	3°C superheated $P_5 = P_4 - \Delta P_{PoH}$ & $\Delta P_{PoH} \approx 1$ psi	
6	$h_5=h_6$ (valves are isenthalpic) Condenser P_6=210 psi	Evaporator P_6=192.5 psi

The pressure drops in the postheater, preheater, shell and tube HX and TES HX all depend on component selection. The postheater and preheater selection will be discussed in more detail in this subsection. The design assumed a pressure drop of ~10 kPa in the TES HX based on prior experience testing microchannel HX's, and the design of the TES HX is discussed in detail in Chapter 3. Furthermore, the pump efficiency was not given by a pump supplier so 90% was

assumed. Lastly, the pressure at state 6 was set at a constant value to constrain the back pressure so the pump and state 5 needle valve could control the inlet pressure to the system.

4.1.2 Design Component Selection

Each component in the facility serves a purpose, which is motivated by facility operational requirements. This subsection documents the detailed logic behind choosing each component in the facility. As discussed in the previous subsection, the preheater achieves the desired TES HX inlet enthalpy and the post heater facilities measurement of the outlet enthalpy. The variable speed pump, pump bypass valve, and state 5 needle valve all set the flow rate of the experimental facility. The flow control components, chiller (and by extension shell and tube HX), and piston accumulator set the pressure of the system. The chiller sets the refrigerant saturation temperature in the shell and tube HX, slow pressure control, meanwhile the piston accumulator and needle valve provide fast pressure control. The needle valve is controlled via an electrical actuator to aid in setting the flow rate and pressure. Furthermore, the piston accumulator has a regulated supply of nitrogen on the side of the piston opposite the refrigerant to control system pressure.

The details of each component selected contribute to meeting operational requirements and mechanical and electrical design considerations. A summary of the components selected is presented in Table 4.3.

Table 4.3: Part numbers and specifications of all components in the experimental facility.

Component	Supplier	Part Number	Specifications
Pump	MicroPump	GJ-N23-DEMSE[1]	Pump Max ΔP: 5.6 Bar (80 psi) Max pressure: 300 psig Flow Rate Range: 0.4-3.25 L/min Displacement: 0.64 mL/rev Motor Speed Range: 250-10000 rpm Input Voltage: 10-38 VDC Max Amperage: 2 A @ 24 VDC Speed control: 0-5 VDC
Pump Bypass Valve	Swagelok	SS-4MG-BU-MH	C_v = 0.03 Max pressure: 3435 psig
Preheater	CastX Aluminum Solutions	BX8L4M200ASK100	Max power: 240 V, 3000 W Max pressure: 2100 psi
Post heater	CastX Aluminum Solutions	WX6E2A300HSM00	Max power: 240 V, 1500 W Max pressure: 5100 psi
Needle Valve	Swagelok	B-1RS8	C_v = 0.73 Max pressure = 2100 psig
Needle Valve Actuator	Hanbay	MCL-050AB	24 V excitation 0-5 V input Max current draw: 3 Amps
Shell and Tube HX	Exergy	00540-17	37 Tubes Tube max pressure: 1500 psig Shell max pressure: 1000 psig
Piston Accumulator	Parker (McMaster)	ACP05AA100E1KTC	Max pressure: 4000 psi Size: 32 fl oz
Chiller	Thermo Fischer Scientific	Thermoflex-5000	T1 Pump 3.5 gpm @ 60 psid 4.5 gpm typical* 5 gpm max flow rate 5000 W capacity Temp range: 5°C – 40°C Max pressure: 100 psig

[1]The motor controller spec. is DEMSE (Eagle Drive), it came as a package with the pump head

*See chiller manual in LET+S Lab Guide for pump curves

Pertinent high level operating specifications are included in Table 4.3. The rest of the section walks through how each component was selected, and detailed information on each component is available in the LET+S lab guide, including manuals.

The pump was selected based on the operating flow rates for the system and it's maximum operating pressure. The mass flow rate range for R410a 1800 kPa and 1°C subcooled are approximately 7 g/s – 61.2 g/s based on the pump operating curve for a viscosity of 0.4 Cp, which is much higher than R410a, which has a viscosity of 0.119 Cp at 1800 kPa and 1°C subcooled. The 0.4 Cp pump curve was the best information that could be obtained from the supplier for R410a. The pump's maximum operating pressure limits the system's maximum working pressure. Future facility users using R410a, or other high pressure refrigerants should consider upgrading the pump to a higher working pressure. The relief valve for the system triggered prematurely at a pressure of 280 psi at state 2 (state 2 is the highest pressure measured), and preliminary test matrix design revealed pressures near 280 psi could be a desirable inlet condition. Information on the relief valve and other miscellaneous components can be found in Appendix B.

The target flow rate of the facility was 3 g/s, and the lowest pump flow rate on the operating curve was 7 g/s so a pump bypass loop was included. The pump bypass loop sends excess flow to through a loop outside of the main flow loop and includes a needle valve that matches the pressure drop of the loop. The needle valve was sized using Swagelok's flow coefficient technical bulletin [83]. The equation for flow coefficient of a liquid is presented in Equation (31), and was used to select the valve.

$$C_v = \frac{\dot{V}}{N_1}\sqrt{\frac{SG}{\Delta P}} \tag{31}$$

In Equation (31) $\dot{V}$ is the volumetric flow rate, ΔP is the pressure drop, SG is the specific gravity relative to water at standard conditions, and N_1 is a unit constant that can be found in the technical bulletin. The flow coefficient (C_v) represents the volumetric flow rate of in gallons per minute of water that would flow through the valve at standard inlet conditions and with a 1 psi pressure drop. Although, the flow coefficient is always reported as dimensionless even though it isn't. Swagelok's standard conditions are a temperature of 60°F and absolute pressure of 1 atm. Standard conditions can vary between manufactures, but are typically similar to Swagelok's.

To size the valve some assumptions were made about pump operation. The facility design assumed a volumetric flow rate of 0.35 L/min, and that the desired mass flow for the test section would vary between 1.5 g/s and 5.4 g/s. These flow rates were used instead of 3 g/s because some initial investigation was done to specify the minimum and maximum possible flow rate the facility would have. Since the design assumed that the pump would operate at a constant flow rate, as the required flow rate through the test section increased so did the flow rate sent to the bypass loop.

To determine the appropriate valve the percentage open of the valve during operation needs consideration. Comparing the flow coefficient for a fully open valve to the flow coefficient needed for a given operational condition determines the percentage open for a given flow rate according to Equation (32).

$$PO\% = C_v/C_{v-open} \tag{32}$$

A percentage open between 10 and 90% (sometimes 20 and 80% is specified) is desirable because most valves have linear behavior in this range. In practice this depends on the flow coefficient curve specified by the manufacturer. The minimum flow coefficient required was 0.002429, and the maximum was 0.01803. A valve with a fully open flow coefficient of 0.03 was selected because its percentage open varied from 8.1 to 60% for the operating conditions modeled during design.

Verification of the actual flow coefficient, and bypass loop behavior was not conducted, as the facility did not have proper instrumentation for this. However, no notable issues were encountered.

The preheater and postheater were both sized to accommodate the maximum mass flow rate expected by the system. The preheater is oversized and does not limit the mass flow rate of the system. The preheater was oversized because it was a generous gift from Professor Mark Anderson's lab. The postheater is smaller than the preheater and limits the capacity of PCM TES HX that can be tested. As the mass flow rate of the system increases the heating capacity required for the post heater to heat a saturated liquid to a superheated vapor increases proportionally. This is described by the energy balance in Equation (33).

$$\dot{Q_{post}} = \dot{m}(h_5 - h_4) \tag{33}$$

In Equation (33) $\dot{Q_{post}}$ is the post heater power required to heat from state 4 to 5, which at worst is heating from 2°C subcooled to 3°C superheated. The postheater selected can accommodate flow rates up to 5.75 g/s, based on its maximum power at 208 V – 1125 W. The manufacturer for the post heater and preheater specified a pressure drop of 1 psi for R410a and the flow conditions tested. Because boiling occurs in the preheater and postheater the refrigerant was plumbed to flow upward.

When the TES HX operates as an evaporator the post heater requires minimal heating to achieve a superheated vapor state so it doesn't constrain test section capacity. Instead, the shell and tube heat exchanger limits the flow rate since it must change the state of the fluid to a subcooled liquid. The shell and tube heat exchanger was modeled with the effectiveness NTU method using sub heat exchangers for each phase of fluid flow. There was a sub heat exchanger for the initial superheated region, the condensing region, and the subcooled region. The effectiveness NTU modeling makes many assumption, and the Engineering Equation Solver program used to design

the facility has detailed comments to describe the choices made when modeling this heat exchanger. The design of the heat exchanger was ultimately completed by the supplier, Exergy, so the estimates of shell and tube heat exchanger limits (capacity failure) should be taken skeptically because they do not reflect the supplier's modeling. The supplier's modeling technique was never discussed, but the major difference is likely the quality of the condensation modeling as the superheated and subcooled sub heat exchangers have little impact on the capacity of the heat exchanger. According to the Engineering Equation Solver model, at a flow rate of 5.75 g/s 91% of the shell and tube heat exchanger is utilized to condense the refrigerant. Thus, leading to a 5.1°C subcooled state. The flow rate could increase until the design meets the target of 1 K subcooling. However, at 6 g/s the subcooling drops to 2.2°C, so small increases beyond 5.75 g/s will lead to drastic drops in performance. Therefore, for practical reasons, the facility has a maximum flow rate of 5.75 g/s for condenser and evaporator mode.

The chiller was selected as part of the heat exchanger design. Its flow rate and low temperature were adequate for cooling down the superheated refrigerant. Propylene glycol from the chiller flowed through the tube side of the shell and tube heat exchanger and was plumbed upward. The refrigerant was plumbed downward to help with condensation. The minimum temperature of the chiller affects the minimum pressure the system can achieve, because the saturation pressure on the refrigerant side of the shell and tube heat exchanger sets the system back pressure. To reduce the minimum system pressure a chiller with a lower minimum set point should be selected. Achieving pressures below 190 psi were challenging for the system, because the system pressure is a function of refrigerant charge, loop volume, and saturation temperature in the shell and tube heat exchanger. Appendix C discusses how to start up the loop at different operating pressures so TES HX inlet pressures below 190 psi can be achieved.

The primary consideration for selection of the state 5 needle valve was a flow coefficient that would allow the needle valve to control the system pressure. The needle valve was intended to set the back pressure to be 192.5 psi during evaporator operation and 210 psi during condenser operation for a PCM transition temperature of 25 °C. These requirements would have been lower for the actual PCM used, but the design was never updated. The pressure requirements were set based on the allowable system pressure drop, which was governed by the pump operating curve, which will be discussed in more detail later in this subsection. The state of the fluid in the needle valve is superheated, which requires a different equation for flow coefficient according to the technical bulletin from Swagelok [83]. The Equation for sizing a gas needle valve is given in Equation (34).

$$C_v = \frac{\dot{V}}{N_2 P_{in}\left(1 - \frac{2\Delta P}{3P_{in}}\right)}\sqrt{\frac{P_{in} SGT_{in}}{\Delta P}} \tag{34}$$

If flow is choked a different equation is needed, which can be found in Swagelok's Technical Bulletin. The specific gravity for gas is calculated relative to air rather than water.

The state 5 needle valve was chosen because its flow coefficient was within the range acceptable for the pressure drop and flow rate set by the constraints at state 6 and it was available for free from an old experiment. The required flow coefficient ranged from 0.07181- 0.5251. A valve with a flow coefficient of 0.73 was found in the scrap parts within the lab and repurposed for this experiment. The valve's percentage open ranges from 9.84% to 79.8%, making it a good fit. Although, in practice using this valve proved challenging, which will be discussed in the loop validation section. The loop validation section will also discuss the addition of the piston accumulator to the system.

The needle valve actuator was repurposed from a prior experiment to control the valve position for various desired TES HX inlet pressures. As the pressure at the TES HX inlet varies so does the pressure drop across the state 5 needle valve requiring adjustment to maintain operating requirements. The main design considerations for the needle valve actuator are the resolution of signal it can receive, and whether or not the torque applied matches the valve. If the torque does not match the actuator can damage the valve or itself. The resolution for a 0-5V signal was 0.013 V, which equates to 0.25°, and is so small it shouldn't reasonably affect the ability of the valve to respond to control inputs.

Component selection for measurements was completed with measurement of thermodynamic states and TES HX inlet conditions in mind. A summary of the components used for facility measurements is presented in Table 4.4

Table 4.4: The components used for measurements..

Sensor	Supplier	Part Number	Specifications
Coriolis flow meter	Micro Motion	CMFS010M	+/- 0.1% accuracy
Temperature	Omega	TMQSS-062G-6	Type T thermoucouples +/- 0.25 °C Accuracy
Pressure	Omega	PX309-500G/A	0-500 psig or psia range +/- 1.25 psi accuracy +/- 0.25% repeatability
Differential Pressure	Rosemount Emerson	3051C3A22A1AM4Q4	-1000 to 1000 inH_2O range 4-20 mA output +/- 0.0775% accuracy
Postheater Power Transducer	Ohio Semitronics	PC5-011DY25	Instrument Power: 120 V wall excitation (5 VA) Measurement Info: 2 kW, 300 VAC, 10 Amps Uncertainty: +/- 10 W
Preheater Power Transducer	Ohio Semitronics	PC5-020DY25	Instrument Power: 120 V wall excitation (5 VA) Measurement Info: 3 kW, 300 VAC, 15 Amps Uncertainty: +/- 15 W

The thermodynamic states at locations 1-3 and 5 were measured with thermocouples and pressure sensors. The type T thermocouples used throughout the experiment were calibrated using a Fluke 7109 calibration bath to ensure an uncertainty of +/- 0.25 °C. The pressure at state 6 was measured and used as the pressure at state 1 with a slight adjustment for change in height. The temperature at state 6 was not measured so it's thermodynamic state could not be determined. This would be valuable to validate facility design, but was not important to operating the facility. State 4 was measured through the energy balance in Equation (31), by rearranging to find h_4 and measuring h_5 which temperature and pressure sensors. The rearranged equation is given in Equation (35).

$$h_4 = h_5 - \frac{\dot{q}_{post}}{\dot{m}} \tag{35}$$

The post heater power in Equation (35) is measured by the preheater pressure transducer, and the mass flow rate is measured by the Coriolis flow meter. Furthermore, the pressure at state 4 is calculated using the differential pressure sensor by measuring the pressure drop across the TES HX. The pressure at state 4 can be found as described in Equation (36)

$$P_4 = P_3 - \Delta P \tag{36}$$

The enthalpy at state 4 was also measurable using a thermocouple and the pressure if the outlet was not saturated. This was used briefly in the experimental campaign, which is discussed in detail in Appendix D. Measurement of the thermodynamic states is the primary measurement goal of the facility. Instrumentation for the TES HX is discussed in a separate section.

4.2 Facility Validation

Loop validation focused on verifying proper functioning of components in the loop. The initial plan was to operate tests with a dynamic inlet condition that varied to create a constant power test. The validation was conducted in two phases. Initial results showed a piston accumulator was needed to control backpressure. This component was added and then other measurements were validated.

Initial loop validation was done with a small-scale version of the test facility. A schematic and picture of the initial loop build is included in Figure 4.4.

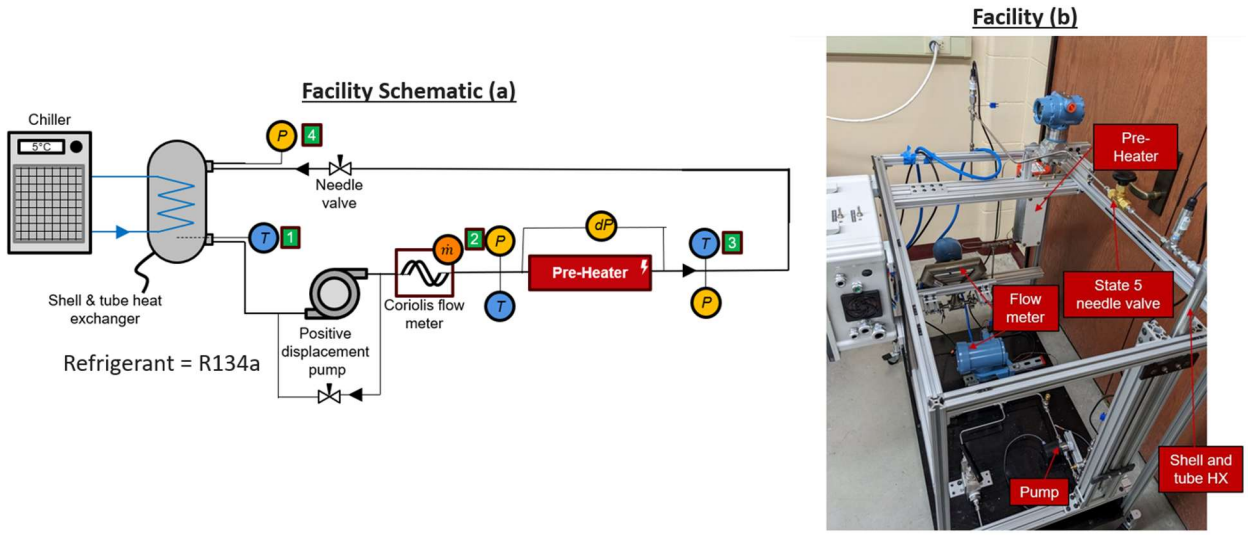

Figure 4.4: The initial test facility build. (a) shows the schematic (b) shows the physical facility built for initial validation.

A minimum viable working facility was constructed as seen in Figure 4.4b. The facility was tested with R134a rather than R410a because it had a lower pressure. Additionally, the flow meter in the first build was oversized so it was upgraded in the second build. None of the results from the initial build are presented, however, the results for needle valve flow coefficient validation were initially observed in the phase 1 facility build and confirmed in the second facility build.

Results of the initial validation showed that changing the back pressure with the state 5 needle valve was ineffective, so a piston accumulator was added to the system. The state 5 needle valve was likely ineffective because it's flow coefficient did not match the supplier flow coefficient curve, as seen in Figure 4.5.

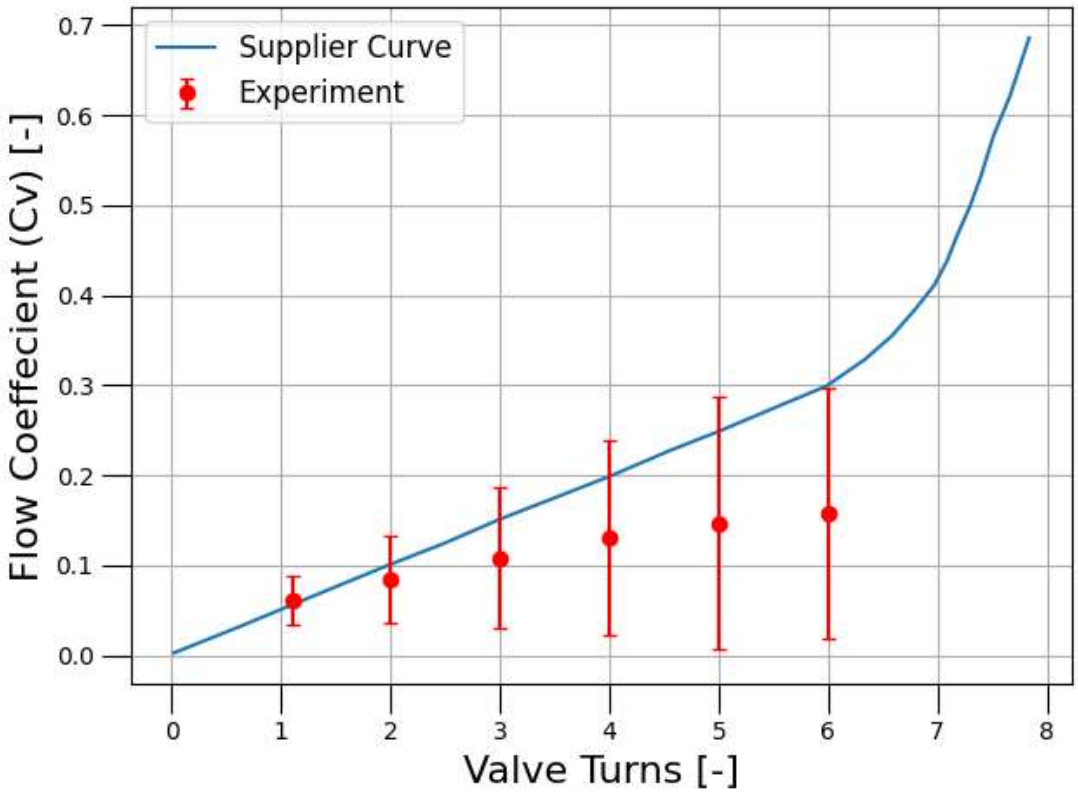

Figure 4.5: The Flow coefficient validation for the state 5 needle valve.

Figure 4.5 was created with data from the second phase of validation, but similar results were observed in the first phase. Figure 4.5 is the flow coefficient for subcooled R410a, so Equation (31) was used to calculate the flow coefficient. The experimental measurements and supplier flow coefficient do not agree. Although, the supplier curve is within the measurement uncertainty of the experiment. The calculation of the uncertainty is discussed in the final section of this chapter. The lack of agreement between the experimentally measured coefficient and supplier results may be the reason why the state 5 needle valve was ineffective at controlling system pressure. A piston accumulator was added to compensate for the needle valve's inability to control pressure.

The piston accumulator aided in control of the back pressure of the system, but was not digitally controlled, so did not allow for dynamic TES HX inlet conditions. The piston accumulator has nitrogen on one side of the piston and refrigerant on the other. The nitrogen side is attached to

a nitrogen cylinder with a pressure regulator, which allows the facility operator to manually change the volume of the loop. There is also a vent to atmosphere with a needle valve in case pressure needs to be released.

The main consideration for selecting the piston accumulator was the working pressure and the volume. The volume was selected by comparing the mass of liquid refrigerant that the accumulator could accommodate to the mass of refrigerant charged in the loop. The mass in the loop was approximately 1 lbs and the mass that the accumulator could accommodate was 1.27 lbs if cooled. In reality the accumulator was not actively cooled so assuming it would have a low temperature was poor. The accumulator was effective during condenser operation, but ineffective during evaporator operation, likely because of the poor temperature assumption.

The second phase of validation required a rebuild of the facility and included the piston accumulator. The test facility prior to test section implementation is shown in Figure 4.6.

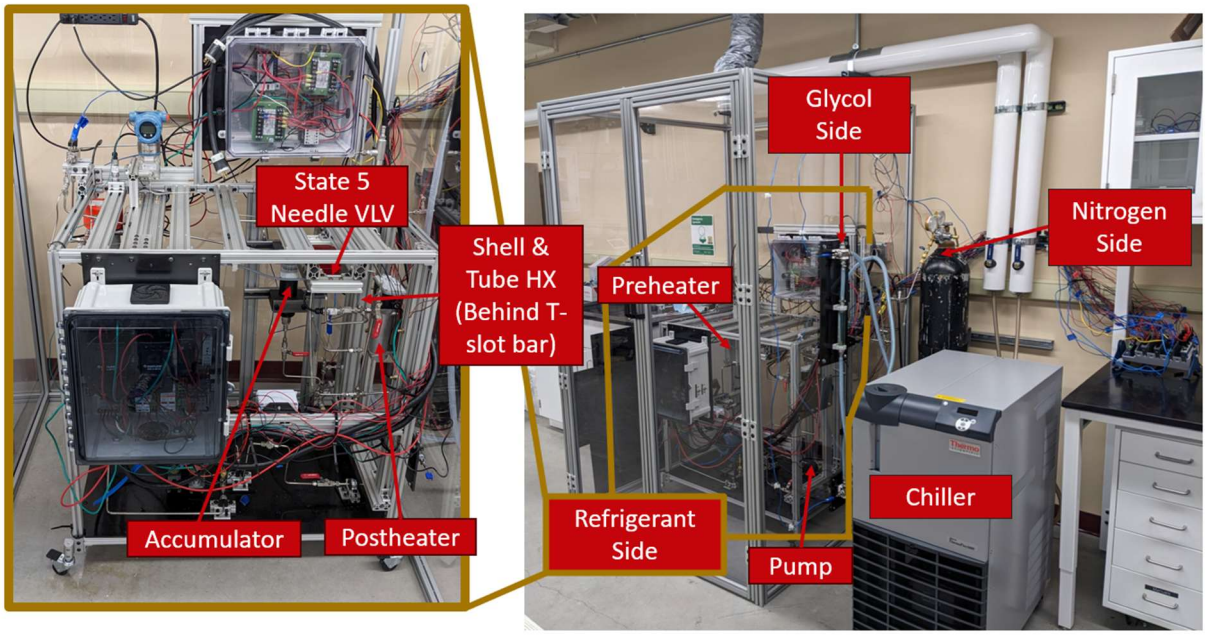

Figure 4.6: The physical refrigerant conditioning facility.

It took a year to build the facility and an additional 3 months to validate the facility, add the TES HX to the facility, and collect initial data. The second phase of validation was done without a TES heat exchanger to ensure accurate measurements. The validation focused on verifying the mass flow rate of the system and correct post heater operation, because the post heater was the principal component for measuring outlet state.

To validate the energy balance measurement and Coriolis flow meter the mass flow rate was measured using two different methods. The mass flow rate was measured directly using a Coriolis flow meter (the preferred method of measurement for tests) and an energy balance across the post heater. The flow rate measurement across the preheater are described by Equation (37).

$$\dot{m}_{post} = \frac{\dot{q}_{post}}{h_5 - h_4} \tag{37}$$

In Equation (37) $\dot{q}_{post}$ is measured by a watt transducer described in the previous section. The enthalpy h is measured by pressure transducers and thermocouples as previously discussed. To conduct the test flow was bypassed around the TES HX as seen in Figure 4.7a.

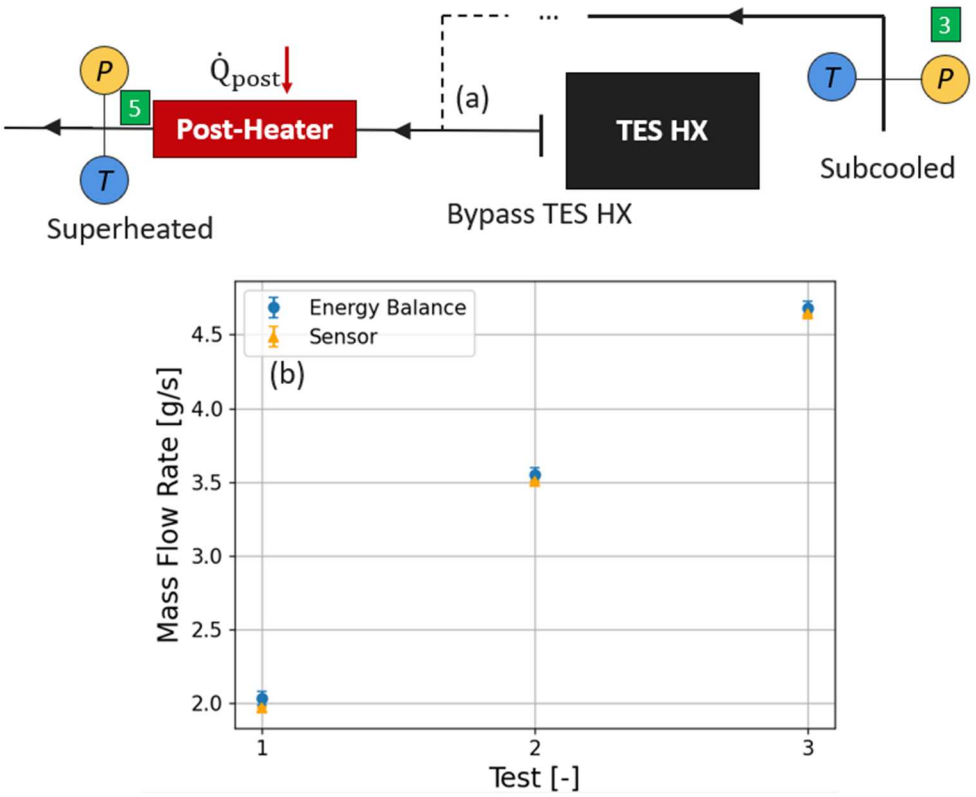

Figure 4.7: (a) the loop schematic for post heater validation. (b) the mass flow rate validation data.

Additionally, the inlet to the postheater was subcooled and the exit was superheated allowing for the measurement of the enthalpy at state 3 and 5 using pressure transducers and thermocouples. The results of the mass flow rate validation can be seen in Figure 4.7b. The mass flow rate is consistent at different flow rates between each method. Slight deviations are likely because of thermal losses. Therefore, the post heater and mass flow rate sensor were deemed adequate for use.

Thermal losses in the post heater were measured using the same flow configuration as seen in Figure 4.7a. Instead of calculating the mass flow rate using an energy balance, Equation (37) was rearranged to solve for $\dot{Q}_{post}$, which is the refrigerant heat in Figure 4.8.

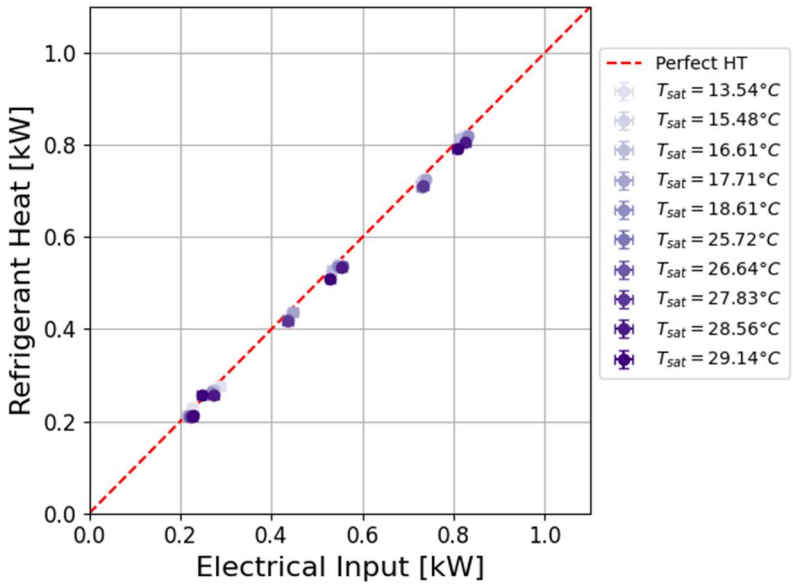

Figure 4.8: The post heater electrical loss characterization.

Mass flow rate was varied from 1 g/s to 3.75 g/s and pressure was varied from 175 psi to 268 psi to collect the data presented in Figure 4.8. The full test matrix for heater losses is available in Appendix E. In Figure 4.8 perfect heat transfer would mean all heat input by the resistive heater goes to the refrigerant. The results show that this is nearly the case at a variety of low rates and saturation temperatures (pressures). The losses are further analyzed in the post processing section.

The pressure transducers and thermocouples were verified as well. Thermocouples and static pressure transducers did not receive significant analysis. Each responded as expected. However, the differential pressure transducer had issues. The differential pressure transducer measured a negative pressure drop in the beginning of each condenser test run on the system. The pressure drop for a condenser test with a flow rate of 1.25 g/s, pressure of 264 psi, and inlet super heat of ~12 K is shown in Figure 4.9 as an example.

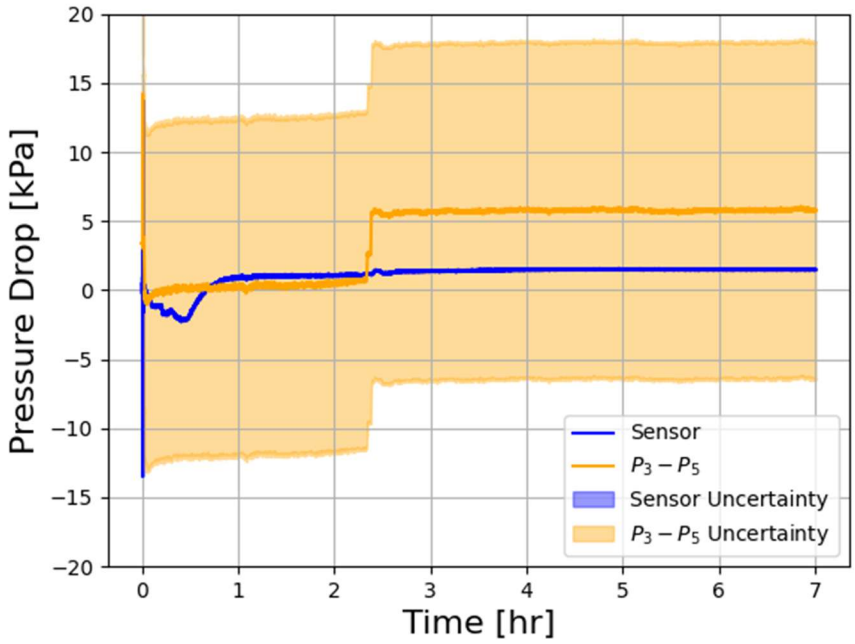

Figure 4.9: The pressure drop data for a condenser test.

Figure 4.9 shows the pressure drop through the TES HX and the pressure drop between states 3 and 5. The uncertainty of the pressure sensor is very small relative to the uncertainty of the static pressure sensors. The pressure drop measured in the first half hour of the test is negative due to plumbing issues. The pressure transducers are plumbed as seen in Figure 4.10a.

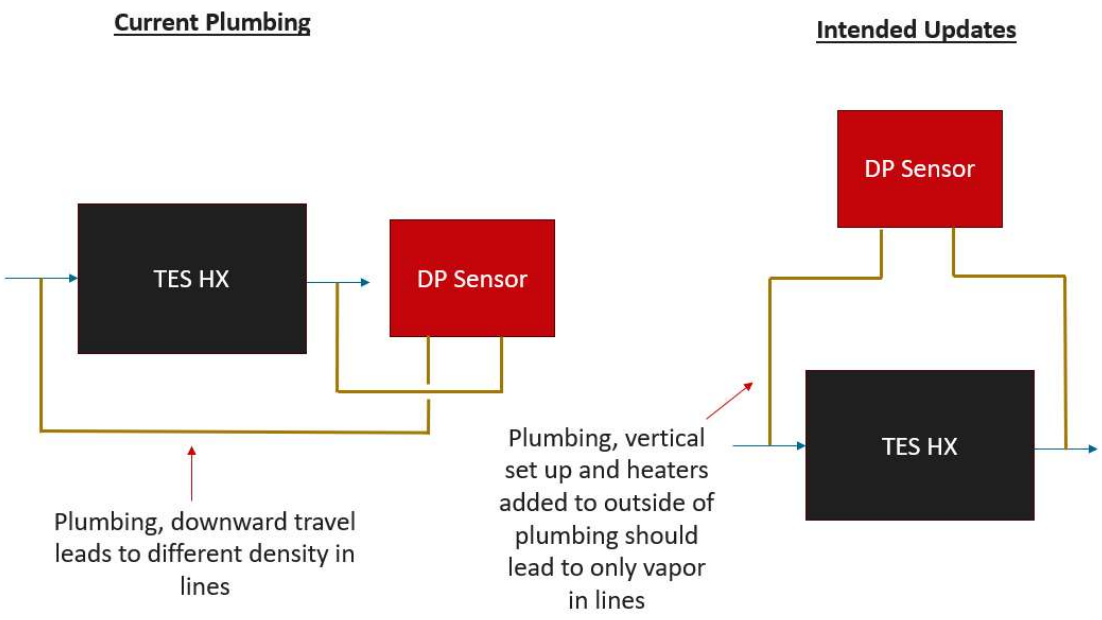

Figure 4.10: The TES HX pressure drop current sensor orientation (left), and intended upgrades (right).

Because the current plumbing only includes pipes that travel downward there are different phases of fluid in each respective line to the pressure drop sensor ("DP Sensor"). Redoing the plumbing so the flow travels upwards (Figure 4.10b) and adding heaters should fix this issue. Figure 4.9 also shows a clear change in pressure drop behavior between state 3 and 5 at around 2.25 hours. This occurs because at this point in the test the outlet of the TES HX becomes two phase and the pressure drop increases because two phase fluids have higher pressure drops than single phase fluids.

4.3 TES HX Fabrication and Instrumentation

A TES heat exchanger was built and installed between states 3 and 4 in the experimental facility (see Figure 4.1). A photograph of the assembled component is shown in *Figure 4.11*.

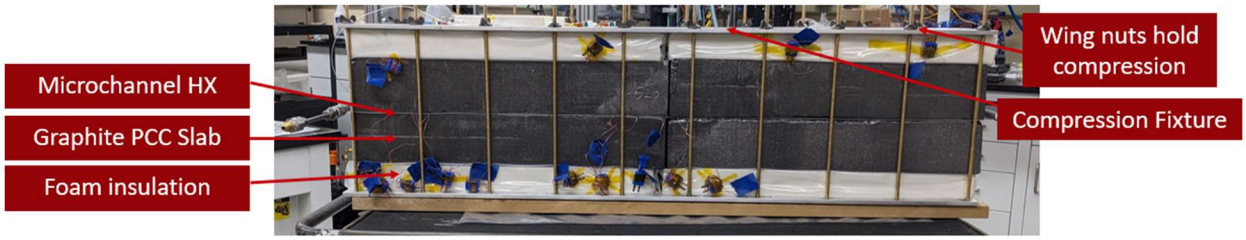

Figure 4.11: The fully assembled TES heat exchanger.

The TES heat exchanger was built in collaboration with NETenergy. NETenergy supplied graphite/PCM composite slabs, a microchannel heat exchanger, and a compression fixture. The composite slabs were made by soaking a highly porous compressed expanded graphite matrix, which has been done many times before in literature [84], [85]. The properties measured for the PCC slab differed slightly from the design discussed in Chapter 2. The slabs had a final mass fraction of 57.7% based on NETenergy's testing, which changed the latent heat of the PCC slab slightly from 114 J/g to 114.6 J/g.

Additionally, the density of the slabs after transport were lower due to expansion observed during soaking. A density of 636 kg/m^3 was measured for the composite slab at UW-Madison. The density measured at NETenergy was 670 kg/m^3. A value near the average of the density measured at UW-Madison and NETenergy was used (654.1 kg/m^3, the average was 653 kg/m^3) for initial model validation (prior to the thesis) and kept for this thesis. The capacity of a device between 18 and 28°C (the target PCM temperature range for this device) is 0.846 kW-hr for a density of 654.1 kg/m^3 and 0.823 kW-hr for a density of 636 kg/m^3 in melting. Therefore, the relatively small changes in density pre- and post-shipment only changes the theoretical capacity by 2.7% and shouldn't have a significant impact on the model validation results. Still, in future work the density should be updated.

Four slabs with a target thickness of 8 cm, length of 0.5 m, and depth of 0.25 m were integrated into the TES component. The naming of each slab is shown in Figure 4.12.

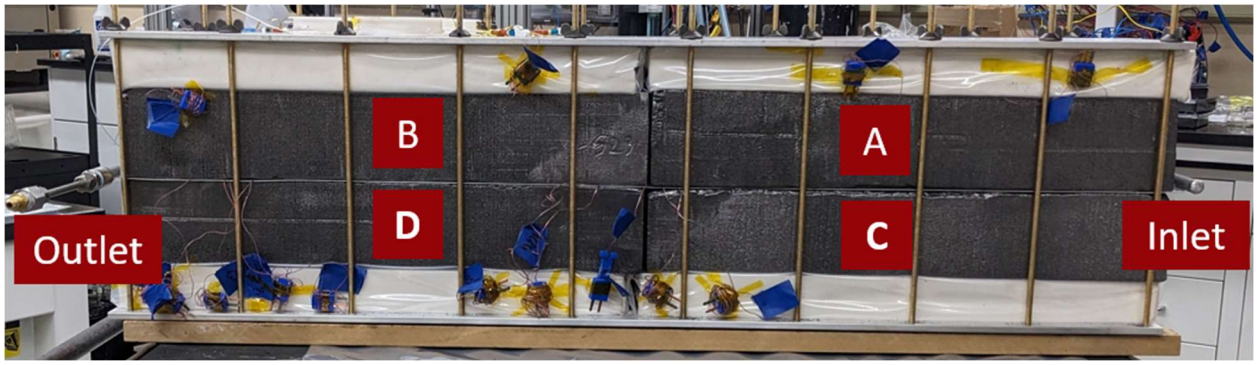

Figure 4.12: The slab naming nomenclature.

The material expanded in the compression direction during soaking leading to some slabs exceeding the thickness target, as shown in Table 4.5.

Table 4.5: The dimension and weight measurements of the actual slabs used in the design

Slab Name	**A**	**B**	**C**	**D**
Length (x dir.) [m]	0.465	0.485	0.465	0.487
Width (z dir.) [m]	0.270	0.271	0.270	0.271
Thickness (y dir.) [cm]	8.57	8.57	7.94	8.09
Mass [lbs]	15.1	15.3	14.1	15.8

There was also some evidence of delamination of the graphite during soaking Figure 4.13.

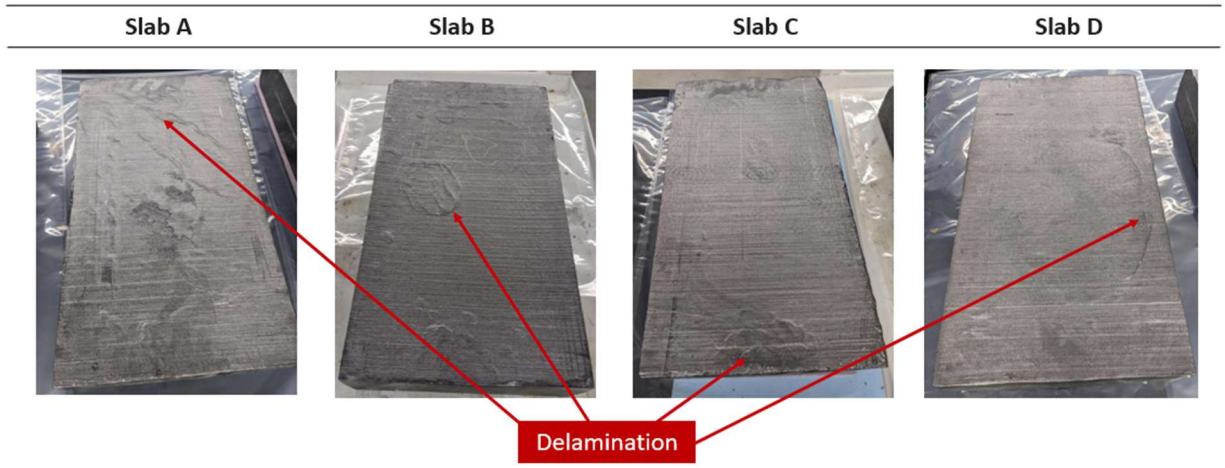

Figure 4.13: The delamination of the graphite, present on each slab.

NETenergy is exploring modifications to the soaking procedure to prevent these expansion and delamination issues in future prototypes.

The TES heat exchanger was instrumented with calibrated T-type thermocouples and fiber optic cables to measure phase front and refrigerant maldistribution as seen in Figure 4.14

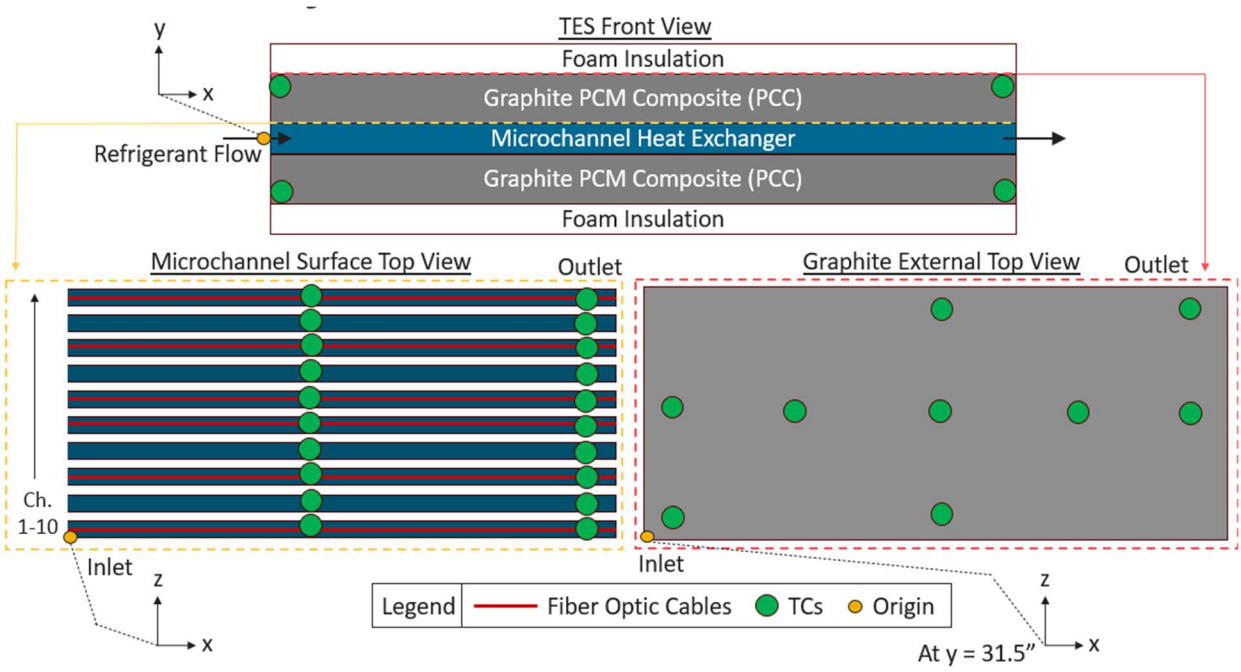

Figure 4.14: The location of all TES heat exchanger instrumentation: (a) shows a front view, identical instrumentation is included on the rear of the heat exchanger, (b) shows a top view of the microchannel surface, and (c) shows a top view of the graphite.

All thermocouple welds were embedded in thermal paste and secured with tape to ensure good thermal contact to the microchannel and insulation surfaces. The insulation was wrapped in plastic to ensure it wouldn't interact with the PCM. The thermocouples in Figure 4.14a were placed in 40-mm deep holes in the PCC XY plane in the front view. The picture does not show the 4 thermocouples that are in the back view of the heat exchanger in the XY plane. These 8 thermocouples are used to verify symmetry of the PCM in the XZ plane relative to the microchannel. The fiber optic sensors were taped to the heat exchanger surface, but thermal paste was not used. A photograph showing the instrumentation on the microchannel surface is shown in Figure 4.15.

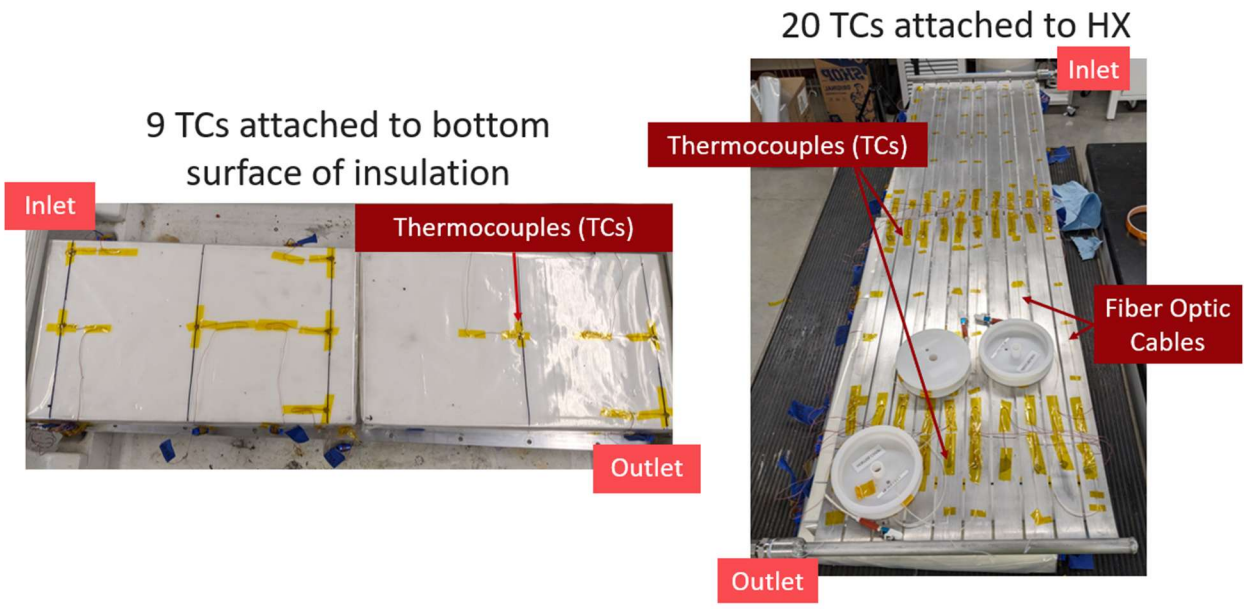

Figure 4.15: The TES HX thermometry placement..

The fiber optic cables were placed at the refrigerant channel/PCC interface on channels 1, 3, 5, 6, 8 and 10 (see Figure 4.14b). Each fiber optic cable is 3 meters long and connected to a Luna ODiSI 7108 Multi-Channel Distributed Sensing Instrument. Three fibers were used in total, each taking two passes in the refrigerant flow direction on two separate channels.

The approach for instrumenting the fiber optic cables is illustrated in Figure 4.16.

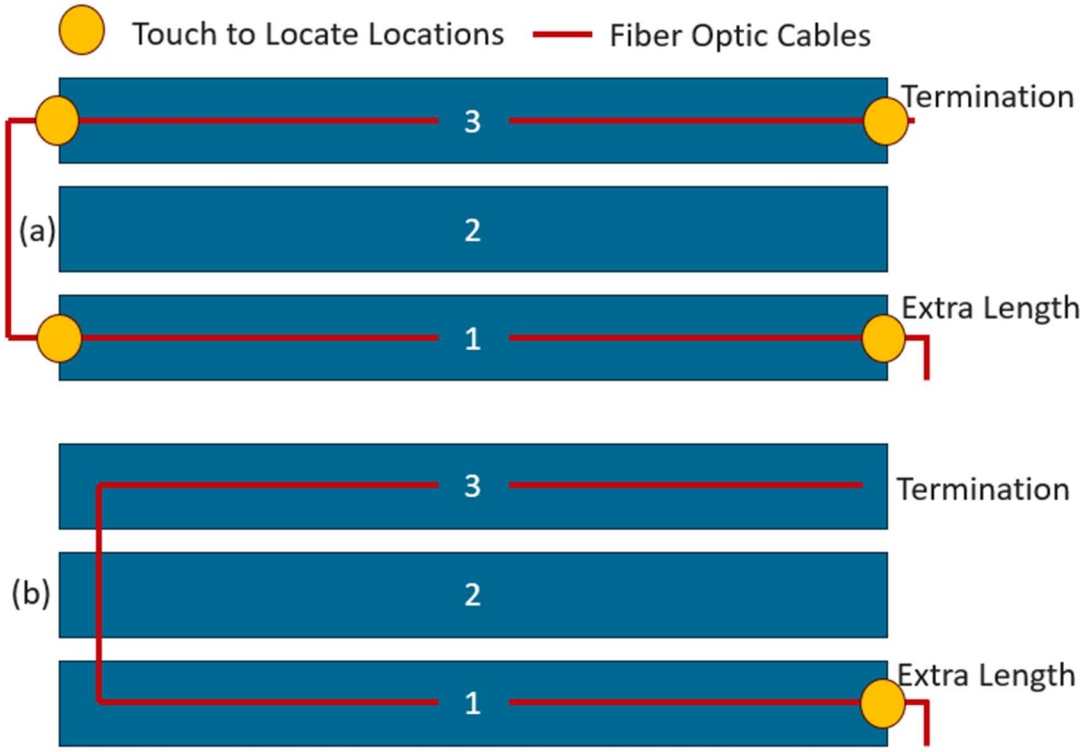

Figure 4.16: (a) the ideal technique to place the fiber optic cable (b) and the technique used.

In Figure 4.16 the touch to locate location is touched with the users hand, and then the location can be identified on the fiber optic controller. The ideal set up then is to create segments with touch to locate as seen in Figure 4.16a. Each portion of cable on the channel between the orange dots indicates a segment. Future fiber optic cable users should use this method of setting up the instrumentation. For this work, only the entry of the fiber optic cable could be identified because the rest of the cable was buried below the PCC slab. Therefore, two segments were made from the touch to locate location in Figure 4.16b to the termination by dividing the length of this portion of the cable by 2. The fibers provided temperature measurements every 0.65 mm along the length of the fiber at a frequency of 0.51 hz. The sensors have an uncertainty of 2.2°C.

After all instrumentation was placed, the PCM heat exchanger was assembled in a compression fixture (*Figure 4.11*) and placed into a hydraulic press (Figure 4.17).

Figure 4.17: The TES heat exchanger in the hydraulic press apparatus

The hydraulic press applied 2000 lbs of force onto a steel bar placed on top of the assembly. The target force was set to achieve greater than 4 psi of pressure at the PCM composite/microchannel heat exchanger interface to reduce contact resistance. This pressure was selected because increasing the pressure above 4 psi had little impact on further lowering the contact resistance in a similar heat exchanger [57]. The applied load was measured with a load cell. More information on the load cell can be found in Appendix F.

After the required force was added, the compression fixture was tightened, which maintains the required pressure throughout testing. The compression fixture used is made up of 2 Aluminum plates that are connected with threaded rods. The threaded rods are superglued into the bottom Aluminum plate. Wing nuts are tightened to finger tight on the top face of the compression fixture to maintain the compression after removal from the hydraulic press.

Finally, after the heat exchanger was fully instrumented and assembled, foam insulation was added to the external surfaces of the TES heat exchanger to minimize losses to the environment. The heat exchanger was then placed in the experimental facility and connected to the inlet and outlet refrigerant lines.

4.4 Post Processing Measurements

To post process data, some intermediate calculations, uncertainty analysis, and corrections to measurements were needed. Intermediate calculations were done to find the discharge rate and discharged energy of the PCM TES HX. Uncertainty analysis was also done for these parameters. Uncertainty analysis used theory of uncertainty propagation described in Taylor and Kuyatt [86]. Also, not all data was accurate without modifications. Fiber optic temperature measurements and post heater refrigerant power measurements needed corrections. Fiber optic temperature measurements were consistently off during testing – it seems like the zero for the sensors became outdated following initial validation efforts – so an offset based on microchannel surface thermocouples was applied at the first channel. The refrigerant power measurements were corrected for thermal losses using a regression model that will be discussed in greater detail. Lastly, experimental and model outputs were also smoothed using a Savitsky Golay filter [87] to reduce noise. The noise distracted from comparison. The smoothing parameters used for smoothing were the default parameters in scipy [88], 5^{th} order polynomials, and window length depending on the use case. The window length was modified for several different cases. The window length was set to 501 indices (in increments of 2 s) to for everything except the experimental heat transfer rate, which applied a window length of 701 twice.

4.4.1 Discharge Rate, Discharged Energy, and Uncertainty Calculations

A couple quantities beyond thermodynamic states were calculated to determine the performance of the PCM TES HX – specifically the discharge rate and discharged energy. The discharge rate was calculated using an energy balance described by Equation (38).

$$\dot{q} = \dot{m}(h_3 - h_4) \tag{38}$$

Equation (38) is valid for a condenser test, if the test is done for an evaporator the right hand side of Equation (38) changes so the difference in enthalpy is now: $h_4 - h_3$. To calculate the discharged energy, Equation (38) is integrated with respect to time, which is shown in Equation (39).

$$E = \sum_{t=t_{begin}}^{t_{stop}} \dot{q}dt \tag{39}$$

Equation (39) is a numerical integration using left hand rule, which is sometimes referred to as a left sided Riemann sum. This method was adopted from Mahvi et al.'s work [57]. Left hand rule estimates the value of some function by approximating the value of the area under a particular segment of time (dt) with the value at the beginning of the segment. This isn't the most accurate numerical integration method, but the sampling frequency of the measurements, dt, was 2 s and tests ran anywhere from 4-7 hrs so the time step was small enough that choice of integration method didn't matter for accuracy. The left hand rule was chosen over the trapezoid method because it is much more convenient to use for uncertainty propagation.

A majority of the uncertainty calculations were done using the uncertainties package in Python, which can handle first order propagation [89]. However, a few calculations needed special treatment. Fluid properties like enthalpy and density were calculated using the CoolProp Python package [90] so their uncertainty was estimated using Engineering Equation Solver's uncertainty propagation tool. The worst case uncertainty for enthalpy was 386 J/kg and the worst case uncertainty for density was 1.07 kg/m^3, which were used as the uncertainty for all enthalpy and

temperature measurements. Uncertainty calculations for discharged energy used first order uncertainty propagation extended from Mahvi et al. [57]. The uncertainty for the discharged energy is presented in Equation (40).

$$u_E = \sqrt{\left(\frac{\partial E}{\partial \dot{m}} u_{\dot{m}}\right)^2 + \left(\frac{\partial E}{\partial h_3} u_{h_3}\right)^2 + \left(\frac{\partial E}{\partial h_4} u_{h_4}\right)^2} \tag{40}$$

In Equation (40) the uncertainty is u. The derivates of E with respect to each variable can be calculated using Equation (39).

4.4.2 Post Heater Thermal Loss Correction

To compensate for the thermal losses in the post heater, a regression model was created to predict the losses after data collection using the measured post heater pressure, mass flow rate, outlet superheat, and heating element temperature. The regression model is applied to the measured discharge rate described by Equation (38) to get a corrected value for discharge rate. The correction is presented in Equation (41).

$$\dot{q}_{corrected} = \dot{q} - \dot{q}_{reg}\left(P_{post}, \dot{m}, T_{heat-element}, T_{super}\right) \tag{41}$$

The model was created using the SciPy Python package, and a Huber Regression was used to reduce bias from a few large outliers. The default Huber Regression in the SciPy package was used [88]. There was a strong correlation between pressure and losses, so the maximum and minimum pressure data points were excluded from the testing data. The model was created using an 80/20 split between training and testing data. The regression was trained using the training data, and scored on the training and testing data to determine performance.

The results of training and scoring the regression model are presented in Figure 4.18.

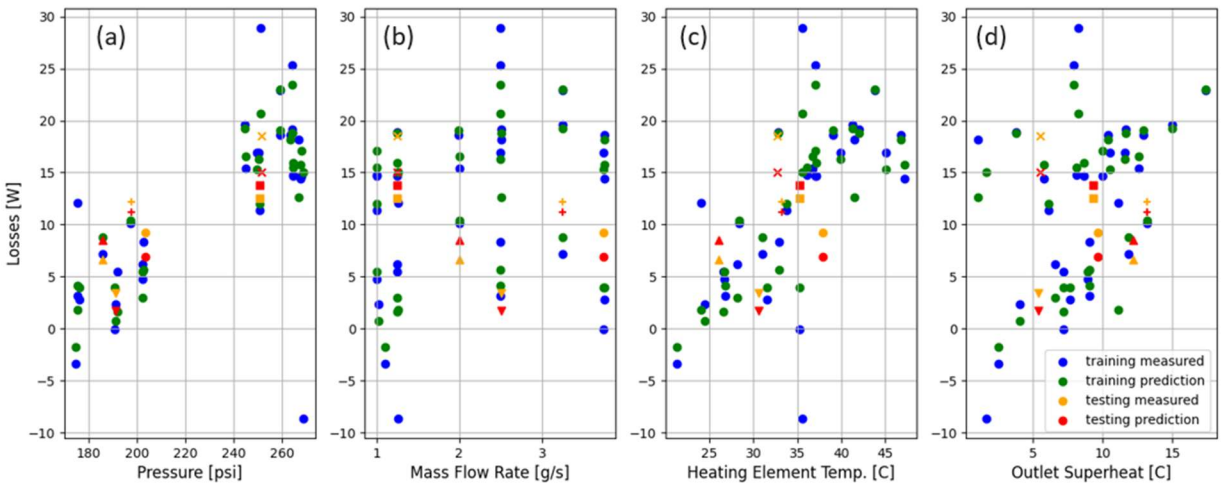

Figure 4.18: The regression model loss prediction performance compared against all 4 input variables. Each test measurement and prediction pair is given it's own unique marker for easy comparison of results. The comparison of losses to (a) pressure, (b) mass flow rate, (c) heating element temperature, and (d) outlet superheat is presented. The uncertainty is not plotted to not distract from the comparison, however it is significant because the uncertainty of the power transducer is +/- 10 W.

Each plot shows a different input variable and the training and testing data. Each testing measurement and prediction pair is plotted using a different symbol to allow the reader to distinguish measurement and prediction pairs that weren't used for training. Moreover, the error bars from measured values are omitted because they are so large that they obstruct the rest of the plot. The error in measured electrical power by the watt transducer is +/- 10 W, which is pretty significant in this case. Figure 4.18a shows that there is a large correlation between postheater pressure and losses. The pressure dictates the saturation temperature in the postheater, so higher saturation temperature in the postheater indicates on average higher temperatures. Higher refrigerant temperatures drive heat transfer from the heater to the ambient leading to more losses. Figure 4.18b shows that the mass flow rate doesn't cause great losses, and Figure 4.18c and d also show that the postheater losses are strong functions of post heater heating element temperature and outlet superheat, as expected.

The scores for the regression model are presented in Table 4.6.

Table 4.6: The regression model performance for several data categories

	r^2 [-]	Percent Error [%]
Training	0.614	331.75
Training w/o Outliers	0.8305	23.42
Testing	0.807	21.88

The training data has a poor r^2 score and percent error because of the outlier that can be clearly seen in the bottom right corner of Figure 4.18a. If outliers are removed (there is a second outlier that isn't as easily identifiable) the training data's score improves and is comparable to the testing data's scores, which were deemed satisfactory for the thermal loss correction. The accuracy of regression model was a function of the random seed chosen for the train test split so multiple were tested and the best was chosen as the final result, which is what is plotted in Figure 4.18a and tabulated in Table 4.6. Ideally the regression model would predict the losses independent of the random train, test split, but creating a robust regression model to predict heater losses was not the purpose of this work, and the model was deemed good enough.

Chapter 5: Experimental Results

This chapter presents experimental results from the PCM TES HX prototype described in Chapter 4. It begins with an overview of the test matrix, followed by a discussion of the data. A section on component level performance defines the devices functioning as a battery in a constant inlet condition set up. Analogies are drawn to constant power operation but limited because of the conditions tested. Then, a section on fundamental behavior digs into the reasons for higher level trends observed in the component performance section. For the evaluation of high-level results like discharge rate and discharged energy uncertainty is included. However, in many of the plots for other values uncertainty is not included to not distract from comparison of results.

5.1 Test Matrix

The TES device was evaluated as both a condenser (melting) and an evaporator (freezing) with constant refrigerant inlet conditions. Three nominal inlet conditions were evaluated to represent on-design and off-design conditions: baseline, increased load, and increased peak shaving. The baseline case was designed to discharge in approximately 4 hours with constant inlet conditions and has a relatively long constant power region. Therefore, the baseline test is also considered on-design. The increased load and increased peak shaving cases are off-design cases. The increased load case represents a higher required TES discharge rate, which in practice could be represented an increase in the cooling or heating load of the building. The increased peak shaving case represents a larger decrease in the compressor power . In implementation the higher peak shaving function could prevent a blackout if the grid is overloaded. A heat pump TES system achieves this by lowering the driving temperature difference across the TES HX (reduces $|T_{sat} - T_t|$), which lowers the pressure ratio across the compressor – as discussed in Chapter 1.

To set the test matrix, the finite difference model was run with various mass flow rates and driving temperature differences to determine what conditions would be near baseline, but discharge the full TES capacity in a reasonable amount of time. The test matrix used in this work is presented in Table 5.1.

Table 5.1: The test matrix used to validate the computational models. Three different runs were performed for the evaporator and condenser respectively, represented by this test matrix.

	Baseline	**Increased Load**	**Increased Peak Shaving**
Driving ΔT [°C]	6	6	4
Mass Flow Rate [g/s]	1.25	2.5	1.25

The baseline case fully discharged in about 4 hours, with a driving temperature difference of 6°C and a refrigerant mass flow rate of 1.25 g/s. The driving temperature difference was defined based on a PCM transition temperature of 22.65°C (measured using DSC), meaning the refrigerant target saturation temperature was 28.65°C for the condensing baseline and 16.65°C for the evaporating baseline. The inlet pressure (which sets the saturation temperature) was controlled to change the driving temperature difference for each test. For the increased load case, the mass flow rate of the refrigerant through the test section was doubled, increasing the maximum heat transfer rate from approximately 250 W to 500 W. For the increased peak shaving case, the driving temperature difference was reduced to 4°C. Appendix G and H discuss the loop interface and operation respectively.

5.2 Experimental Inlet Conditions

Maintaining constant inlet conditions while discharging the TES proved challenging. This section shows the actual inlet conditions achieved during the experimental campaign, along with their associated uncertainty.

The mass flow rate was controlled by modulating the pump speed with a PID controller. The measured and target mass flow rate for all test cases is shown in Figure 5.1.

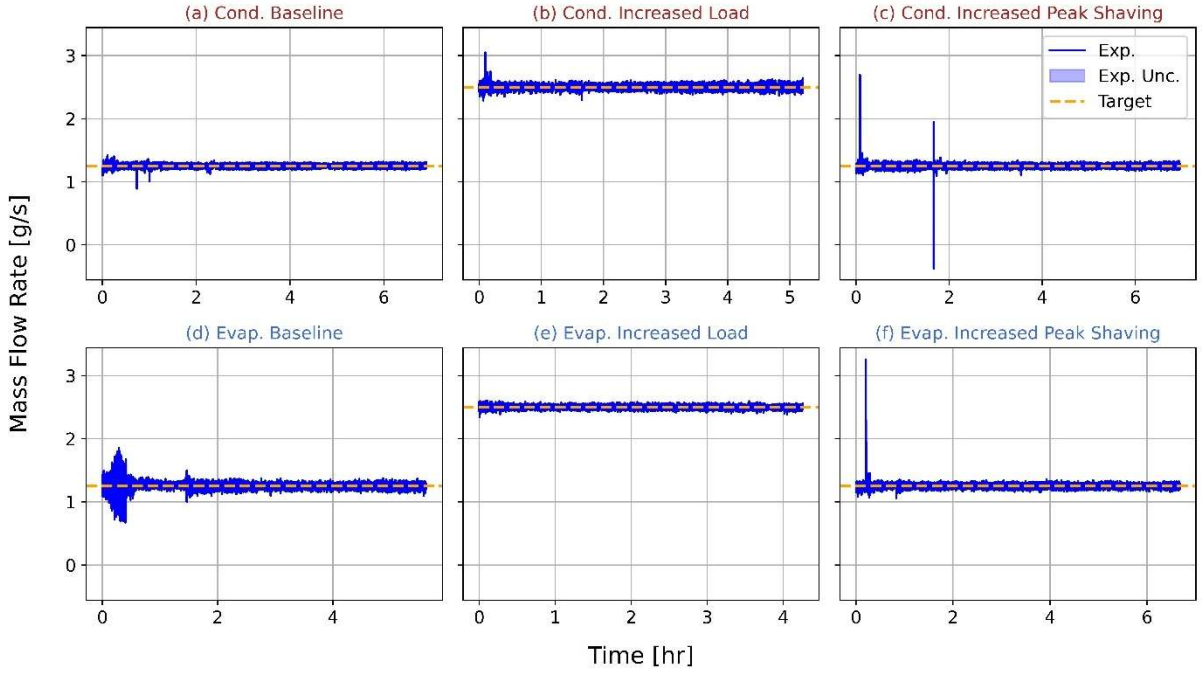

Figure 5.1: The experimentally measured mass flow rate for all test cases. (a)-(c) present condenser and (d)-(f) present the evaporator. (a) and (d) are baseline cases, (b) and (e) are the increased load case, and (c) and (f) are increased peak shaving.

The light blue band around the experimental data indicates measurement uncertainty, although for this measurement the uncertainty is small and not easily visible in the plots. The mass flow rate was typically on target because the PID controller functioned well.

The inlet pressure was manually adjusted using the chiller set point or accumulator pressure. The inlet pressure for each test is plotted in Figure 5.2.

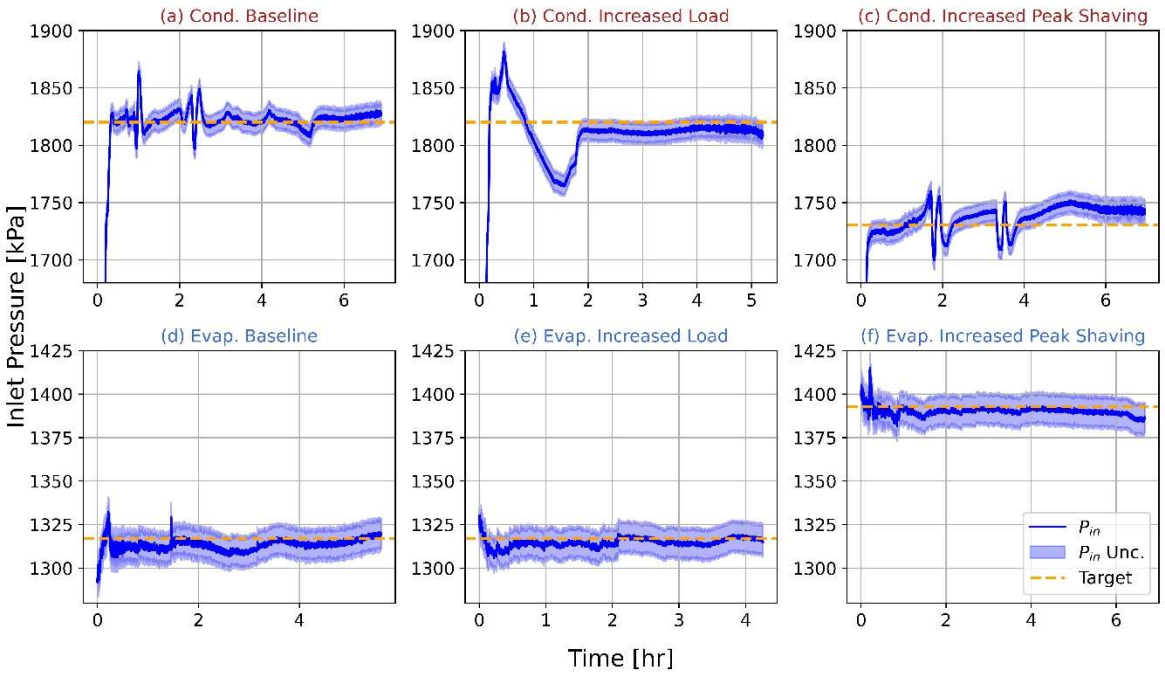

Figure 5.2: The inlet pressure for each test. (a)-(c) present condenser and (d)-(f) present the evaporator. (a) and (d) are baseline cases, (b) and (e) are the increased load case, and (c) and (f) are increased peak shaving.

The refrigerant pressure was more challenging to dynamically control because of the strong relationship with refrigerant charge and overall liquid volume in the loop, as discussed in Chapter 4. The measured and target driving temperature difference is shown in Figure 5.3.

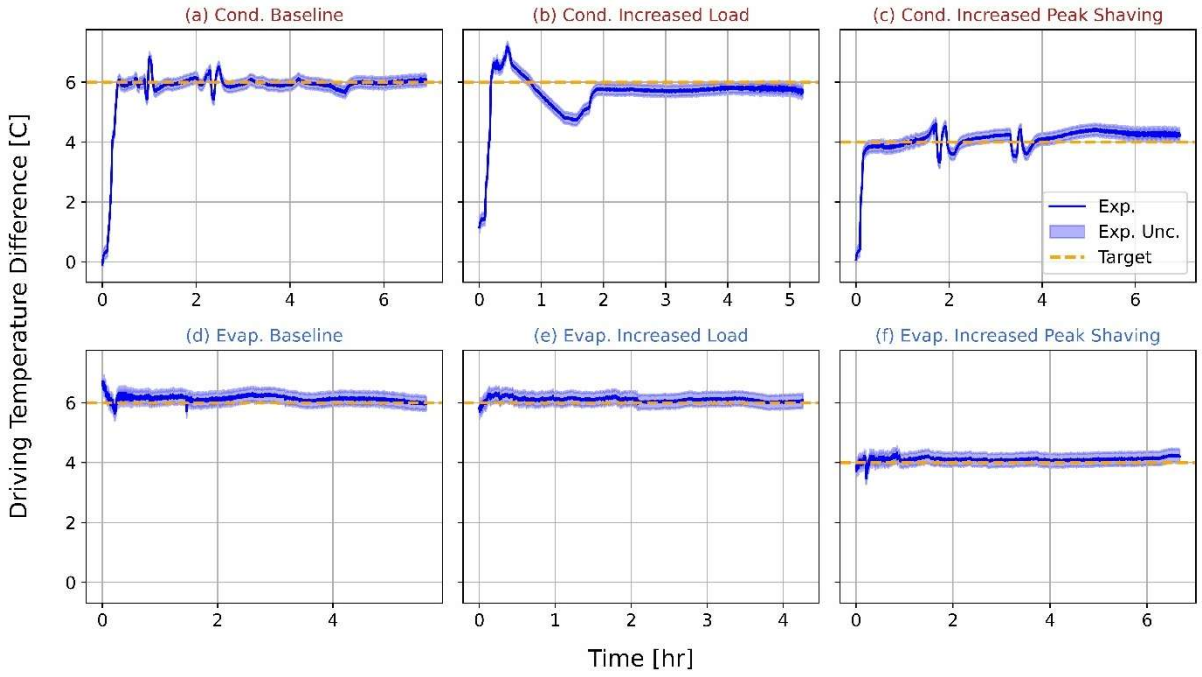

Figure 5.3: The driving temperature difference for each test. (a)-(c) present condenser and (d)-(f) present the evaporator. (a) and (d) are baseline cases, (b) and (e) are the increased load case, and (c) and (f) are increased peak shaving.

Figure 5.3 shows the experimental conditions had some variation early in the test, but stayed on target.

Finally, the thermodynamic inlet condition was controlled using the preheater. For each test case, the refrigerant entered the TES device as a single-phase fluid (targets of 15°C superheated for condenser mode and 2°C subcooled for evaporator mode). While a superheated inlet is typical for condenser operation, evaporators in vapor compression cycles generally receive saturated refrigerant with a vapor quality around 0.2. However, due to observed flow maldistribution under two-phase inlet conditions (see section 5.2), a subcooled inlet was used for evaporator testing. This approach allowed for a more direct validation of the proposed models by eliminating additional errors from maldistribution, which was not captured in either framework.

The condenser inlet superheat is shown in Figure 5.4(a-c) and the evaporator subcooling is shown in Figure 5.4(d-f).

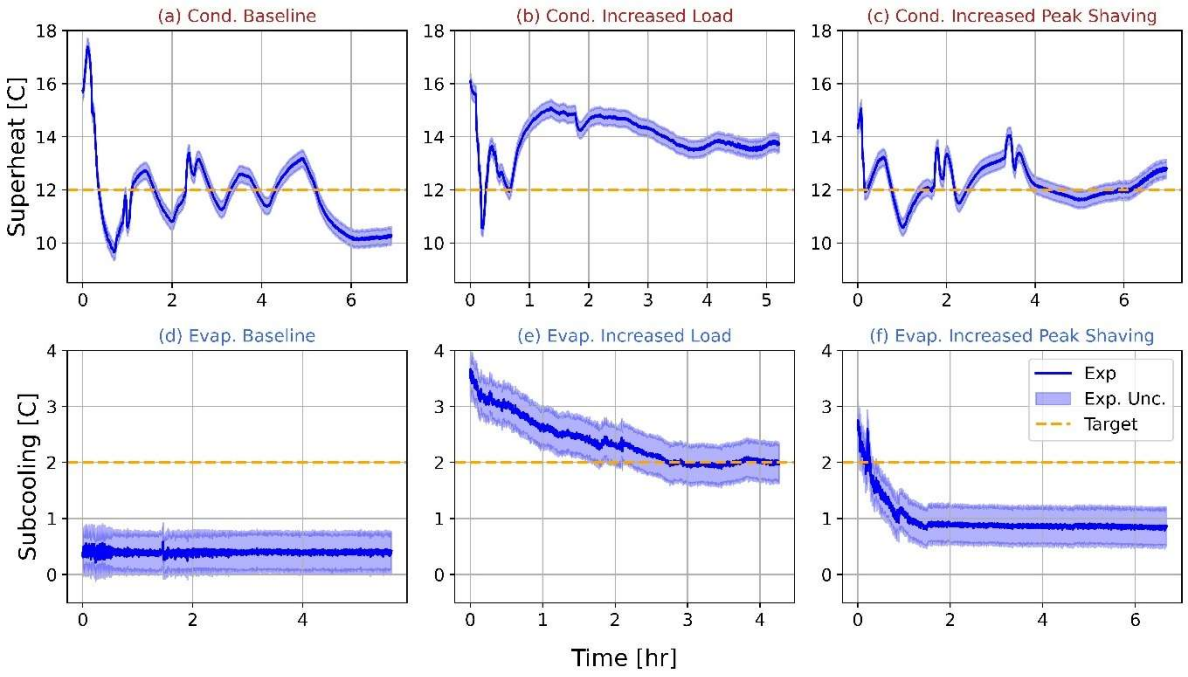

Figure 5.4: The inlet superheat for all condenser tests. (a)-(c) present condenser and (d)-(f) present the evaporator. (a) and (d) are baseline cases, (b) and (e) are the increased load case, and (c) and (f) are increased peak shaving.

For the condenser case, the inlet superheat oscillates due to pressure oscillations and transients in the preheater (see Appendix I). These oscillations are not concerning because changes in superheat do not significantly affect the inlet enthalpy relative to the change in refrigerant enthalpy across the TES. For the evaporator cases, the preheater was turned off, and subcooling was set based on the performance of the shell-and-tube heat exchanger connected to the chiller. Although there was no clear evidence of two-phase flow in the inlet manifold, there is low confidence that the flow was subcooled in baseline and increased peak shaving cases because the subcooling is remarkably constant late in time. The increased peak shaving case illustrates this issue well – in the beginning of the test the temperature varies, and then at 1.5 hours there is a small jump and the temperature becomes relatively constant. Even if the inlet is subcooled it would be low quality because the heat gain from natural convection is not large. In the case of the postheater (which has a higher driving temperature difference), the losses were a maximum of 30 W (see Chapter 4), which would not be

significant compared to the maximum heat transfer rater observed in the experiments which ranged from 250-513 W.

5.3 Component Level Performance

The experimental observations summarize the component level performance and fundamental behavior of the heat exchanger. The component level performance covers the discharge rate and discharged energy of the thermal energy storage device. The analysis assumes symmetry between the top and bottom PCC slab, which is discussed in Appendix J.

The discharge rate of the device reveals a few general trends for operating a PCM TES HX at constant inlet conditions as seen in Figure 5.5.

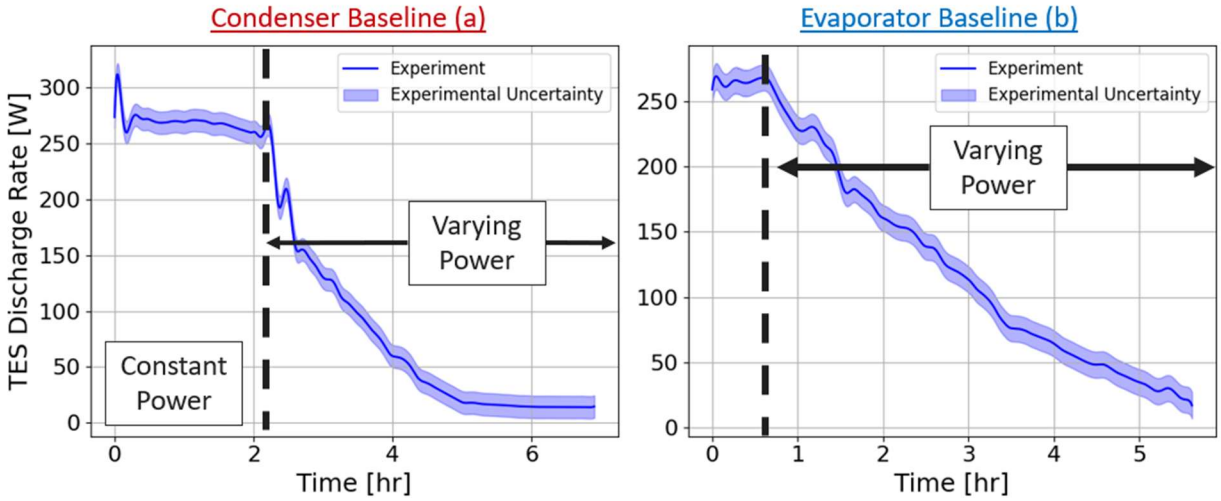

Figure 5.5: Experimental results for baseline (a) condenser and (b) evaporator

Initially, the total thermal resistance between the refrigerant and solid-liquid interface of the PCM (which is at the transition temperature) is small, which allows the refrigerant to fully condense or evaporate. In this region, the thermal power is approximately constant and equal to the product of the mass flow rate and the enthalpy of vaporization of the refrigerant ($\dot{m}_{ref}\Delta h_{fg}$). As the device discharges, the solid-liquid interface moves away from the refrigerant channel, increasing the total thermal resistance. Eventually, this resistance is too large to accommodate full condensation or

evaporation, and the outlet refrigerant exits the heat exchanger saturated. At this point, the total heat transfer rate begins to fall, inversely proportional to the increase in resistance.

The TES can fully condense much longer than it can fully evaporate for the baseline conditions. The next subsection investigates this behavior in more detail. In the varying power region similar nonlinear behavior occurs for the condenser and evaporator. The tests finish as their discharge rates approach zero, which is defined in greater detail later in this subsection.

The holistic discharge rate results illustrate macro level trends for mass flow rate and driving temperature differences as seen in Figure 5.6.

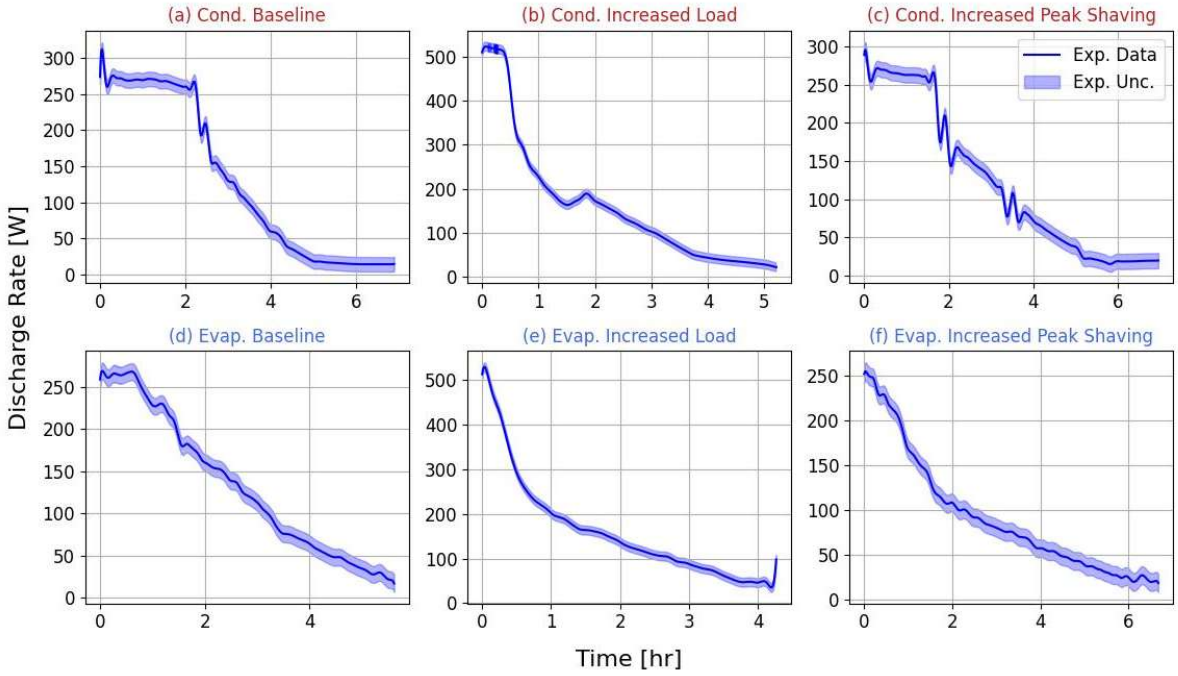

Figure 5.6: Experimental condenser results for (a)-(c) present condenser and (d)-(f) present the evaporator. (a) and (d) are baseline cases, (b) and (e) are the increased load case, and (c) and (f) are increased peak shaving.

As the mass flow rate increases between Figure 5.6(a) and (b) for the condenser, Figure 5.6 (d) and (e) for the evaporator the constant power region becomes insignificant. When the driving temperature difference is decreased and the mass flow rate is held constant as in Figure 5.6(a) and (c) for the condenser and Figure 5.6(d) and (f) for the evaporator, the constant power region

shrinks as well, but remains significant for the condenser. The evaporator sees a smaller constant power region when the driving temperature difference is lowered, but it's similar to the increased load case.

The discharged energy profile also delivers interesting results for each operational mode, which help draw conclusions about the prototypes ability to operate in heating and cooling modes. The results are presented in Figure 5.7.

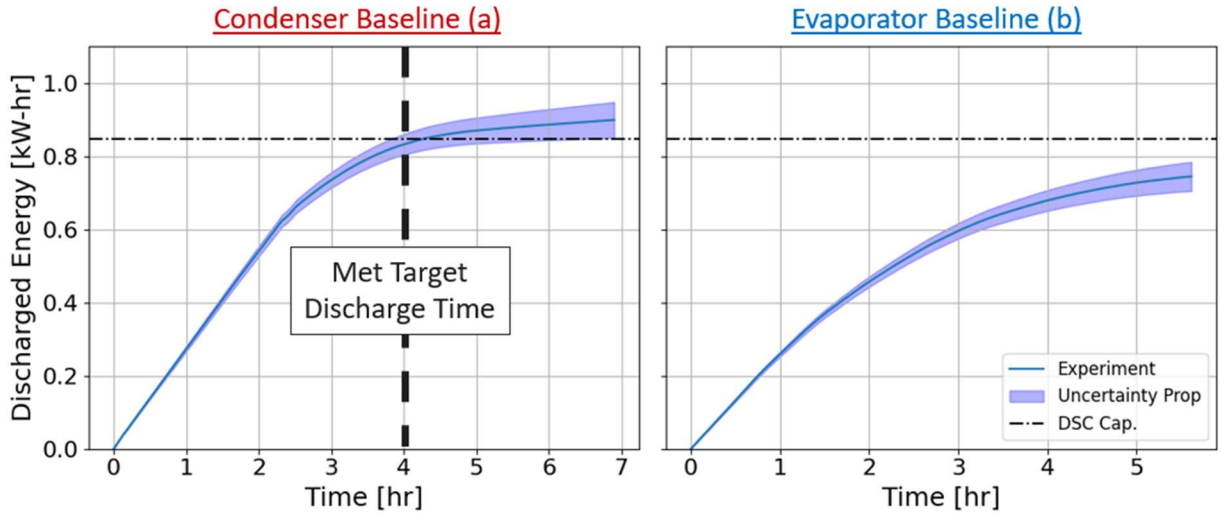

Figure 5.7: The baseline discharged energy results for the (a) condenser and (b) evaporator

The DSC capacity in Figure 5.7 was calculated for the mass PCC slabs tested using Texas A&M's DSC data for melting. The condenser baseline results show that during cooling mode, the condenser achieves the expected DSC capacity at the target discharge time (4 hours). Then the PCM TES HX continues to discharge at a slower rate, likely because it's heating sensibly. The condenser and evaporator curves follow similar trends, but have a notable difference in capacity (final discharged energy). The evaporator never reaches the expected DSC capacity, which is likely because the DSC curve at Texas A&M was measured for melting data, and separate melting and freezing DSC curves would be more appropriate for characterizing the heat exchanger in evaporator mode (for building heating). The evaporator results do appear to begin approaching

steady state near 4 hours, which makes sense when reviewing the discharge rate plots in Figure 5.5.

Reviewing each test's discharged energy results reveals consistent performance for condenser tests and inconsistent performance for evaporator tests as seen in Figure 5.8.

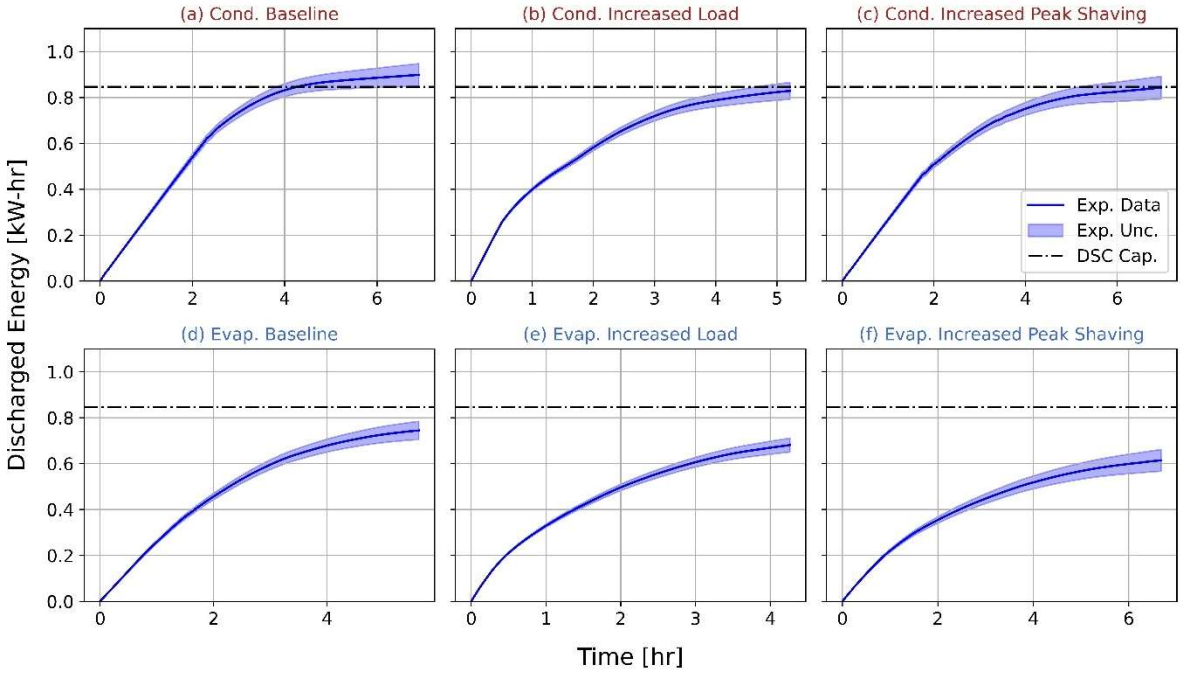

Figure 5.8: Experimental condenser results for (a)-(c) present condenser and (d)-(f) present the evaporator. (a) and (d) are baseline cases, (b) and (e) are the increased load case, and (c) and (f) are increased peak shaving

The condenser reaches the DSC capacity (within measurement error) for all cases, but does not for any of the evaporator cases. Furthermore, the measured final discharged energy for the evaporator is inconsistent, varying from 0.744 to 0.614 kWhr. The temperature distribution results in the fundamental behavior section illustrate that these differences can be explained partially by mass flow rate and driving temperature difference. Mass flow rate increases the freezing discharge rate at the beginning of the test. Moreover, as the driving temperature difference decreases the PCC slab cannot reach as cold of temperatures which leads to lower capacity measurements. The final temperatures of the PCC slab will receive thorough discussion the fundamental behavior section.

The experimental results were considered fully discharged when the slope in Figure 5.8 began to approach 0, which was determined by finding the time when the discharge rate was 50 W. This represents a slope of 0.05 kW in Figure 5.9, approximately 20% of the or maximum discharge rate for the baseline and increased peak shaving discharge rate and approximately 10% of the maximum discharge rate for the increased load case. The final discharge times for each case are presented in Table 5.2.

Table 5.2: The full discharge time of the experiment.

	Baseline	Increased Load	Increased Peak Shaving
Condenser	4.26 hrs	3.74 hrs	4.56 hrs
Evaporator	4.39 hrs	3.68 hrs	4.44 hrs

The discharge time for the condenser baseline case was consistently near the 4 hours ballparked in the discussion of baseline condenser and evaporator results. The evaporator baseline end time was close in value to the condenser and the 4-hour target as well. For both the condenser and evaporator, the increased load was the fastest and the increased peak shaving was the slowest. These results were expected based on and Figure 5.6 and Figure 5.8. While this analysis indicates full discharge it's still more complete to take note of the discharge rate and discharged energy profiles qualitatively when determining whether the test has finished discharging for a given application.

5.4 Fundamental Behavior of the Heat Exchanger

Analysis of temperature measurements reveal why the heat exchanger has a constant power region and a varying power region, as well as why there are differences between the condenser and evaporator component level performance. The results are reviewed by working from the

surface of the heat exchanger to the top of the PCC slab to illustrate the behavior through the phase front.

5.4.1 Refrigerant Temperature Distribution

The microchannel surface measurements for a condenser test are illustrated in Figure 5.9.

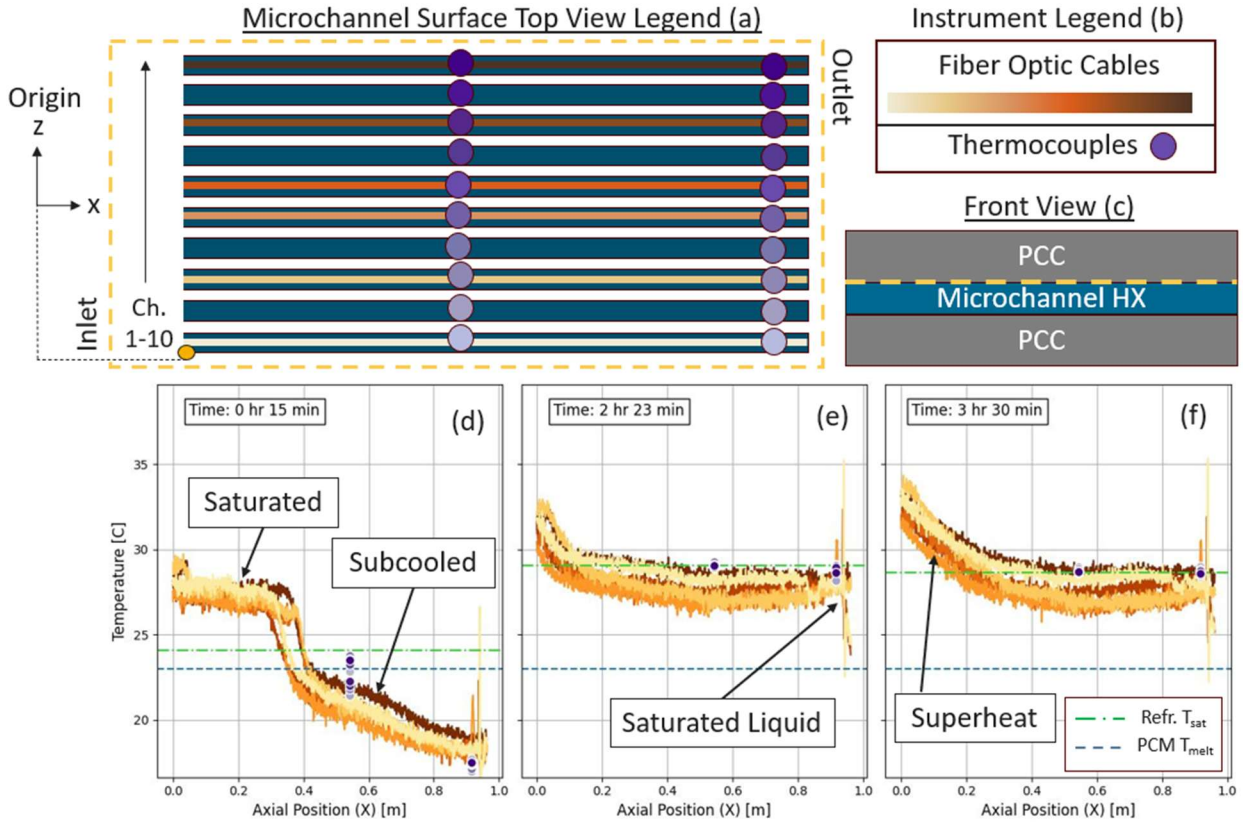

Figure 5.9: (a) the microchannel surface measurements (b) and the corresponding instrument legend (c) and front view to contextualize the location of the measurements. The measured refrigerant distribution is plotted in (e)-(f) through time. (d) is an initial state, (e) is when the outlet is saturated, and (f) is when sensible heating in the PCM is predicted by the finite difference model (see Chapter 6).

As the test begins the refrigerant is at the temperature of the PCC slabs' initial condition, which was approximately 18 °C for all condenser tests. Then, the refrigerant begins to reach the saturation condition as seen in the first 0.4 m Figure 5.9d. Initial saturation temperature measurements are slightly off because it takes time to achieve proper controls and the temperature of the PCC slab doesn't respond to pressure fluctuations quickly. The temperature of the fiber optic cables in the first 0.4 m is quite similar to the saturation temperature throughout the rest of the test. Figure 5.9e

shows the approximate time when the outlet becomes saturated. This is almost exactly when the constant power region ends. As the phase front progresses along the surface of the heat exchanger with time, the PCC takes on energy until it has little or no capacity to change phase left at the microchannel surface. This corresponds to when the outlet is saturated because the majority of heat transfer on the refrigerant side is due to the latent heat of condensation. Finally, towards the end of the test Figure 5.9f shows that the superheat inlet condition begins impose itself upstream in the microchannel, which makes sense because the PCC should heat sensibly at this point.

The evaporator baseline test has similar results at the microchannel surface as seen in Figure 5.10 – all other refrigerant distribution results are plotted in Appendix K.

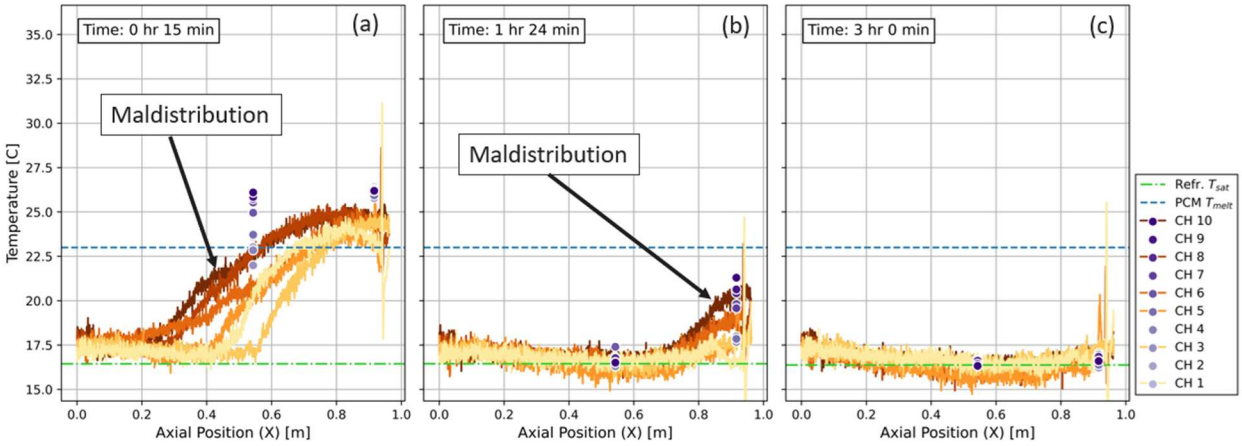

Figure 5.10: The measured refrigerant distribution in the evaporator baseline.(a)-(c) represent the evolution of the distribution in time. (a) is an initial state, (b) is when the outlet is saturated, and (c) is when sensible heating in the PCM is predicted by the finite difference model (see Chapter 6).

Initially the test begins at the initial state of the PCC slab, which is 26.6°C. Then, as the phase front progresses the refrigerant becomes saturated upstream (Figure 5.10a) until it achieves a saturated vapor outlet (Figure 5.10b). In Figure 5.10a and b there is clear evidence of mass maldistribution in the refrigerant channels, which will be explained in greater detail for a two phase inlet later in this section. As the test progresses the refrigerant continues at a saturated state

throughout the heat exchanger (Figure 5.10c) unlike the condenser test. The difference occurs because the inlet condition is a saturated liquid, so the refrigerant is never outside of the dome.

The refrigerant's average saturated length for each baseline test is plotted in Figure 5.11 to further investigate how refrigerant temperature distribution can help define what causes the constant power region and varying power region.

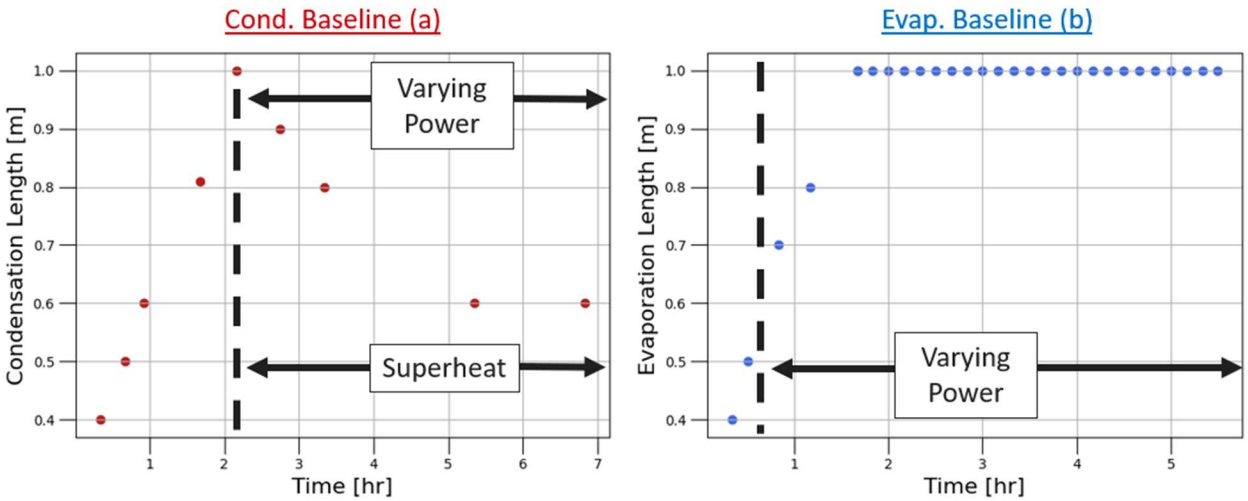

Figure 5.11: The saturated length of the PCM TES HX for (a) the condenser baseline and (b) the evaporator baseline.

The constant power region end is indicated on the plot by the dashed line. Initially the condenser condensation length increases until it reaches the full length of the heat exchanger, when it also transitions to the varying power region. In the varying power region, the condensation length decreases as the superheated inlet conditions bleeds into the front of the HX. Very different behavior is observed for the evaporator. The evaporation length increases, but the time when it reaches the full length of the heat exchanger doesn't match when the constant power region ends, which is odd. Comparing the time when the varying power region begins and the outlet is saturated based on the microchannel surface measurements reveals that the Evaporator is consistently off in all cases as seen in Table 5.3.

Table 5.3: The time when the varying power region begins for condenser and evaporator cases. The evaporator also includes times when a saturated outlet is observed at the manifold.

	Condenser		Evaporator	
	End of Constant Power Region	**Time when last surface measurement reaches saturation**	**End of Constant Power Region**	**Time when last surface measurement reaches saturation**
Baseline	2 hr 23 min	2 hr 23 min	50 min.	1 hr. 40 min.
Increased Load	30 min.	30 min.	15 min.	40 min.
Increased Peak Shaving	1 hr 44 min.	1 hr 44 min.	10 min.	53 min.

It consistently takes the evaporator longer to reach a saturated outlet than it does for it to reach the varying power region. The condenser's varying power onset and saturated outlet condition (based on microchannel surface measurements) are never different so they are reported together.

The measurements of the actual outlet condition downstream of the heat exchanger reveal why the evaporator varying power region and microchannel outlet condition do not match as seen in Figure 5.12.

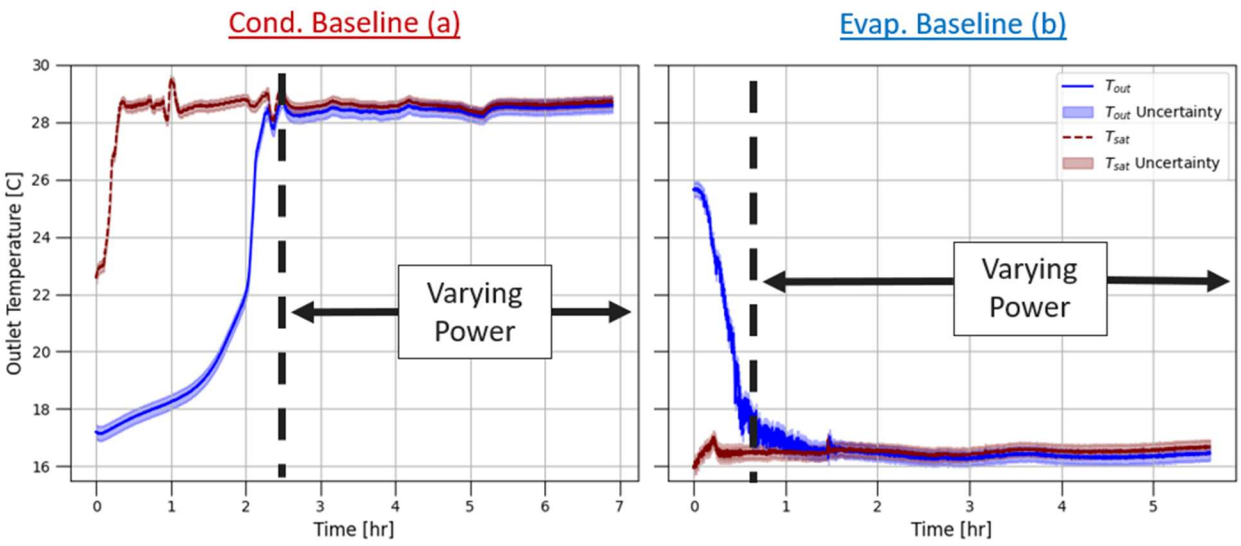

Figure 5.12: The outlet temperature for the (a) condenser and (b) evaporator. The saturation temperature is also plotted for reference on the state of the fluid.

The measurement in Figure 5.12 is measured at the outlet of the microchannel manifold rather than on the surface of the microchannel in Figure 5.10. So this measurement captures the effect of traveling through the microchannel manifold, which isn't captured by Figure 5.10. It appears that the outlet temperature actually does reach the saturated condition at the onset of the varying power region, as expected based on the condenser. The difference between the final microchannel surface temperature measurements and the outlet are likely caused by slight maldistribution in the manifold and pressure drop, which is easily observed in Figure 5.10a and b at the end of the length of the HX. The pressure drop measurements for all tests are documented in Appendix L.

Maldistribution was a problem observed initially in testing for two phase inlet conditions. Maldistribution refers to unequal mass distribution between the channels the refrigerant enters following the header of the heat exchanger, as seen in Figure 5.13. Maldistribution was observed experimentally for an evaporator case, as seen in Figure 5.13 for a 2.44 g/s flow rate and 0.2 inlet quality with a pressure that varied from 1325 kpa to 1475 kPa. The pressure varied because the

loop was running at the minimum possible pressure and pressure increased throughout the test due to increasing vapor in the microchannels.

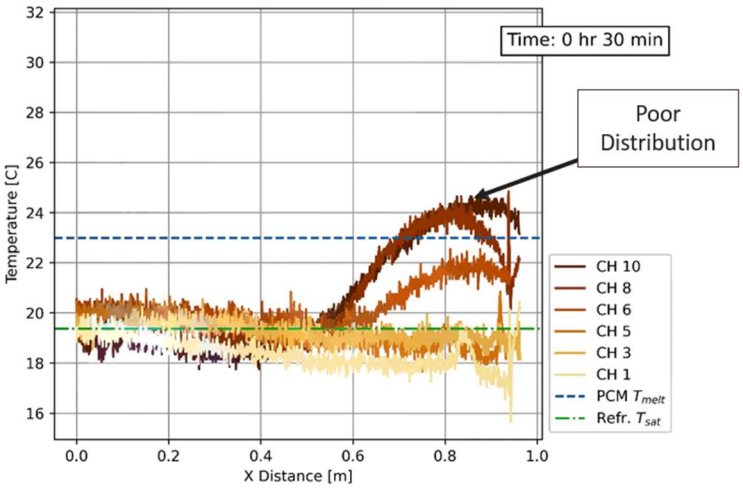

Figure 5.13: The plot of temperature vs. axial distance shows the location of refrigerant distribution by illustrating different temperature profiles in each refrigerant channel. Ch. 10 appears to have the least mass since it has the greatest superheat. Meanwhile channels3 and below have the most mass because they don't leave the dome.

A clear relationship can be seen in Figure 5.13 - the channels farthest back in the heat exchanger have the least mass. Channel 10 has the least mass because the refrigerant entered the channel at a higher quality and lower mass flow rate, making it easier to vaporize. For this channel, the refrigerant evaporates in the first 50% of the heat exchanger length and then superheats. In Figure 5.13, channels 3 and 1 don't have any superheat at the outlet because the heat transfer rate is not great enough to bring them outside of the dome. This maldistribution occurs because the header is not properly designed to distribute a two-phase fluid. The density difference between the solid and liquid entering the header leads to unequal distribution amongst the channels.

The outlet temperature results, including all inlet conditions, show a few interesting findings regarding each operating mode as well as seen in Figure 5.14.

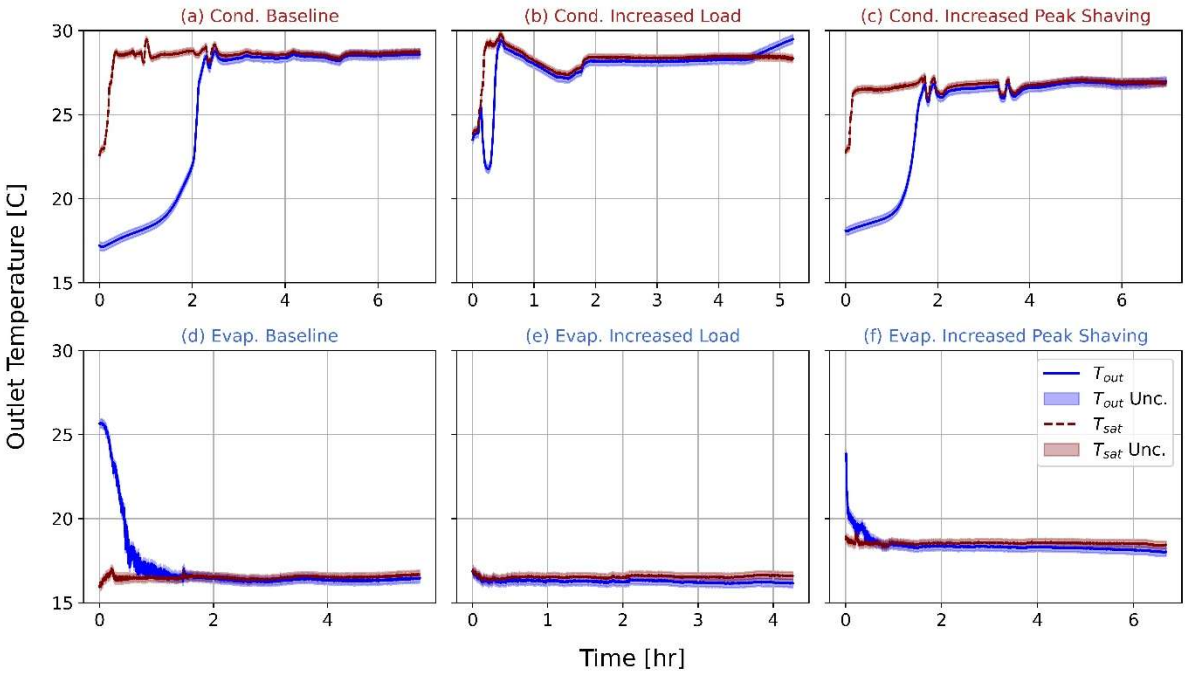

Figure 5.14: The outlet refrigerant temperatures for all tests. (a)-(c) present condenser and (d)-(f) present the evaporator. (a) and (d) are baseline cases, (b) and (e) are the increased load case, and (c) and (f) are increased peak shaving.

After the constant power period, the condenser tests maintain a saturated outlet for the remainder of the discharge process for most of the conditions tested. However, the condenser increased load case eventually reaches a superheated outlet state because it's operating at a higher flow rate and therefore discharges faster. In theory the baseline and increased peak shaving case would eventually have a superheated outlet for a constant inlet condition, but the test would need to run longer. The evaporator always ends as a saturated outlet because it's inlet condition is only slightly subcooled.

5.4.2 PCC Slab Temperature Distribution

The PCC slab temperature distribution measurements show the PCM heat transfer regimes. The heat top slab temperature distribution results are plotted in Figure 5.15 for the baseline condenser test.

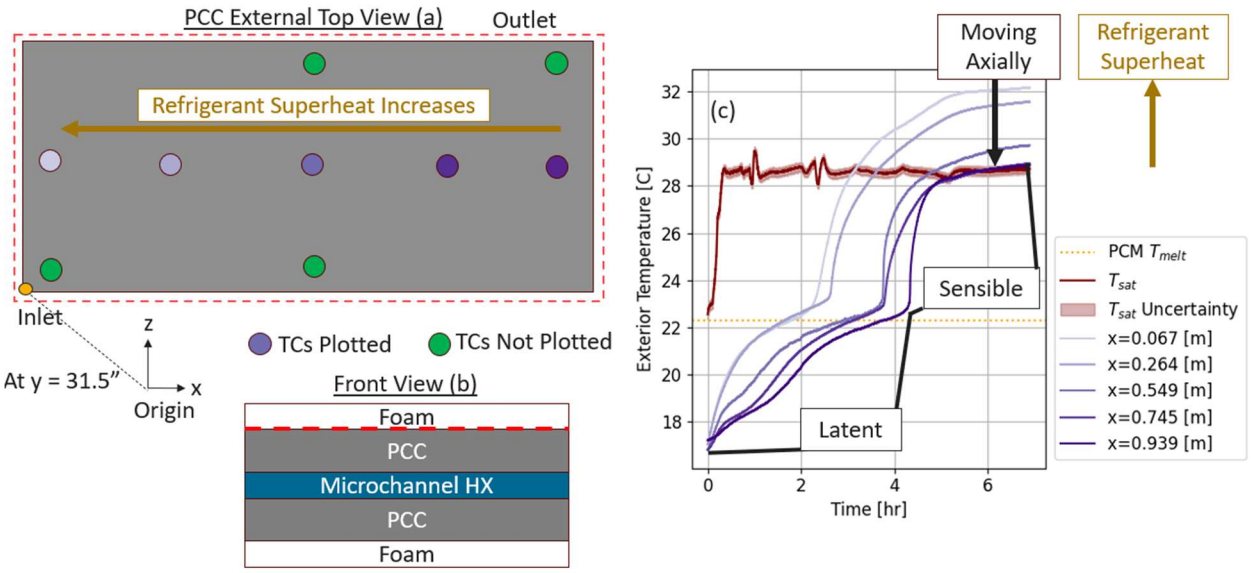

Figure 5.15: (a) a visual legend of the heat exchanger, (b) a front view to contextualize the layer viewed, (c) the exterior temperature distribution results.

The test begins in the latent region – 18°C isn't fully solid based on Texas A&M's differential scanning calorimetry results. Then as the test progresses the PCC gradually moves through the latent region as there is no sharp transition for PT23 during melting. The latent region ends when the temperature begins to shoot up sharply which happens between 2.1 hours and 4.1 hours. The variation in the onset of the sensible region corresponds to the axial position of the heat exchanger. Then, when the test finishes, a temperature gradient develops axially due to the refrigerant superheat upstream in the HX.

The evaporator has similar PCC slab temperature distribution results, but doesn't see as much variation in temperature because the physics of freezing is different than melting and the inlet condition is saturated. The results for the evaporator are plotted in Figure 5.16.

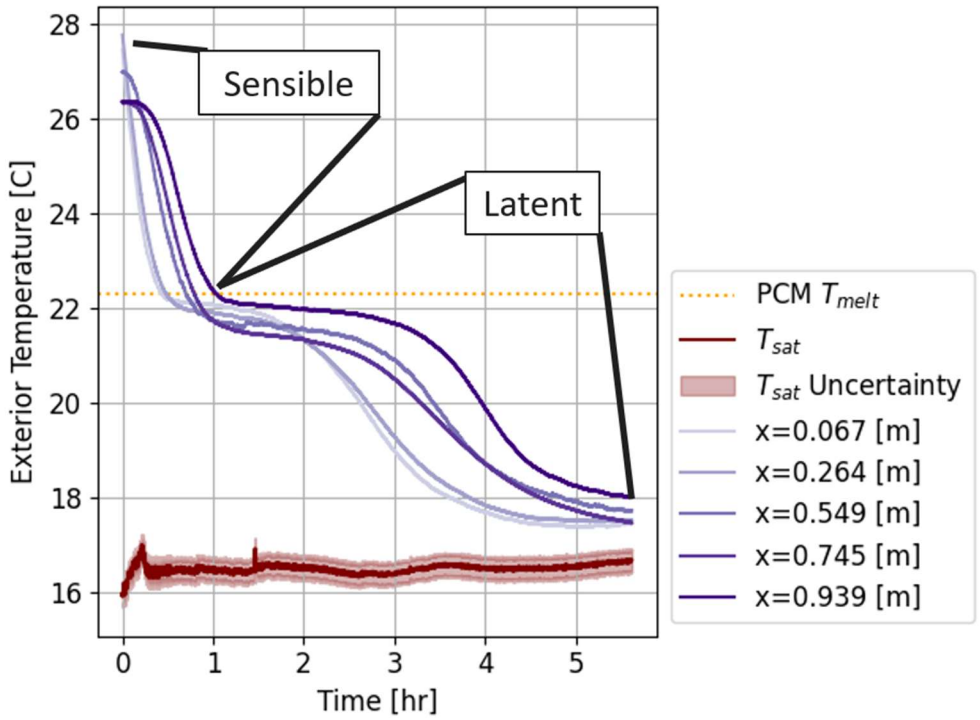

Figure 5.16: The evaporator baseline exterior temperature results.

The evaporator test sharply transitions from the sensible region to the latent region, which is similar to the end of the condenser test. The latent region remains at constant temperature initially and then begins to gradually drop until it approaches the saturation temperature and levels off. The initial constant temperature in the latent region is very different from the condenser results. This is because the physics that describe the onset of freezing is very different from the onset of melting.

The differences between the melting and freezing of the PCC slab are better illustrated by directly comparing the top slab temperature profiles and discharged energy for the baseline cases as seen in Figure 5.17.

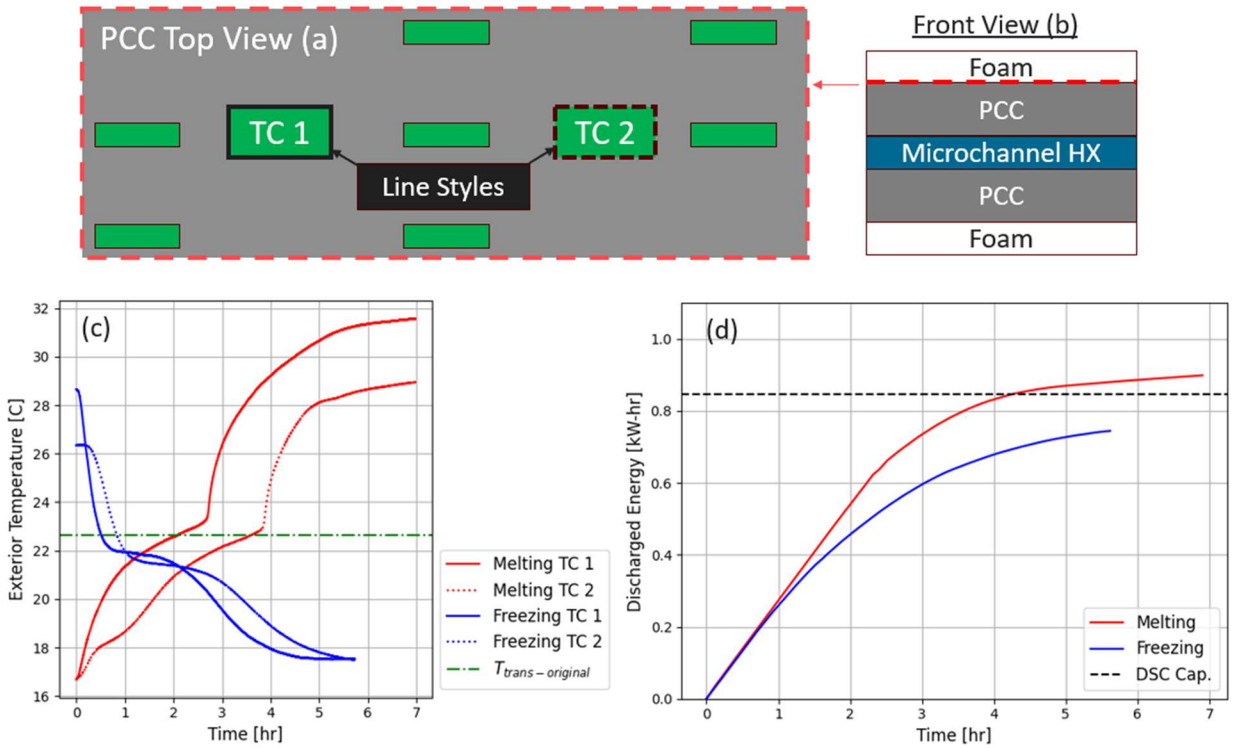

Figure 5.17: (a) gives a visual legend of the thermocouples plotted, (b) contextualizes plane plotted in the front view, and (c) shows the discharged energy for each case.

The difference in latent regions of the exterior temperature is very clear in Figure 5.17c illustrating the difference in physics of freezing vs. melting. According to Fultz, premelting occurs for most solids, which is characterized as a lack of atomic ordering relative to a frozen solid at a lower temperature [91]. Premelting allows for ease of nucleation of liquid crystals because lower activation energy is needed to achieve the critical atomic radius for nucleation to occur. The difference in melt temperature can help explain why the measured discharged energy between freezing and melting is different. Figure 5.17b clearly indicates differences in the discharged energy for freezing and melting tests. Ultimately, energy is still conserved, but the differences in nucleation cause the latent heat of melting to be different than the latent heat of freezing within this temperature range.

A test was run for 2.5 g/s and 1210 kPa to confirm that their was significant additional energy below 18 C. The pressure lowered the saturation temperature below 14 C for a majority of the test. The capacity and temperature results are shown in Figure 5.18.

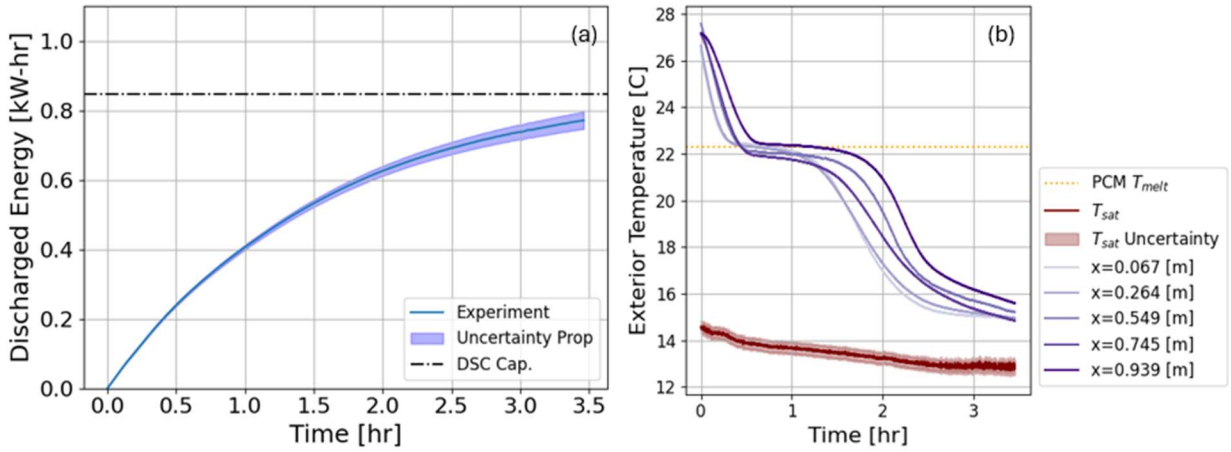

Figure 5.18: The (a) discharged energy and (b) top slab temperature distribution results for the test run to confirm energy is stored below18 C.

The discharged energy plot finishes with a final capacity of 0.77 kW-hr. Therefore, there is significant capacityincrease at lower temperatures because the highest capacity measured from the test matrix was 0.744 kW-hr. The sensible specific heat of liquid would only add 0.026 kW-hr when freezing between 17 and 14 °C, further corroborating this claim. However, the measured freezing capacity is still not close to the theoretical melting capacity in Figure 5.18a (0.846 kW-hr). Figure 5.18b shows that the temperatures for the test get down to approximately 15.1 C, so there could be additional capacity stored below 15.1 C.

Additional experimental evidence of this has been observed by other researchers. Mathis et al. observed this phenomena for PT23 [92], and during the preparation of this thesis testing was conducted on PT23 slab at NETenergy using 3 layer calorimetry. The data was collected and shared by Dr. Yana Galazutdinova. The sample tested at NETenergy was a composite, which included graphite and was soaked with PT23. Unfortunately, more information is not available on

the sample used for testing. The graphite in the sample and the prototype tested in this thesis will increase the likelihood of nucleation compared to a pure PCM because it introduces impurities that can act as nucleation sites. Therefore, their data is a better representation of the prototype tested in this work than NETenergy's prototype. The 3 layer calorimetry technique NETenergy is developing is adequate for measuring PCM properties at large volumes resolving issues with DSC, which only works for small volumes. Their preliminary findings are shown in Figure 5.19.

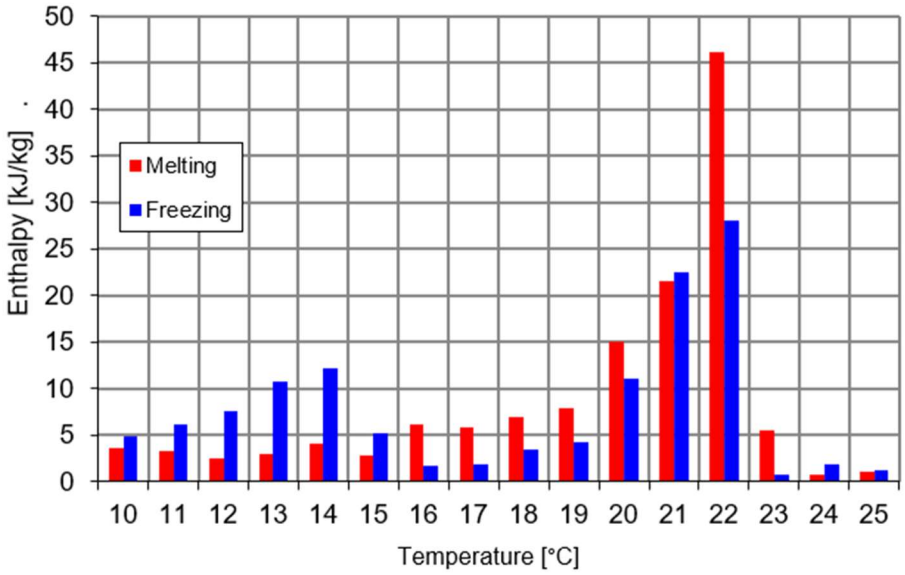

Figure 5.19: The 3 layer calorimetry data from NETenergy for composite PT23 and expanded graphite.

The heat (enthalpy) measured during melting is much larger than that measured during freezing. At lower temperatures the melting test indicates little change in enthalpy, but freezing has a second peak at 13-14°C. This clearly shows that energy conservation is not violated because energy would still be stored in the chemical bonds of the material if freezing were stopped at 18°C or 15 C if compared to the additional test run with the prototype discussed in this work. Additionally, the transition temperature of freezing is lower than that of melting based on Figure 5.19. The term hysteresis is often used to characterize a reduction in capacity or transition temperature when

freezing PCM. Therefore, hysteresis is observed in this work. Additionally, the differing activation energy for liquid and freezing nucleation is cited as a cause of hysteresis by Que et al. [93] .

Hysteresis is different than supercooling, which is a metastable thermodynamic state. The differences are illustrated in Figure 5.20.

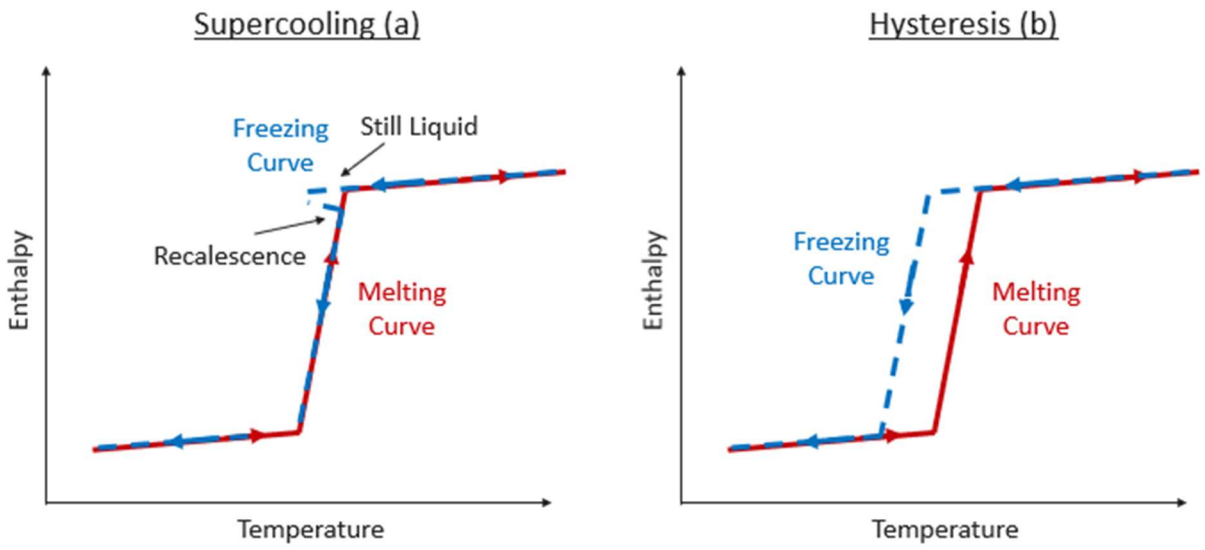

Figure 5.20: Temperature vs. Enthalpy curves for (a) supercooling and (b) hysteresis

Supercooling describes the suppression of nucleation until a lower temperature causes rapid nucleation and recovery of the melting enthalpy vs. temperature curve. The event when nucleation occurs is sometimes called recalescence in supercooling. This is different than hysteresis because a material experiencing hysteresis never has the same properties as it does in melting. Ultimately, differences in chemical bonds require different activation energy for nucleation of solid crystals than nucleation of liquids.

PCC slab temperature distribution results show signs of hysteresis and help explain other issues with capacity measurements as seen in Figure 5.21

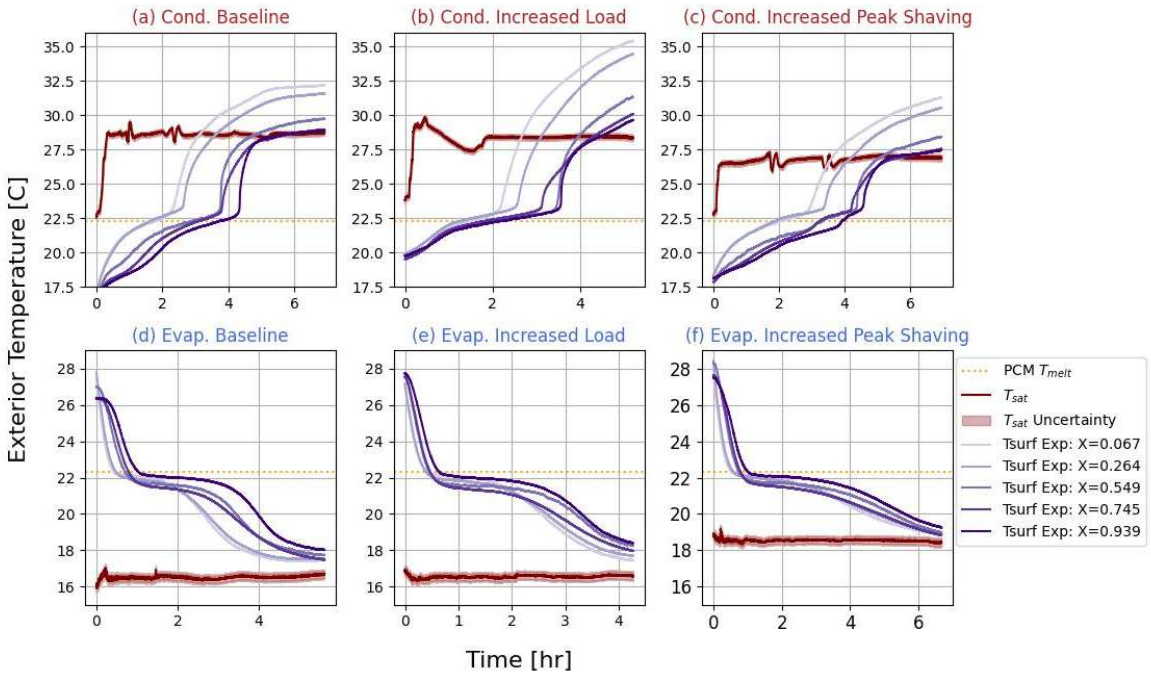

Figure 5.21: The measured exterior temperatures for all tests.

The key takeaway from the condenser temperature profiles is that the increased load case starts at 20°C rather than the target of 18°C, which may explain why the measured capacity is slightly lower – this will be discussed further in Chapter 6. Comparing the condenser and evaporator it's clear that different physical phenomena occur between melting and freezing regardless of HX operating condition because the condenser always has a more gradual transition, while the evaporator's transition happens at constant temperature. Furthermore, the evaporator capacity results showed differing discharged energy, decreasing from the baseline case to the increased peak shaving case. The discharged energy is different between tests because the discharged energy is sensitive to the final state of the PCC slab. In the baseline case the slab ends at an average temperature final of 17.65°C and in the increased peak shaving case it ends at an average final temperature of 18.97 °C. Additional capacity is still stored in the PCC slab between 17.65°C and 18.97 °C, which is why the measured capacities are drastically different.

Chapter 6: Model Complexity Study

The model complexity study aims to answer the second research question in this thesis and builds on the experimental observations discussed in Chapter 5. The study validates each model and compares the models to determine when each model is useful and when it breaks down.

6.1 Finite Difference Model Validation

The finite difference model validation preceded the analytical model, and allowed for detailed investigation of the experimental results to help determine proper material properties and phenomenological behavior.

6.1.1 Inlet Conditions Input into the Model

The model inputs for the finite difference model were experimental measurements from Chapter 5 or were derived from DSC data. Each model used inlet conditions derived from the experimental inlet conditions discussed in section 5.2. However, a few of the cases tested required modifications for the finite difference model to converge. Additionally, the initial temperature of the PCC slab was taken as an average of the top thermocouples for the simulation.

The condenser increased peak shaving case struggled with convergence so it's inlet conditions were averaged as seen in Figure 6.1.

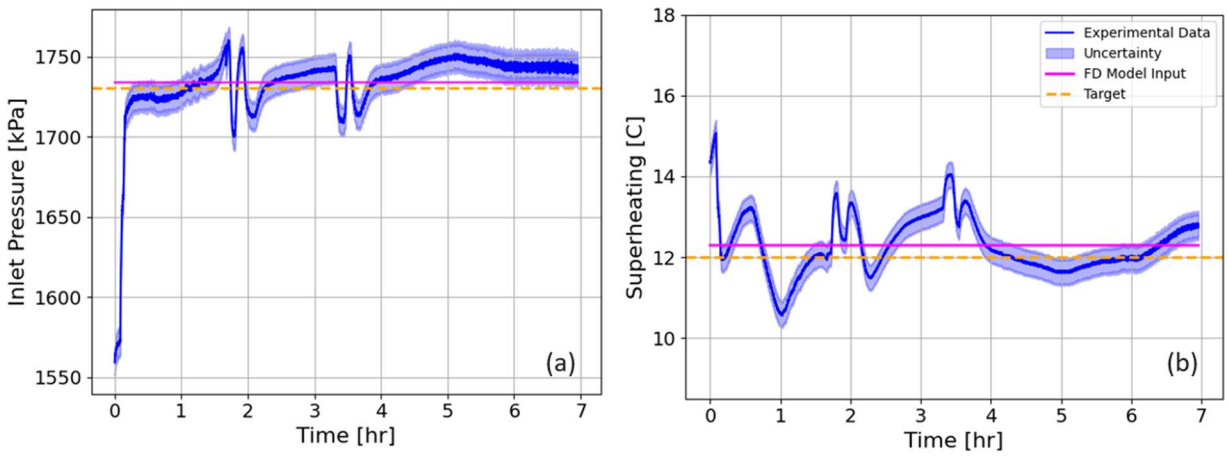

Figure 6.1: The finite difference model inputs compared to the target and experimental results for (a) inlet pressure, (b) the inlet superheat.

Comparing the measurements and inputs show that using the average inlet conditions are a good representation of the actual conditions observed in the experiment. The only inlet condition not averaged is the mass flow rate because it did not have sharp discontinuities.

The baseline evaporator case also suffered from convergence issues so its values for the first 1.86 hours of the experiment were altered to be an approximate representation of the values in this region. The inlet pressure was set to 1316 kPa and the inlet temperature was set to 16.2 °C. The inlet pressure and temperature were the only finite difference model inputs altered and are shown in Figure 6.2.

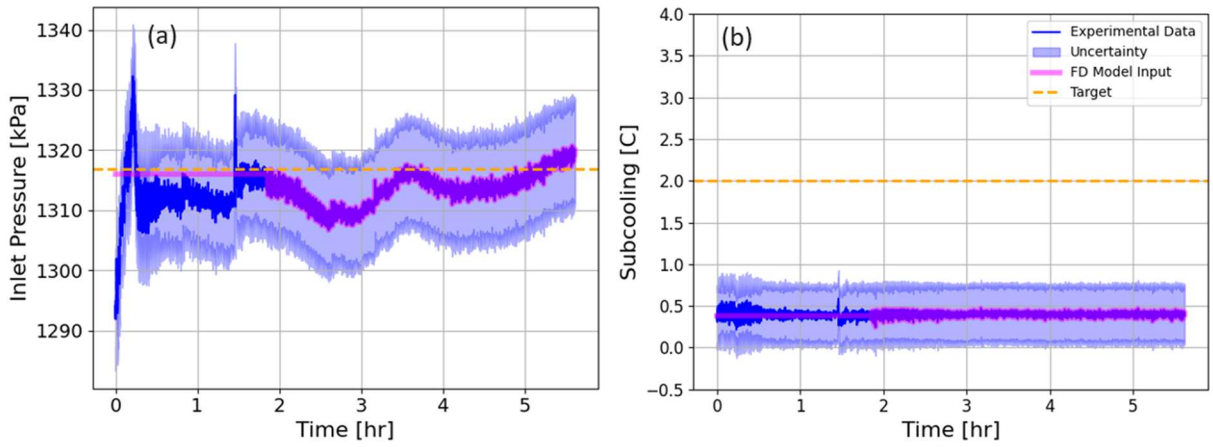

Figure 6.2: The modified finite difference model inputs for the evaporator case. (a) is the inlet pressure and (b) is the subcooling

The modification of the pressure in Figure 6.2a isn't quite the average of the data, but is the closest the pressure could be set to achieve convergence. In contrast, the subcooling is very close to the experimental results. Regardless, both are a good enough representation of the experimental data for ensuring the experiment and simulation are using the same inlet conditions. Sharp oscillations in the first 1.86 hrs of the test were the reason a convergence issue was encountered. Later in the experiment the inlet conditions were smoother and were used as inputs.

6.1.2 Material Property Verification and Modification

The finite difference modeling effort initially used the idealized melting curve described in Chapter 3, and a conductivity of 9 W/m-K. Each of these parameters received significant modification as part of a model validation effort.

The results for the original conductivity and the final conductivity used, are illustrated in Figure 6.3.

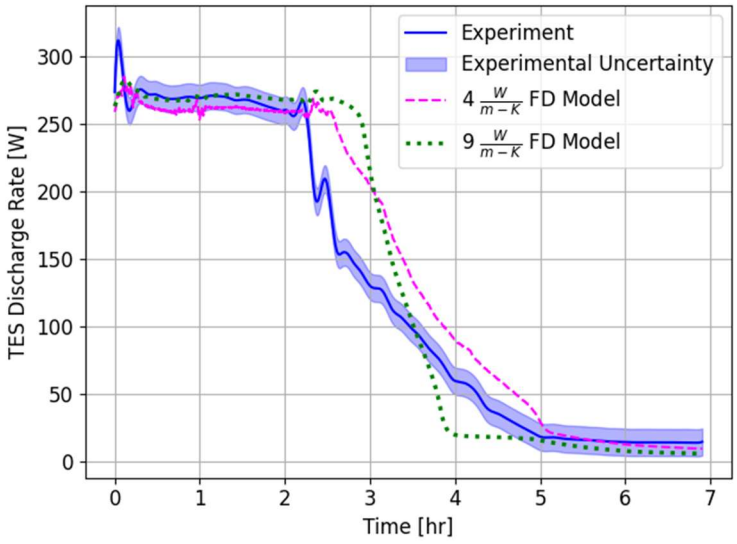

Figure 6.3: The discharge rate results for 2 different simulated conductivities and the experiment.

Moving from a conductivity of 9 W/m-K to 4 W/m-K, the model agreement improves. The onset of the varying power region isn't predicted very accurately, which causes large errors in this region for both conductivities. However, the 4 W/m-K model predicts the trend more accurately. It's thought that the conductivity is lower than original predictions by NETenergy because of the delamination of the graphite discussed in Chapter 4. However, no measurement has been taken to confirm the conductivity of the composite slabs. Following the completion of this thesis and wrap up of testing PCC slab samples will be characterized for conductivity. For all of the following validation efforts a conductivity of 4 W/m-K was used.

Agreement for a conductivity of 4 W/m-K is still imperfect, which is likely because of additional material property inputs. The result for the evaporator and condenser baseline cases are shown in Figure 6.4 for a conductivity of 4 W/m-K.

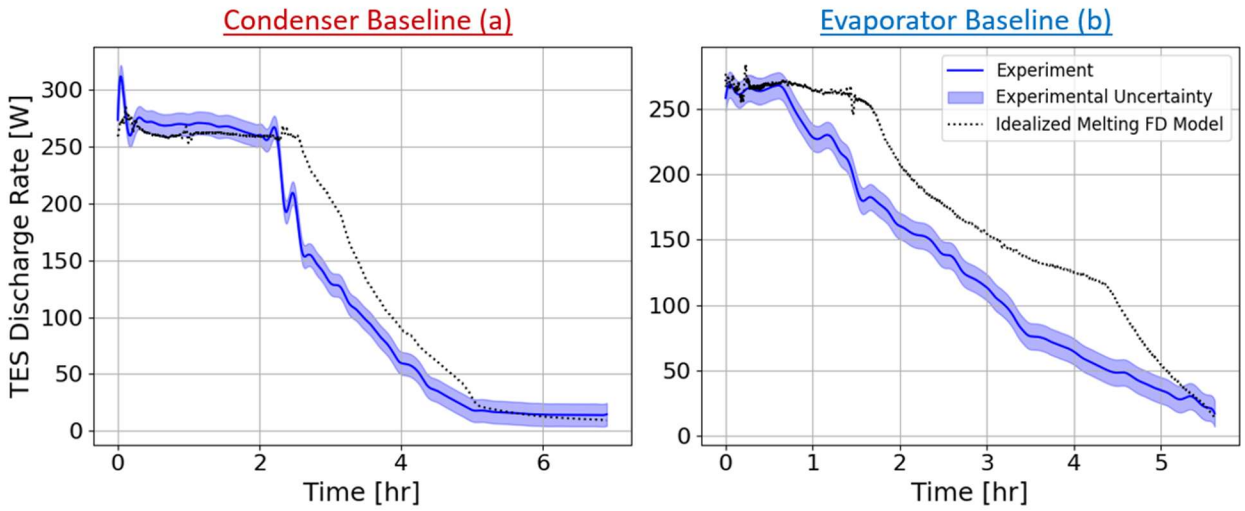

Figure 6.4: A comparison of the baseline finite difference predictions and experimental results for (a) the condenser and (b) the evaporator.

The results show significant error for each case. The condenser has significant error in the varying power region until the test ends. Furthermore, the evaporator is much worse because it overpredicts the length of the constant power region by a larger margin. It's reassuring that the constant power experimental results match the model predictions in magnitude though. Errors could be the result of modeling inputs or numerical singularities. The former was investigated initially – modeling inputs include boundary conditions, material properties, and geometric simplifications relative to the experiment. Because of the hysteresis observed in Chapter 5, the investigation focused on material properties. The hysteresis observation also likely explains why the evaporator baseline predictions significantly disagree with the experiment. Additionally, the idealized melting curve doesn't represent the actual enthalpy vs. temperature curve for this material (see Chapter 3), which may explain the error in the condenser baseline case.

Modifications to material properties enhance model agreement. The initial poor model agreement and hysteresis prompted adding the DSC generated melting enthalpy vs. temperature curve and a dedicated freezing curve to the model, and investigating a curve to represent freezing (this was prior to receiving NETenergy's data). The enthalpy vs. temperature curves used in this

work are presented in Figure 6.5 with the evaporator (freezing) baseline model result simulations that correspond to each enthalpy vs. temperature curve input.

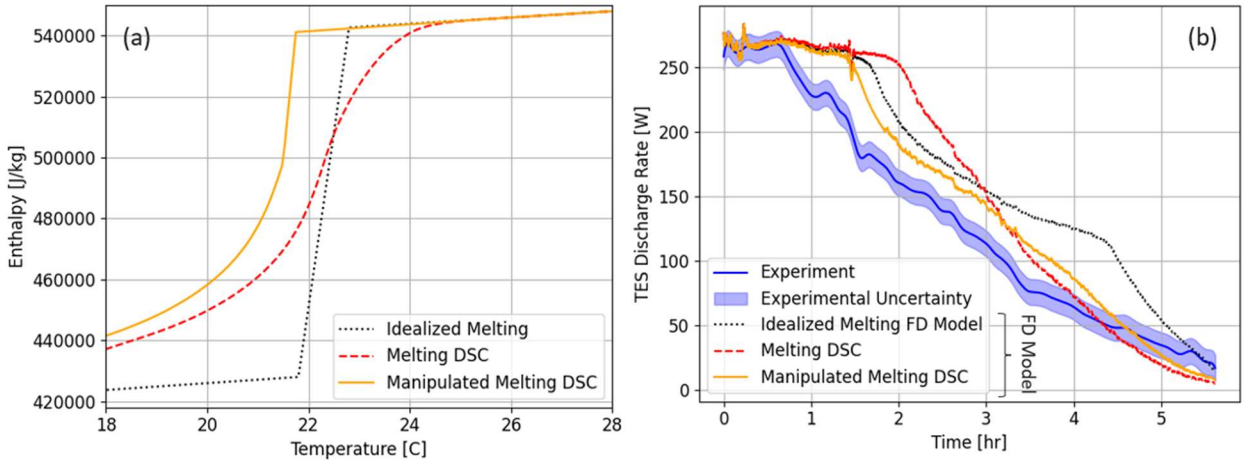

Figure 6.5:Observations of hysteresis are presented by plotting the (a) enthalpy vs. temperature curves and (b) discharge rate curves.

The enthalpy vs. temperature curves in Figure 6.5 were investigated in the following order: idealized melting, melting DSC, and manipulated melting DSC. The progression from iteration to iteration shows increasing model agreement in Figure 6.5b. Applying the melting DSC curve to the model increased the error in prediction of the onset of the varying power region, but had better late time performance. Then, manipulating the melting curve to achieve good agreement and capture freezing had the best performance. The manipulated curve predicted the onset of the varying power region the best, but still had some error. Following the onset of the varying power region the manipulated curve follows the trend of the experiment and eventually catches up late in time. The reasons for improved agreement and the process behind selecting the manipulated DSC curve are discussed throughout the rest of this subsection.

The original enthalpy vs temperature in Figure 6.5a was created from melting DSC data but was idealized to only capture the latent heat the peak melting temperature. The idealized curve assumes that all phase change happens at 22.3 ±0.5°C to try to capture the transition temperature.

The enthalpy vs. temperature curve generated from the DSC curve clearly shows that there is significant energy content outside of the phase change peak, which explains why the idealized curve has poor agreement. This motivated comparing the results to an enthalpy vs. temperature curve generated from the DSC melting data, which improved model agreement, but still left room for improvement.

Additionally, the condenser agreement also improves when the melting DSC curve is used for predictions. The result is seen in Figure 6.6.

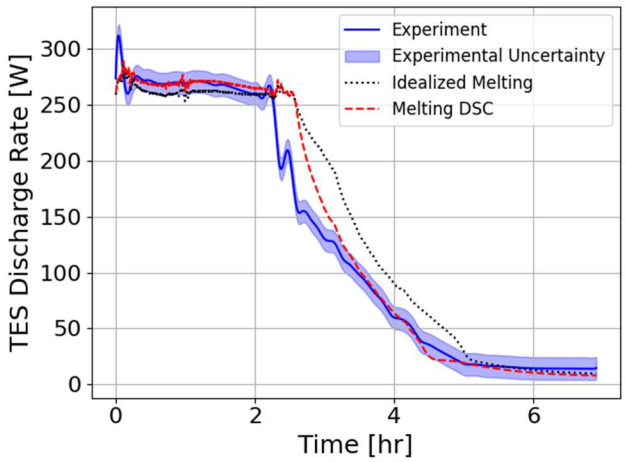

Figure 6.6: The progression from idealized melting to the full melting DSC curve shows increasing model agreement.

In Figure 6.6 the experiment-model agreement got better when the melting DSC curve was used. Although, the model still over predicts the onset of the varying power region to the same degree it did when using the idealized curve. In contrast to the idealized curve though the DSC curve begins to track the experiment eventually and is within the measurement error from 3 hours onwards in the varying power region.

Refocusing on the freezing results in Figure 6.5b, there was still significant enough disagreement between the experiment and model to motivate further enthalpy and temperature curve modifications. This lead to the creation of the manipulated melting DSC curve. The

manipulated melting curve in Figure 6.5a was created in two parts – the first used results from Mathis et al. [92] to qualitatively inform the shape of the curve and the second was created by shifting the melting curve to meet the first part of the freezing curve. This curve was generated in several iterations to fit the results, but only the final iteration is presented, as seen in Figure 6.7.

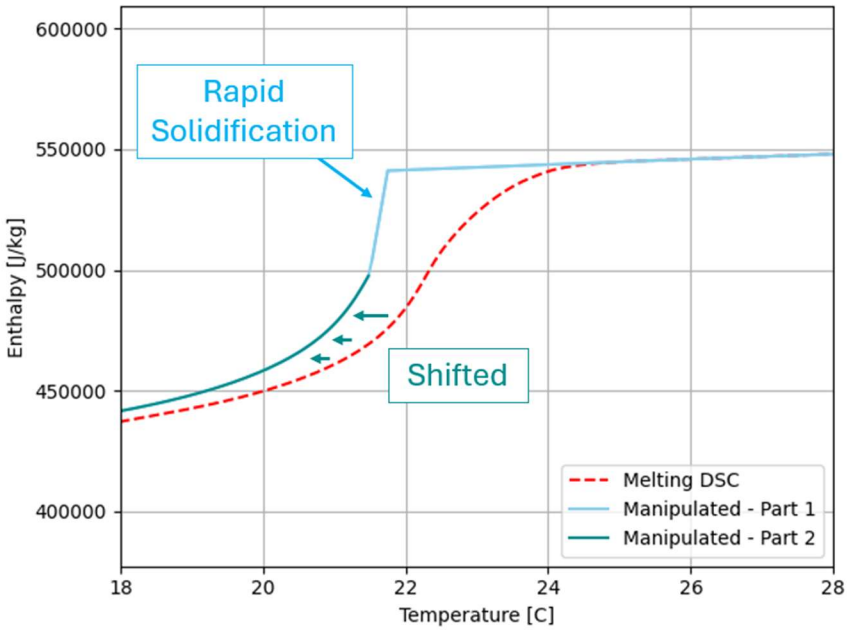

Figure 6.7: The manipulated DSC curve was generated in two parts, one (part 1) informed by Mathis data, and one (part 2) by shifting the melting DSC measured at Texas A&M.

Part 1 in Figure 6.7 indicates rapid solidification (nucleation) because Mathis work showed similar behavior. Using this modified curve as an input to the model achieved good agreement with the experimental results as seen in Figure 6.5b. Further modifications could be made to increase the agreement.

To increase agreement additional computational and experimental efforts could be pursued. An optimization could be run to fit the enthalpy vs. temperature curve for freezing to the experimental data and achieve perfect model agreement. However, this is left as future work since material level measurements (for example, DSC) would be needed to generate higher confidence in the enthalpy vs. temperature curve. While the experimental results presented in this work can

be taken as the ground truth with confidence the set up does not isolate the material and instead confirms the freezing characteristics of the PCM, microchannels, and insulation (the device) holistically. Additionally, using the results from the experiment itself likely would generate good agreement, but would cloud the validity of the model validation. Therefore, the manipulated freezing curve is not a replacement for a material level measurement, only a stopping point in the investigation for now. The results from NETenergy satisfy the need for new material level measurement results but were not received with enough time to include them in the modeling study.

Additionally, accurate characterization of PCM freezing behavior is an active research topic in the material science community [19], [93] due to phenomena like hysteresis and super cooling. Therefore, further work may be needed to develop accurate material level measurement methods. Mathis used a dynamic heat flow measurement technique [94] to measure the enthalpy vs. temperature curve. Furthermore Song et al. [19] investigated stochastic modeling techniques for large volume samples. Progress in these techniques may be needed before accurate freezing enthalpy vs. temperature characterization can be used at the device level, but for this work the manipulated melting DSC curve does well enough. The 3 layer calorimetry technique, and the data presented from it in Chapter 5, may resolve this issue, but this technique is still under development.

The final melting and freezing curves used for device performance and model fidelity investigations are presented in Figure 6.8 to provide clarity on the inputs used in the rest of the analysis.

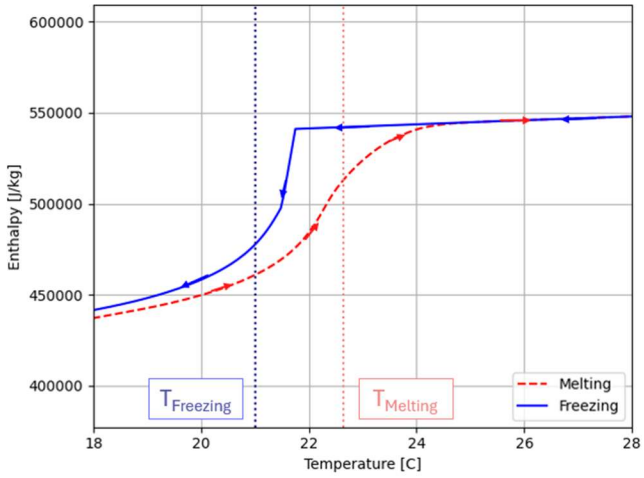

Figure 6.8: The final inputs for PCM melting and freezing are presented. The transition temperatures for each phenomena are also identified.

The melting profile in Figure 6.8 is the melting DSC curve in Figure 6.5a and the freezing profile is the manipulated melting curve in Figure 6.5a. Furthermore, this plot illustrates the hysteresis clearly. The arrows indicate the path the material follows, which shows that less latent heat is available at from 18-28°C (the target temperature range of the tests). This is apparent since the enthalpy at 18°C is greater in freezing than melting and the enthalpy at 28°C is the same for freezing and melting. It's not clear how close these results match the 3 layer calorimetry data in Figure 5.20, but it shows the same trend. Moreover, a difference in freezing and melting temperature is illustrated in Figure 6.8. Ultimately, the transition temperature in melting was taken as 22.65°C from Texas A&M's DSC work described in Chapter 3. The melt temperature differs slightly from the original 22.3°C, which is discussed later in this chapter. The freezing temperature is taken as 21°C even though the first peak in the transition occurs at 21.5°C. This is because freezing continues to occur below 21.5°C due to the second peak in the DSC curve discussed in Chapter 3.

The DSC curves were used as inputs for validation of each test as seen in Figure 6.9, which presents the discharge rate validation results for all experiments.

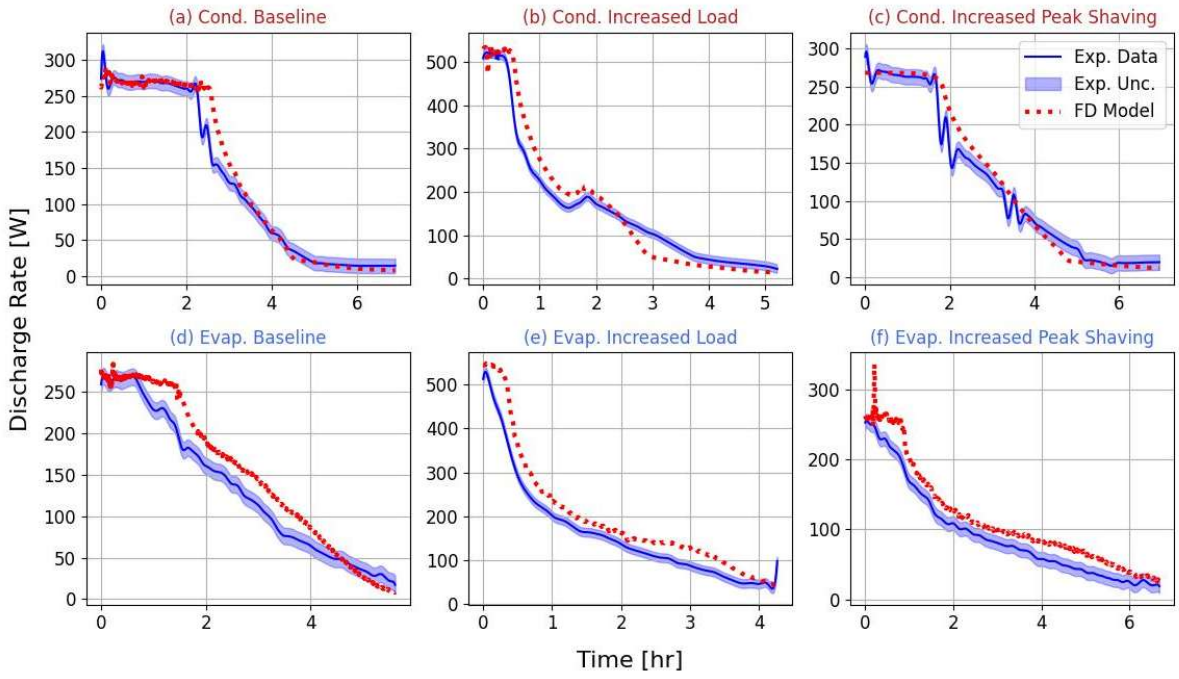

Figure 6.9: The discharge rate finite difference model predictions and experimental results for all experiments. (a)-(c) present condenser and (d)-(f) present the evaporator. (a) and (d) are baseline cases, (b) and (e) are the increased load case, and (c) and (f) are increased peak shaving.

The condenser tests show consistent high agreement with experimental data. There are some gaps at the onset of the varying power region for each case, which could possibly be explained by slightly inaccurate contact resistances as there are no measurements to confirm the values used in the finite difference model. As discussed in Chapter 4, they were set with prior experience from a similar set up [57]. The increased load condenser case appears to have consistently larger gaps in agreement than the other condenser cases. The evaporator results have a consistent error, which makes sense because optimization for perfect enthalpy vs. temperature curve agreement wasn't conducted, and NETenergy's data was not used as a model input.

The discharged energy calculations reveal similar trends, as seen in Figure 6.10.

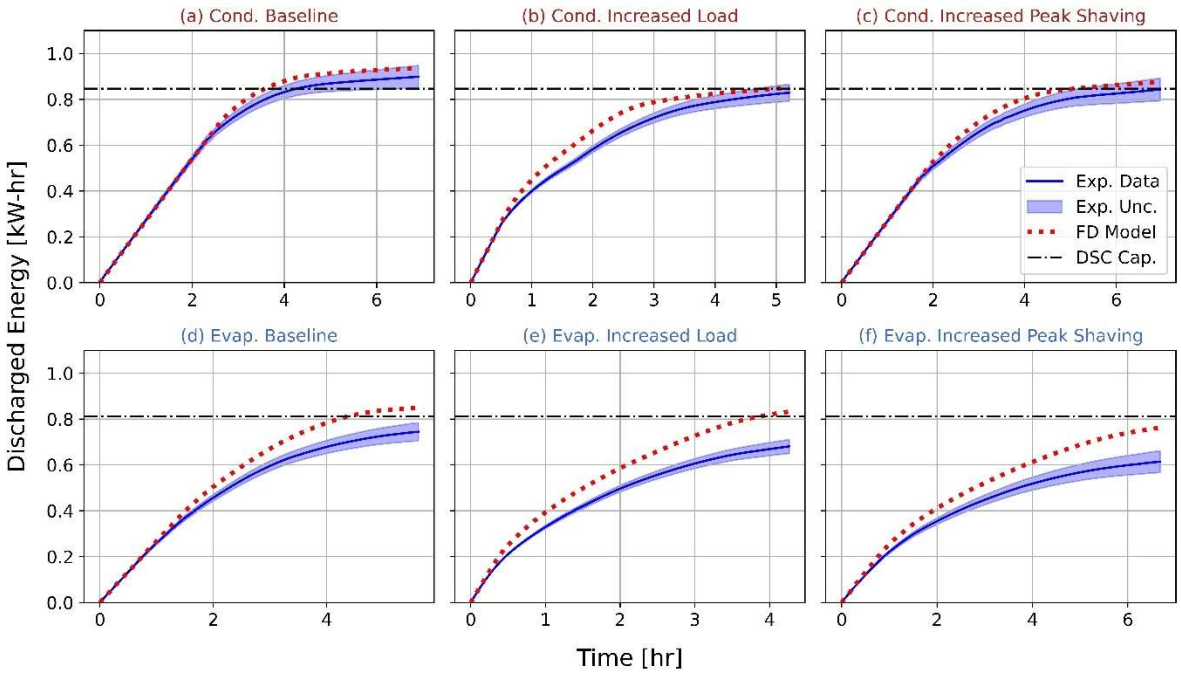

Figure 6.10: The discharged energy results for all experiments. (a)-(c) present condenser and (d)-(f) present the evaporator. (a) and (d) are baseline cases, (b) and (e) are the increased load case, and (c) and (f) are increased peak shaving.

The condenser results show high agreement, but the increased load case deviates quite a bit in the middle of the test. The evaporator results are consistently off the mark, although this is expected based on the discharge rate results as this discharged energy is just the integral of the discharge rate. They're only within the error of the measurement early in the test. The DSC capacity in the evaporator test is adjusted for the modified DSC curve, and the finite difference model results approach this value. This makes sense because the modified DSC curve is the input for the evaporator cases, so the results should approach the "DSC capacity".

The overall discharge rate and discharged energy results were close enough to move forward with using the model as a tool to investigate additional issues with finite difference model agreement and model complexity and why additional agreement was not present.

6.1.3 Refrigerant Temperature Distribution Comparison

The refrigerant distribution measurements match pretty well, the microchannel surface comparison is presented in Figure 6.11 for the condenser baseline.

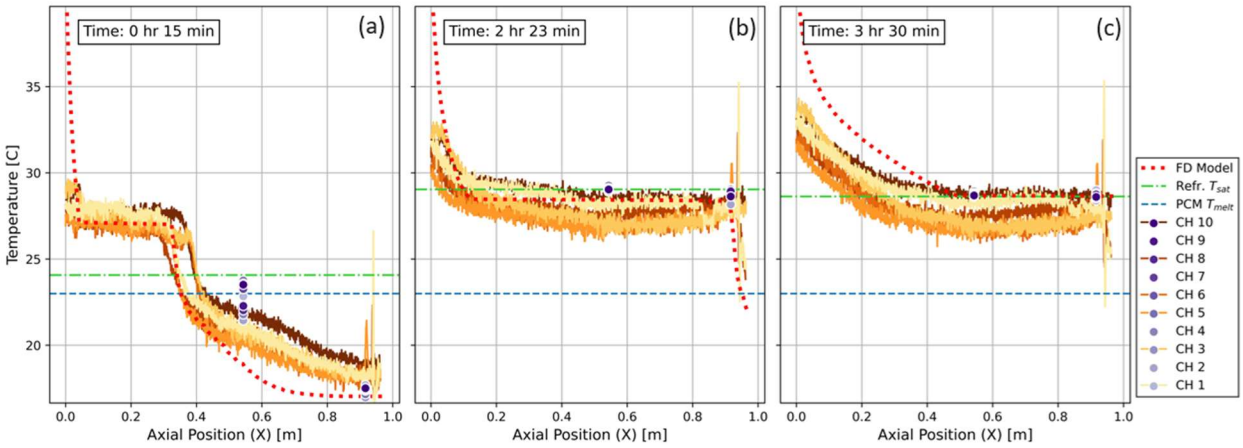

Figure 6.11: The finite difference prediction of refrigerant distribution in the condenser baseline and the experimental results..(a)-(c) represent the evolution of the distribution in time. (a) is an initial state, (b) is when the outlet is saturated, and (c) is when sensible heating in the PCM is predicted by the finite difference model (see Chapter 6).

The finite difference model predicts the length of the saturated region very well in Figure 6.11a and b. However, it doesn't perfectly predict the temperature distribution in the superheated region as seen in Figure 6.11a in the back half of the heat exchanger and Figure 6.11c in the front half when superheat begins to manifest upstream.

Comparison of the evaporator refrigerant distribution results reveals varied agreement due to the effect of maldistribution. The results are presented in Figure 6.12.

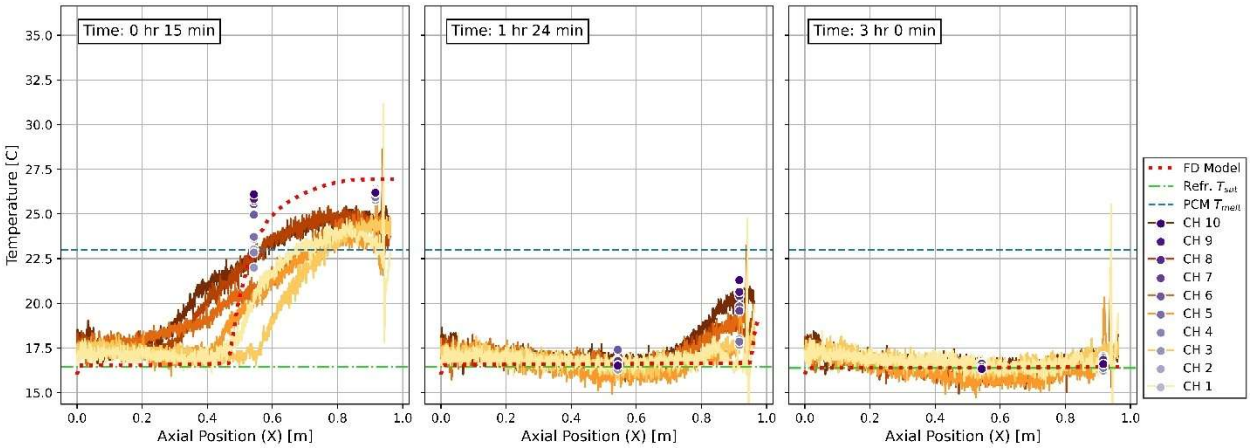

Figure 6.12: The finite difference prediction of refrigerant distribution in the evaporator baseline and the experimental results..(a)-(c) represent the evolution of the distribution in time. (a) is an initial state, (b) is when the outlet is saturated, and (c) is when sensible heating in the PCM is predicted by the finite difference model (see Chapter 6).

In Figure 6.12a and b there is significant evidence of maldistribution as discussed in Chapter 5, which causes poor experiment-model agreement. The model assumes that the mass flow is perfectly distributed so maldistribution causes this assumption to be invalid. This could lead to temperature gradients in the XZ plane of the device, which also would make the 2D approximation for the PCC slab inappropriate. The maldistribution existed on a small time scale though, as the temperature distribution in Figure 6.12a appears to still be quite similar between each of the sensors.

The model's prediction of the transient outlet condition reveals some larger errors as seen in Figure 6.13 for the condenser and evaporator baseline.

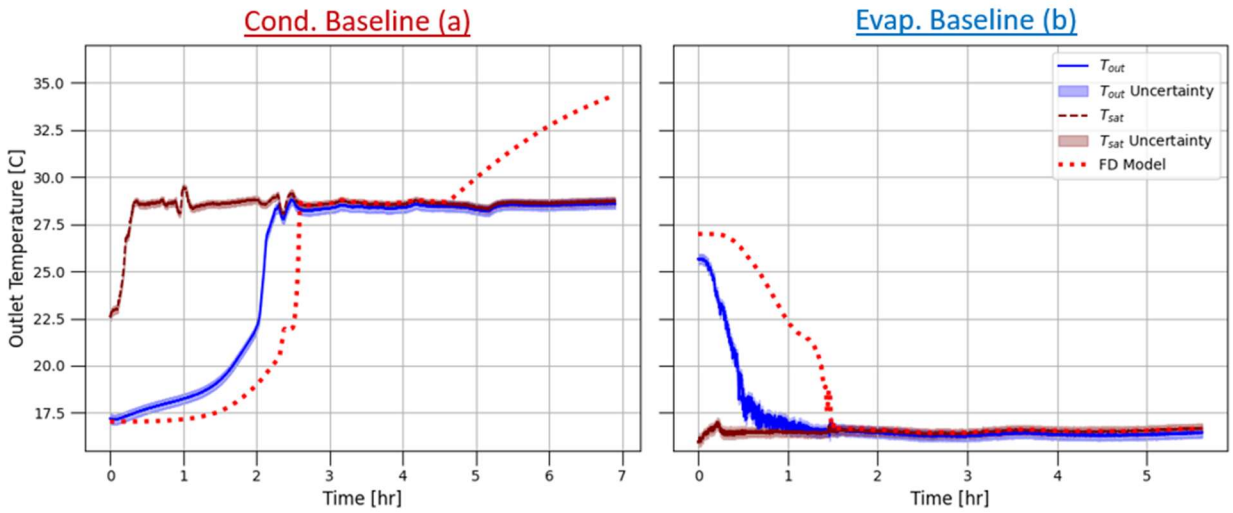

Figure 6.13: The refrigerant outlet temperature for (a) the condenser baseline and (b) the evaporator baseline.

The comparison shows that the condenser model outlet condition initially lags the experimental results. Then following the saturated region the model predicts superheat, while the experiment shows no evidence of superheat. Additionally, the evaporator also lags the experiment initially prior to entering the saturated region. The evaporator never exits the saturated region as expected.

The results for all outlet temperature predictions reveal similar trends to the baseline for all tests as seen in Figure 6.14.

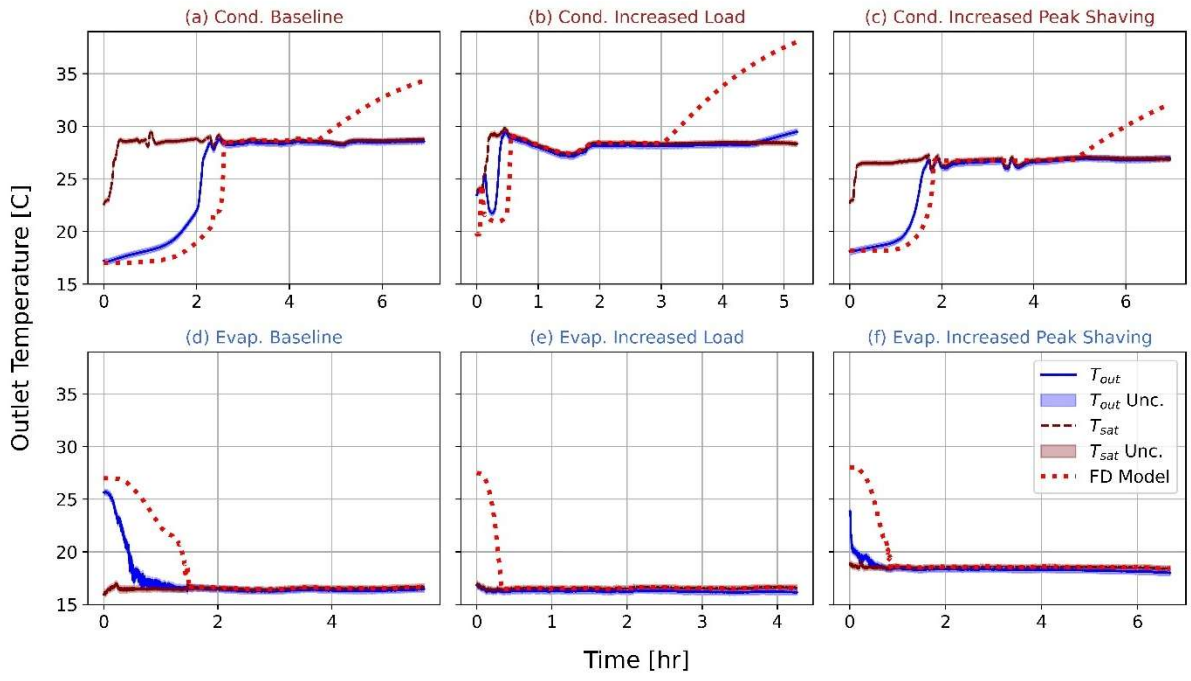

Figure 6.14: The refrigerant outlet temperature for all tests. (a)-(c) present condenser and (d)-(f) present the evaporator. (a) and (d) are baseline cases, (b) and (e) are the increased load case, and (c) and (f) are increased peak shaving.

The condenser and evaporator results in Figure 6.14 consistently lag the experimental results. Furthermore, the condenser always fails to correctly predict the onset of outlet superheat, which was only observed in the increased load case. The differences in temperatures here make sense because the model is not perfect and does a better job at predicting outlet enthalpy than temperature as seen in Figure 6.15.

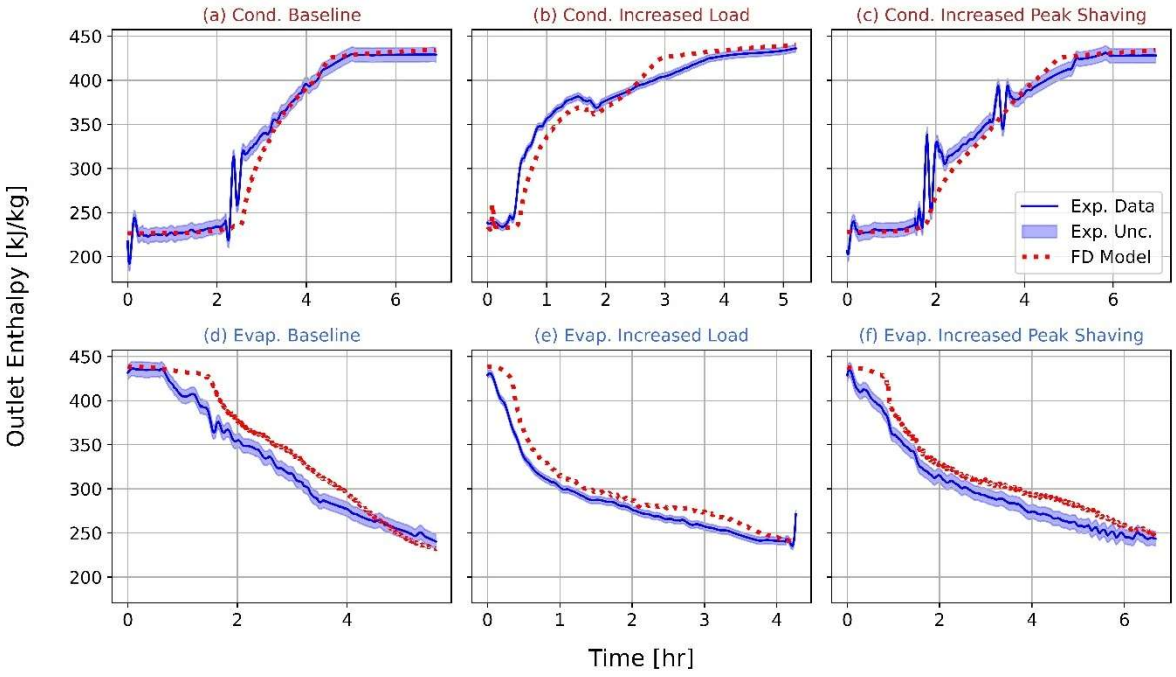

Figure 6.15: The outlet enthalpy for all tests. (a)-(c) present condenser and (d)-(f) present the evaporator. (a) and (d) are baseline cases, (b) and (e) are the increased load case, and (c) and (f) are increased peak shaving.

Figure 6.15 shows that the outlet enthalpy for each test shows good agreement. This makes sense despite the poor agreement for outlet temperature because the energy needed to cause a change in temperature in the superheated region is insignificant compared to energy within the vapor dome. Small losses in the manifold could result in large differences in the outlet superheat. So, determining model performance based on outlet temperature should only be done if it's needed to control the system, as it doesn't accurately represent the transient thermodynamic outlet state.

6.1.4 PCC Slab Temperature Distribution Verification

The PCC slab comparison yields results that indicate poor model agreement in the sensible heating region. The results for the condenser and evaporator baseline are presented in Figure 6.16, comparing the nearest node in the finite difference model to the thermocouple locations.

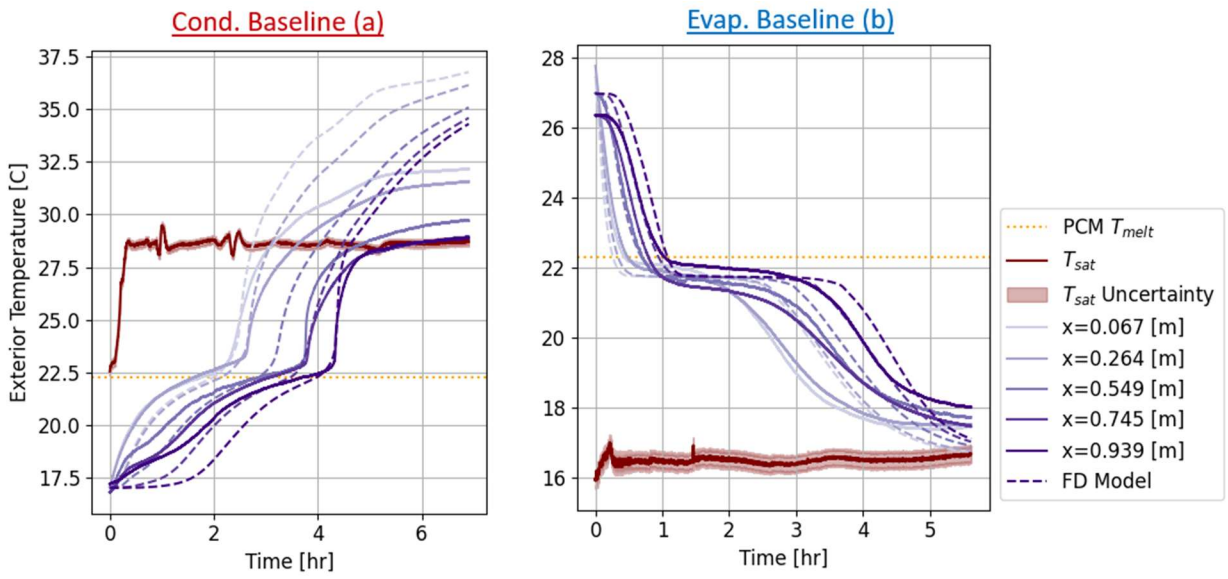

Figure 6.16: The finite difference prediction and experimental results comparison for the (a) condenser and (b) evaporator baseline exterior temperature results

The condenser results show decent agreement within the latent region. Although, the predictions at the end of the HX tend to lag, but catch up and predict the onset of the latent region correctly. The middle prediction does not predict the onset of the sensible region accurately, which is likely because the model assumes that the PCC slab is a single piece. The experiment was built with a PCC slab that consists of two pieces (see Chapter 4 for what one horizontal slab looks like), which likely explains this error. Later in time when the slab temperatures rise above the refrigerant saturation temperature the model predictions completely diverge from the experimental conditions. This is not concerning because the sensible region's energy content is small compared to the latent. The evaporator has much better experimental-model agreement than the condenser, partly because the model material property tuning considered the agreement of these results. An additional reason for the disagreement is that the phase transition occurs at constant temperature, which leaves less opportunity for glaring errors. The finite difference model does fail to predict onset of the varying temperature latent region inaccurately. In all cases the prediction is delayed, however the general trend is close to the observed experimental results.

The results for all the top slab finite difference model runs show similar trends to the evaporator baseline and condenser as seen in Figure 6.17.

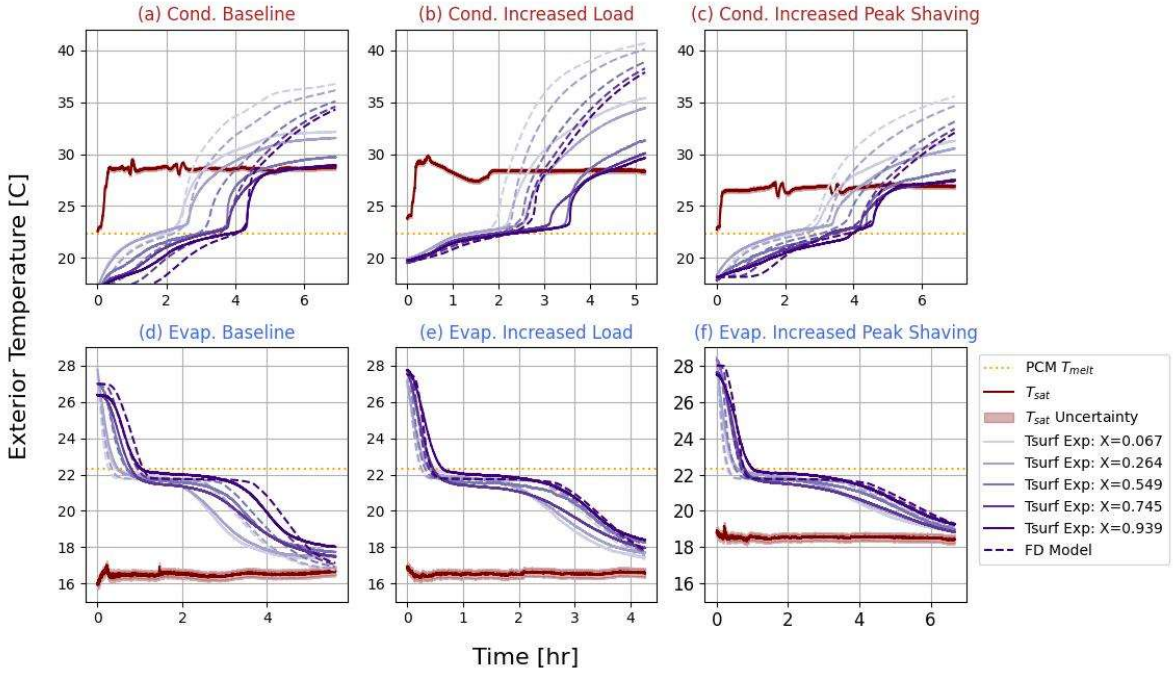

Figure 6.17: The exterior temperature finite difference model prediction results for all experiments. (a)-(c) present condenser and (d)-(f) present the evaporator. (a) and (d) are baseline cases, (b) and (e) are the increased load case, and (c) and (f) are increased peak shaving.

The condenser results match the trend previously described except the increased load case sensible region error increases relative to the other condenser results. This makes sense as starting the test at approximately 20°C moves the initial condition closer to the peak in latent heat, which makes it more sensitive to the accuracy of the initial state given to it. The evaporator results are consistent with analysis for the baseline case – the prediction of the onset of the varying temperature later region is delayed.

A sensitivity study of initial starting temperature for the increased load case reveals better agreement if the initial temperature of the test is decreased by 1.5°C as seen in Figure 6.18.

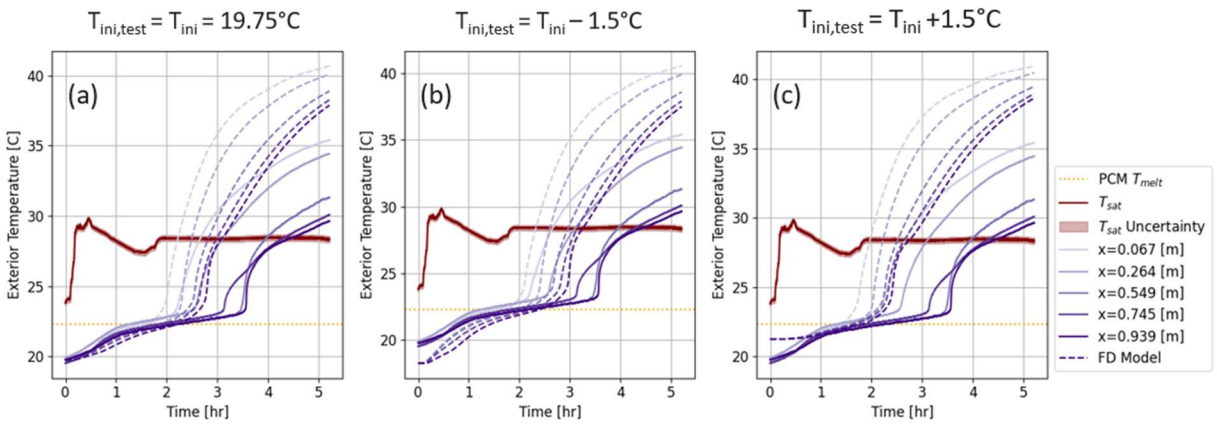

Figure 6.18: A study of different starting temperatures for the increased load case. (a) is the original (b) is 1.5°C lower and (c) is 1.5°C higher.

The model does because if the temperature initial temperature is decreased by 1.5°C, and worse if it's increased. This makes sense because the original data in Figure 6.18a shows that the model predicts the onset of the sensible region too early. Decreasing the initial temperature by 1.5°C has worse results for the discharged energy as seen in Figure 6.19.

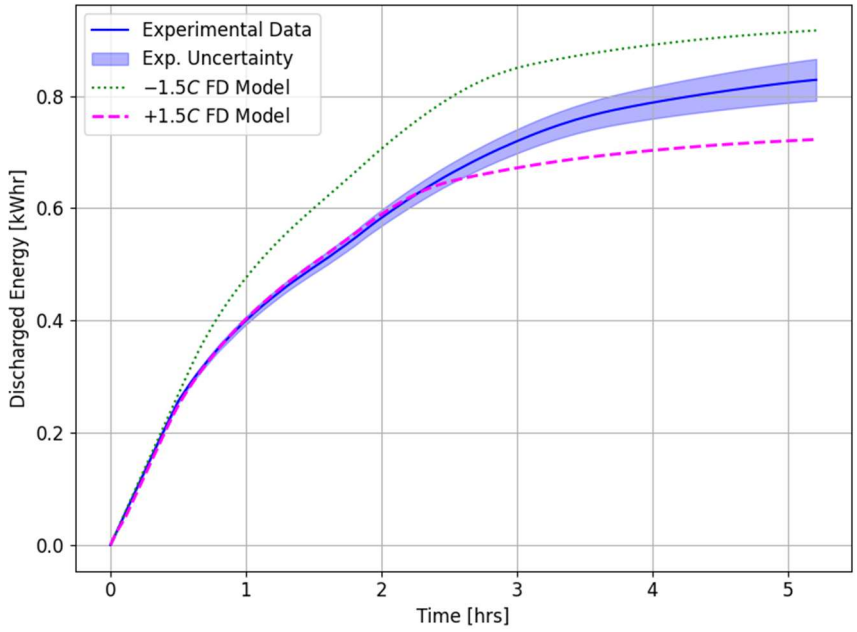

Figure 6.19: The discharged energy curve for the +/-1.5°C initial condition investigation.

Figure 6.19 shows that decreasing the initial temperature increases the error in the prediction late in the test, but decreases it early in the test. If the temperature is raised however the agreement

early in the test gets better and is worse later in time. This makes sense because increasing the temperature decreases the energy content available. Therefore, the fact that the experiment begins at a higher starting temperature than the target doesn't offer a full explanation for the errors observed.

6.2 Required Model Fidelity

George Box famously said, "all models are wrong, but some are useful" [95]. This section tries to determine the degree of detail needed in models of PCM TES HX's by comparing the finite difference model to the analytical model. The analytical model can predict discharged energy, heat transfer rate, and outlet condition (enthalpy or temperature). However, only discharge rate and discharged energy are discussed because they are proxies for outlet temperature and enthalpy. Part of the discussion is on validation of the analytical model. The design conditions where each model is most useful will be summarized as part of the analysis.

Prior to comparing the results, the experimentally measured initial and inlet conditions were input into the analytical model. The mass flow rate and pressure were taken as averages from each experimental run, and an effective melting and freezing temperature defined in the finite difference model validation were used as inputs. Lastly, the effective properties and conductivity of the PCC composite were also used for the analytical model.

6.2.1 Comparison of the Analytical and Finite Difference Models

Comparison of the discharge rate for the condenser and evaporator baseline case provides some insight into where the analytical model fails. The results are presented in Figure 6.20.

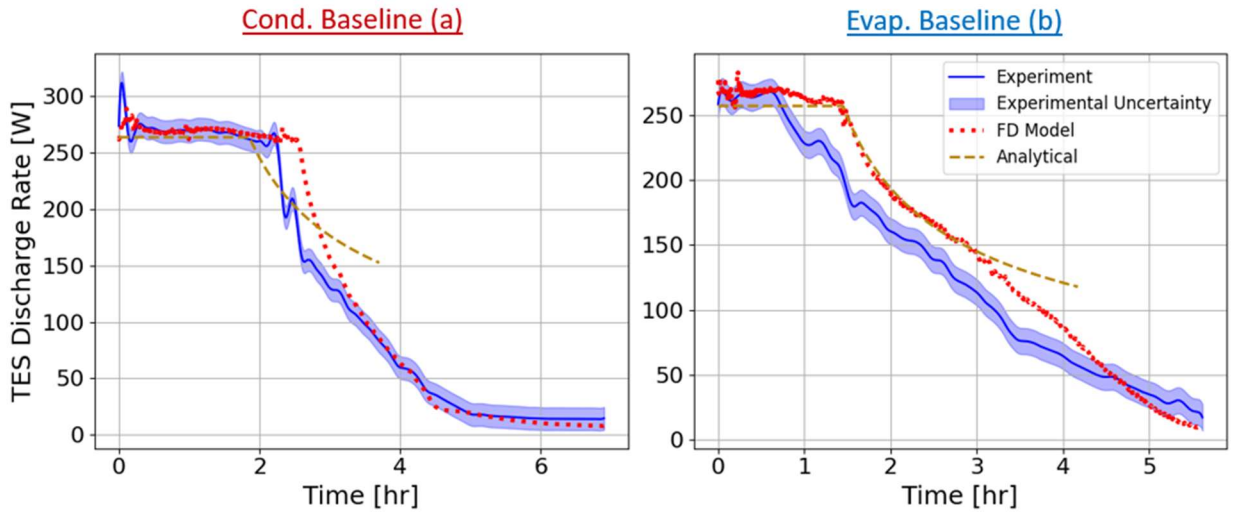

Figure 6.20: The discharge rate predictions for both models compared to the experimental baseline results for the (a) condenser and (b) evaporator.

The condenser baseline analytical prediction agrees with the experiment and finite difference model initially but doesn't predict the onset of the constant power region accurately. Additionally, in the condenser region the model fails to capture the trend in the varying power region. However, given the low complexity of the model, it's surprising how well it predicts the discharge rate. The evaporator baseline analytical prediction has a few similarities. It predicts the magnitude of the heat transfer in the constant power region correctly, but fails to predict the onset of the varying power region. However, the analytical and finite difference predictions of onset of the varying power region match, which is reassuring. Each model fails to predict the onset of the varying power region because the material properties used in each model do not perfectly reflect the freezing observed in the experiment or by NETenergy in their 3-layer calorimetry data. In the varying power region, the evaporator analytical condition matches the trend of the experiment and the prediction of the finite difference model until 3 hours when it diverges.

The trends between the condenser and evaporator for all tests provide further evidence of differences in analytical agreement for each mode of operation as seen in Figure 6.21

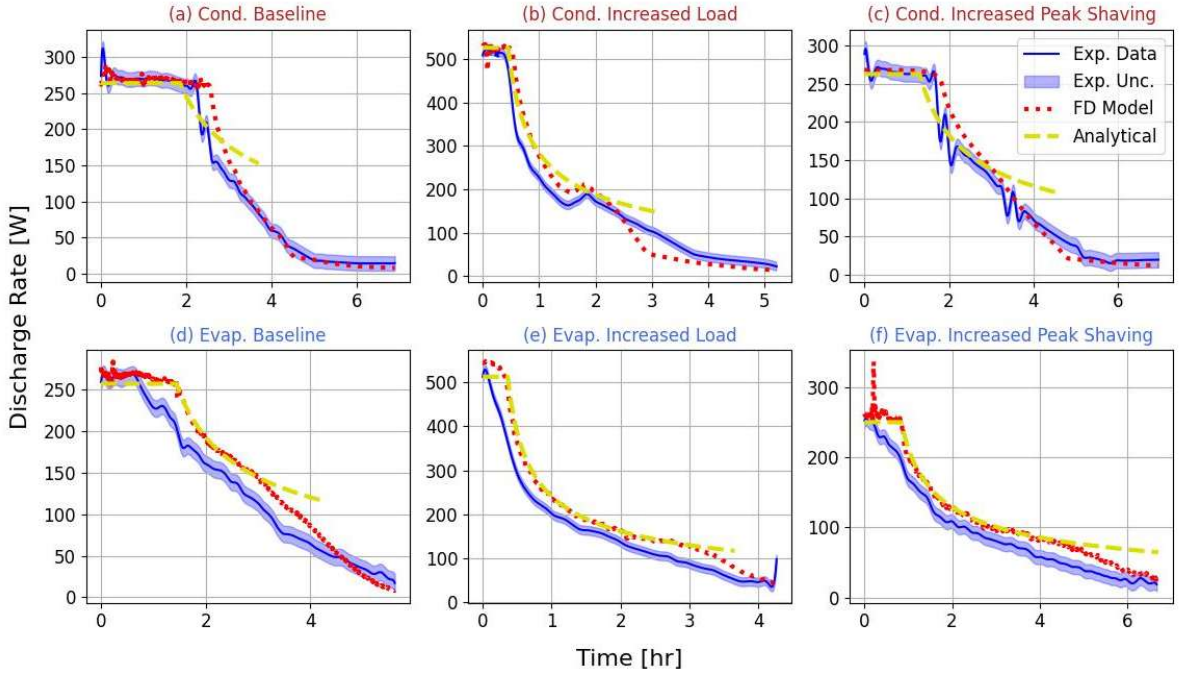

Figure 6.21: A comparison of the models and experimental results discharge rate for all tests. (a)-(c) present condenser and (d)-(f) present the evaporator. (a) and (d) are baseline cases, (b) and (e) are the increased load case, and (c) and (f) are increased peak shaving.

The off-design condenser results show better agreement between the analytical model and experiment than the baseline. The condenser increased load case predicts the onset of the varying power region accurately and only begins to diverge from the experiment and finite difference model at 3 hours - it offers the prediction out of all other condenser cases. The condenser increased peak shaving case also follows the experiment and finite difference model trend well, but fails to predict the onset of the varying power region correctly. In general, the analytical model predicts evaporator performance slightly better than condenser based on comparison to finite difference model predictions. Each evaporator analytical prediction matches the finite difference model's prediction of the onset of the varying power region, and the trend in the constant power region until late in time. Although, each prediction is still slightly off due to non-ideal material properties.

The error in the discharge rate predictions provide insight into the magnitude of disagreement between each model and the experiment as seen in Figure 6.22.

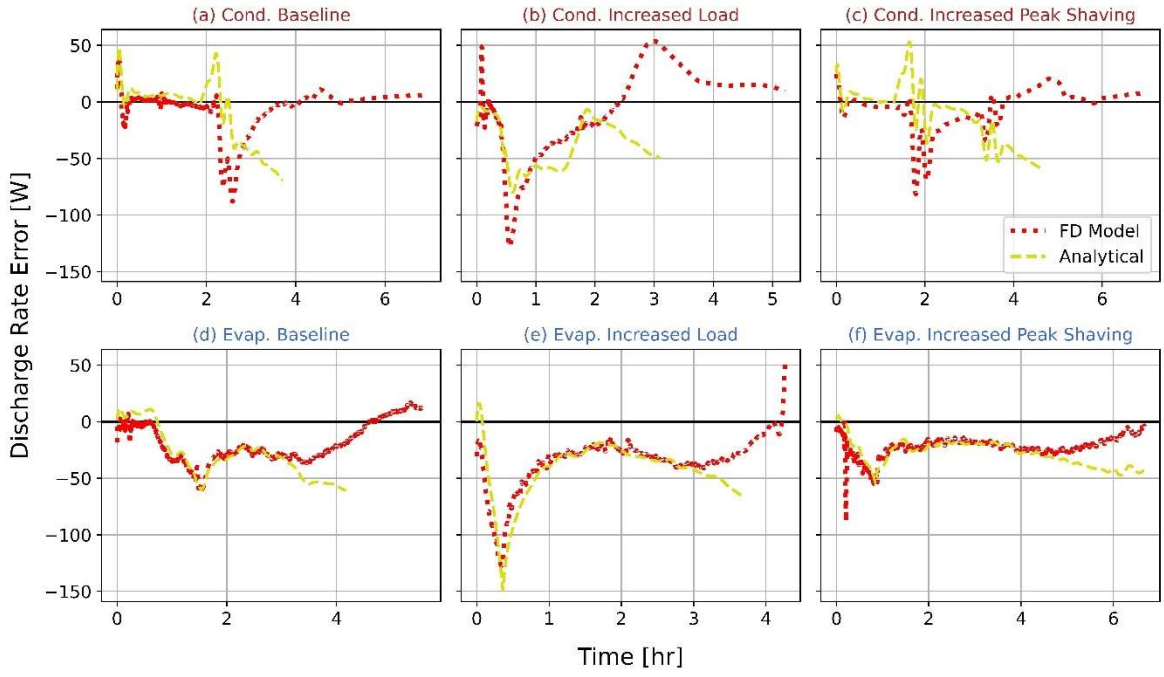

Figure 6.22: The heat error between the experiment and the models. (a)-(c) present condenser and (d)-(f) present the evaporator. (a) and (d) are baseline cases, (b) and (e) are the increased load case, and (c) and (f) are increased peak shaving.

The condenser error appears to stay near zero in all cases aside from the increased load case. The condenser increased load case prediction's higher deviation from experimental results is expected based on prior observations in section 6.1 and Chapter 5. The initial deviation in predictions for all cases occurs at the onset of the varying power region. The greatest heat transfer rate error occurs in the evaporator increased load case when the onset of the varying power region occurs. Similar large errors are seen at the same time in the condenser increased load case. In the evaporator increased load case the error gets much better because the models begin to track the trend observed in the experiment. The condenser results have lower error on average than the evaporator aside from the increased load case, as seen in Figure 6.22 and the average error in Table 6.1.

Table 6.1: The average discharge rate error.

		Baseline	Increased Load	Increased Peak Shaving
Condenser	Finite Difference	9.97 W	29.72 W	11.95 W
	Analytical	21.94 W	27.21 W	15.82 W
Evaporator	Finite Difference	21.73 W	35.81 W	22.14 W
	Analytical	28.90 W	51.28 W	25.72 W

The average error in the condenser case is lower because material properties are well understood. In most cases (except the evaporator increased load) the analytical model's average error is within 30 W of the finite difference model, with the maximum analytical model average error being 51.28 W for the evaporator increased load case. The larger error in prediction of the onset of varying power has a strong effect on the evaporator increased load case. The maximum error for each case is documented in Table 6.2.

Table 6.2: The maximum discharge rate error.

		Baseline	Increased Load	Increased Peak Shaving
Condenser	Finite Difference	87.97 W	127.86 W	81.26 W
	Analytical	69.53 W	79.99 W	58.78 W
Evaporator	Finite Difference	60.64 W	127.27 W	88.47 W
	Analytical	60.74 W	148.66 W	53.87 W

The finite difference model has the largest error in the condenser case, but the analytical model has the worst error in the evaporator case. The magnitude of the error increases due to the increase in mass flow rate, which also increases the maximum possible heat transfer rate in the heat

exchanger. In general, the analytical and finite difference model's maximum error is similar in each case.

Analysis of the measured discharged energy doesn't reveal significant additional insights and truncates error. The predicted discharged energy for each test is presented in Figure 6.23.

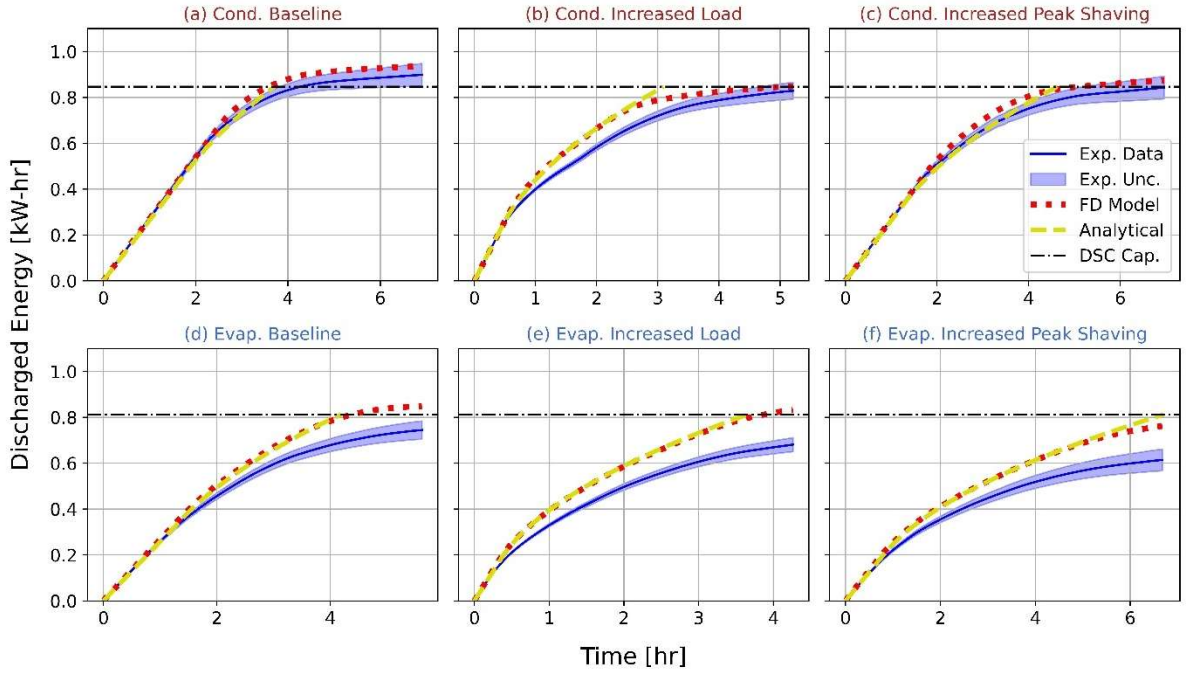

Figure 6.23: All of the results for the discharged energy comparisons between the models and experiment. (a)-(c) present condenser and (d)-(f) present the evaporator. (a) and (d) are baseline cases, (b) and (e) are the increased load case, and (c) and (f) are increased peak shaving.

The results indicate good agreement for the condenser case and poor agreement for the evaporator case, which has been consistent throughout the results for the finite difference and analytical model validation. The discharged energy is calculated via integration, which truncates the error and makes it difficult to see where the models break down relative to one other. So, if the goal is to predict state of charge for a constant inlet condition, the results indicate really good agreement. However, actual TES HX operation will likely partially charge and discharge the unit based on optimal benefits for social, economic, and carbon emissions, which could see a variety of differing drive cycles from the conditions tested. Therefore, predicting the instantaneous heat transfer rate

is a better measure of the error and discharged energy error is not discussed. Results for discharged energy percent error are included in Appendix M for completeness.

To provide a sanity check on each model's ability to predict discharge rate and energy discharged the capacity of the model and experiment were compared. The error in the capacity for each test is presented in Table 6.3.

Table 6.3: The maximum error in the capacity for each test and model.

		Baseline	Increased Load	Increased Peak Shaving
Condenser	Finite Difference	4.15%	2.35%	3.71%
	Analytical	9.16%	2.11%	0.37%
Evaporator	Finite Difference	13.99%	22.13%	24.03%
	Analytical	9.16%	19.23%	32.27%

Table 6.3 shows low error for the condenser, below 10% for all models. The maximum error for the condenser was 4.15% for the finite difference model and 9.16% for the analytical model, both occurring in the baseline case. The evaporator has consistently higher error because it's material inputs don't perfectly match it's physical behavior (hysteresis) so errors as large as 32.27% are not concerning, which is the maximum error the analytical model sees. The finite difference model has maximum evaporator final capacity error of 24.03%. Both occur for the increased peak shaving case. The error for the increased peak shaving is probably higher because it finishes at a higher temperature than the baseline and increased load, which has a significant effect on the measured discharged energy as discussed in Chapter 4.

The analytical and finite difference model predict similar test finish times. The analytical model reached full discharge when the phase front reached the full thickness of the PCC slab. In contrast the finite difference model's full discharge time was determined in the same fashion as

the experiment – when the heat transfer rate was equal to 50 W. The predicted discharge times are presented in Table 6.4.

Table 6.4: The predicted full discharge time for each experiment and model.

		Baseline	Increased Load	Increased Peak Shaving
Condenser	Finite Difference	4.22 hrs	2.98 hrs	4.31 hrs
	Analytical	3.71 hrs	3.10 hrs	4.62 hrs
Evaporator	Finite Difference	4.56 hrs	4.10 hrs	5.50 hrs
	Analytical	4.19 hrs	3.66 hrs	6.71 hrs

In the condenser case the finite difference model and analytical model predict similar values for all cases. The largest difference in prediction is 0.51 hrs for the baseline and the smallest is 0.12 hrs for the increased load case. The evaporator results have larger discrepancies with a maximum difference in analytical and finite difference predictions of 1.21 hrs for the increased load case, and a minimum of 0.44 hrs for the baseline case. The difference is much larger for the increased peak shaving case because high saturation temperature significantly lowers the energy available for the PCM TES HX to discharge as discussed in Chapter 5.

Predicting the discharge time is a key performance metric for the analytical model because the goal of the simulation problem is to predict discharge time given a PCC slab thickness, while the goal of the design problem is to predict a slab thickness given a desired discharge time. So, predicting the discharge time in this experiment serves as a primary validation metric. The error of each model's discharge time prediction is included in Table 6.5.

Table 6.5: The percent error in predicted discharge time for each model relative to the experiment and model.

		Baseline	Increased Load	Increased Peak Shaving
Condenser	Finite Difference	-1.11%	-20.45%	-5.48%
	Analytical	-13.10%	-17.36%	1.39%
Evaporator	Finite Difference	3.81%	11.30%	23.98%
	Analytical	4.39%	0.73%	51.22%

The condenser baseline case has the lowest finite difference model prediction error, -1.11%, which is also the lowest global error for the finite difference model's discharge time predictions. Meanwhile, the increased peak shaving case has lowest analytical model percent error for the condenser, 1.39%. The increased load case sees the maximum error for each model's condenser predictions. The evaporator analytical predictions are of similar magnitude to the condenser for every case except the increased peak shaving case. The evaporator peak shaving case sees the maximum discharge error because it doesn't go to as low of a temperature as the other evaporator cases, as already discussed in this chapter and Chapter 5. The evaporator analytical predictions have a minimum error of 0.73% for the increased load case, which makes sense given how well it follows the heat transfer rate trend in Figure 6.21. Meanwhile, the finite difference model has a minimum discharge time error prediction of 3.81% for the baseline case. Discharge time predictions by the finite difference model are in general pretty accurate, but not the best way to characterize the model because the model can accurately predict the heat transfer rate beyond the full discharge time predicted. The analytical model doesn't have this capability because it cannot predict sensible heat transfer in the PCC.

6.2.2 Usefulness of the Models

A few clear trends were observed in the analytical model and finite difference model comparison that highlight when the error in the analytical model is significant. The errors were prediction of:

- The onset of the varying power region in all cases
- The trend within the varying power region for the condenser baseline case
- The magnitude of discharge rate and trend late in time in each case
- The discharge time in the condenser increased load case and evaporator peak shaving case

The errors in the prediction of the onset of the varying power region in the evaporator do not represent pitfalls of the analytical model because the analytical predictions match the evaporator predictions in this case. However, the prediction of the onset of the varying power region in the condenser does present pitfalls in the analytical model because the errors are different than those which the finite difference model predicts. The analytical model also fails to predict the trend of the discharge rate in the baseline case, which again represents a breakdown of the assumptions used to derive the analytical model. The error in magnitude and trend of discharge rate late in time represents a pitfall of the analytical model as well because the finite difference model doesn't follow this trend. Finally, the errors in discharge time prediction reflect fundamental issues in the freezing material properties used, and increased load initial conditions (although that doesn't capture the full picture and additional investigation would be needed to do so). Each of these errors have been discussed at length in this chapter and Chapter 5, and don't represent failures of either model.

The inability of the analytical model to predict late time discharge rate can be explained by the heat transfer regime present in the PCM slab, because the analytical model doesn't capture

sensible heating or cooling. Figure 6.24 plots the temperature field predicted by the finite difference model to visualize this for the condenser baseline and evaporator baseline – plots of temperature fields for all tests are included in Appendix N.

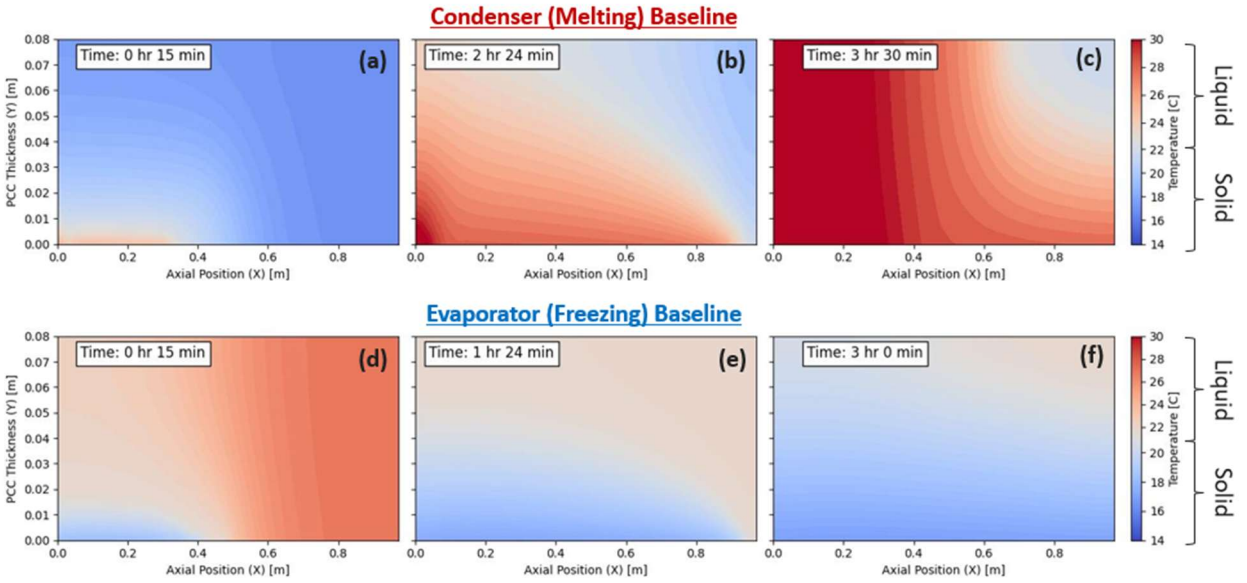

Figure 6.24: The temperature field in the PCC slab predicted by the finite difference model for the condenser in (a)-(c), and the evaporator in (d)-(e). The times represented are the same as those in the microchannel surface plots. The plane pictured is the XY plane. (a) and (d) represent the initial discharge, (b) and (e) represent the final discharge, and (c) and (f) represent a state late in time. (b) and (f) show the onset of sensible heating.

As the melt front progresses in time for the condenser baseline, a sensible region appears upstream in the HX late in time indicated by the large presence of liquid. The same thing happens in the evaporator, however, which is indicated by the large presence of solid. However, it's a bit inaccurate to call the heat transfer regime late in time in the evaporator sensible because phase change is still ongoing according Texas A&M's melting DSC results and NETenergy's freezing 3-layer calorimetry results. The analytical model predicts discharge is still ongoing at each of these times as seen in Table 6.4 and Figure 6.21. Therefore, the error late in time is explained by the difference in heat transfer regimes modeled in the analytical model and present in the finite difference model and experiment. The experiment also shows evidence of sensible heating at these times as indicated by the thermocouples on the top of the PCC slab. The analytical model assumes

phase change is always occurring and terminates its prediction when phase change ceases as discussed earlier in this chapter and in Chapter 3.

The inability of the model to predict the onset of the varying power region in the condenser and track the trend in heat transfer rate in the condenser increased load case can be explained by the direction the melt front travels. This can be visualized by plotting the temperature field in the finite difference model at the onset of the varying power region as seen in Figure 6.25.

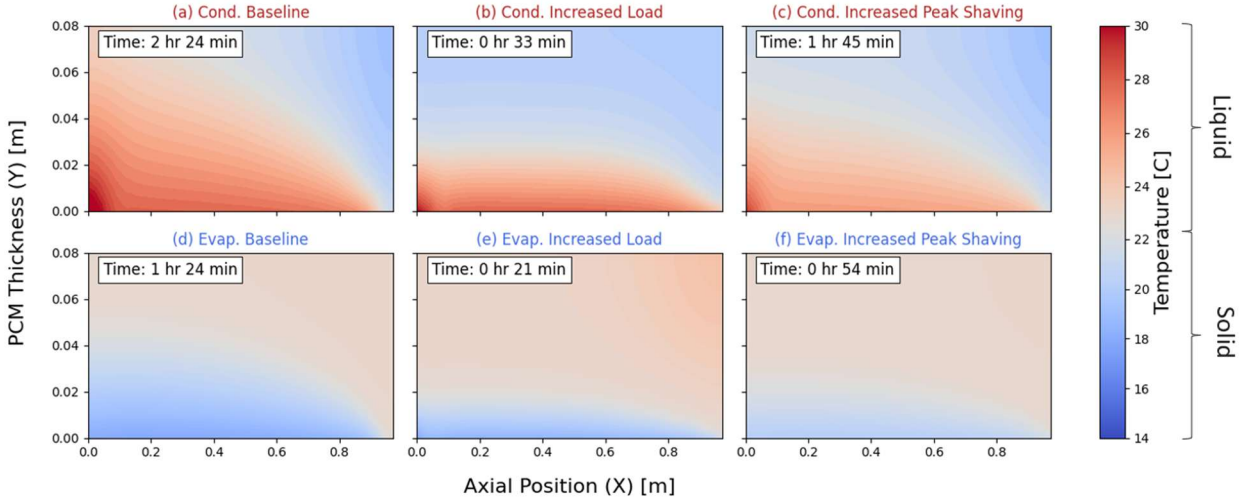

Figure 6.25:The prediction of the temperature field by the finite difference model at the onset of the varying power region for each test. (a)-(c) present condenser and (d)-(f) present the evaporator. (a) and (d) are baseline cases, (b) and (e) are the increased load case, and (c) and (f) are increased peak shaving.

Figure 6.25 shows that the baseline case moves diagonally, while the increased load moves vertically, and increased peak shaving case is somewhere in between – diagonal, but not as diagonal as the baseline. In fact, the condenser baseline moves so dominantly diagonally that it's sensible heat transfer region begins at the same time as it's varying power region begins. This explains why the condenser baseline varying power trend doesn't match the experiment or finite difference model. The analytical model derivation assumes a vertical phase front so the condenser baseline, condenser increased peak shaving, and evaporator baseline case violates this based on the plots in Figure 6.25. This occurs to some degree in the increased peak shaving case as well,

explaining why both cases have an error when predicting the start of the varying power region. The condenser increased load analytical prediction of the onset of varying power is as far off as the other condenser cases, but causes significant error because the maximum heat transfer rate is large for the higher flow rate cases. The magnitude of diagonal movement for the evaporator cases isn't as large as the condenser, which explains why the finite difference model and analytical model match well until the sensible heat transfer regime begins for evaporator mode.

The analytical model's assumptions break down in several cases, but the model could be useful for design problems in these cases based on the discharge time error in Table 6.5. The on-design conditions discharge time prediction has a maximum error of -13.1%. Errors less than +/-10% would be ideal, however, -13.1% is very close so it's still possible this model could be useful for design. Therefore, the use of the model is up to the tolerance of design firm for the extra 3.1% error. If designers are not ok with large errors they could use the analytical model as a starting point while using a detailed, but more accurate finite difference model. In this work the finite difference model had a maximum on-design (baseline) discharge time error of 3.81%, so it was very high accuracy. Currently the analytical model can only predict constant inlet condition experimental results, which limits its usability for load shaving and shifting PCM TES HX's discussed in this work. Further work is needed to upgrade the analytical model to predict constant power operation, where it will likely be more accurate. This validation makes the case for making that upgrade since the analytical model's error relative to the experiment is tolerable, and near the finite difference model error in some cases.

The analytical model should not be used as a standalone simulation tool because it does not accurately predict the heat transfer rate or discharge time when the assumptions fail. Instead, it should be used as a first step before building or using a finite difference model. If a diagonal phase

front is present in a device, it would be preferable to use the finite difference model as a design tool. However, if the phase front is horizontal then the analytical model does a good job and could be used to predict the thickness of a PCC slab if the model user can tolerate the chance of model errors as high as 148.66 W at the onset of the varying power region.

The analytical model would likely not be as useful for debugging material property issues because it does not provide temperature distribution predictions. Errors for sensible heating are also present. These errors manifest in the discharge time error, which can be as large as -17.36%, when the increased peak shaving case is not considered. Prior solutions for single phase fluids included the sensible heat transfer region in the PCC, and could be combined with the approach developed in this work for increased accuracy for PCMs where the sensible region takes up a larger portion of the capacity [71], [72].

Run time is one obvious advantage the analytical model currently has over the finite difference model, but the sacrifices in accuracy discussed outweigh the benefits in some cases. To predict more complex behavior quickly the finite difference model could likely be packaged to run much faster than it does, because it's not compiled and solves in less than 2 minutes in some cases. Writing the model in a compiled language and optimizing the code further for run time could make the model very accessible to engineers outside of academia, but the geometry will be limited. Practicing engineers in HVAC R&D firms and building construction companies could use the finite difference model in a compiled state as calculator for simulation-based sensitivity studies that could build a design space for them to make decisions based off of rather than solving a design problem. Reformulating the finite difference model to solve a design problem could also be done. However, reformulation to solve for an optimal point in the design space could increase run time significantly.

In summary the following recommendations are made:

- **Design Problems:** The analytical model can be used as a design tool in lieu of the finite difference model for constant pressure operation, but needs upgrades to be used for constant power operation. The error in on-design predictions of full discharge time were low enough to corroborate this, and the finite difference model doesn't offer further benefits.
- **Simulation Problems**: In simulation problems the analytical model error is small enough to use it as a sanity check for the finite difference model. It's comparable in some cases, but the finite difference model can help debug non-ideal material properties through temperature distribution predictions and therefore is recommended for simulation problems.

Chapter 7: Conclusion

This thesis accomplished several things by answering the research questions posed in Chapter 1:

1. *How is this PCM TES HX original, and how does it perform?*
2. *What computational complexity is needed to characterize PCM TES HX devices with evaporating or condensing heat transfer fluids?*

The literature review in Chapter 2 demonstrated the novelty of the PCM TES HX built as part of this work, and the analytical model validation effort. The literature review also summarized how PCM TES HX's have been integrated in vapor compression cycles in the past. Additionally, building the experimental facility and deriving the analytical model were significant accomplishments detailed in Chapter 2 and 3 respectively. Finally, the experimental results (Chapter 5), and model complexity study (Chapter 6) show the general behavior of the proposed PCM TES HX, and point towards key future work to improve the design.

To determine the novelty of the heat exchanger tested a literature review of PCM TES HX's in vapor compression cycles was conducted in Chapter 2. The literature review in Chapter 2 demonstrated that PCM TES HX's have been integrated with two phase fluids before, but never for a system that can actively charge and discharge. This work did not demonstrate charging operation in condenser or evaporator mode, but the experimental and modeling findings can easily be extended to include charging. Charging would likely occur over a longer period than the discharge cycles tested, which occur over four hours. Admittedly many of the findings in other work could be extended to actively charged systems, so the novelty of the device itself is minor. Still, the exact heat exchanger geometry and materials have not been tested before in literature at this scale with a two-phase fluid to the best of the author's knowledge.

The results in Chapter 5 also addressed the first research question by demonstrating the performance of the PCM TES HX. The analysis of the measurements showed that the PCM TES HX bench scale prototype built can achieve a 4-hour discharge, which would be essential for load shaving and shifting. The baseline case achieved a full discharge time of 4.26 hours, while the evaporator achieved a time of 4.39 hours for constant inlet conditions designed to mimic the constant power conditions that will actually be present for a real device. Therefore, it seems like the bench scale device could scale and achieve similar results given the modular TES device design discussed in Chapter 1. However, non-ideal material properties were observed, namely a reduction in transition temperature and heat discharge while freezing the PCM, which was the result of hysteresis. The capacity reduced from a theoretical value of 0.846 kWhr to as low as 0.614 kWhr in the increased peak shaving case. Testing lower saturation temperature conditions illustrated that more capacity was available below the target temperature – 18°C. A capacity of 0.744 kW-hr was observed at a final temperature of 17.65°C., while a capacity of 0.77 kW-hr was observed at a final temperature of 15.1°C.

The hysteresis observed presents a barrier to commercialization that needs to be resolved. Modeling and experiments need to look at partially charging and discharging these devices for realistic operation cycles (drive cycles) to determine if hysteresis presents a barrier to operation. Hysteresis may present a barrier to the degree the PCM TES HX's can shift loads in heating operation. Therefore, testing for realistic drive cycles is left as future work. It would be nice to conduct these tests for a bench scale device on the facility built as part of this work. However, the controls for the experiment discussed in Appendix G and H need to be automated for this to be achievable. Automation is likely possible but poses some significant challenges.

The model validation of the device in Chapter 6 also identified some fundamental issues with experimental results. First, the thermal conductivity of the PCC seemed to be lower than initially anticipated, likely due to the soaking procedure. Based on model agreement, the thermal conductivity seems to be around 4 W/m-K parallel to the compression direction, a ~56% decrease from the expected value of 9 W/m-K. The hysteresis was also investigated further in this section. The enthalpy vs. temperature curve was tuned based on the experimental results to account for the hysteresis effects. Future work could refine the enthalpy-temperature relationship during freezing for PT23, potentially using the 3-layer calorimetry data shown in Figure 5.20. Lastly, an issue was presented in Chapter 5 and investigated in Chapter 6 relative to the condenser increased load PCC initial condition. The temperature was higher than the target (19.75 vs. 18°C). It was thought that this caused poor agreement between the models and experiments. However, adjusting the finite difference model's initial condition showed that a deviation of +/- 1.5°C did not explain the deviation in capacity, so there is still more investigation needed to rectify this issue.

Chapter 6 also addressed the second research question, which focused on the modeling detail needed to select the PCC slab thickness by validating and comparing the analytical and finite difference models. Ultimately, the analytical model did well for its relative simplicity. The finite difference model's max average error of 35.81 W in the evaporator increased load case and 9.97 W in the condenser baseline case. Both finite difference errors are of similar magnitude to the maximum and minimum discharge rate average error of the analytical model. The analytical model predicted the average heat transfer with an average discharge rate error as low as 15.52 W (in the increased peak shaving case), and as high as 52.28 W. The high error occurred for the evaporator increased load case. The maximum heat transfer error for the finite difference model and analytical model were much larger than their averages, due to experimental issues in the condenser and

evaporator increased load case, as high as 148.66 W in the increased load case. The analytical model also predicted the full discharge time well, with a minimum error of 0.73% for the evaporator increased load case and a maximum of 51.22%, which occurred for the evaporator increased peak shaving case. The discharge time error for the evaporator increased peak shaving case increased in value due to hysteresis and the next largest value was 17.36%, which shows the error was pretty low. The maximum absolute error in the on-design discharge time prediction was 13.1%, which allows the analytical to be used for design for constant inlet conditions. Further work is needed to extend the analytical model to constant power conditions, which are more realistic for vapor compression cycles.

To investigate the second research question in greater detail Chapter 6 discusses when the analytical model fails, identifying two occasions where assumptions used to derive the model were invalid. First, errors were observed late in time for analytical model heat transfer rate in all cases due to sensible heat transfer in the PCC slab. The analytical model assumes that only phase change occurs in the PCC slab and terminates the model when phase change ceases (when the phase front in the model reaches the total thickness of the slab simulated), which is also how the prediction for full discharge time is made. Therefore, the analytical model doesn't capture sensible heat transfer in the PCC, which occurs in the experiment. Furthermore, the analytical models assumes that the phase front moves vertically, which isn't the case for a few of the condenser tests. Namely, the condenser baseline and peak shaving case. This causes errors in the prediction of the onset of the varying power region and the analytical model discharge rate trend, especially for the condenser baseline. The finite difference model also captures vertically traveling phase front. Therefore, the finite difference model should be used if these two features are relevant to the user.

Ultimately, the analytical model isn't a full replacement for the finite difference model as it stands. The analytical model cannot predict temperature distribution it cannot be used for debugging non-ideal material properties. Furthermore, the analytical model fails to predict sensible heat transfer, which leads to errors as high as 17.36% for final discharge time predictions in off design cases. Thus, the analytical model isn't recommended for simulation problems. For simulation problems, it's suggested to use the analytical model as a hand calculation in conjunction with more detailed methods like the finite difference model discussed in this work. This is typical practice in computational design. Additionally, if packaged and compiled the finite difference model could likely run much faster than it does and be used as a calculator for design sensitivity studies by engineers outside of academia. However, turning the finite difference model into a design problem could greatly increase the simulation time, and would be future work.

Although lots of progress was made by answering the research questions and developing the methods associated with this work there is further investigation needed to rectify some issues. Future work includes the following possible directions:

- Improving microchannel header design distribution performance
- Upgrading the experimental facility for constant power operation
- Doing model validation for constant power operation
- Upgrading the experimental facility for realistic operation cycles
- Doing model validation for realistic operating cycles
- Testing and modeling other PCMs and PCCs with these modeling frameworks
- Improving model agreement for hysteresis
- Coming up with a first principles prediction of hysteresis
- Improving the analytical model in sensible regions and for diagonal phase fronts

- Packaging the finite difference model into a compiled language
- Reformulating the finite difference model for design problems

References

[1] Lazard, “Levelized Cost of Energy Plus Report June 2025.” Lazard, June 2025.

[2] “Electricity generation, capacity, and sales in the United States - U.S. Energy Information Administration (EIA)”.

[3] S. Forrester, G. Barbose, and C. A. Miller, “Private vs. public value of U.S. residential battery storage operated for solar self-consumption,” *iScience*, vol. 25, no. 8, p. 104714, Aug. 2022, doi: 10.1016/j.isci.2022.104714.

[4] “NREL Researchers Reveal How Buildings Across United States Do—and Could—Use Energy | NREL.” Accessed: June 10, 2025. [Online]. Available: https://www.nrel.gov/news/detail/features/2023/nrel-researchers-reveal-how-buildings-across-the-united-states-do-and-could-use-energy

[5] Department of Energy (DOE), “Findings from Storage Innovations 2030: Thermal Energy Storage,” July 2023.

[6] EPA, “Inventory of U.S. Greenhouse Gas Emissions and Sinks: 1990-2022.” U.S. Environmental Protection Agency, 2024. [Online]. Available: https://www.epa.gov/ghgemissions/inventory-us-greenhouse-gas-emissions-and-sinks-1990-2022

[7] A. Odukomaiya *et al.*, “Addressing energy storage needs at lower cost *via* on-site thermal energy storage in buildings,” *Energy Environ. Sci.*, vol. 14, no. 10, pp. 5315–5329, 2021, doi: 10.1039/D1EE01992A.

[8] “Thermochemical Energy Storage: The next generation thermal batteries? – SINTEF Blog”.

[9] X. Zhang *et al.*, “Values of latent heat and thermochemical energy storage technologies in low-carbon energy systems: Whole system approach,” *J. Energy Storage*, vol. 50, p. 104126, June 2022, doi: 10.1016/j.est.2022.104126.

[10] N. James, R. Huang, J. Woods, and E. Kozubal, “Investigation of ventilation-coupled high energy density sensible thermal energy storage,” *Appl. Energy*, vol. 387, p. 125576, June 2025, doi: 10.1016/j.apenergy.2025.125576.

[11] C. K. Ho and A. Ambrosini, “CHAPTER 12 THERMAL ENERGY STORAGE TECHNOLOGIES,” *Therm. Energy Storage*.

[12] “An innovative ‘ice battery’ system is being used to cool buildings and lower energy costs - CBS News”.

[13] D. Guittet, E. Bonnema, M. S. Mitchell, A. Mahvi, and J. Woods, “Ice Storage Model-Predictive Control in an Office Building With Pv: Scenario, Error and Sensitivity Analysis,” 2025, *SSRN*. doi: 10.2139/ssrn.5145271.

[14] D. Ibbotson, S. Ahmed, and P. J. Shamberger, “Mutability of Nucleation Particles in Reactive Salt Hydrate Phase Change Materials,” *J. Phys. Chem. C*, vol. 128, no. 41, pp. 17282–17290, Oct. 2024, doi: 10.1021/acs.jpcc.4c03913.

[15] J. Woods, A. Mahvi, A. Goyal, E. Kozubal, A. Odukomaiya, and R. Jackson, "Rate capability and Ragone plots for phase change thermal energy storage," *Nat. Energy*, vol. 6, no. 3, pp. 295–302, Feb. 2021, doi: 10.1038/s41560-021-00778-w.

[16] N. Zaleski, E. Barbosa, and A. K. Menon, "Evaluating the potential of thermochemical energy storage to decarbonize buildings: A case study in the United States," *MRS Energy Sustain.*, vol. 12, no. 1, pp. 2–13, Nov. 2024, doi: 10.1557/s43581-024-00120-3.

[17] Y. Zeng *et al.*, "Open-cycle thermochemical energy storage for building space heating: Practical system configurations and effective energy density," *Appl. Energy*, vol. 376, p. 124218, Dec. 2024, doi: 10.1016/j.apenergy.2024.124218.

[18] Y. Galazutdinova, R.-J. Clark, S. Al-Hallaj, S. Kaur, and M. Farid, "New Thermochemical Salt Hydrate System for Energy Storage in Buildings," *Energies*, vol. 17, no. 20, p. 5228, Oct. 2024, doi: 10.3390/en17205228.

[19] Y. Song, D. Lilley, D. Chalise, S. Kaur, and R. S. Prasher, "Predicting supercooling of phase change materials in arbitrarily varying conditions," *Cell Rep. Phys. Sci.*, vol. 4, no. 6, p. 101462, June 2023, doi: 10.1016/j.xcrp.2023.101462.

[20] J. Shin, M. R. Morrell, E. Barbosa, A. K. Menon, and M. T. McDowell, "Investigating structural and morphological transformations of strontium chloride for thermochemical energy storage," *J. Mater. Chem. A*, p. 10.1039.D5TA02326B, 2025, doi: 10.1039/D5TA02326B.

[21] "Keeping your (food) cool: From ice harvesting to electric refrigeration | National Museum of American History".

[22] Sapir, "11 Madison Avenue." [Online]. Available: https://www.sapir.com/11-madison

[23] T. B. Freeman *et al.*, "Advanced Materials and Additive Manufacturing for Phase Change Thermal Energy Storage and Management: A Review," *Adv. Energy Mater.*, vol. 13, no. 24, p. 2204208, June 2023, doi: 10.1002/aenm.202204208.

[24] "Ice Blocks Help New York Office Cut Energy Bill : NPR".

[25] S. Bista, S. E. Hosseini, E. Owens, and G. Phillips, "Performance improvement and energy consumption reduction in refrigeration systems using phase change material (PCM)," *Appl. Therm. Eng.*, vol. 142, pp. 723–735, Sept. 2018, doi: 10.1016/j.applthermaleng.2018.07.068.

[26] M. Visek, C. M. Joppolo, L. Molinaroli, and A. Olivani, "Advanced sequential dual evaporator domestic refrigerator/freezer: System energy optimization," *Int. J. Refrig.*, vol. 43, pp. 71–79, July 2014, doi: 10.1016/j.ijrefrig.2014.03.001.

[27] R. Elarem, S. Mellouli, E. Abhilash, and A. Jemni, "Performance analysis of a household refrigerator integrating a PCM heat exchanger," *Appl. Therm. Eng.*, vol. 125, pp. 1320–1333, Oct. 2017, doi: 10.1016/j.applthermaleng.2017.07.113.

[28] M. Rahimi, A. A. Ranjbar, and M. J. Hosseini, "Experimental investigation on PCM/fin slab incorporation in a evaporator side of a household refrigerator," *Energy Rep.*, vol. 10, pp. 407–418, Nov. 2023, doi: 10.1016/j.egyr.2023.06.053.

[29] P. Arumugam, V. Ramalingam, and P. Vellaichamy, "Effective PCM, insulation, natural and/or night ventilation techniques to enhance the thermal performance of buildings located

in various climates – A review," *Energy Build.*, vol. 258, p. 111840, Mar. 2022, doi: 10.1016/j.enbuild.2022.111840.

[30] W.-L. Cheng, B.-J. Mei, Y.-N. Liu, Y.-H. Huang, and X.-D. Yuan, "A novel household refrigerator with shape-stabilized PCM (Phase Change Material) heat storage condensers: An experimental investigation," *Energy*, vol. 36, no. 10, pp. 5797–5804, Oct. 2011, doi: 10.1016/j.energy.2011.08.050.

[31] G. Sonnenrein, A. Elsner, E. Baumhögger, A. Morbach, K. Fieback, and J. Vrabec, "Reducing the power consumption of household refrigerators through the integration of latent heat storage elements in wire-and-tube condensers," *Int. J. Refrig.*, vol. 51, pp. 154–160, Mar. 2015, doi: 10.1016/j.ijrefrig.2014.12.011.

[32] A.-J. N. Khalifa, "Natural convective heat transfer coeÅcient ± a review I. Isolated vertical and horizontal surfaces".

[33] A. Gönül, Ö. Ağra, Ş. Ö. Atayılmaz, H. Demir, M. K. Sevindir, and İ. Teke, "Experimental and numerical investigation of air-side forced convection on wire-on-tube condensers," *Int. J. Therm. Sci.*, vol. 151, p. 106241, May 2020, doi: 10.1016/j.ijthermalsci.2019.106241.

[34] M. Harun-Or-Rashid, M. T. Hasan, T. B. Alam, and S. Hossain, "Energy efficient refrigeration system using latent heat storage, PCM," *Int. J. Thermofluids*, vol. 23, p. 100717, Aug. 2024, doi: 10.1016/j.ijft.2024.100717.

[35] W. Cheng, M. Ding, X. Yuan, and B.-C. Han, "Analysis of energy saving performance for household refrigerator with thermal storage of condenser and evaporator," *Energy Convers. Manag.*, vol. 132, pp. 180–188, Jan. 2017, doi: 10.1016/j.enconman.2016.11.029.

[36] D. Dandotiya and N. D. Banker, "Energy Efficiency Improvement of a Refrigerator Integrated With Phase Change Material-Based Condenser," *J. Energy Resour. Technol.*, vol. 143, no. 8, p. 082105, Aug. 2021, doi: 10.1115/1.4048871.

[37] L. S. Rodrigues, D. L. Marques, J. A. Ferreira, V. A. F. Costa, N. D. Martins, and F. J. Neto Da Silva, "The Load Shifting Potential of Domestic Refrigerators in Smart Grids: A Comprehensive Review," *Energies*, vol. 15, no. 20, p. 7666, Oct. 2022, doi: 10.3390/en15207666.

[38] R. Barzin, J. J. J. Chen, B. R. Young, and M. M. Farid, "Peak load shifting with energy storage and price-based control system," *Energy*, vol. 92, pp. 505–514, Dec. 2015, doi: 10.1016/j.energy.2015.05.144.

[39] J. Taneja, K. Lutz, and D. Culler, "The impact of flexible loads in increasingly renewable grids," in *2013 IEEE International Conference on Smart Grid Communications (SmartGridComm)*, Vancouver, BC, Canada: IEEE, Oct. 2013, pp. 265–270. doi: 10.1109/SmartGridComm.2013.6687968.

[40] P. Promoppatum, S.-C. Yao, T. Hultz, and D. Agee, "Experimental and numerical investigation of the cross-flow PCM heat exchanger for the energy saving of building HVAC," *Energy Build.*, vol. 138, pp. 468–478, Mar. 2017, doi: 10.1016/j.enbuild.2016.12.043.

[41] Y. Hu, P. K. Heiselberg, C. Drivsholm, A. S. Søvsø, P. J. C. Vogler-Finck, and K. Kronby, "Experimental and numerical study of PCM storage integrated with HVAC system for energy

flexibility," *Energy Build.*, vol. 255, p. 111651, Jan. 2022, doi: 10.1016/j.enbuild.2021.111651.

[42] P. T. Sardari, D. Giddings, D. Grant, M. Gillott, and G. S. Walker, "Discharge of a composite metal foam/phase change material to air heat exchanger for a domestic thermal storage unit," *Renew. Energy*, vol. 148, pp. 987–1001, Apr. 2020, doi: 10.1016/j.renene.2019.10.084.

[43] A. Maccarini, G. Hultmark, N. C. Bergsøe, and A. Afshari, "Free cooling potential of a PCM-based heat exchanger coupled with a novel HVAC system for simultaneous heating and cooling of buildings," *Sustain. Cities Soc.*, vol. 42, pp. 384–395, Oct. 2018, doi: 10.1016/j.scs.2018.06.016.

[44] A. Aljehani, L. C. Nitsche, and S. Al-Hallaj, "Numerical modeling of transient heat transfer in a phase change composite thermal energy storage (PCC-TES) system for air conditioning applications," *Appl. Therm. Eng.*, vol. 164, p. 114522, Jan. 2020, doi: 10.1016/j.applthermaleng.2019.114522.

[45] A. Goyal, E. Kozubal, J. Woods, M. Nofal, and S. Al-Hallaj, "Design and performance evaluation of a dual-circuit thermal energy storage module for air conditioners," *Appl. Energy*, vol. 292, p. 116843, June 2021, doi: 10.1016/j.apenergy.2021.116843.

[46] T. Xiong, G. Liu, S. Huang, G. Yan, and J. Yu, "Two-phase flow distribution in parallel flow mini/micro-channel heat exchangers for refrigeration and heat pump systems: A comprehensive review," *Appl. Therm. Eng.*, vol. 201, p. 117820, Jan. 2022, doi: 10.1016/j.applthermaleng.2021.117820.

[47] M. Kedzierski and L. Lin, "Design of a direct-contact thermal energy storage heat exchanger for the NIST net-zero residential test facility," National Institute of Standards and Technology, Gaithersburg, MD, NIST TN 2104, July 2020. doi: 10.6028/NIST.TN.2104.

[48] M. A. Kedzierski, W. V. Payne, and H. M. Skye, "Thermal energy storage for the NIST net-zero house heat pump," National Institute of Standards and Technology, Gaithersburg, MD, NIST TN 2005, Sept. 2018. doi: 10.6028/NIST.TN.2005.

[49] Y. Qiao, Y. Du, J. Muehlbauer, Y. Hwang, and R. Radermacher, "Experimental study of enhanced PCM exchangers applied in a thermal energy storage system for personal cooling," *Int. J. Refrig.*, vol. 102, pp. 22–34, June 2019, doi: 10.1016/j.ijrefrig.2019.03.006.

[50] R. Dhumane *et al.*, "Improving system performance of a personal conditioning system integrated with thermal storage," *Appl. Therm. Eng.*, vol. 147, pp. 40–51, Jan. 2019, doi: 10.1016/j.applthermaleng.2018.10.004.

[51] J. Ling *et al.*, "Energy savings and thermal comfort evaluation of a novel personal conditioning device," *Energy Build.*, vol. 241, p. 110917, June 2021, doi: 10.1016/j.enbuild.2021.110917.

[52] F. Wang, G. Maidment, J. Missenden, and R. Tozer, "The novel use of phase change materials in refrigeration plant. Part 1: Experimental investigation," *Appl. Therm. Eng.*, vol. 27, no. 17–18, pp. 2893–2901, Dec. 2007, doi: 10.1016/j.applthermaleng.2005.06.011.

[53] F. Wang, G. Maidment, J. Missenden, and R. Tozer, "The novel use of phase change materials in refrigeration plant. Part 2: Dynamic simulation model for the combined system,"

Appl. Therm. Eng., vol. 27, no. 17–18, pp. 2902–2910, Dec. 2007, doi: 10.1016/j.applthermaleng.2005.06.009.

[54] A. Riahi, H. J. Mosleh, S. Kavian, and M. B. Shafii, "Performance analysis and transient simulation of a vapor compression cooling system integrated with phase change material as thermal energy storage for electric peak load shaving," *J. Energy Storage*, vol. 35, p. 102316, Mar. 2021, doi: 10.1016/j.est.2021.102316.

[55] B. K. Choure, T. Alam, and R. Kumar, "A review on heat transfer enhancement techniques for PCM based thermal energy storage system," *J. Energy Storage*, vol. 72, p. 108161, Nov. 2023, doi: 10.1016/j.est.2023.108161.

[56] CALMAC, "CALMAC IceBank Energy Storage Model C."

[57] A. Mahvi, K. P. Shete, A. Odukomaiya, and J. Woods, "Measuring the maximum capacity and thermal resistances in phase-change thermal storage devices," *J. Energy Storage*, vol. 55, p. 105514, Nov. 2022, doi: 10.1016/j.est.2022.105514.

[58] C. Zhao, J. Wang, Y. Sun, S. He, and K. Hooman, "Fin design optimization to enhance PCM melting rate inside a rectangular enclosure," *Appl. Energy*, vol. 321, p. 119368, Sept. 2022, doi: 10.1016/j.apenergy.2022.119368.

[59] B. Fekadu and M. Assaye, "Enhancement of phase change materials melting performance in a rectangular enclosure under different inclination angle of fins," *Case Stud. Therm. Eng.*, vol. 25, p. 100968, June 2021, doi: 10.1016/j.csite.2021.100968.

[60] T. Wang and X. Qian, "Topology optimization of HCM/PCM composites for thermal energy storage," *J. Energy Storage*, vol. 73, p. 108972, Dec. 2023, doi: 10.1016/j.est.2023.108972.

[61] R. S. Ferfera and B. Madani, "Thermal characterization of a heat exchanger equipped with a combined material of phase change material and metallic foams," *Int. J. Heat Mass Transf.*, vol. 148, p. 119162, Feb. 2020, doi: 10.1016/j.ijheatmasstransfer.2019.119162.

[62] A. Cavargna, L. Mongibello, M. Iasiello, and N. Bianco, "Analysis of a Phase Change Material-Based Condenser of a Low-Scale Refrigeration System," *Energies*, vol. 16, no. 9, p. 3798, Apr. 2023, doi: 10.3390/en16093798.

[63] F. Miccoli, A. Cavargna, L. Mongibello, M. Iasiello, and N. Bianco, "Experimental Characterization and Numerical Simulation of a Low-Scale Personal Cooling System with Integrated PCM," *Energies*, vol. 17, no. 5, p. 1118, Feb. 2024, doi: 10.3390/en17051118.

[64] M. A. Messenger, R. M. Manglik, and S. K. S. Boetcher, "Thermal Energy Storage Heat Exchanger Design: Overcoming Low Thermal Conductivity Limitations of Phase-Change Materials," *ASME J. Heat Mass Transf.*, vol. 146, no. 5, p. 054501, May 2024, doi: 10.1115/1.4064563.

[65] Y. Qiao, T. Cao, Y. Hwang, and R. Radermacher, "Investigation on Phase change material (PCM)-to-refrigerant Heat Exchanger in Air-conditioning Systems," 2021.

[66] R. Huang, A. Mahvi, W. Odukomaiya, A. Goyal, and J. Woods, "Reduced-order modeling method for phase-change thermal energy storage heat exchangers," *Energy Convers. Manag.*, vol. 263, p. 115692, July 2022, doi: 10.1016/j.enconman.2022.115692.

[67] M. Parhizi and A. Jain, “Solution of the Phase Change Stefan Problem With Time-Dependent Heat Flux Using Perturbation Method,” *J. Heat Transf.*, vol. 141, no. 2, p. 024503, Feb. 2019, doi: 10.1115/1.4041956.

[68] J. Guo and Y. Jiang, “A semi-analytical model for evaluating the thermal storage capacity and heat use efficiency of flexible thermal storage heating floor,” *Appl. Therm. Eng.*, vol. 198, p. 117448, Nov. 2021, doi: 10.1016/j.applthermaleng.2021.117448.

[69] A. T. Wijayanta, M. Xu, M. Mohit, S. Akhtar, A. F. Zueter, and A. P. Sasmito, “An analytical prediction for charging–discharging cycles of metal foam composite phase change materials thermal energy storage,” *Case Stud. Therm. Eng.*, vol. 74, p. 106674, Oct. 2025, doi: 10.1016/j.csite.2025.106674.

[70] A. König-Haagen and G. Diarce, “Prediction of the discharging time of a latent heat thermal energy storage system with a UA approach,” *J. Energy Storage*, vol. 73, p. 108849, Dec. 2023, doi: 10.1016/j.est.2023.108849.

[71] W. Beyne, R. Tassenoy, and M. De Paepe, “An approximate analytical solution for the movement of the phase change front in latent thermal energy storage heat exchangers,” *J. Energy Storage*, vol. 57, p. 106132, Jan. 2023, doi: 10.1016/j.est.2022.106132.

[72] W. Beyne, M. Johnson, A. Gutierrez, and M. D. Paepe, “Experimental validation of a lower order model for a flat-plate latent thermal energy storage heat exchanger,” *Appl. Therm. Eng.*, vol. 274, p. 126733, Sept. 2025, doi: 10.1016/j.applthermaleng.2025.126733.

[73] W. Beyne, I. T’Jollyn, S. Lecompte, L. F. Cabeza, and M. De Paepe, “Standardised methods for the determination of key performance indicators for thermal energy storage heat exchangers,” *Renew. Sustain. Energy Rev.*, vol. 176, p. 113139, Apr. 2023, doi: 10.1016/j.rser.2022.113139.

[74] B. Šarler, “Stefan’s work on solid-liquid phase changes,” *Eng. Anal. Bound. Elem.*, vol. 16, no. 2, pp. 83–92, Jan. 1995, doi: 10.1016/0955-7997(95)00047-X.

[75] A. Tamraparni *et al.*, “Design and optimization of composite phase change material for cylindrical thermal energy storage,” *Int. J. Heat Mass Transf.*, vol. 208, p. 123995, July 2023, doi: 10.1016/j.ijheatmasstransfer.2023.123995.

[76] M. Bechiri and K. Mansouri, “Exact solution of thermal energy storage system using PCM flat slabs configuration,” *Energy Convers. Manag.*, vol. 76, pp. 588–598, Dec. 2013, doi: 10.1016/j.enconman.2013.07.051.

[77] C. Ding, Z. Niu, B. Li, D. Hong, Z. Zhang, and M. Yu, “Analytical modeling and thermal performance analysis of a flat plate latent heat storage unit,” *Appl. Therm. Eng.*, vol. 179, p. 115722, Oct. 2020, doi: 10.1016/j.applthermaleng.2020.115722.

[78] T. Glisczinski, “Private Communication.”

[79] A. Mahvi, “Private Communication.”

[80] P. Shamberger and D. Ibbotson, “Private Communication.” Texas A&M.

[81] S. Al-Hallaj, M. Cook, and Y. Galazutdinova, “Private Communication.” NETenergy.

[82] J. Woods and R. Huang, “Private Communication.” NREL.

[83] “Valve Sizing Technical Bulletin.” Swagelok.

[84] A. Mills, M. Farid, J. R. Selman, and S. Al-Hallaj, “Thermal conductivity enhancement of phase change materials using a graphite matrix,” *Appl. Therm. Eng.*, vol. 26, no. 14–15, pp. 1652–1661, Oct. 2006, doi: 10.1016/j.applthermaleng.2005.11.022.

[85] A. Bulk, A. Odukomaiya, E. Simmons, and J. Woods, “Processing Compressed Expanded Natural Graphite for Phase Change Material Composites,” *J. Therm. Sci.*, vol. 32, no. 3, pp. 1213–1226, May 2023, doi: 10.1007/s11630-022-1578-9.

[86] B. N. Taylor and C. E. Kuyatt, “Guidelines for Evaluating and Expressing the Uncertainty of NIST Measurement Results”.

[87] Abraham. Savitzky and M. J. E. Golay, “Smoothing and Differentiation of Data by Simplified Least Squares Procedures.,” *Anal. Chem.*, vol. 36, no. 8, pp. 1627–1639, July 1964, doi: 10.1021/ac60214a047.

[88] P. Virtanen *et al.*, “SciPy 1.0: fundamental algorithms for scientific computing in Python,” *Nat. Methods*, vol. 17, no. 3, pp. 261–272, Mar. 2020, doi: 10.1038/s41592-019-0686-2.

[89] E. Lebigot, *Uncertainties: a Python package for calculations with uncertainties*. [Online]. Available: http://pythonhosted.org/uncertainties/.

[90] I. H. Bell, J. Wronski, S. Quoilin, and V. Lemort, “Pure and Pseudo-pure Fluid Thermophysical Property Evaluation and the Open-Source Thermophysical Property Library CoolProp,” *Ind. Eng. Chem. Res.*, vol. 53, no. 6, pp. 2498–2508, 2014, doi: 10.1021/ie4033999.

[91] B. Fultz, *Phase Transitions in Materials*, 2nd ed. Cambridge University Press, 2020.

[92] D. Mathis, P. Blanchet, V. Landry, and P. Lagière, “Thermal characterization of bio-based phase changing materials in decorative wood-based panels for thermal energy storage,” *Green Energy Environ.*, vol. 4, no. 1, pp. 56–65, Jan. 2019, doi: 10.1016/j.gee.2018.05.004.

[93] L. Que *et al.*, “Numerical simulation and experimental research progress of phase change hysteresis: A review,” *Energy Build.*, vol. 253, p. 111402, Dec. 2021, doi: 10.1016/j.enbuild.2021.111402.

[94] C16 Committee, *Test Method for Using a Heat Flow Meter Apparatus for Measuring Thermal Storage Properties of Phase Change Materials and Products*. doi: 10.1520/C1784-20.

[95] G. Box, “Science and Statistics,” *J. Am. Stat. Assoc.*, doi: 10.1080%252F01621459.1976.10480949.

Appendix A: Post Processing DSC Data

The material model used in design (Chapter 3) simplifies the behavior of the phase change process using global PCM properties and linear assumptions about the enthalpy-temperature relationship during phase change. Although convenient, the original assumptions do not accurately capture the phase change process. This is obvious when comparing our assumed PCM enthalpy with the PT23 differential scanning calorimetry (DSC) data collected by Texas A&M (

Figure A.1).

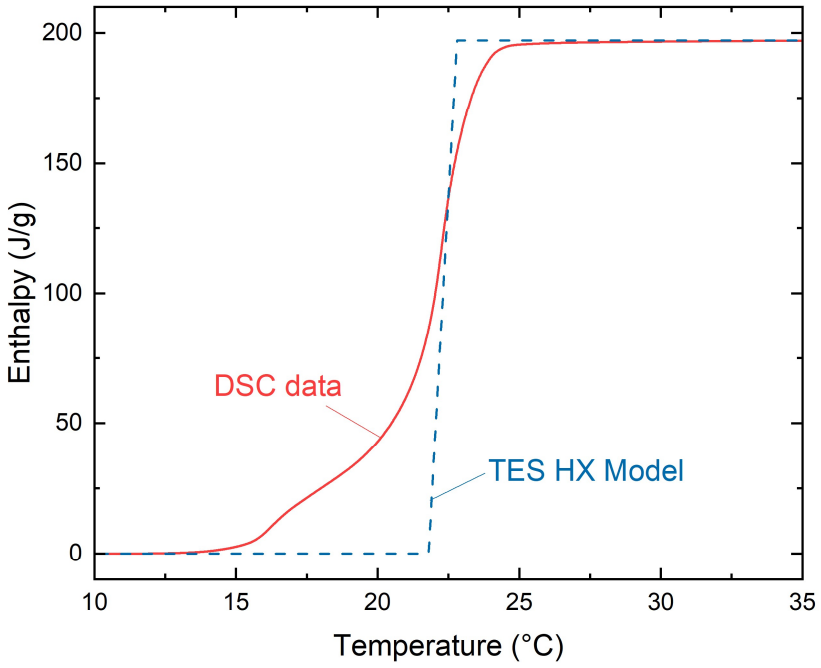

Figure A.1: Enthalpy-temperature relationship during the melting process for PT23 derived from Texas A&M's DSC data and assumed in the current version of the model (as of July 2025).

The comparison of the experimental data and finite difference model in Chapter 5 showed this discrepancy was causing poor model predictions as. Chapter 5 discusses how this data was used to increase agreement in the condenser and evaporator case. This document describes how the DSC data was integrated into the model.

First, the enthalpy-temperature relationship was extracted from the DSC data. The analysis was done in Origin Lab using the "Peaks and Baseline" analysis tool. First, the measured heat flow vs. time was plotted, then the melting temperature curve was flipped onto the positive y-axis, next appropriate baseline was selected, and finally the heat flow curve was integrated between about 4250 seconds and 6000 seconds. This is summarized in Figure A.2

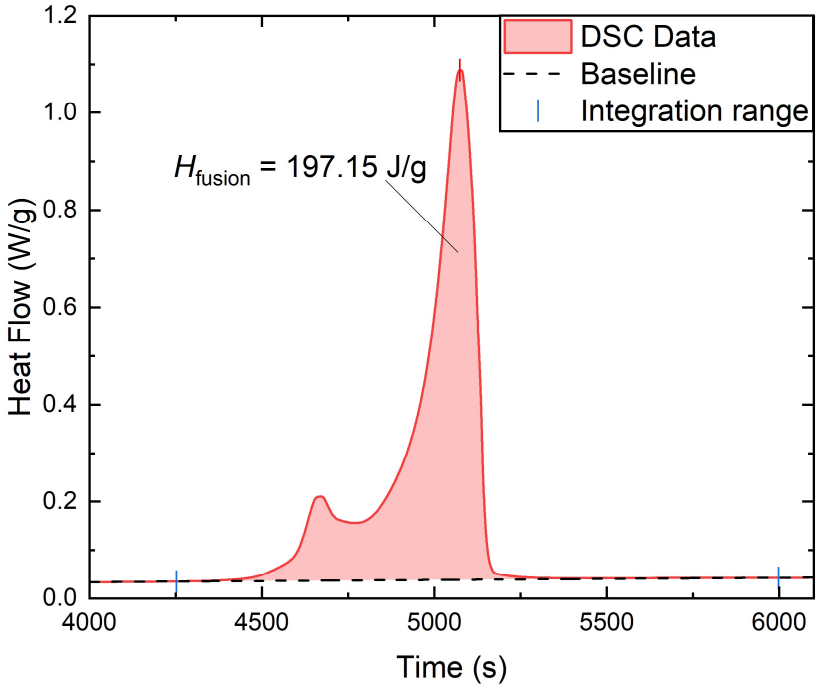

Figure A.2: Heat flow measured by the DSC vs. time. The raw data was flipped onto the positive x-axis and integrated with a lower baseline. The calculated heat of fusion is identical to the value calculated by the Texas A&M group.

The total area was used to verify the heat of fusion reported by Patrick Shamberger's group at Texas A&M. This method found the same total heat of fusion (197.15 J/g), so their data is being interpreted correctly. Origin provides the total integrated data, as well as the integrated values as a function of time (starting from 4250 seconds). The integrated values (enthalpy) were used to generate the enthalpy-temperature curve in the phase change region shown in

Figure A.*1* (red line).

Then the DSC was incorporated directly into the finite difference TES HX model. First, a matlab script that outputs temperature and equilibrium enthalpy arrays for the PCC. The enthalpy in the solid region is calculated with the manufacturer provided solid specific heat, $c_{p,s}$, in the current models using the idealized enthalpy vs. temperature curve. The reference enthalpy is set to 387731.18 J/kg at -13.15°C (260 K) and Equation (A.A.1) is applied to all temperatures between the reference temperature and the saturated solid temperature ($T_t - 0.5\Delta T_{glide}$) in the current model, and 13°C in the modified version).

$$h[i] = c_{p,s}\big(T[i] - T_{ref}\big) + h_{ref} \tag{A.1}$$

In Equation (A.A.1) i represents and indices in the temperature array that makes up the enthalpy vs. temperature curve. The liquid enthalpy is calculated in a similar fashion, but the temperature and enthalpy at the saturated liquid state is used instead of the reference.

All temperatures in the phase change region ($T_t \pm 0.5\Delta T_{glide}$) in the current model and between 13°C and 25.3°C in the modified version) are calculated with the DSC data shown in Figure 1. First, the curve was adjusted to account for the composite material matrix in Equation (A.):

$$h_{PC,PCC} = \underbrace{h_{DSC}\left(\frac{L_{PCC}}{L_{PCM}}\right)}_{Latent} + \underbrace{\bar{c_p} * (T - T_s)}_{sensible} \tag{A.2}$$

where L_{PCC} is the measured latent heat of the phase change composite (114.6 J/g in the current prototype), L_{PCM} is the latent heat of pure PT23 between the saturated solid and liquid temperatures (195.4 J/g), $\bar{c_p}$ is the average single-phase specific heat capacity, T_l is the saturated liquid temperature (lowest single-phase liquid temperature) and T_s is the saturated solid temperature. The sensible capacity was added to the latent term because the DSC data only includes the latent

contribution (integral is taken from a user specified baseline that is selected to exclude the sensible contribution).The equilibrium enthalpy in the phase change region was then calculated by interpolating the $h_{PC,PCC}$ data as seen in Equation (A.3),

$$h[i] = h_s + interp(T_{DSC}, h_{PCC}, T[i]) \tag{A.3}$$

where h_s is the enthalpy at the saturated solid state.

The new temperature/enthalpy curve is shown in Figure A.3 and compared to the one in the current model. There is a slight difference between the two models once the PCM is in the liquid phase. This discrepancy can be attributed to differences in the average specific heat ($\bar{c_p}$ = 1.085 J/g-K) and the solid specific heat ($c_{p,s}$ = 1.130 J/g-K). The DSC data disproportionately removes sensible heating in the solid phase. Although a sensible heating contribution is still considered in the phase transition region, it assumes a lower specific heat, thereby reducing the total enthalpy change.

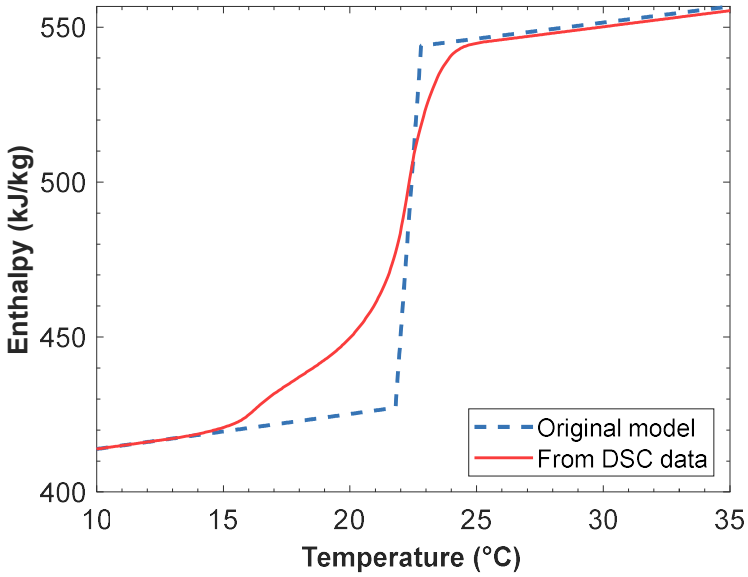

Figure A.3: Current and modified temperature/enthalpy curves in the finite difference TES HX model.

Finally, this data was converted into specific heat capacity. This is required to step the phase change composite forward in time using the RK-4 technique. The effective specific heat capacity was found by differentiating the red curve in Figure 3. This was done using the *gradient* function in Matlab, as shown in Equation (A.4).

$$c_{data} = gradient(h_{data})./gradient(T_{data}) \tag{A.4}$$

The new specific heat capacity is shown in Figure 4 as a function of temperature. With this information, the specific heat of each PCC node in each time step is found using the *interp1* function in Matlab as seen in Equation (A.5)

$$c = interp1(T_{data}, c_{data}, T) \tag{A.5}$$

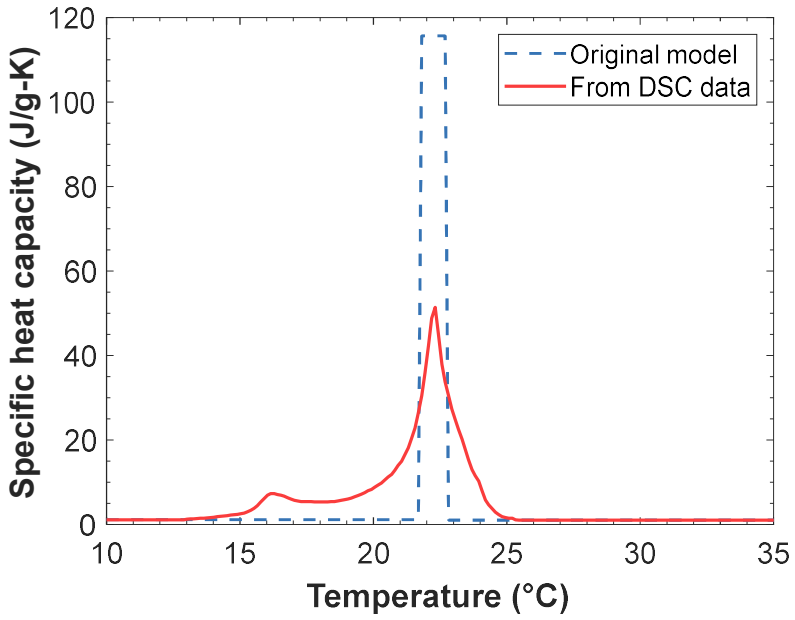

Figure A.4: Current and modified temperature/specific heat capacity curves in the finite difference TES HX model.

Appendix B: Additional Experimental Facility Parts (Not Electrical)

Additional plumbing components used to build the experimental facility are included in Table B.1. The specifications are not meant to be comprehensive. Comprehensive information (for example, product manuals) is included in the LET+S lab guide.

Table B.1: The non-electrical parts used to build the experimental facility.

Component	Supplier	Part Number	Specifications
TES Bypass Valve	Hamlet (McMaster-Carr)	N/A	$C_v = 4.6$ Max Pressure = 6000 psi
Shut off Valves	Hamlet (McMaster-Carr)	N/A	Cv = 1.3 Max Pressure = 2000 psi
Relief Valve	Kingston	111X	300 psig set pressure

A significant effort was spent designing the electrical portion of the facility. However, it is not relevant to the work so it was not included. Documentation on the electrical design will be included in the LET+S laboratory guide as well.

Appendix C: Loop Start Up (from 0 charge)

After loop repairs and upgrades are made the loop needs to be recharged. Additionally, the loop needs to be charged and recovered during operation to maintain operating conditions because a wide range of pressures (191-264 psi in this campaign) are used as test parameters. To achieve the minimum operating pressure for tests – the lowest ever achieved was 180 psi – the loop needs to operate at minimum charge. The mass needed for minimum charge isn't known. Instead, an ad hoc approach was taken to achieve minimum charge. A fraction of the refrigerant in the loop was recovered, and then the loop was charged with refrigerant in the smallest increments possible until the pump was able to operate without any signs of dry running or cavitation. This was done without any heaters on, the only thing that was on when updating charge to meet operating conditions was the chiller, because the pump always needs a subcooled fluid at its inlet. The condenser ideally needs to operate a pressure higher than the minimum operating pressure. However, if the condenser is over charged then the relief valve will likely be triggered for high pressure cases. It was observed that the relief valve triggered prematurely at 280 psi. Although, no direct pressure measurements were taken at the location of the relief valve (the outlet of the pump).

Appendix D: Increased Load Discharge Rate Correction

Measuring the state 4 enthalpy via energy balance had error in the beginning of the condenser increased load test, which lead to the use of the outlet enthalpy measured by a thermocouples and pressure transducer and differential pressure transducer pair (see Chapter 4) for the first 1800 s. This version of the discharge rate measurement is called the outlet state is called the sensible discharge rate because the outlet state is sensible without an energy balance. The post heater power was incorrectly controlled for the first 1800s leading to faulty measurement of the outlet enthalpy and discharge rate during this time. The error and correction is illustrated in Figure D.1.

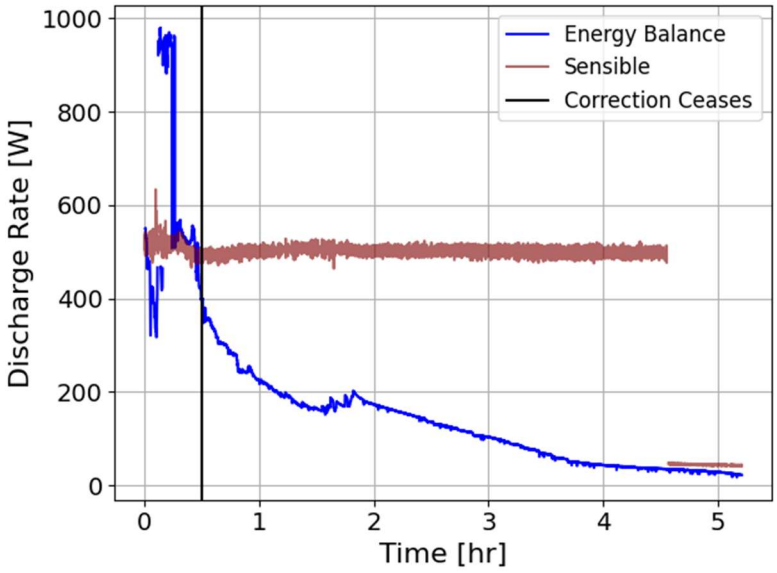

Figure D.1: The discharge rate measurement methods for the increased load case.

The energy balance-based measurement spikes up near 1000 [W], then it falls back to the original value after the first 15 min. Therefore, the discharge rate in the sensible region was used in the beginning of this test. The black vertical line indicates the location the correction ends and the discharge rate measurement becomes the energy balance measurement again. This is at the onset

of the varying power region. The sensible region isn't used again for the discharge rate because the outlet becomes saturated and the outlet state is no longer sensible.

Appendix E: Heater Losses Test Matrix

The test matrix used to correct the heater loss data is presented in Table E.1.

Table E.1: The mass flow rate and pressure for the heater loss data collection.

Mass Flow Rate [g/s]	Pressure [psi]
1	202
1	251
1	264
1	268
1	175
1	191
1.25	191
1.25	202
1.25	251
1.25	264
1.25	268
1.25	175
2.5	191
2.5	202
2.5	251
2.5	264
2.5	175
2.5	268
3.75	191
3.75	202
3.75	251
3.75	264
3.75	175
3.75	268

The mass flow rates and pressures were selected to include and bound conditions tested in the experimental campaign summarized in this thesis. The upper and lower bounds on mass flow rate are slightly lower and higher than the desired operating conditions so the loss regression model is trained on a “surface” who’s N-Dimensional area doesn’t contain the conditions operated under at the boundaries of the surface. Instead the conditions tested lie within the area, making the

regression model more believable. This is why the regression model excluded these boundary values from the testing dataset.

Appendix F: Hydraulic Press Set Up Information

The TES HX was compressed at UW-Madison's design and innovation labs at UW-Madison. The TES HX the method for compressing the TES HX utilized a supporting structure as illustrated in Figure F.1.

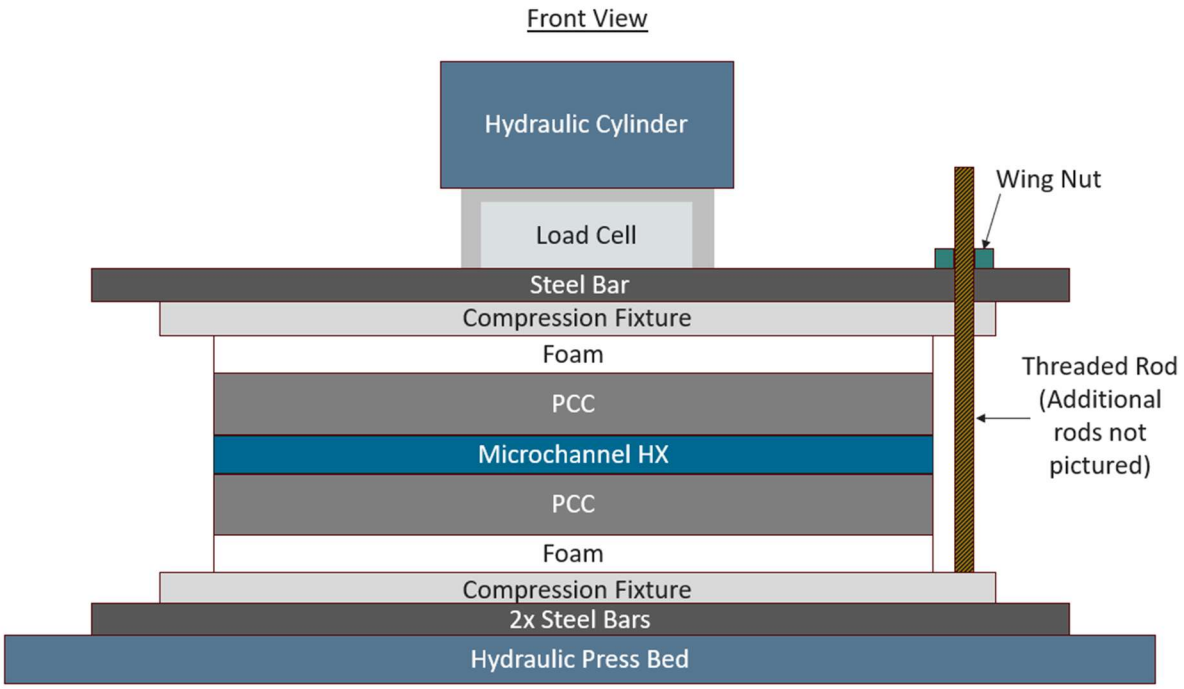

Figure F.1: The setup for compressing the TES HX in the hydraulic press at UW Madison.

The steel bars were added for additional stiffness and the load cell was used to measure the force through the TES HX. The compression was completed at 2000 lbs. Then wing nuts were hand tightened on threaded rods that spanned the length of the TES HX on the front and back. These nuts held the compression after the hydraulic cylinder was retracted to maintain low contact resistance. The load cell used was an 3000 lbs capacity IDS672-3klb-C3 load cell and was paired with an Optima LP7515 weight indicator. Load cells are extremely sensitive to their environment. The load cell used's original calibration become skewed in transport so a new calibration was completed using random weights in the lab. It was difficult to find anything that weighed over 10 lbs and could fit on the load cell so this limited the accuracy of the calibration. It's recommended

that future work look at coming up with a more accurate way to calibrate the load cell to increase confidence in the level of compression achieved. Because of the calibration issues it's hard to gauge the accuracy of the compression achieved.

Appendix G: Experimental Facility LabView Interface

Figure G.1 shows the LabVIEW interface for "05_system_control.vi". Olivia Dobson made significant contributions to this appendix. This is the control panel for the flow loop where the user can set flow rates, specify heater output, and monitor system conditions to ensure everything is running as expected.

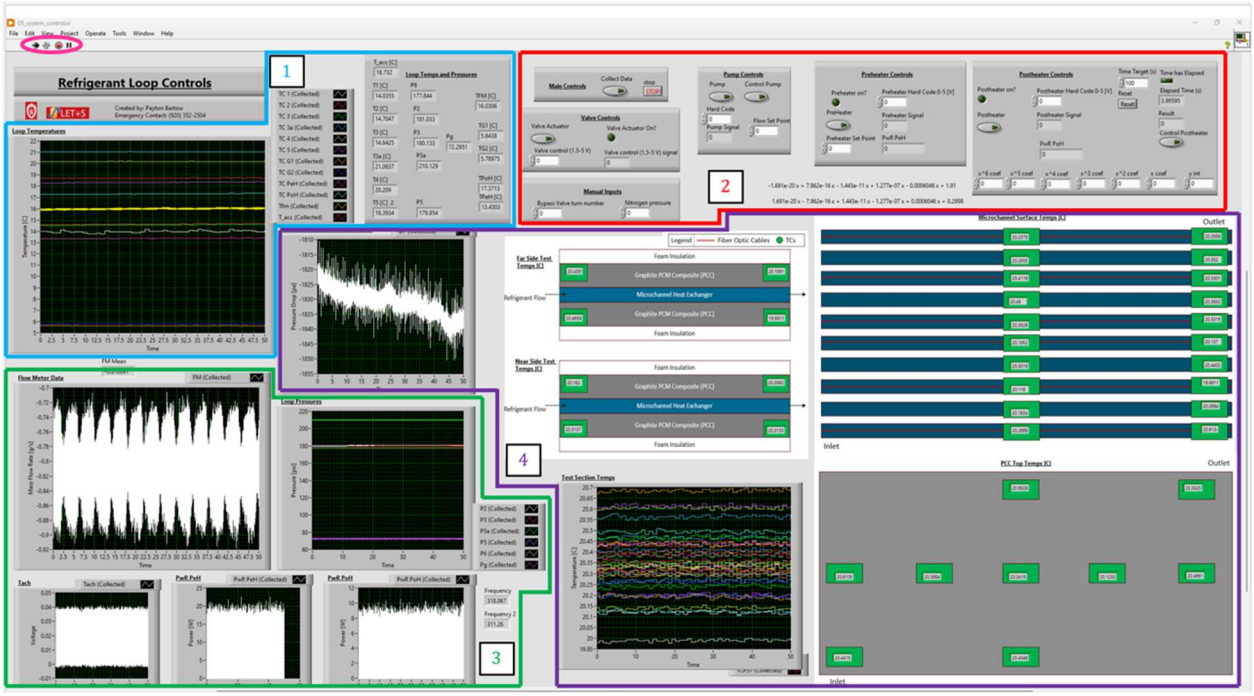

Figure G.1: The LabView interface for the experimental facility.

Circled in pink:

- The "run" and "stop" buttons are located along the top bar of the LabVIEW interface right below the "file", "edit", and "view" buttons.
- The "run" button should be pressed at the beginning of start up, and the "stop" button should be pressed at the very end of shut down.

Section 1: System Temp + Pressure

- The plot displays the refrigerant temperature at different locations along the flow loop

    - Thermocouple numbering corresponds to the facility schematic discussed in Chapter 4.
- The "Loop Temps and Pressures" box lists the temp and pressure of the refrigerant at differing locations in the loop. Observing temperatures is easier using the plot, but observing pressures is easier using this box
    - There is a pressure plot included in Section 3, but since it includes glycol pressure, the vertical axis is too stretched out for it to be a good tool for observing pressure in the loop
- Use both the temp plot of temps + pressure box as tools to ensure system pressures and temperatures do not exceed allowable values. These are the first areas you should check to make sure the system is running as expected.
    - Do not let pressures exceed 280 psi
    - Do not let temperatures ramp up past 60 C
    - Shut down the system if things are behaving erratically

Section 2: User Controls

- Section 2 contains all interfaces where the user must input information to change flow conditions
    - Valve, Pump, Preheater, and Postheater boxes contain the controls for each individual component
    - Must first hit the start button to turn on each component
    - User inputs a voltage to send to each component in the "Hard Code" boxes
- Listed in the order of usage:
    - Valve Controls:

- Pump Controls:
- Preheater Controls:
- Postheater Controls:

Section 3: Equipment Output

- The top two graphs show the flow rate output and the measured pressure from left to right.
- The bottom 3 graphs show the measured pump frequency (first on the left) and the power from the heaters. The middle plot is the preheater power and the plot farthest right is the postheater power.

Section 4: Test Section Conditions

- The test section measurements collected in LabVIEW are the pressure drop and thermocouple measurements. The thermocouple calibration is input to LabVIEW using the calibration curve function. An additional point is added at 100°C so the thermocouple signal doesn't saturate.
- The pressure drop measurement is plotted in the top left corner and all thermocouple measurements are plotted in the bottom left corner.
- The other plots have digital read outs for the thermocouples in their corresponding locations

Appendix H: Loop Operation

To operate a test the user needs to be familiar with the procedure for running a test. Olivia Dobson made significant contributions to this appendix. The procedures for running tests is documented below:

Safety:

- PPE should be worn when operating the loop
    - PPE for the loop consists of safety glasses, long pants, and closed toe shoes
- Potential hazards are compressed gases, refrigerants, and electrical hazards
    - Make sure you are trained on these items before using the loop
- Other potential issues are thermal runaway or negative operating conditions for the pump
    - Thermal runaway can occur if the pre/postheaters are left at too high of heat or left on without any flow
    - The pump should never be left on unsupervised and should not be left on if charge is low or cavitation could occur.

READ ME - Shut down the loop if:

- If any loop temperatures are above 70 deg. C - shut down.
- If any heater temperatures are above 60 deg. C - shut down.
- If the flow rate indicates pump cavitation/dry running for greater than 30 seconds - shut down.
- Always shut down the loop when finished with an experiment or leaving for the day.

Start Up:

1. Turn on all (5) electrical switches
    a. 4 on main electrical box, 1 on back wall outlet strip as seen in Figure H.1 and Figure H.2.

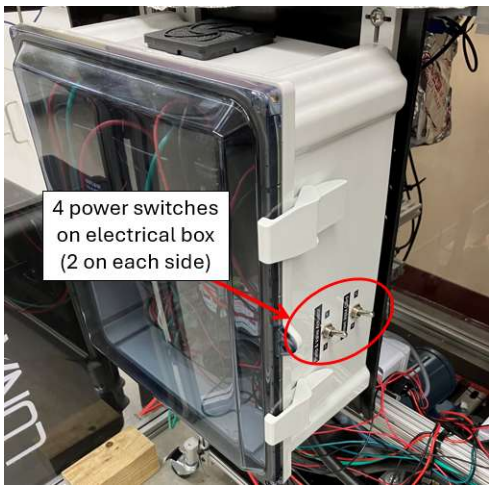

Figure H.1: The electrical box used to turn on power supplies for the experimental facility.

Figure H.2: The outlet strip used to turn on some of the auxiliary low power for electronics on the test facility.

2. Check that the pressure and temperature in the loop make sense (near room temperature and saturation pressure). If the pressure is particularly low there could be a refrigerant leak.
    a. Open up 05_system_control.vi in LabVIEW and hit "Run"
    b. If sitting at room temp: approx. 20 deg. C, approx. 200-220 psi for R410a
3. Turn on the valve actuator and set it to 3 V using the menu in Figure H.3. Then, drop it to 1.5 V - if it's operating correctly you should hear a whirring noise (motor).

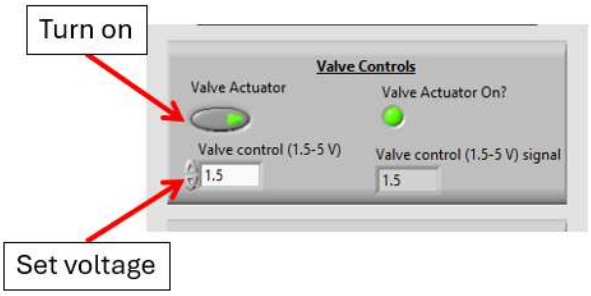

Figure H.3: The valve control menu on the LabView interface.

a. Note: Valve control < 1.12 V will close the valve. DO NOT set valve control lower than 1.12 V while pump is running. There are fail safes in place in case a mistake is made, but still try to avoid this.

4. Make sure the manual red and black valves are in the correct orientation:
    a. Black valve: located at the top, left-hand side of the loop by the outlet strip and pre-heater. The short arrow side of the valve handle points to the flow direction. Make sure it is pointing AWAY from the TES
    b. Red valve: located on the right-hand side of the loop back by where the nitrogen is routed into the chamber. Make sure it is fully CLOSED, I.e. perpendicular to the tubing.
    c. The initial valve orientations ensure no flow through the TES during start up is shown in Figure H.4 and Figure H.5.

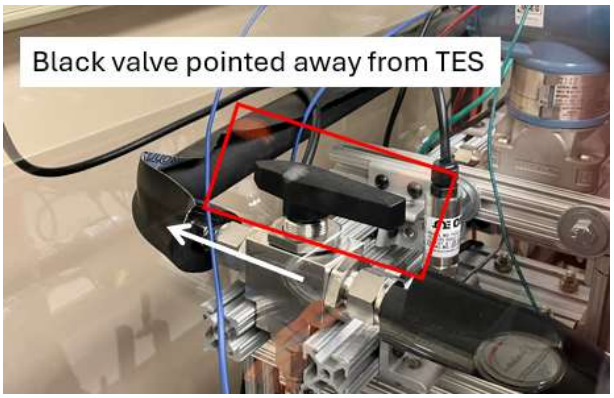

Figure H.4: The initial position of the diverting valve that sets the flow through the TES HX or the TES bypass.

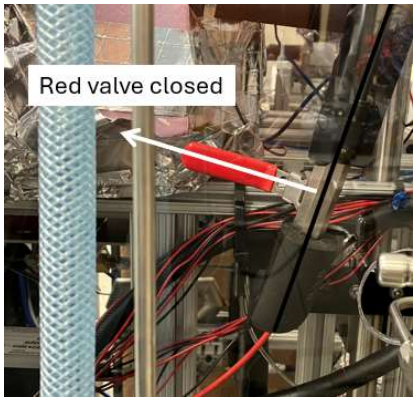

Figure H.5: The shut off valve that closes the TES HX off from pressure fluctuations in the bypass loop during start up.

5. Start the chiller
    a. Turn the electrical switch on the chiller on (white switch located on the backside of the chiller), the chiller will need to go through a start up procedure before you can press the power button. The chiller will make a lot of clicking noises when it does this.
    b. The chiller will begin at its previous set point.
    c. If this set point isn't desired or the set point is below 10 deg. C you will need to put in a new set point in the control menu shown in Figure H.6:

i. Hit mode and then use the arrow keys to change the number and hit enter

ii. If you are going to a set point below 10 deg. C, you first must reach steady state at a set point of 10 deg. C

1. If, 7.5 deg. C < setpoint < 10 deg. C, then go to your set point after 10 deg. C
2. If, 5 deg. C<setpoint<7.5 deg. C, then reach steady state at 7.5 deg. C after 10 deg. C and then go to your set point
3. These procedures are to prevent the chiller from shutting down due to temperature swings below 10 deg. C

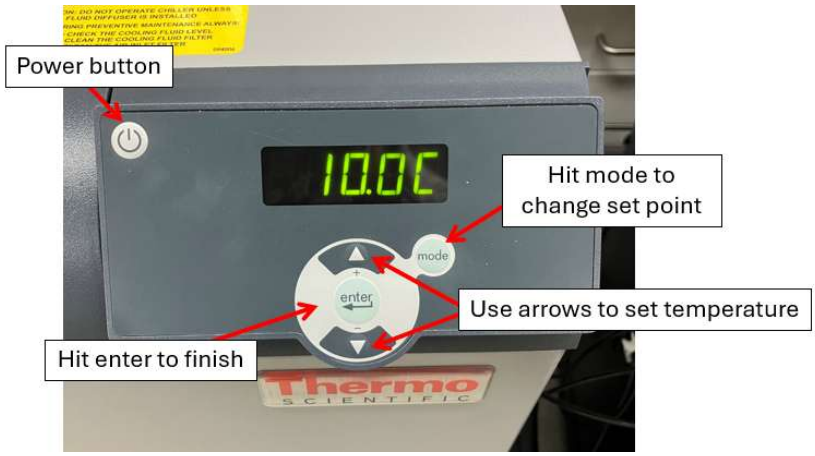

Figure H.6: The manual menu for the chiller.

6. Once the chiller is at its final set point, start the pump using the menu in Figure H.7.

a. ONLY START PUMP IF VALVES ARE IN THE CORRECT ORIENTATION

i. Valve actuator open, red valve closed, black valve pointing away from TES

ii. Could dead head the pump if the valves are not oriented properly

b. Set pump to 1.5 V to begin with

c. It should operate at a consistent flow rate for 30 seconds.

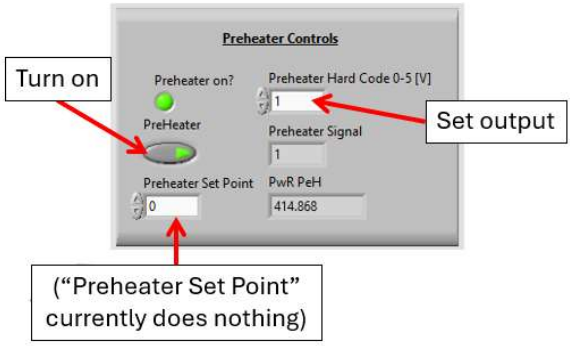

Figure H.7: The preheater control menu.

7. After the pump has been operating consistently for a minute or two it is okay to turn on the preheater
    a. Turn the preheater to 1V regardless of your intended set point. (Hard Code)
    b. After the preheater has been on for a couple minutes, or if the flow rate starts to fall, turn the pump signal up to 3V.
    c. The flow rate should become more consistent and T2 should spike briefly.
        i. Shut down if it doesn't
    d. Drop the pump signal down gradually to 1.5 V. (3V -> 2V -> 1.5 V)
8. Start gradually moving the preheater signal to its desired value and let the loop reach steady state.
9. Next turn on the pump controls and set the set point to the desired flow rate for your test.
10. Now you are ready for the test specific controls

Condenser Test controls:

- At this point the preheater should be at its set value but the post heater will need adjustments

1. The post heater should be on at a signal of 0.3 V to start to get it started up, but not at a high level since excessive heat will cause thermal runaway here as there is no energy being removed from the fluid prior to the post heater until the test begins.
2. The inlet of the test section (3a) should have 15 deg. C of superheat, adjust the preheater accordingly if this isn't the case.
3. When ready switch flow to run through the test section:
    a. FIRST: open the red valve, I.e. orient the valve to be parallel with the tubing
    b. THEN: twist the black valve to point towards the TES
    c. MUST DO IN THAT EXACT ORDER TO PREVENT DEAD HEADING THE PUMP
4. Immediately after switching:
    a. Ramp up the post heater to fully cross the dome
    b. Use the piston accumulator to set the pressure of the system to the desired test pressure
    c. Now the test will run for approximately 30 minutes
5. The TES outlet will switch from single phase to two phase at some point
    a. When this happens the postheater will need to follow its operating curve to accurately measure the TES capacity. The post heater curve is generated from constant inlet conditions for the test and input as 5^{th} order polynomial curve fit to the controls so the power is ramped down with time as the TES discharges less and less. This is done to avoid losing the measurement of the outlet state or overheating the refrigerant.

   b. Ensure the outlet is at least 10 deg. C superheated at all times, but no more than 20 deg. C superheated
      i. To adjust change the y intercept of the postheater curve
6. The test is finished when the outlet of the TES superheats for 15-30 min or when the output power remains at 50 W or less for 15-30 min.
7. To Adjust pres

Evaporator Test controls (single phase inlet):

1. This test will not use the preheater at all so turn it off
2. Make sure the post heater is operating correctly before starting your test
3. While running flow through the bypass loop ramp up the signal for the post heater to the signal needed to cross the dome at the desired flow rate for the system
4. You're ready to adjust the post heater to 0.3 V once you confirm that the post heater crosses the dome at an input signal. A reasonable input signal should match the expected amount of heat needed to cross the dome
5. The post heater should be on at a signal of 0.3 V, which is the desired starting set value. The outlet of the TES will be superheated to start and then eventually drop to two phase.
6. Note: no piston accumulator is needed during this test
7. The TES outlet will switch from single phase to two phase at some point
8. When this happens the post heater will need to follow its operating curve to accurately measure the TES capacity.
9. The operating curve is in place to maintain a superheated post heater outlet (measurable capacity)

10. Ensure the outlet is at least 10 deg. C superheated at all times, but no more than 20 deg. C superheated
11. To adjust: change the y intercept of the post heater curve
12. The test is finished when the outlet of the TES superheats for 15-30 min.
13. To adjust pressure during the test use the set temperature on the chiller

Shut Down:

- Turn off all signals in LabVIEW (4), but don't turn off LabVIEW yet
- Power down the chiller
- After the chiller is off turn its electrical switch to off
- Release the nitrogen from the piston accumulator to bring the piston to top dead center
    - Make sure that the supply valve to the compressed nitrogen is shut before starting this.
- Completely shut all safety mechanisms on the nitrogen tank
    - The supply valve, regulator and shut off valve should all be in their off positions and the pressures should read 0
- Go back to the control screen and make sure all pressures and temperatures are reasonable. If so shut off the LabVIEW
- Last, shut off the 5 additional electrical switches.

Appendix I: Transients of Postheater Measurements

The postheater measurements had a small ammount of transients from the thermal mass of the postheater and the refrigerant. To characterize this a test was run through the TES bypass as illustrated in Figure I.1.

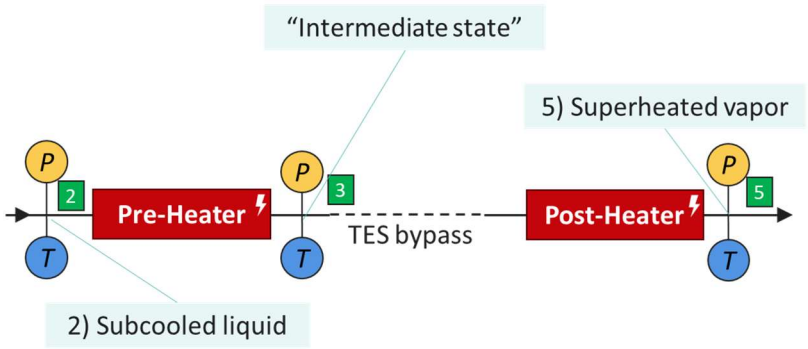

Figure I.1: The test set up for quantifying the transients.

The refrigerant came into the preheater subcooled, then it was heated to a saturated intermediate state of known enthalpy. The intermediate state's enthalpy was known because the heat input by the preheater was measured so an energy balance across the preheater could tell us the outlet enthalpy. Then, the saturated fluid traveled through the bypass loop to the post heater where it was heated to a superheated vapor so the enthalpy at the outlet of the postheater could be measured. The power input to the postheater was measured as well so an energy balance across the postheater could give the enthalpy at the intermediate state.

The energy balances for a test with a flow rate of approximately 2.1 g/s and pressure of 1700 kPa are illustrated in Figure I.2.

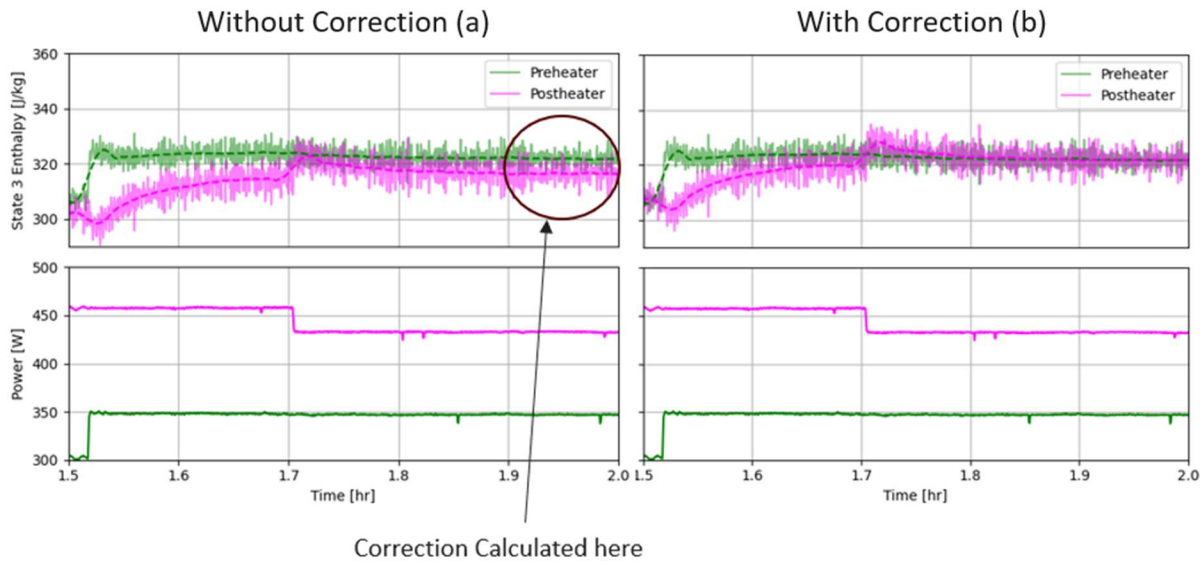

Figure I.2: The transients test results (a) without the correction and (b) with the correction.

In Figure I.2 the shaded region is the actual data and the lines are their smoothed values. The test began at a step up in preheater power. Then, once the postheater outlet enthalpy had nearly reached steady state the postheater power was stepped down to simulate the postheater adjusting it's power to measure the outlet state in the varying power region. The preheater power was unchanged, which means the intermediate state was unchanged. Because of thermal losses the measurements of the enthalpy at state 3 don't match in Figure I.2a, which makes comparison difficult. To solve this problem the difference between the measured enthalpies at the end the test (as indicated in the plot) were used to calculate a correction factor to make the postheater enthalpy coincident with the preheater. The outlet state in Figure I.2b is much easier to compare with this correction. When the step down in postheater power occurs the postheater measured state 3 enthalpy deviates slightly from the true value (indicated by the preheater) briefly and then begins to track again after 0.1 hours or 6 minutes. So the transients in the measurement is insignificant because the tests discussed in this thesis happen over multiple hours.

Appendix J: PCC Slab Symmetry Assumption Discussion

First, the general progression and symmetry of the phase front is plotted using the thermocouples in front and back view of the PCM TES HX (see Chapter 4) to verify the symmetry assumptions used to develop the finite difference model are valid. The temperature profiles are presented in Figure J.1 for condenser mode.

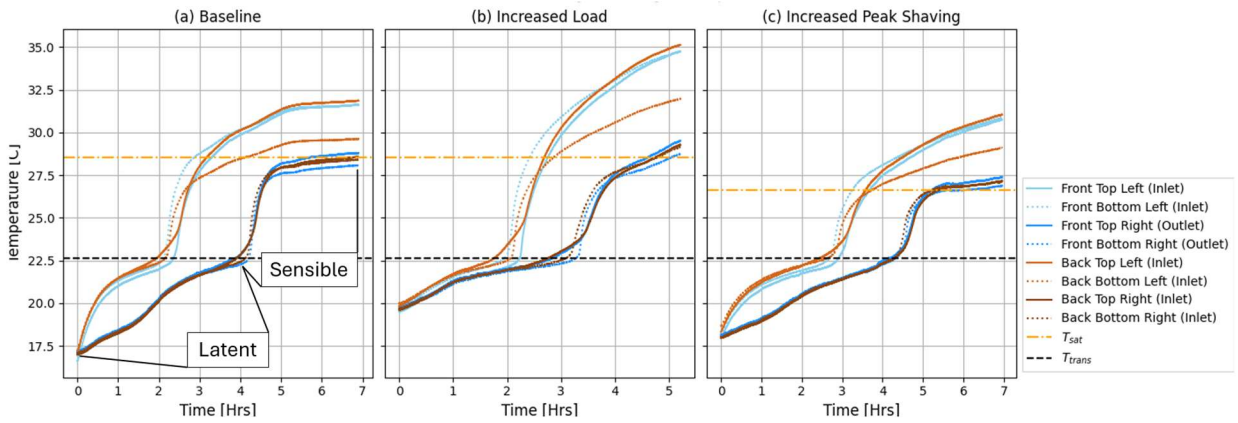

Figure J.1: The temperature profiles of the thermocouples placed to determine symmetry of the phase front are plotted. (a) is the baseline case. (b) is the increased load case, and (c) is the increased peak shaving case. Each color is a thermocouple pair that is compared to determine symmetry of the heat transfer in the top and bottom slabs. The solid lines are the top thermocouples and the dotted are the bottom thermocouples. The blue colors indicate thermocouples in the front view and brown colors indicate thermocouples in the back view. Lastly, the lighter shade of each color indicate thermocouples on the left and the darker shade indicates thermocouples on the right.

In Figure J.1 features of the DSC profile can be seen. Figure J.1a shows the latent region, which is broad, as discussed in Chapter 3. The sensible region is also annotated and is indicated. The sensible region rapidly approaches the refrigerant temperature, either superheated or saturated depending on the axial location inside the heat exchanger. Figure J.1 also gives information about the symmetry of the melt front and heat transfer between top and bottom slabs. The thermocouples near the outlet (darker colors) seem to match quite well. However, the thermocouples near the inlet (lighter colors) diverge when the temperature transitions from the latent region to the sensible region. One plausible explanation for this is an uneven distribution of PCM within the composite slab, although this hasn't been systematically investigated. Observations of nonideal soaking of

the graphite slabs (discussed in Chapter 4) could help explain this. If there is less PCM in one location then it would progress more quickly through the melt region. Additionally, uneven contact resistances could also explain this. If the contact resistance isn't uniform between each side of the microchannel then the side with lower contact resistance would melt faster. Because the majority of heat transfer/discharge occurs outside of the sensible region the uneven distribution can be ignored for comparison to the finite difference and analytical models.

The plots for the evaporator symmetry illustrate similar results to the condenser as seen in Figure J.2.

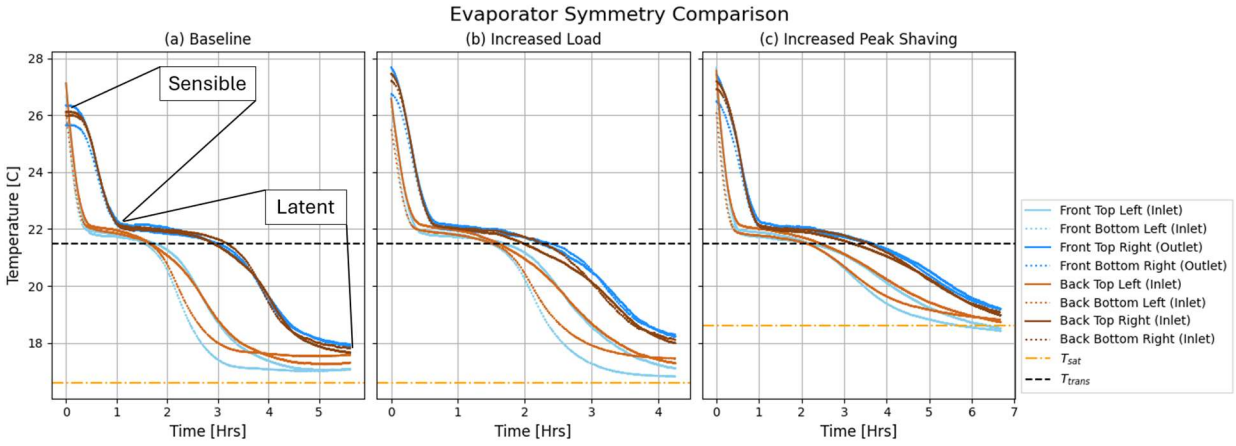

Figure J.2: The temperature profiles of the thermocouples placed to determine symmetry of the phase front are plotted. (a) is the baseline (b) is the increased load case, and (c) is the increased peak shaving case. Each color is a thermocouple pair that is compared to determine symmetry of the heat transfer in the top and bottom slabs. The solid lines are the top thermocouples and the dotted are the bottom thermocouples. The blue colors indicate thermocouples in the front view and brown colors indicate thermocouples in the back view. Lastly, the lighter shade of each color indicate thermocouples on the left and the darker shade indicates thermocouples on the right.

Figure J.2 shows freezing profile of the PCC slab. Figure J.2a shows the latent region, which is more sharp in nature than the melting latent region in Figure J.2a. The sensible region is also indicated in Figure J.2a. The sensible region rapidly approaches the saturation temperature of the refrigerant, but typically does not exceed the melt temperature since the inlet condition is near saturation if not saturated. The sharpness of the latent region contributes to enhanced symmetry in freezing, however there is still some disagreement near the inlet.

Appendix K: Refrigerant Distribution Results (All Tests)

The refrigerant distribution results for all condenser tests are plotted in Figure K.1.

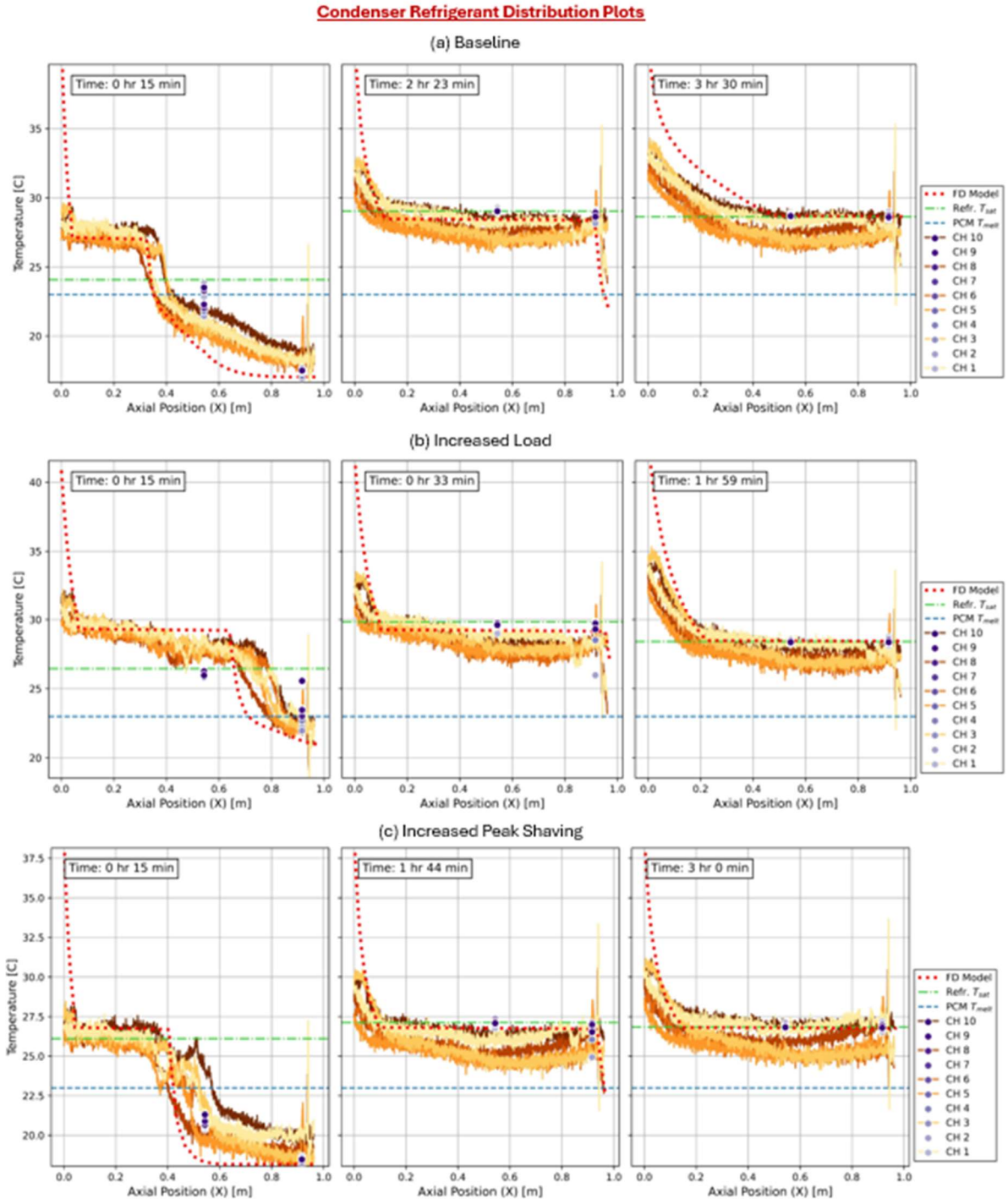

Figure K.1: The heat exchanger surface measurements are plotted for all condenser tests. (a) is the baseline (b) is the increased load case, and (c) is the increased peak shaving case. The legend indicates the color of

the thermocouple on each channel and the corresponding color of the fiber optic cables if relevant. The thermocouples are indicated as dot, while the fiber optic cables are indicated as solid lines.

Figure K.1 includes plots at three different times during each test. The first time plotted is the same for each test, and is early in the test to show the refrigerant condensation progressing axially along the heat exchanger. Before the test begins the test section is isolated from the rest of the loop and the refrigerant is isothermal with the PCC temperature. Then as the test progresses the refrigerant reaches its saturation temperature (for example, positions less than 0.4 m in Figure K.1a). The second time plotted is when the refrigerant is a saturated liquid at the outlet. All plots (at the second time) indicate that the outlet has just become a saturate liquid since the temperature profile at the outlet has a small portion still below the saturation temperature. Finally, the third time plotted is a time late in the test and shows that little condensation is occurring since increased superheat is present at the inlet relative to earlier times. This occurs because the PCC slab has depleted its capacity. The thermocouples agree with the fiber optic cables qualitatively but have some significant deviation. This is acceptable given the issues instrumenting the test section with the fiber optic cables described in Chapter 4 on test section set up. Lastly, the finite difference model agrees with the phase front measurements within reason. There is some difference between the experimental data and the model in sensible regions but this is not of concern. The model is accurately predicting the transition from sensible to two phase for superheating and subcooling, which is more important than predicting the exact temperature with sensible regions.

The refrigerant distribution for the evaporator case is plotted in Figure K.2.

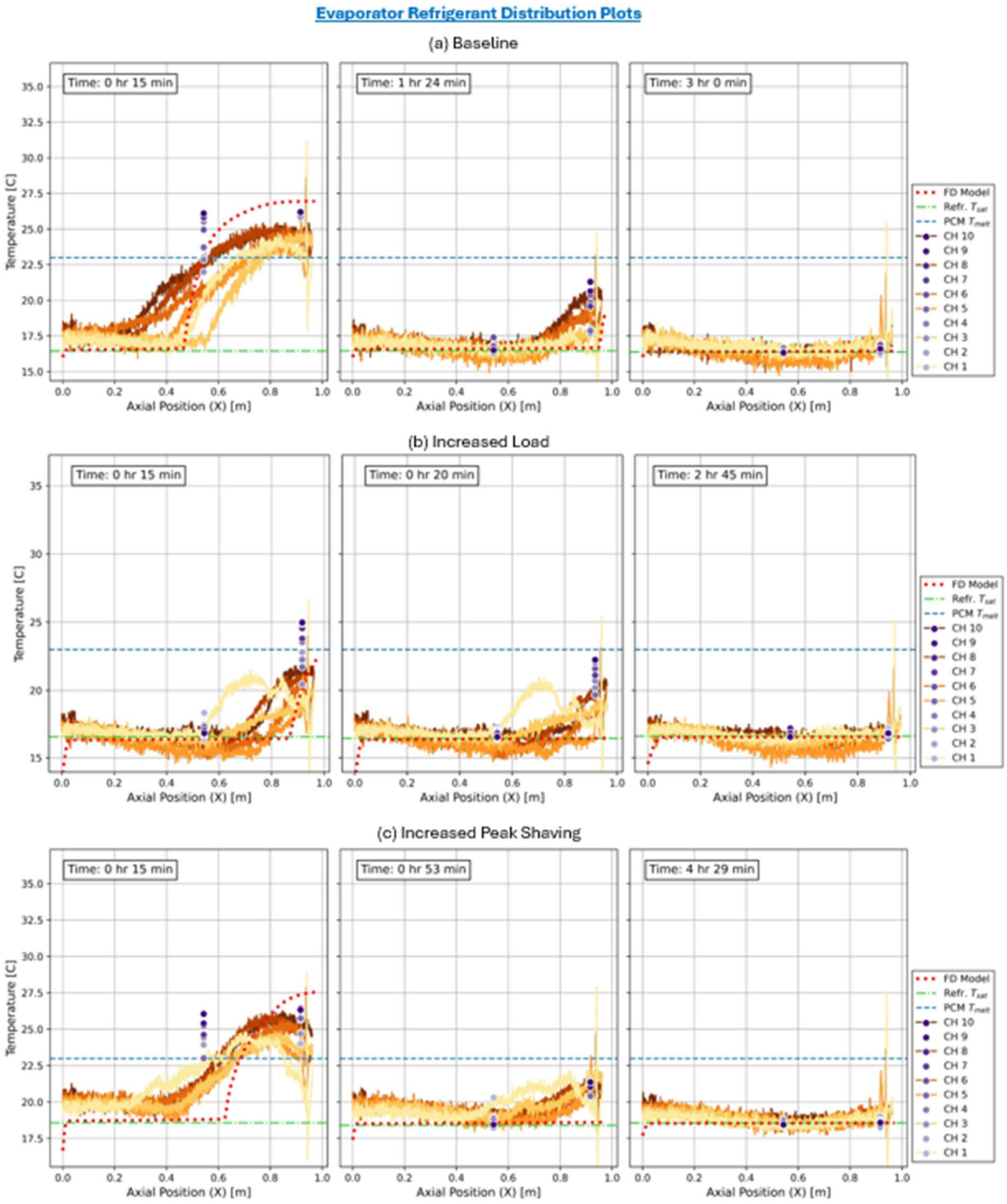

Figure K.2: The heat exchanger surface measurements are plotted for all condenser tests. (a) is the baseline (b) is the increased load case, and (c) is the increased peak shaving case. The legend indicates the color of the thermocouple on each channel and the corresponding color of the fiber optic cables if relevant. The thermocouples are indicated as a dot, while the fiber optic cables are indicated as solid lines.

The first time plotted in Figure K.2 is the same for each test, and is the same as the condenser plots. Similar behavior is seen in the first temporal plot as the condenser. The second time plotted is when the refrigerant is a saturated vapor at the outlet. All tests indicate that the outlet has just become a saturated vapor since the temperature profile at the outlet has a small portion still above the saturation temperature. Finally, the third time plotted is a time late in the test and shows that little evaporation is occurring since the temperature is at the saturation temperature. This occurs because the PCC slab has depleted its capacity. Agreement between the fiber optic data, thermocouples, and finite difference model is similar to the condenser case. The prediction of the finite difference model is good enough because it accurately predicts the onset of refrigerant phase change in time. Additionally, there is evidence of maldistribution in all of the plots, in particular for the baseline and increased load case. Maldistribution is indicated by differences in temperature profiles between channels as discussed in Chapter 5. Maldistribution is suboptimal because it means the PCM will freeze unevenly and it will be hard to control and discharge in the target period (4 hours in this case).

Appendix L: Pressure Drop Results

The pressure drop results for each test are presented in Figure L.1.

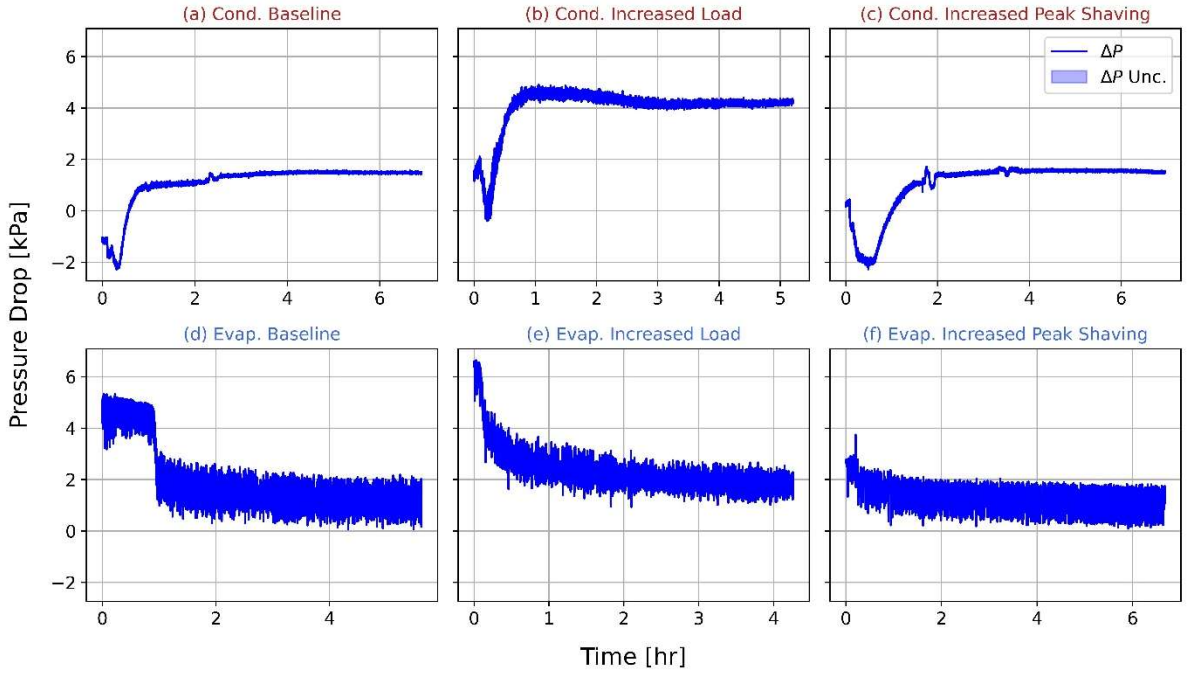

Figure L.1: The pressure drop results for each test. (a)-(c) present condenser and (d)-(f) present the evaporator. (a) and (d) are baseline cases, (b) and (e) are the increased load case, and (c) and (f) are increased peak shaving.

The pressure drop results for the condenser have negative values early in the test because of the set up issues discussed in the validation section in Chapter 4. Eventually the condenser pressure drop becomes positive, although there is no obvious indication of why when the results are compared with other information from the plots. What likely occurs is that the density in the lines that go to the pressure transducer becomes comparable. Although, this would likely not happen until the varying power region, and it happens much earlier, before 1 hour in the condenser baseline. Completing the pressure drop plumbing upgrades discussed in Chapter 4 should lead to improved condenser pressure drop measurements. The evaporator tests don't have negative pressure drop. In contrast to the condenser the pressure drop is very high in the beginning of the test and then drops. This makes sense because the velocity of the fluid slows down throughout the

test because the density in the microchannel decreases throughout the varying power region in evaporator tests. It appears that the effect of a two phase fluid is only

Appendix M: Capacity Error Results

The discharged energy error of each model relative to the experiment defines is not used to define the model performance because it truncates errors in agreement, however it still offers some valuable insights for state of charge estimates of these results. The error in discharged energy was computed using Equation (M. 1).

$$\% \, Error = \frac{\left|E_{exp} - E_{model}\right|}{E_{exp}} * 100 \qquad \text{(M. 1)}$$

The error vs. time is plotted in Figure M.1 - the profiles help describe the issues each model has estimating discharged energy at different times, which would be important for a control scheme.

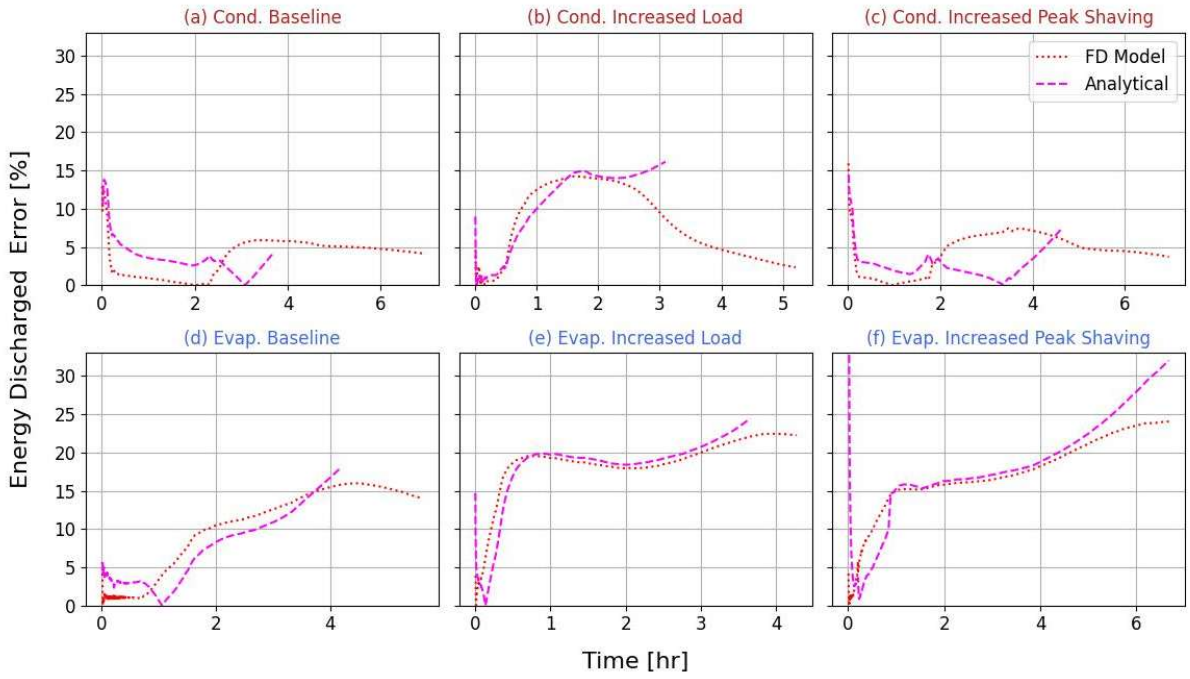

Figure M.1: The discharged energy for each test is computed which clearly defines the performance of each model. (a)-(c) present condenser and (d)-(f) present the evaporator. (a) and (d) are baseline cases, (b) and (e) are the increased load case, and (c) and (f) are increased peak shaving.

Figure M.1 shows that each test initially has a spike in error – this can be ignored because it's a result of the small amount of discharged energy at this time which cause little differences to lead to big errors. As time increases the condenser tests having varying error between each test. The

finite difference model seems to increase in error when the constant power region ends and then decrease again towards the end of the test. The condenser analytical model experiences similar behavior for the baseline and increased peak shaving tests. The error decreases and eventually the energy discharged is equal before the error increases again. This happens because of issues predicting the onset of the varying power region discussed in Chapter 5. When experiment and analytical model are late in time equal sensible PCC heat transfer becomes more significant and the discharge rate diverges from the experiment as seen in Chapter 6. The increased load condenser case sees increasing error throughout time for the analytical model because the temperature starts in the latent region in the experiment, making the assumption that the heat is discharged between 18 and 28°C inaccurate. The evaporator error increases in time for both models and every tests. This makes sense as the freezing DSC curve is not properly derived as discussed in Chapter 6 in the finite difference model validation tests.

To compare the usefulness of each model's predictions their error in Figure M.1 must be analyzed. The maximum evaporator errors from Figure M.1 are presented in Table M.1.

Table M.1: Average discharged energy error.

		Baseline	Increased Load	Increased Peak Shaving
Condenser	Finite Difference	15.96%	22.45%	24.04%
	Analytical	17.98%	24.45%	32.28%
Evaporator	Finite Difference	5.90%	14.23%	7.43%
	Analytical	4.39%	16.13%	7.36%

For all evaporator tests the maximum is 31.86% while the minimum is 15.94%. None of these errors are below 10% and are therefore improvement is needed before either model can be used to predict state of charge. In Figure M.1 both models agree with each other well though and follow

the trend of the experiment in Chapter 6. The errors in the evaporator case are due to the suboptimal freezing profile discussed in Chapter 5. Each model's ability to predict state of charge should be evaluated on the condenser accuracy because poor material inputs will most certainly lead to poor predictions.

Due to the irrelevance of the evaporator error without proper material inputs the condenser error provides a clear verdict on the fidelity of modeling required for different purposes. The condenser has a maximum finite difference error of 14.23% and a maximum hand calculation error of 16.13%. Both errors come in the increased load case, which has known issues with its initial state that cause this error. The maximum error for other condenser tests along with evaporator tests is shown in Table M.1. In Table M.1 the next highest error is 7.43% and 7.7% for the finite difference and analytical models respectively. This error is below 10%, which is acceptable in both cases. Although the error is comparable for both models the analytical model doesn't predict the behavior of the heat exchanger for the entirety of the test because it cannot capture sensible heat transfer in the PCC. Models for similar geometry have been developed by Wim Beyme and colleagues [71] that could be integrated with the model developed in Chapter 2 and allow for prediction in this region. Therefore, for the condenser the analytical solution can be used in design problems with confidence but should be used cautiously for simulation of device performance if the sensible region is relevant.

Lastly, the average error indicates similar results for the condenser and evaporator as seen in Table M.2.

Table M.2: Average discharged energy error.

		Baseline	Increased Load	Increased Peak Shaving
Condenser	Finite Difference	3.72%	8.08%	6.40%

	Analytical	3.47%	6.89%	2.86%
Evaporator	Finite Difference	10.55%	18.74%	17.40%
	Analytical	6.74%	12.21%	13.16%

All condenser errors in Table M.2 are below 10%, while most evaporator errors are above 10%. All are except for the baseline analytical model prediction. This is expected based on the maximum error and the results in Figure M.1. Therefore, the analytical model could be used to predict state of charge for a test that starts and ends in similar

Appendix N: Finite Difference Model Temperature Field Predictions

The finite difference model predicts the temperature field over the entire PCC slab, which helps visualize the progression of the phase front. The results for all condenser PCC temperature predictions are presented in Figure N.1.

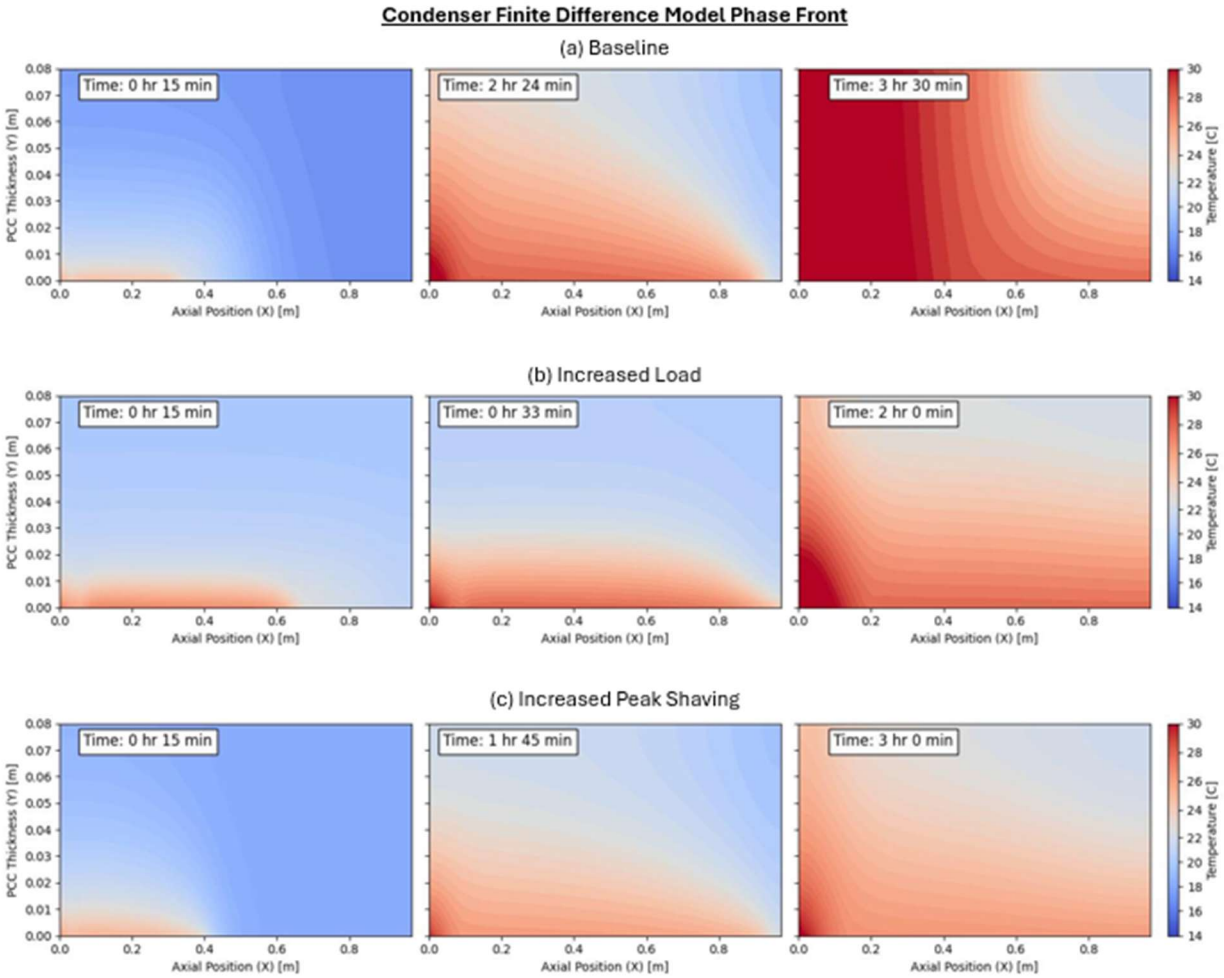

Figure N.1: The PCC temperature distribution over time for all condenser tests. (a) is the baseline (b) is the increased load case, and (c) is the increased peak shaving case. The color scale is centered at 22.3 C - the phase transition temperature used in model.

Figure N.1 shows the finite difference models temperature distribution predictions at the same times as plotted in Figure K.1. The initial time plotted shows the melt front beginning near the inlet. The second time plotted shows when the melt front reaches the full axial length of the heat exchanger. Finally, the last time plotted is arbitrary in Figure N.1a (baseline), but in Figure N.1b

and c (increased load and peak shaving) the melt front reaches the top of the PCC slab. Figure N.1a's final temperature distribution was arbitrarily selected because the melt front reaches the top of the PCC slab at the second time plotted – when the melt front reaches the outlet. The second and third time plotted in Figure N.1 provide a clear visualization the direction of progression. The baseline test (Figure N.1a) progresses on a diagonal. Meanwhile, the increased load case (Figure N.1b) progresses near vertical and the increased peak shaving case (Figure N.1c) is somewhere in between the baseline and increased load case. Therefore, the assumptions used to derive the analytical solution hold well for the increased load case, are questionable for the increased peak shaving case, and do not hold for the baseline case.

Predictions of the temperature field for the evaporator case verify the validity of the analytical solution's assumption that the melt front progresses vertically. Predictions of the temperature field are displayed in Figure N.2.

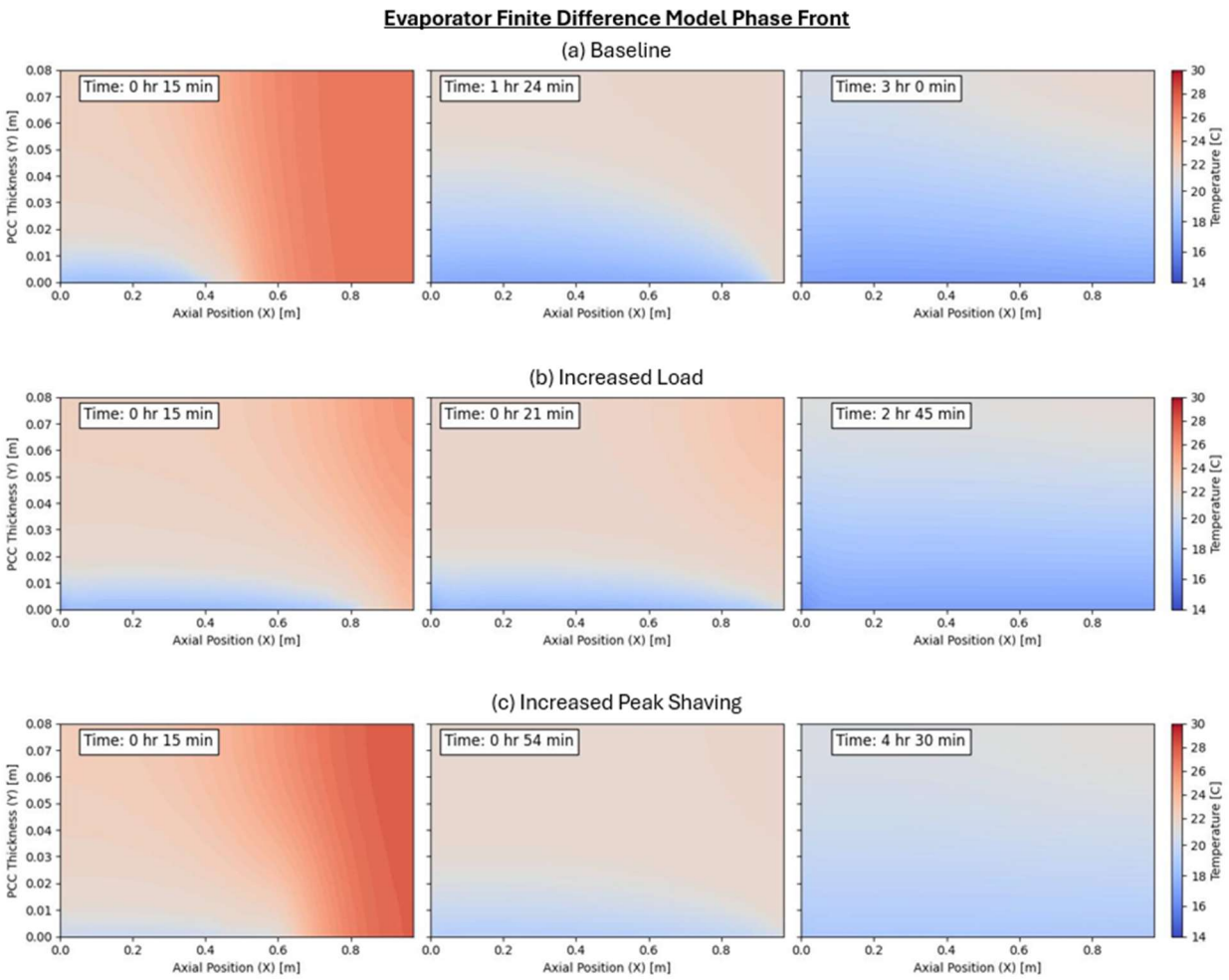

Figure N.2: The PCC temperature distribution over time for all condenser tests. (a) is the baseline (b) is the increased load case, and (c) is the increased peak shaving case. The color scale is centered at 21 C - the phase transition temperature used in model.

Figure N.2 shows the finite difference models temperature distribution predictions at the same times as plotted in the fiber optic cable plot (Figure K.2). The initial time plotted shows the freezing front beginning near the inlet. The second time plotted shows when the freezing front reaches the full axial length of the heat exchanger. Finally, the last time plotted when the melt front reaches the top of the PCC slab. The second and third time plotted in Figure N.2 provide a clear visualization the direction of freeze front progression. The behavior between baseline, increased load, and increased peak shaving cases is the same for each test. However, in general, the evaporators profile is more vertical than the condenser. The difference is likely due to the

difference in Enthalpy vs. Temperature curves, which is discussed in Chapter 5. Because the transition temperature for freezing is lower than melting the driving temperature difference is actually smaller than that defined in the test matrix – Table 5.1. In summary, the analytical model's assumptions are still valid for the increased load case, and increase confidence in the analytical model for baseline and increased peak shaving cases.